# Wave Propagation Algorithms
# for Multicomponent Compressible Flows
# with Applications to Volcanic Jets

Marica Pelanti

A dissertation submitted in partial fulfillment
of the requirements for the degree of

Doctor of Philosophy

University of Washington

2005

Program Authorized to Offer Degree:  Department of Applied Mathematics

University of Washington

Graduate School

This is to certify that I have examined this copy of a doctoral dissertation by

Marica Pelanti

and have found that it is complete and satisfactory in all respects,
and that any and all revisions required by the final
examining committee have been made.

Chair of Supervisory Committee:

_____

Randall J. LeVeque

Reading Committee:

_____

Randall J. LeVeque

_____

Loyce M. Adams

_____

Ka K. Tung

Date: _____

University of Washington

Abstract

# Wave Propagation Algorithms
## for Multicomponent Compressible Flows
## with Applications to Volcanic Jets

by Marica Pelanti

Chair of the Supervisory Committee:

Professor Randall J. LeVeque
Applied Mathematics

Numerical algorithms are developed for compressible multicomponent flow problems in the framework of wave propagation finite volume methods based on approximate Riemann solvers. Both models for multifluid flows, which involve pure species separated by well-defined interfaces, and for two-phase flows made of gas carrying a particulate suspension are studied.

In the context of multifluid problems, I propose a method for flows governed by an arbitrary equation of state $p(\mathcal{E}, \rho)$ based on a local linearization of the pressure law. The scheme is able to guarantee pressure equilibrium at material interfaces, avoiding the well-known numerical difficulty of the appearance of spurious pressure oscillations.

A two-phase model for particle-laden gases is then studied, which accounts for inter-phase drag and heat transfer, and gravity for both phases. A wave propagation algorithm is proposed to solve the governing equations, designed to guarantee an efficient treatment of source terms, and overcome the difficulties related to the non-strictly hyperbolic character of the equations of the pressureless particulate phase. In this context, the *f-wave* approach is employed, which enters into the framework of a general class of Riemann solvers (*Relaxation Riemann Solvers*) that we have introduced in a parallel study on the relation between relaxation schemes and approximate Riemann solvers.

The multi-dimensional two-phase *dusty gas* model is then applied to the simulation of jets and pyroclastic dispersion processes that characterize explosive volcanic events. In particular, I focus on the decompression phase of underexpanded supersonic volcanic jets on different crater morphology, describing the fluid dynamic structures that develop in the jet thrust region, such as internal shock waves. By means of numerical simulation I investigate the main factors controlling the expansion of the eruptive mixture and the generation of wave patterns above the conduit exit, with the aim of contributing to a better understanding of the complex and highly nonlinear thermo-fluid dynamic mechanisms governing these processes.

# TABLE OF CONTENTS

# LIST OF FIGURES

# LIST OF TABLES

# ACKNOWLEDGMENTS

Chapter 1

# INTRODUCTION

## *1.1 Thesis Objectives*

Hyperbolic conservation laws play a central role in physical modeling in several areas of science, as for instance fluid dynamics, geophysics, astrophysics, elastodynamics, magnetohydrodynamics, to mention only a few.

Among the numerical techniques for the solution of hyperbolic systems of conservation laws, a popular class of methods are finite volume schemes based on Godunov-type solvers. The contribution of Godunov in his celebrated paper [69] of 1959 is the idea of utilizing the solution of local Riemann problems in the construction of numerical schemes. Following Godunov, a wide variety of *approximate Riemann solvers* have been developed, especially in the context of Computational Fluid Dynamics. An important advance was in particular the solver of Roe presented in his famous paper [169] of 1981. Notable progress has been made in the design of Godunov-type algorithms, but further work is needed in the development of new and improved numerical methods. The general objective of my research activity that has led to the results reported in this thesis is the desire of contributing to this task.

This thesis concerns the numerical approximation of hyperbolic conservation laws by means of finite volume methods based on Riemann solvers with a special focus on compressible multicomponent fluid dynamics problems. Several theoretical and numerical challenges arise in the field of single, multifluid, and multi-phase flow modeling. Some aspects to be studied are for example the proper numerical treatment of source terms for gravity as well as terms expressing mechanical and thermal inter-phase energy exchange, and the need of avoiding unphysical solutions in the numerical approximation, such as negative densities or spurious pressure oscillations. Another challenging task is the design of solvers for systems with a non classical structure, as for instance the non-strictly hyperbolic system which arises in particle-laden flows modeling (zero pressure gas dynamics equations).

The work presented here is a collection of several distinct but related topics reflecting my research activity as a graduate student. In the context of multicomponent flows, two different physical problems have been studied: the case of two-fluid flows consisting of two pure species separated by well-defined interfaces, and the case of a two-phase flow made of a gaseous phase with suspended solid particles. My main interest in the latter model has been its application to volcanic processes occurring during explosive events. In the following, I give an overview of the various work done illustrating motivations and purposes.

## *1.2 Relaxation Riemann Solvers*

With the aim of overcoming some difficulties of existing methods and developing more robust and efficient numerical schemes, I have investigated the relation between relaxation schemes and approximate Riemann solvers. This has led to the work [124], which I partially incorporated in Chapter 5. In this paper we illustrate how a simple relaxation scheme of the type proposed by Jin and Xin [93] can be reinterpreted as defining a particular approximate Riemann solver for the original system of conservation laws. Based on this observation, a more general class of approximate Riemann solvers

(*relaxation* solvers) is proposed, and connections with standard solvers such as Roe's [169] and HLL [78] are explored. These relaxation solvers present a noticeable flexibility that can be exploited in deriving more efficient schemes.

In this framework enters the so-called *f-wave* formulation of the finite volume wave propagation algorithms described in [120], which has many useful applications, for example in the treatment of source terms and in the solution of conservation laws with spatially varying flux functions [10]. In particular, in our subsequent work on modeling two-phase particle-laden flows we have taken advantage of this f-wave approach to handle gravity source terms and to design a scheme that helps overcome the difficulties related to the non-strictly hyperbolic character of the equations of the pressureless particulate phase.

### 1.3   *Real Compressible Multifluid Flows*

Multifluid flows consist of pure fluids separated by well defined material interfaces. A classical example of multifluid problems is the simulation of shock-bubble interactions [73, 87, 165], which has applications for instance in the study of shock-induced mixing enhancement, underwater explosions, and lithotripsy.

A well-known difficulty [2, 108, 96, 193] in the computation of such flows by means of the Euler equations in conservative form is the possible appearance of spurious pressure oscillations at material interfaces. Many of the methods developed for compressible multifluid problems that are able to guarantee pressure equilibrium at material interfaces are restricted to the ideal polytropic gas law or the slightly more general stiffened gas equation of state [3, 4, 178, 74, 182]. Only recently has progress been made to build methods for multifluid flows governed by more general pressure laws [177, 179, 184, 5].

With the aim of ultimately contributing to the design of efficient algorithms for real multifluid problems, I have first developed a method for the computation of single-fluid real flows. This has been designed with the purpose of constructing a framework that could then be used in the solution of multifluid flows. The main idea of the method is to perform a local linearization of the governing equation of state. The approach of this Pressure Linearization Method (PLM) [163] defines a general and simple procedure for constructing finite volume methods for the computation of real fluids, and in particular it is advantageous in the extension of some classical solvers designed for a restricted class of equations of state to problems involving general pressure laws. An interesting feature of this method is its interpretation as a relaxation scheme. From this point of view it has similarity with the *energy relaxation* theory of Coquel and Perthame [39].

I have then extended this method to multifluid problems with arbitrary equations of state. This has led to the definition of a general and flexible algorithm for real multifluids which is able to avoid unphysical pressure oscillations at material interfaces. Although some work is still in progress, the results obtained until now are satisfactory.

### 1.4   *Dusty Gas Flows and Applications to Volcanic Jets and Plumes*

Another primary focus of my thesis is the analysis and development of numerical algorithms for gaseous flows carrying a particulate suspended phase (*dusty gas flows*), with applications to the modeling of the dynamics of volcanic explosive processes. Explosive volcanic eruptions release a hot dense mixture of gas and particulate material into the atmosphere. Characteristic features of these processes are the jet thrusting at the vent exit, pyroclastic dispersion in the atmosphere, and pyroclastic flows on the ground surface.

Since the mid-1970s notable progress has been made in the physical modeling of the eruption dynamics, and in particular of pyroclastic dispersion mechanisms. The first step was the formulation of one-dimensional steady-state single-phase and incompressible flow models that attempted to investi-

gate the main features of Plinian (buoyant) and collapsing columns (Sparks and Wilson in 1976 [185], Wilson in 1976 [204], Sparks et al. in 1978 [186]). Although these and following theoretical models, e.g. Wilson and Walker [205] (1987), Woods [208] (1988), Bursik and Woods [23] (1996), are effective in describing some of the mechanisms of eruption phenomena, they are unable to address time-dependent or multidimensional processes, and thus their simplified formulation limits their applicability to real volcanic events.

A fundamental advance in the analysis of eruption dynamics processes has been the introduction of numerical multidimensional multi-phase flow models. Some early numerical studies on explosive volcanic phenomena were made in 1984 by researchers at the Los Alamos National Laboratory, who performed simulations of caldera-forming eruptions (Wohletz et al. [206]).

Further progress and considerable work have been made since then in the numerical multi-phase modeling of volcanic plumes and pyroclastic flows. Among the relevant contributions let us mention for instance the work of Valentine and Wohletz [197] (1989), Wohletz and Valentine [207] (1990), Dobran et al. [51] (1993), Neri and Dobran [150] (1994), Papale et al. [162] (1998), Neri et al. [156] (1998), Neri et al. [153] (2003), Dartevelle et al. [44] (2004).

These numerical studies have provided new insight into many relevant features of volcanic phenomena, and in particular have allowed the description of the unsteady and transient behaviour of eruption columns. The results obtained have shown how numerical simulation is an important tool in the understanding of the complex and highly nonlinear mechanisms that govern the thermo-fluid dynamics of volcanic eruptions.

Well established numerical models used in volcanology to simulate explosive eruption processes, like those employed in the works mentioned above, commonly use a numerical methodology based on the technique for multi-phase flows presented by Harlow and Amsden in 1975 [75], and known as Implicit MultiField method (IMF). Here the time-dependent two-phase compressible Navier–Stokes equations are solved by a finite difference algorithm that uses an iterative procedure for pressure to satisfy mass conservation. Moreover, an implicit treatment is adopted for the momentum exchange term. First computer codes to implement this approach were the KACHINA program [6] (Amsden and Harlow, 1974) and the KACHINA with Fully Implicit Exchange (K-FIX) of Rivard and Torrey [168] (1977). Different computer programs were later used by Wohletz and co-workers [206, 207, 197], Neri and co-workers [51, 150, 162, 156, 155], Dartevelle et al. [44], but all belong to the so called "FIX" family descending from the K-FIX code of [168].

Here we propose a different numerical approach in this field, modeling the dynamics of explosive eruptions by means of the wave propagation algorithms as implemented in the CLAWPACK software [115]. These are high resolution finite volume methods based on Riemann solvers used for the hyperbolic conservation law portion of the governing equations. Moreover, interphase momentum and energy exchange terms are treated explicitly, by employing a fractional step technique combined with a semi-analytical solver (see Chapter 7).

Although to start the numerical study a simple physical model based on the compressible Euler equations has been adopted, which neglects some effects such as viscosity and turbulence, we will show that we are able to capture some of the characterizing features of volcanic columns and pyroclastic flows.

A primary objective of our numerical investigation is to study the structure and dynamics of over-pressured volcanic jets. Gas flows containing particulate material can have very low sound speed, so that volcanic jets are often supersonic, and they undergo an expansion at the exit of the conduit in which complex fluid dynamic structures such as internal shock waves may develop.

The decompression process is very important in determining the evolution of the volcanic column above the conduit exit and its atmospheric dispersal behaviour (e.g. [210]). This phase of the eruption is not a process susceptible to direct observation, and the internal structure of volcanic jets is very

difficult to document. Theoretical analyses such as the one of Woods and Bower [210] (1995) are based on simplified models, which use a homogeneous pseudo-gas approximation. Although important, they are unable to describe transient processes and flow unsteadiness and instabilities. Laboratory experiments have also been performed on volcanic jets, e.g. Kieffer and Sturtevant [100] (1984). The main limit of this experimental approach is the lack of a scaling relation for gravity and the description of the related buoyancy forces. Therefore, numerical simulation is a precious tool to investigate the mechanisms of the decompression phase of volcanic jets.

While extensive studies have been done on the numerical modeling of pyroclastic dispersion dynamics processes, little numerical work exists on the description of the jet internal structure. This motivates further our investigation. Moreover, because of the conservative shock-capturing character of our numerical algorithm, we expect our method to be particularly effective in modeling the development of shock wave patterns in the jet thrust region.

On the simulation of overpressured jets joint work is also in progress with A. Neri and T. Esposti Ongaro of INGV (Istituto Nazionale di Geofisica e Vulcanologia, Pisa, Italy), who already made preliminary studies on this subject [159] (1999), and suggested to us the guidelines of our investigation. The aim of this joint project is to compare results obtained with two different numerical multi-phase models, our model that uses CLAWPACK and their model that employs PDAC (Pyroclastic Dispersion Analysis Code) [155], which is based on the Harlow and Amsden technique [75]. Preliminary results are encouraging. In the context of this work we study in particular the role played in the expansion process by the crater morphology. As it will be shown by the numerical simulations reported in Chapter 8 the type of internal shock structure can be significantly different depending on the geometry of the crater.

Another challenge in the context of the simulation of volcanic phenomena is the development of a fully three dimensional model, which in particular could be useful in the assessment of volcanic hazard. We will return to discuss this in outlining the directions of future work in Chapter 9.

### 1.5   Thesis Outline

The general notions of hyperbolic conservation laws, together with the standard compressible Euler equations of gas dynamics, are introduced in Chapter 2 of the thesis. Chapter 3 is dedicated to presenting multicomponent flow models on which I focused my work. The numerical algorithms used, and in particular their wave propagation formulation, are presented in Chapter 4. Chapter 5 is dedicated to reporting the results of the study on the relation between relaxation schemes and approximate Riemann solver [124]. In Chapter 6 I will describe the Pressure Linearization Method for single and multifluid real compressible flows. In Chapter 7 the proposed physical and numerical model for dusty gas flows is illustrated, and results of the numerical simulation of the dynamics of volcanic eruption processes performed by applying this model are reported and discussed in Chapter 8. Finally, in Chapter 9, I write some concluding remarks and outline some directions for future work.

Chapter 2

# HYPERBOLIC SYSTEMS OF CONSERVATION LAWS AND THE COMPRESSIBLE EULER EQUATIONS OF GAS DYNAMICS

## 2.1 Hyperbolic Systems of Conservation Laws

The general form of a system of $m$ conservation laws in $d$ space dimensions is

$$\frac{\partial q}{\partial t} + \sum_{j=1}^{d} \frac{\partial f_j(q)}{\partial x_j} = 0\,, \quad x = (x_1, \ldots, x_d)^{\mathrm{T}} \in \mathbb{R}^d\,, \quad t > 0\,, \tag{2.1}$$

where $q = (q_1, \ldots, q_m)^{\mathrm{T}}$, $q_p = q_p(x,t)$, $1 \leq p \leq m$, is the vector of the state variables, and $f_j = (f_{1j}, \ldots, f_{mj})^{\mathrm{T}}$, $1 \leq j \leq d$, are called *flux functions*.

We can see that formally the system (2.1) expresses the conservation of the $m$ quantities $q_1, \ldots, q_p$. In fact, let $\Omega$ be an arbitrary domain in $\mathbb{R}^d$, and $n = (n_1, \ldots, n_d)^{\mathrm{T}}$ the outward unit normal to the boundary $\partial\Omega$ of $\Omega$. Then, from (2.1) we have

$$\frac{d}{dt} \int_{\Omega} q\, dx + \sum_{j=1}^{d} \int_{\partial\Omega} f_j(q) n_j dS = 0\,. \tag{2.2}$$

This balance equation states that the positive time variation of $\int_{\Omega} q\,dx$ is equal to the inward flux of $q$ through the boundary $\partial\Omega$.

We are here interested in studying system of conservation laws that are *hyperbolic* in the following sense:

DEFINITION 2.1 *For $j = 1, \ldots, d$, let*

$$A_j(q) = \left( \frac{\partial f_{ij}}{\partial q_p}(q) \right)_{1 \leq i, p \leq m}$$

*be the Jacobian matrix of $f_j(q)$; the system (2.1) is called hyperbolic if for any $q \in \Omega$ and any $\omega = (\omega_1, \ldots \omega_d)^T \in \mathbb{R}^d$, $|\omega| = 1$, the matrix*

$$A(q, \omega) = \sum_{j=1}^{d} \omega_j A_j(q)$$

*has $m$ real eigenvalues $\lambda^1(q, \omega) \leq \lambda^2(q, \omega) \leq \ldots \leq \lambda^m(q, \omega)$ and $m$ linearly independent corresponding eigenvectors $r^1(q, \omega), \ldots, r^m(q, \omega)$, that is*

$$A(q, \omega) r^p(q, \omega) = \lambda^p(q, \omega) r^p(q, \omega)\,, \qquad 1 \leq p \leq m\,.$$

*If, in addition, the eigenvalues $\lambda^p(q, \omega)$ are all distinct, then the system (2.1) is called strictly hyperbolic.*

For the hyperbolic systems introduced here we shall consider the initial value problem (*Cauchy problem*) consisting of the equations (2.1) augmented with the initial condition $q(x, 0) = q_0(x)$, where $q_0(x)$ is a given function defined on $\mathbb{R}^d$.

## 2.2  Weak Solutions

A *classical* solution of (2.1) is a smooth function $q$ that satisfies (2.1) pointwise. An important feature of the problems we are interested in is that we want to allow for solutions having discontinuities. Such functions cannot satisfy the partial differential equations (2.1), but do satisfy the integral form of the conservation laws

$$\int_{\mathcal{T}}\int_{\Omega} q\,dxdt + \sum_{j=1}^{d}\int_{\mathcal{T}}\int_{\partial\Omega} f_j(q)n_j dSdt = 0\,, \qquad \forall \Omega \subseteq \mathbb{R}^d\,, \ \ \forall \mathcal{T} \subseteq [0,+\infty)\,. \tag{2.3}$$

Hence we appeal to the integral form (2.3) to define a solution $q$ in a generalized sense, or *weak solution*[1] of (2.1).

 If we consider a piecewise smooth function $q$, then in the regions where $q$ is smooth it is a classical solution, while we can use the integral form of the equations to derive conditions that hold across discontinuities. Specifically, denoting with $q_\pm$ the limits of $q$ on each side of a surface of discontinuity, the following *Rankine–Hugoniot* condition is satisfied:

$$s(q_+ - q_-) = \sum_{j=1}^{d} n_j (f(q_+) - f(q_-))\,, \tag{2.4}$$

where $s$ represents the speed of propagation of the discontinuity and $n \in \mathbb{R}^d$ is a unit vector indicating the direction of propagation.

 To end this section, we remark that a weak solution of a system of conservation laws is not necessarily unique, hence we need to select among the possible weak solutions the unique physically relevant solution of the problem. This is called *entropy solution* by analogy with gas dynamics, and can be viewed as the limit of the viscous (parabolic) problem associated to the considered hyperbolic problem as the viscosity parameter goes to zero (vanishing viscosity solution). See e.g. [118, 68].

## 2.3  One-Dimensional Riemann Problem

We now focus on the one-dimensional system

$$\frac{\partial q}{\partial t} + \frac{\partial f(q)}{\partial x} = 0\,, \quad x \in \mathbb{R}\,, \quad t > 0\,. \tag{2.5}$$

Here $q$ is a vector of $m$ conserved quantities and $f(q)$ the corresponding flux function. We will assume that (2.5) is strictly hyperbolic, that is, according to Definition 2.1, for any $q \in \Omega \subset \mathbb{R}^m$ the Jacobian matrix $A(q) = f'(q)$ has $m$ distinct real eigenvalues $\lambda^p(q)$ and $m$ linearly independent eigenvectors $r^p(q)$, $1 \le p \le m$. We remark that most of the results reported in this section will hold also for a (non strictly) hyperbolic system, provided the eigenvectors are complete and the eigenvalues have constant multiplicity.

 For (2.5), we shall consider initial data with the particular form:

$$q_0(x) = \begin{cases} q_\ell & \text{if } x < 0\,, \\ q_r & \text{if } x > 0\,. \end{cases} \tag{2.6}$$

In such a case, problem (2.5), (2.6) is called the (one-dimensional) *Riemann problem.*

 It is important to note that solutions $q(x,t)$ to this problem are self-similar, that is $q(x,t) = q_{\mathrm{R}}(\frac{x}{t})$.

---

[1]A rigorous mathematical definition of weak solution of a hyperbolic system of conservation laws is based on distribution theory.

### 2.3.1  Linear Systems

For a linear system $\partial q/\partial t + A\,\partial q/\partial x = 0$, with a constant coefficient matrix $A$, the solution of the Riemann problem consists of $(m+1)$ constant states $\tilde{q}^{\,0} = q_\ell, \tilde{q}^{\,1}, \ldots, \tilde{q}^{\,(m-1)}, \tilde{q}^{\,m} = q_r$, separated by $m$ discontinuities that propagate at speeds given by the eigenvalues of $A$. Each constant state can be expressed as $\tilde{q}^{\,p} = q_\ell + \sum_{k=1}^{p} \alpha^k r^k$, where the coefficients $\alpha^1, \ldots, \alpha^m$ are obtained by projecting the jump $q_r - q_\ell$ onto the eigenvectors of $A$, i.e., $q_r - q_\ell = \sum_{p=1}^{m} \alpha^p r^p$.

### 2.3.2  Nonlinear Systems

We introduce the following definitions:

DEFINITION 2.2  *The $p$-th characteristic field is said to be genuinely nonlinear if*

$$\nabla \lambda^p(q) \cdot r^p(q) \neq 0 \,, \quad \forall q \in \Omega \,. \tag{2.7}$$

DEFINITION 2.3  *The $p$-th characteristic field is said to be linearly degenerate if*

$$\nabla \lambda^p(q) \cdot r^p(q) = 0 \,, \quad \forall q \in \Omega \,. \tag{2.8}$$

Let us consider a single discontinuity connecting two states $q_\ell$ and $q_r$ and travelling at speed $s$. In order for this discontinuity to be a (weak) solution of the Riemann problem, the Rankine–Hugoniot condition (2.4) must be satisfied:

$$s(q_r - q_\ell) = f(q_r) - f(q_\ell) \,. \tag{2.9}$$

In a genuinely nonlinear field a discontinuous solution of this type is a *shock wave*, whereas in a linear degenerate field it is called *contact discontinuity*, and in this case $s = \lambda^p(q_\ell) = \lambda^p(q_r)$. Note that for shock waves proper conditions will be needed in addition to (2.9) in order to select the unique physically relevant solution. In particular, the so-called *Lax entropy condition* requires that $\lambda^p(q_\ell) > s > \lambda^p(q_r)$, this meaning that the characteristic lines should go into the shock.

In a genuinely nonlinear field a smoothly varying solution, a *rarefaction wave*, can also occur. This solution has the property of lying on integral curves of the characteristic field, i.e. curves $v(\xi)$ satisfying $v'(\xi) = r^p(v(\xi))$.

Let us conclude with the following result (e.g. [68]): under the hypothesis that the characteristic fields of the system (2.5) are either genuinely nonlinear or linearly degenerate, the Riemann problem (2.5),(2.6) has a unique (weak) solution, assuming $|q_r - q_\ell|$ is sufficiently small; moreover, this solution consists of at most $(m+1)$ constant states separated by rarefaction waves, shocks, or contact discontinuities.

## 2.4  The Compressible Euler Equations of Gas Dynamics

The Euler equations for a compressible inviscid fluid with no thermal conductivity can be written, in the one-dimensional case, as the following system of conservation laws:

$$\frac{\partial q}{\partial t} + \frac{\partial f(q)}{\partial x} = 0 \,, \tag{2.10a}$$

with

$$q = \begin{bmatrix} \rho \\ m \\ E \end{bmatrix} \quad \text{and} \quad f(q) = \begin{bmatrix} m \\ \dfrac{m^2}{\rho} + p \\ \dfrac{m}{\rho}(E + p) \end{bmatrix} \,. \tag{2.10b}$$

Here $\rho$ is the fluid density, $m = \rho u$ the linear momentum, with $u$ denoting the velocity along the $x$ axis, $E = \mathcal{E} + \frac{1}{2}\rho u^2$ the total energy per unit volume, $\mathcal{E} = \rho\varepsilon$ the internal energy per unit volume, and $\varepsilon$ the internal energy per unit mass (specific internal energy). Finally $p$ denotes the pressure. The complete definition of the problem requires the specification of the relation between the pressure and the conserved variables.

In condition of local equilibrium, the pressure can be expressed as a function of two other thermodynamic variables through an equation of state (EOS). Unless otherwise specified, we will assume the pressure is a function of the variables $\mathcal{E}$ and $\rho$, $p = p(\mathcal{E}, \rho)$, hence the closure of the system (2.10) is obtained through the relation:

$$p = p(\mathcal{E}, \rho) = p\left(E - \frac{m^2}{2\rho}, \rho\right). \tag{2.11}$$

For convenience in describing some thermodynamic properties, exclusively at this point in this section, let us consider the pressure in terms of the specific entropy $s$ and the density $\rho$, $p = p(s, \rho)$. Assuming that $(\partial p / \partial \rho)_{s=\text{const.}} > 0$, as required for thermodynamic stability, we can introduce the speed of sound $c$,

$$c = \sqrt{\left.\frac{\partial p}{\partial \rho}\right|_s} \tag{2.12}$$

and the so-called *fundamental derivative*

$$\mathcal{G} = \frac{1}{c} \left.\frac{\partial(\rho c)}{\partial \rho}\right|_s . \tag{2.13}$$

We will assume $\mathcal{G} > 0$ (*convex* equation of state), which implies in particular that the density and the pressure of the fluid increase across the shock waves (compression shocks).

Returning from now on to the equation of state in terms of the variables $(\mathcal{E}, \rho)$, we introduce the thermodynamic derivatives

$$\kappa(\mathcal{E}, \rho) \equiv \frac{\partial p(\mathcal{E}, \rho)}{\partial \mathcal{E}} \qquad \text{and} \qquad \chi(\mathcal{E}, \rho) \equiv \frac{\partial p(\mathcal{E}, \rho)}{\partial \rho} . \tag{2.14}$$

The speed of sound is related to the above quantities through the equality:

$$c^2 = \kappa h + \chi , \tag{2.15}$$

where

$$h = \frac{\mathcal{E} + p}{\rho} \tag{2.16}$$

is the specific enthalpy. We also define here the total specific enthalpy:

$$H = h + \frac{1}{2}u^2 . \tag{2.17}$$

The Jacobian matrix $A(q) = f'(q)$ of the Euler system is

$$A(q) = \begin{bmatrix} 0 & 1 & 0 \\ \chi + \kappa \frac{u^2}{2} - u^2 & (2 - \kappa)u & \kappa \\ u\left(\chi + \kappa \frac{u^2}{2} - H\right) & H - \kappa u^2 & (1 + \kappa)u \end{bmatrix}, \tag{2.18}$$

and it has eigenvalues

$$\lambda^1 = u - c, \qquad \lambda^2 = u, \qquad \lambda^3 = u + c, \tag{2.19}$$

with right eigenvectors:

$$r^1 = \begin{bmatrix} 1 \\ u - c \\ H - uc \end{bmatrix}, \quad r^2 = \begin{bmatrix} 1 \\ u \\ H - \frac{c^2}{\kappa} \end{bmatrix}, \quad r^3 = \begin{bmatrix} 1 \\ u + c \\ H + uc \end{bmatrix}. \tag{2.20}$$

For the eigenstructure above, under the hypothesis $\mathcal{G} > 0$, we find that the first and third characteristic fields are genuinely nonlinear, while the second field is linearly degenerate. As a consequence, the solution of the Riemann problem for the Euler equations will be composed by three waves, of which the first and the third can be either shocks or rarefactions (*acoustic waves*), while the second wave will always be a contact discontinuity. It is important to note that across the contact wave the pressure and the velocity are invariant. It carries however a jump in entropy and for this reason is also called *entropy wave*. A typical solution is shown in Fig. 2.4.
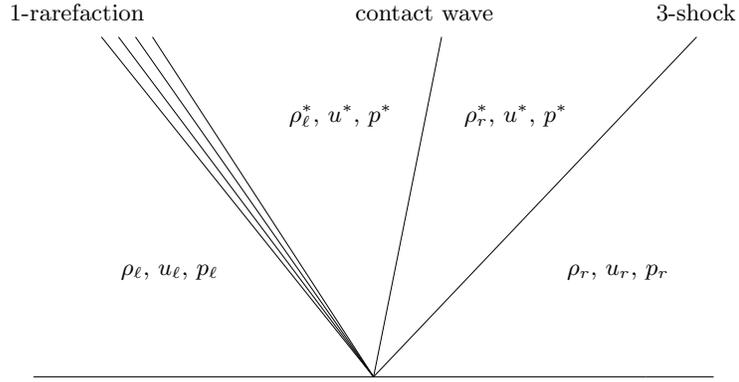


Figure 2.1: Typical solution of the Riemann problem for the Euler equations.

### 2.4.1 Two-Dimensional Euler Equations

In two space dimensions the Euler equations take the form:

$$\frac{\partial q}{\partial t} + \frac{\partial f(q)}{\partial x} + \frac{\partial g(q)}{\partial y} = 0, \tag{2.21a}$$

with

$$q = \begin{bmatrix} \rho \\ \rho u \\ \rho v \\ E \end{bmatrix}, \quad f(q) = \begin{bmatrix} \rho u \\ \rho u^2 + p \\ \rho u v \\ u(E + p) \end{bmatrix}, \quad g(q) = \begin{bmatrix} \rho v \\ \rho u v \\ \rho v^2 + p \\ v(E + p) \end{bmatrix}. \tag{2.21b}$$

The components of the velocity in the $x$ and $y$ direction are denoted with $u$ and $v$, respectively. The total energy is $E = \mathcal{E} + \frac{1}{2}(u^2 + v^2)$, and the total enthalpy $H = h + \frac{1}{2}(u^2 + v^2)$.

Let us consider the matrix $A(q, \omega)$ introduced in Definition 2.1:

$$A(q, \omega) = f'(q)\omega_1 + g'(q)\omega_2, \quad \omega = (\omega_1, \omega_2)^{\mathrm{T}}, \ |\omega| = 1, \tag{2.22}$$

where

$$
f'(q) = \begin{bmatrix}
0 & 1 & 0 & 0 \\
\chi + \kappa \frac{u^2+v^2}{2} - u^2 & (2-\kappa)u & -\kappa v & \kappa \\
-uv & v & u & 0 \\
u\left(\chi + \kappa \frac{u^2+v^2}{2} - H\right) & H - \kappa u^2 & -\kappa uv & (1+\kappa)u
\end{bmatrix},
\tag{2.23}
$$

and

$$
g'(q) = \begin{bmatrix}
0 & 0 & 1 & 0 \\
-uv & v & u & 0 \\
\chi + \kappa \frac{u^2+v^2}{2} - v^2 & -\kappa u & (2-\kappa)v & \kappa \\
v\left(\chi + \kappa \frac{u^2+v^2}{2} - H\right) & -\kappa uv & H - \kappa v^2 & (1+\kappa)v
\end{bmatrix}.
\tag{2.24}
$$

The matrix $A(q,\omega)$ has eigenvalues

$$
\lambda^1 = \mathcal{V} \cdot \omega - c, \qquad \lambda^2 = \mathcal{V} \cdot \omega, \qquad \lambda^3 = \mathcal{V} \cdot \omega, \qquad \lambda^4 = \mathcal{V} \cdot \omega + c,
\tag{2.25}
$$

where $\mathcal{V} = (u, v)^{\mathrm{T}}$. The eigenvectors can be chosen as

$$
r^1 = \begin{bmatrix} 1 \\ u - c\,\omega_1 \\ v - c\,\omega_2 \\ H - \mathcal{V} \cdot \omega\, c \end{bmatrix}, \quad
r^2 = \begin{bmatrix} 1 \\ u \\ v \\ H - \frac{c^2}{\kappa} \end{bmatrix}, \quad
r^3 = \begin{bmatrix} 0 \\ -\omega_2 \\ \omega_1 \\ \mathcal{V} \cdot \omega^{\perp} \end{bmatrix}, \quad
r^4 = \begin{bmatrix} 1 \\ u + c\,\omega_1 \\ v + c\,\omega_2 \\ H + \mathcal{V} \cdot \omega\, c \end{bmatrix}, \quad
\tag{2.26}
$$

with $\omega^{\perp} = (-\omega_2, \omega_1)^{\mathrm{T}}$.

The two distinct eigenvalues $\lambda^1$ and $\lambda^4$ give genuinely nonlinear fields, while the eigenvalue with multiplicity 2, $\lambda^2 = \lambda^3 = \mathcal{V} \cdot \omega$, is associated to distinct linearly degenerate fields corresponding to $r^2$ and $r^3$.

If we consider a plane-wave Riemann problem in the $\omega$ direction (one in which data vary only along $\omega$), then the solution consists of at most four constant states separated by three waves. Two waves are associated to the genuinely nonlinear fields of $\{\lambda^1, r^1\}$ and $\{\lambda^4, r^4\}$, and can be either shocks or rarefactions (acoustic waves). Then there is a contact discontinuity with speed $\lambda^2 = \lambda^3 = \mathcal{V} \cdot \omega$ that can be considered as composed of two independent linearly degenerate waves corresponding to the distinct eigenvectors $r^2$ and $r^3$: an entropy wave, carrying a jump in entropy, and a *shear wave*, which carries a jump in the tangential velocity $\mathcal{V} \cdot \omega^{\perp}$. The pressure $p$ and the normal velocity $\mathcal{V} \cdot \omega$ are invariant across the contact discontinuity.

### 2.4.2   Three-Dimensional Euler Equations

In three space dimensions the Euler equations have a form similar to (2.21), but with an additional conservation equation for the momentum $\rho w$ in the $z$ direction, where $w$ is the $z$-component of the velocity. The system is:

$$
\frac{\partial q}{\partial t} + \frac{\partial f(q)}{\partial x} + \frac{\partial g(q)}{\partial y} + \frac{\partial h(q)}{\partial z} = 0,
\tag{2.27a}
$$

with

$$
q = \begin{bmatrix} \rho \\ \rho u \\ \rho v \\ \rho w E \end{bmatrix}, \quad
f(q) = \begin{bmatrix} \rho u \\ \rho u^2 + p \\ \rho uv \\ \rho uw \\ u(E+p) \end{bmatrix}, \quad
g(q) = \begin{bmatrix} \rho v \\ \rho uv \\ \rho v^2 + p \\ \rho uw \\ v(E+p) \end{bmatrix}, \quad
h(q) = \begin{bmatrix} \rho w \\ \rho uw \\ \rho vw \\ \rho w^2 + p \\ w(E+p) \end{bmatrix}.
\tag{2.27b}
$$

Here the total energy is $E = \mathcal{E} + \frac{1}{2}(u^2 + v^2 + w^2)$. In any direction $\omega = (\omega_1, \omega_2, \omega_3)^{\mathrm{T}}$, $|\omega| = 1$, there are two nonlinear acoustic fields with eigenvalues $\mathcal{V} \cdot \omega \pm c$, $\mathcal{V} = (u, v, w)^{\mathrm{T}}$, and three linearly degenerate fields with eigenvalue $\mathcal{V} \cdot \omega$.

### 2.4.3 Three-Dimensional Euler Equations with Axial Symmetry

If the solution of a three-dimensional problem is known to be axisymmetric, then the equations can be rewritten in cylindrical coordinates $(r, \theta, z)$, and the system we obtain can be reduced to a problem in the two space variables $r$ and $z$.

Denoting with $U$ and $V$ the components of the velocity in the radial and vertical direction, respectively, the Euler equations with axial symmetry take the following form:

$$\frac{\partial}{\partial t} \begin{bmatrix} \rho \\ \rho U \\ \rho V \\ E \end{bmatrix} + \frac{\partial}{\partial r} \begin{bmatrix} \rho U \\ \rho U^2 + p \\ \rho U V \\ U(E + p) \end{bmatrix} + \frac{\partial}{\partial z} \begin{bmatrix} \rho V \\ \rho U V \\ \rho V^2 + p \\ V(E + p) \end{bmatrix} = \begin{bmatrix} -(\rho U)/r \\ -(\rho U^2)/r \\ -(\rho U V)/r \\ -U(E + p)/r \end{bmatrix}. \tag{2.28}$$

Note that system (2.28) has the same form as the two-dimensional system (2.21), but with the addition of a geometric source term on the right-hand side.

Chapter 3

# COMPRESSIBLE MULTICOMPONENT FLOW MODELS

## 3.1 Multicomponent Flows

Multicomponent flows contain distinct species with different physical and thermodynamical properties. Following Saurel and Abgrall [177], we shall distinguish between two situations: multifluid flows and multiphase flows. In the first case, we consider pure fluids separated by well defined material interfaces, as for instance in the classical example of a shock in air interacting with a bubble of helium [73, 87, 165]. On the other hand, multiphase flows consist in general of a carrier phase (gas or liquid) with suspended solid particles, or droplets or bubbles. Computationally, in the case of multifluid flow nearly all control volumes contain pure phases, except for the cells around the interface, whereas in the case of multiphase flows each control volume contains a large number of particles (or droplets, etc.) suspended into the carrier phase.

Typically, these two distinct situations are treated with different mathematical and numerical models, though some models have been proposed in the literature that apply to both cases, e.g. [177, 179, 148]. Here we will consider the mathematical description of the two physical problems and their numerical treatment separately. In the next section we will illustrate a model for compressible multifluid flows. Then, in Section 3.3, we will present a two-phase flow model, focusing our study to the case in which the carried phase is assumed to be dilute, and incompressible at the microscopic scale.

## 3.2 Multifluid Models

A wide variety of methods have been proposed for the computation of compressible multifluid flows. A group of methods corresponds to approaches where the numerical diffusion at the interfaces is eliminated. Among these, there are Lagrangian methods [12], front-tracking methods [67, 72, 34, 135, 125], VOF (volume-of-fluid) methods [80, 141, 193], level set methods [45, 27, 147], and the ghost-fluid method [59]. Some concise review can be found for instance in [178, 179].

Here we are interested instead in methods that allow numerical diffusion at the interface [96, 3, 97, 165, 4, 107, 177, 178, 34, 182, 183, 184, 90, 5], and we shall focus on approaches based on the conservative Euler equations (see e.g. the review of Abgrall and Karni [4]). In this class of methods a *mixture model*, or an artificial equation of state for the mixture, must be provided to describe the region where the interface between different components is numerically spread.

### 3.2.1 Mixture Model

In general, the fluid flow is modeled by the compressible Euler equations, which here we consider in the one-dimensional conservative form (2.10). The flow description is then completed by providing one or more additional equations that govern the dynamics of the fluid composition, and by specifying an equation of state for the fluid mixture.

We will assume for the moment that the fluid consists of two pure components each governed by the ideal polytropic gas law $p = (\gamma - 1)\mathcal{E}$, with the value of the heat coefficient ratio $\gamma$ depending on the material.

Let us denote with $\psi$ a variable describing the flow composition, so that $\gamma = \gamma(\psi)$. Several choices of $\psi$ have been suggested in the literature. For instance in [170] $\psi = \gamma$, while in [2, 107, 106] $\psi$ is defined as the mass fraction of one fluid component. Note that, although formulations based on different definitions of $\psi$ can be mathematically equivalent, they lead to different numerical discretizations, hence special care is needed in the choice of $\psi$, as we will see in the following.

In all the models the variable $\psi$ is governed by an advection equation:

$$\frac{\partial \psi}{\partial t} + u\,\frac{\partial \psi}{\partial x} = 0\,, \tag{3.1a}$$

which can also be written in conservation form, by using the mass conservation equation $\partial\rho/\partial t + \partial(u\rho)/\partial x = 0$:

$$\frac{\partial}{\partial t}\left(\rho\psi\right) + \frac{\partial}{\partial x}\left(u\rho\psi\right) = 0\,. \tag{3.1b}$$

In summary, the mathematical model of the multifluid flow consists of the Euler system (2.10) augmented with the equation (3.1a) (or (3.1b)), with the closure provided by the equation of state

$$p = (\gamma(\psi) - 1)\mathcal{E}\,. \tag{3.2}$$

The structure of the solution of the Riemann problem for this system of equations is the same as the one that characterizes the Euler system, that is there are two acoustic waves, and a contact discontinuity across which the pressure and the velocity are invariant. The variable $\psi$, as well as $\gamma(\psi)$ (also convected by the flow), is invariant across shocks and rarefactions, and can only have discontinuities across the contact wave, which is also called in this context the material interface.

### 3.2.2   Pressure Oscillations

A well known difficulty [2, 108, 96, 193] with the class of multifluid models based on the conservative Euler equations that we have introduced in the previous section is ensuring that pressure equilibrium is maintained at material interfaces.

In order to obtain a method that avoids pressure oscillations, it is necessary to make an appropriate choice of the variable $\psi$ and of the discretization of its governing equation (that is (3.1a) vs. (3.1b)).

For example, the choice $\psi = \gamma$ [170] fails to maintain pressure equilibrium [4]. An effective formulation, adopted for instance by Abgrall [3], Shyue [182], and Saurel and Abgrall [178], is based on taking $\psi = \frac{1}{\gamma-1}$, and describing its dynamics through the *advection equation*:

$$\frac{\partial}{\partial t}\left(\frac{1}{\gamma-1}\right) + u\,\frac{\partial}{\partial x}\left(\frac{1}{\gamma-1}\right) = 0\,. \tag{3.3}$$

Note that it is important to use a discretization of this equation in nonconservative form. The scheme will fail to ensure pressure equilibrium if the corresponding conservative form (3.1b) is used [182].

In the next section we will illustrate how we can devise a model that maintains pressure equilibrium at material interfaces for a more general equation of state which encompasses the ideal polytropic gas law assumed so far.

Moreover, in Chapter 6 we will discuss the problem of pressure oscillations, ascribing it to an intrinsic difficulty of conservative formulations.

### 3.2.3   Shyue-Type Model

Following the method of Shyue [182, 183, 184], we extend the type of model based on (3.3) to the case of a mixture of fluids each governed by an equation of state linear in the thermodynamic variables $\rho$ and $\mathcal{E}$ :

$$p(\mathcal{E}, \rho) = \bar{\kappa}\mathcal{E} + \bar{\chi}\rho + \beta\,. \tag{3.4}$$

The quantities $\bar{\kappa}$, $\bar{\chi}$ and $\beta$ are constant for each component, but have different values depending on the species. These three quantities describe the flow composition and they will be advected by the flow. However, in order to construct a numerical model that avoids pressure oscillations, we need to select three appropriate material-dependent quantities as variables of the problem, in general different from $\bar{\kappa}$, $\bar{\chi}$ and $\beta$. Correspondingly, three equations expressing the advection of these three selected flow-composition variables must be provided, either in the nonconservative form (3.1a) or the conservative one (3.1b). Also this choice is based on the need of maintaining numerically the pressure equilibrium at material interfaces.

To derive an effective formulation, we begin by considering an *interface-only* problem, that is the situation in which both the pressure $p$ and the velocity $u$ are constant in the domain. Other variables such as the density and the material-dependent parameters $\bar{\kappa}$, $\bar{\chi}$, and $\beta$ have discontinuities across some interface.

Using the hypothesis of constant pressure and velocity, from the Euler system we obtain the equations describing the dynamics of interfaces as:

$$\frac{\partial \rho}{\partial t} + u\,\frac{\partial \rho}{\partial x} = 0\,, \tag{3.5a}$$

$$\frac{\partial \mathcal{E}}{\partial t} + u\,\frac{\partial \mathcal{E}}{\partial x} = 0\,, \tag{3.5b}$$

which means that for an interface problem both the density and the internal energy per unit volume are advected. We now introduce the equation of state (3.4) into (3.5b) and obtain

$$\frac{\partial}{\partial t}\left(\frac{p - \bar{\chi}\rho - \beta}{\bar{\kappa}}\right) + u\,\frac{\partial}{\partial x}\left(\frac{p - \bar{\chi}\rho - \beta}{\bar{\kappa}}\right) = 0\,, \tag{3.6}$$

which can then be expanded as:

$$\frac{1}{\bar{\kappa}}\left(\frac{\partial p}{\partial t} + u\,\frac{\partial p}{\partial x}\right) + \left[\frac{\partial}{\partial t}\left(\frac{1}{\bar{\kappa}}\right) + u\,\frac{\partial}{\partial x}\left(\frac{1}{\bar{\kappa}}\right)\right] - \left[\frac{\partial}{\partial t}\left(\frac{\bar{\chi}\rho - \beta}{\bar{\kappa}}\right) + u\,\frac{\partial}{\partial x}\left(\frac{\bar{\chi}\rho - \beta}{\bar{\kappa}}\right)\right] = 0\,. \tag{3.7}$$

Since we consider conditions of pressure equilibrium, $\partial p/\partial t + u\,\partial p/\partial x = 0$, so that the first term of the relation above vanishes. Moreover, the remaining equality must hold for any value of $p$ in the physical space, hence the quantities in the square brackets in the second and third term of (3.7) must vanish simultaneously:

$$\frac{\partial}{\partial t}\left(\frac{1}{\bar{\kappa}}\right) + u\,\frac{\partial}{\partial x}\left(\frac{1}{\bar{\kappa}}\right) = 0\,, \tag{3.8}$$

$$\frac{\partial}{\partial t}\left(\frac{\bar{\chi}\rho - \beta}{\bar{\kappa}}\right) + u\,\frac{\partial}{\partial x}\left(\frac{\bar{\chi}\rho - \beta}{\bar{\kappa}}\right) = 0\,. \tag{3.9}$$

In order to obtain three equations governing the dynamics of the material-dependent quantities, we can split the last equation in two parts, separating the term that involves the density $\rho$:

$$\frac{\partial}{\partial t}\left(\frac{\bar{\chi}\rho}{\bar{\kappa}}\right) + u\,\frac{\partial}{\partial x}\left(\frac{\bar{\chi}\rho}{\bar{\kappa}}\right) = 0\,, \tag{3.10}$$

$$\frac{\partial}{\partial t}\left(\frac{\beta}{\bar{\kappa}}\right) + u\,\frac{\partial}{\partial x}\left(\frac{\beta}{\bar{\kappa}}\right) = 0\,. \tag{3.11}$$

We obtain that (3.8), (3.10) , (3.11) are the effective equations for the interface problem that need to be considered in the formulation of a numerical model to guarantee pressure equilibrium. Based on this result, we define the effective variables that define the flow composition as:

$$\psi = \frac{1}{\bar{\kappa}}\,, \qquad \eta = \frac{\bar{\chi}}{\bar{\kappa}}\,, \quad \text{and} \quad \mu = \frac{\beta}{\bar{\kappa}}\,. \tag{3.12}$$

Then, the transport equations (3.8), (3.10) , (3.11) take the form

$$\frac{\partial \psi}{\partial t} + u \frac{\partial \psi}{\partial x} = 0 \,, \tag{3.13}$$

$$\frac{\partial}{\partial t} (\eta \rho) + u \frac{\partial}{\partial x} (\eta \rho) = 0 \,, \tag{3.14}$$

$$\frac{\partial \mu}{\partial t} + u \frac{\partial \mu}{\partial x} = 0 \,. \tag{3.15}$$

Until this point, we have just focused on the problem of maintaining pressure equilibrium in the case of an interface-only problem. To be able to treat a general solution in which also acoustic waves may be present, we need to take the equations above in a form such that the selected variables $\psi$, $\eta$, $\mu$ remain invariant across shocks and rarefaction. We observe that the advection equations for $\psi$ and $\mu$ are already in the proper form. On the other hand, we need to express the dynamics of $\eta$ through the conservative equation:

$$\frac{\partial}{\partial t} (\eta \rho) + \frac{\partial}{\partial x} (\eta \rho u) = 0 \,. \tag{3.16}$$

In summary, the multifluid model consists of the Euler system (2.10), with the additional equations (3.16), (3.13), (3.15) for $\eta$, $\psi$, $\mu$:

$$\frac{\partial \rho}{\partial t} + \frac{\partial}{\partial x} (\rho u) = 0 \,, \tag{3.17a}$$

$$\frac{\partial}{\partial t} (\rho u) + \frac{\partial}{\partial x} \left( \rho u^2 + p \right) = 0 \,, \tag{3.17b}$$

$$\frac{\partial E}{\partial t} + \frac{\partial}{\partial x} (u(E + p)) = 0 \,, \tag{3.17c}$$

$$\frac{\partial}{\partial t} (\eta \rho) + \frac{\partial}{\partial x} (\eta \rho u) = 0 \,, \tag{3.17d}$$

$$\frac{\partial \psi}{\partial t} + u \frac{\partial \psi}{\partial x} = 0 \,, \tag{3.17e}$$

$$\frac{\partial \mu}{\partial t} + u \frac{\partial \mu}{\partial x} = 0 \,, \tag{3.17f}$$

with the equation of state:

$$p = \frac{1}{\psi} (\mathcal{E} + \eta \rho + \mu) \,. \tag{3.18}$$

The structure of the solution of the Riemann problem for this system is illustrated in Fig. 3.1.

The multifluid model (3.17) extends those of Shyue [182]) and Saurel–Abgrall [178], where an equation of state of the form (3.4) with $\eta = 0$ is considered (*stiffened* gas). On the other hand, the model represents a particular case of the more recent work of Shyue [184] for the Mie–Grüneisen equation of state, which has the form (3.4), but with quantities $\bar{\kappa}$, $\bar{\chi}$ and $\beta$ in general dependent on the density $\rho$. The choice of presenting here the formulation (3.17) is related to the topics that we will discuss in Chapter 6. In particular, we postpone in Section 6.8 a proof of the pressure equilibrium preservation property of (3.17) for a certain class of numerical schemes.

### 3.3  A Multiphase Model

A widely used approach to model multiphase flows consists in treating the different phases as interpenetrating continua, and describing the fluid dynamics of the macroscopic quantities through equations
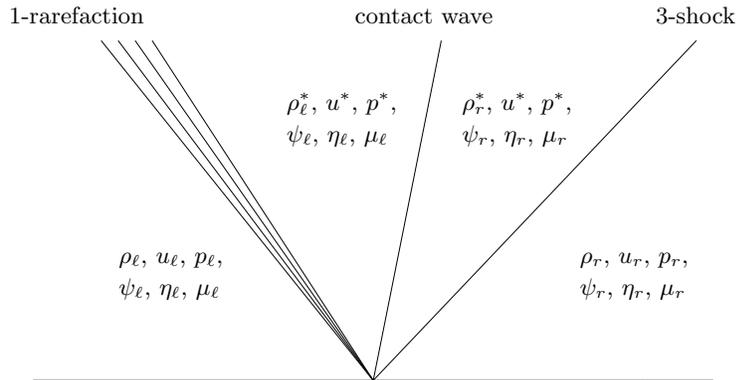
Figure 3.1: Solution of the Riemann problem for the multifluid model of Section 3.2.3.

in Eulerian form that are obtained by averaging the equations governing each single phase at the microscopic scale. For the details of this averaging technique we especially refer to Ishii [85] and Drew and Passman [54]. Models of this type have been adopted to describe multiphase flows arising in different areas of applications, such as vaporizing sprays [173], reactive granular materials undergoing deflagration-to-detonation transition (DDT) [9, 95], volcanic eruptive mixtures [206, 197, 51, 44].

In the framework of this class of models, here we consider a two-phase flow composed by a gaseous carrier phase and a suspended phase that can consist of either solid particles (dust) or liquid droplets. In the following, the subscripts g and d will refer to the gas and the dust (or droplets), respectively. Each phase is modeled as a continuum, with the gas phase being compressible, and the suspended phase incompressible at a microscopic level (microscopic density $\rho_d = $ constant). Moreover, we assume the carried phase is dilute, that is its volume fraction $\vartheta_d \ll 1$, and, finally, no viscous stresses are considered.

The formulation we adopt to describe the dynamics of this two-phase flow under the above assumptions is based mostly on the work of Harlow and Amsden [75], Sainsaulieu [173, 175, 174] and Saito [176]. In particular, the physical and numerical model in [75] has been widely used in the field of geophysics to study the particle-laden flows ejected during volcanic eruptions (see Section 8.1). The derivation of the governing equations of the model presented here through the averaging technique mentioned before has been illustrated in detail by Sainsaulieu in [173].

The flow (here in one space dimension) is described by two sets of equations expressing the conservation of mass, momentum, and total energy per unit volume for each phase:

$$\frac{\partial}{\partial t}\left(\vartheta_g \rho_g\right) + \frac{\partial}{\partial x}\left(\vartheta_g \rho_g u_g\right) = 0\,, \tag{3.19a}$$

$$\frac{\partial}{\partial t}\left(\vartheta_g \rho_g u_g\right) + \frac{\partial}{\partial x}\left(\vartheta_g \rho_g u_g^2 + \vartheta_g p_g\right) = p_g \frac{\partial \vartheta_g}{\partial x} - D(u_g - u_d)\,, \tag{3.19b}$$

$$\frac{\partial}{\partial t}\left(\vartheta_g \rho_g e_g\right) + \frac{\partial}{\partial x}\left((\vartheta_g \rho_g e_g + \vartheta_g p_g)u_g\right) \tag{3.19c}$$

$$= -p_g \frac{\partial}{\partial x}\left((1-\vartheta_g)u_d\right) - D(u_g - u_d)u_d - \mathcal{Q}(T_g - T_d)\,,$$

$$\frac{\partial}{\partial t}\left(\vartheta_d \rho_d\right) + \frac{\partial}{\partial x}\left(\vartheta_d \rho_d u_d\right) = 0\,, \tag{3.19d}$$

$$\frac{\partial}{\partial t}\left(\vartheta_d \rho_d u_d\right) + \frac{\partial}{\partial x}\left(\vartheta_d \rho_d u_d^2 + \varphi\right) = -\vartheta_d \frac{\partial p_g}{\partial x} + D(u_g - u_d)\,, \tag{3.19e}$$

$$\frac{\partial}{\partial t}\left(\vartheta_d \rho_d e_d\right) + \frac{\partial}{\partial x}\left((\vartheta_d \rho_d e_d + \varphi)u_d\right) \tag{3.19f}$$

$$= -\vartheta_d u_d \frac{\partial p_g}{\partial x} + D(u_g - u_d)u_d + \mathcal{Q}(T_g - T_d)\,.$$

Here $\rho_g$, $\rho_d$ are the material microscopic densities, $\vartheta_g$, $\vartheta_d$ the volume fractions, $u_g$, $u_d$ the velocities along the $x$ axis, $e_g$, $e_d$ the specific total energies, and $T_g$, $T_d$ the temperatures. Moreover, $p_g$ denotes the gas pressure, and $\varphi$ a pressure correction for the suspended phase. Finally, $D$ and $\mathcal{Q}$ express a drag and heat transfer function, respectively.

The specific total energies are related to the specific internal energies $\varepsilon_g$, $\varepsilon_d$ through:

$$e_g = \varepsilon_g + \frac{1}{2}|u_g|^2 \quad \text{and} \quad e_d = \varepsilon_d + \frac{1}{2}|u_d|^2\,. \tag{3.20}$$

The gaseous phase is assumed to follow the ideal polytropic gas thermodynamic relations:

$$p_g = (\gamma - 1)\rho_g \varepsilon_g\,, \quad \gamma = \text{constant}\,, \tag{3.21a}$$

$$\varepsilon_g = c_{vg} T_g\,, \quad c_{vg} = \text{constant}\,. \tag{3.21b}$$

The pressure $\varphi$ associated to the suspended phase is small in comparison to the gas pressure $p_g$, and considering negligible interaction between particles (droplets), it can be assumed zero, as in [75, 176]. However, a nonzero $\varphi$ plays an important role from a mathematical point of view, since the homogeneous equations of the suspended phase lose strict hyperbolicity under the the hypothesis $\varphi \equiv 0$. Following [174], here a nonzero $\varphi$ is viewed as a pressure correction that allows one to maintain the strict hyperbolicity of the suspended phase system. We will consider $\varphi$ a function of the macroscopic density only:

$$\varphi = \varphi(\beta)\,, \quad \beta \equiv \vartheta_d \rho_d\,. \tag{3.22}$$

For instance, we can define $\varphi$ based on the pressure law of the isothermal flow equations:

$$\varphi(\beta) = a^2 \beta\,, \tag{3.23}$$

with $a$ small. In [173, 174], where in particular the suspended phase is considered made of droplets, $\varphi$ is expressed in the form

$$\varphi = \varphi_0 \vartheta_d^{\,\delta} = \varphi_0 \left(\frac{\beta}{\rho_d}\right)^\delta\,, \tag{3.24}$$

where $\varphi_0$ is a constant proportional to the rest pressure of the gas flow on the droplets, and $\delta = \frac{4}{3}$. Note that mathematically we recover (3.23) from (3.24) taking $\varphi_0 = \rho_d a^2$ and $\delta = 1$.

The specific internal energy of the suspended phase is related to the temperature through a constant heat coefficient $c_{vd}$ :

$$\varepsilon_d = c_{vd} T_d , \quad c_{vd} = \text{constant} . \tag{3.25}$$

System (3.19) is closed by the equations (3.20), (3.21), (3.22), (3.25), together with the algebraic constraint $\vartheta_g + \vartheta_d = 1$, and definitions for the drag and heat transfer functions $D$ and $\mathcal{Q}$. Specific expressions of $D$ and $\mathcal{Q}$ will be reported in Chapter 7, where we will present a multidimensional version of the two-phase model introduced here, and, moreover, we will describe a numerical method for its solution. Applications to particle-laden flows characterizing volcanic phenomena will be then presented in Chapter 8.

### 3.3.1 Homogeneous System

Let us analyze the structure of the homogeneous part of system (3.19):

$$\frac{\partial}{\partial t} \begin{bmatrix} q_g \\ q_d \end{bmatrix} + \frac{\partial}{\partial x} \begin{bmatrix} f_g(q_g) \\ f_d(q_d) \end{bmatrix} = \begin{bmatrix} 0 \\ 0 \end{bmatrix} , \tag{3.26a}$$

with

$$q_g = \begin{bmatrix} \rho \\ \rho u_g \\ E \end{bmatrix} , \quad f_g(q_g) = \begin{bmatrix} \rho u_g \\ \rho u_g^2 + p \\ (E+p)u_g \end{bmatrix} , \quad q_d = \begin{bmatrix} \beta \\ \beta u_d \\ \Omega \end{bmatrix} , \quad f_d(q_d) = \begin{bmatrix} \beta u_d \\ \beta u_d^2 + \varphi \\ (\Omega + \varphi)u_d \end{bmatrix} , \tag{3.26b}$$

where we have introduced the notation:

$$\rho = \vartheta_g \rho_g , \quad p = \vartheta_g p_g , \quad E = \vartheta_g \rho_g e_g , \quad \beta = \vartheta_d \rho_d , \quad \Omega = \vartheta_d \rho_d e_d . \tag{3.27}$$

We can observe that in the system above the two sets of conservation equations of the two phases are decoupled, and the Jacobian matrix has the block-diagonal form

$$A(q) = \begin{bmatrix} A_g(q_g) & 0 \\ 0 & A_d(q_d) \end{bmatrix} , \tag{3.28}$$

where $A_g(q_g) = f_g'(q_g)$, and $A_d(q_d) = f_d'(q_d)$.

### Gas Phase

The set of equations of the gas phase

$$\frac{\partial q_g}{\partial t} + \frac{\partial f_g(q_g)}{\partial x} = 0 \tag{3.29}$$

is the Euler system presented in section 2.4. We recall here the eigenstructure of this system, specializing the results to the ideal polytropic gas equation of state. The Jacobian matrix has the form:

$$A_g(q_g) = \begin{bmatrix} 0 & 1 & 0 \\ (\gamma-3)\frac{u_g^2}{2} & -(\gamma-3)u_g & (\gamma-1) \\ u_g\left[(\gamma-1)\frac{u_g^2}{2} - H\right] & -(\gamma-1)u_g^2 + H & \gamma u_g \end{bmatrix} , \tag{3.30}$$

where $H = \frac{E+p}{\rho} = \frac{\rho_g e_g + p_g}{\rho_g}$ is the specific total enthalpy. The eigenvalues are

$$\lambda_g^1 = u_g - c_g, \qquad \lambda_g^2 = u_g, \qquad \lambda_g^3 = u_g + c_g, \qquad (3.31)$$

and the corresponding right eigenvectors

$$r_g^1 = \begin{bmatrix} 1 \\ u_g - c_g \\ H - u_g c_g \end{bmatrix}, \quad r_g^2 = \begin{bmatrix} 1 \\ u_g \\ \frac{u_g^2}{2} \end{bmatrix}, \quad r_g^3 = \begin{bmatrix} 1 \\ u_g + c_g \\ H + u_g c_g \end{bmatrix}, \qquad (3.32)$$

where the sound speed $c_g$ is given by

$$c_g = \sqrt{(\gamma - 1)\left(H - \frac{u_g^2}{2}\right)}. \qquad (3.33)$$

*Suspended Phase*

Let us now consider the homogeneous set of equations of the carried phase,

$$\frac{\partial q_d}{\partial t} + \frac{\partial f_d(q_d)}{\partial x} = 0. \qquad (3.34)$$

The Jacobian matrix has the form:

$$A_d(q_d) = \begin{bmatrix} 0 & 1 & 0 \\ -u_d^2 + X & 2u_d & 0 \\ -u_d e_d + Y_1 & e_d + Y_2 & u_d \end{bmatrix}, \qquad (3.35)$$

where

$$X = \varphi'(\beta), \qquad Y_1 = -\frac{u_d \varphi}{\beta} + u_d \varphi', \qquad Y_2 = \frac{\varphi}{\beta}, \qquad (3.36)$$

and the speed of sound is

$$c_d = \sqrt{X} = \sqrt{\varphi'(\beta)}. \qquad (3.37)$$

If for instance we consider the expression (3.23), $\varphi = a^2 \beta$, then

$$X = a^2, \quad Y_1 = 0, \quad Y_2 = a^2, \quad \text{and} \quad c_d = \sqrt{X} = a. \qquad (3.38)$$

For a nonzero function $\varphi$ the system is strictly hyperbolic, and it has three real distinct eigenvalues

$$\lambda_d^1 = u_d - c_d, \qquad \lambda_d^2 = u_d, \qquad \lambda_d^3 = u_d + c_d, \qquad (3.39)$$

with three corresponding independent eigenvectors:

$$r_d^1 = \begin{bmatrix} 1 \\ u_d - c_d \\ e_d - \frac{Y_1}{c_d} - Y_2 \frac{u_d - c_d}{c_d} \end{bmatrix}, \quad r_d^2 = \begin{bmatrix} 0 \\ 0 \\ 1 \end{bmatrix}, \quad r_d^3 = \begin{bmatrix} 1 \\ u_d + c_d \\ e_d - \frac{Y_1}{c_d} + Y_2 \frac{u_d + c_d}{c_d} \end{bmatrix}. \qquad (3.40)$$

The assumption that $\varphi$ depends only on the macroscopic density $\beta = \vartheta_d \rho_d$ implies that the dynamics of this phase in the absence of source terms is fully described by the first two conservation laws, the one for the density and the one for the momentum. However, the energy equation (third conservation law) is needed if we wish to follow the evolution of the energy or of any other quantity related to it such as

the temperature, and it is required when the source terms are taken into account. If we consider the reduced system of the two independent equations of (3.34)

$$\frac{\partial}{\partial t}\begin{bmatrix} \beta \\ \beta u_d \end{bmatrix} + \frac{\partial}{\partial x}\begin{bmatrix} \beta u_d \\ \beta u_d^2 + \varphi \end{bmatrix} = \begin{bmatrix} 0 \\ 0 \end{bmatrix}, \qquad (3.41)$$

the eigenstructure consists of the eigenvalues $u_d \pm c_d$, with eigenvectors $[1, u_d \pm c_d]^{\mathrm{T}}$, $c_d = \sqrt{\varphi'(\beta)}$. As a consequence of the decoupling of (3.41) from the energy equation, the full system (3.34) is characterized by the invariance of both the density $\beta$ and the momentum $(\beta u_d)$ across the second wave associated to $\lambda_d^2 = u_d$ and $r_d^2 = [0, 0, 1]^{\mathrm{T}}$, which carries a jump in the energy.

If we now consider the *pressureless* case $\varphi \equiv 0$, then we lose strictly hyperbolicity of the reduced system (3.41), and hence of the full system (3.34). System (3.41) has one eigenvalue equal to $u_d$ with algebraic multiplicity 2, associated to a single eigenvector $[1, u_d]^{\mathrm{T}}$. For the full system with the energy equation, in the case $\varphi \equiv 0$ we have $X = Y_1 = Y_2 = 0$, and the Jacobian matrix has one eigenvalue equal to $u_d$ with algebraic multiplicity 3 and geometric multiplicity 2. A basis for the space of the eigenvectors can be chosen as $\{[1, u_d, 0]^{\mathrm{T}}, [0, 0, 1]^{\mathrm{T}}\}$.

The pressureless equations given by (3.41) for $\varphi \equiv 0$ have been extensively studied, e.g. [14, 17, 18, 20, 30, 172, 82, 126, 123]. Most of the analyses view these equations as the limit of system (3.41) as a pressure correction $\varphi = \varphi(\beta; \epsilon)$ vanishes with some parameter $\epsilon$. For instance in [18, 123] the isothermal pressure law $\varphi(\beta; a) = a^2 \beta$ is assumed, and the limit $a \to 0$ is taken. Similarly in [30] the authors consider an isentropic law $\varphi(\beta; \epsilon) = \epsilon \frac{\beta^\gamma}{\gamma}$ and study the solution of the pressureless system in the limit $\epsilon \to 0$. The Riemann solution for system (3.41) with a nonzero $\varphi$ consists of two distinct waves, which can be either shocks or rarefactions if $\varphi(\beta)$ is convex, such in the isothermal or isentropic case. In the vanishing pressure limit, the solution to the pressureless equations is found to consist of two contact waves with vacuum in between if $u_{d,\ell} < u_{d,r}$, and of a single delta-shock (singularity in density and momentum) if $u_{d,\ell} > u_{d,r}$. The propagation speed of the delta-shock can be shown to be [30, 123]

$$\hat{u}_d = \frac{\sqrt{\beta_\ell} u_{d,\ell} + \sqrt{\beta_r} u_{d,r}}{\sqrt{\beta_\ell} + \sqrt{\beta_r}}. \qquad (3.42)$$

This corresponds to the expression of the usual Roe average for the dust velocity, based on the dust density (see Section 4.1.3 in the next chapter).

### 3.3.2  Source Terms

The coupling between the two phases takes place through the drag terms $D(u_g - u_d)$, $D(u_g - u_d)u_d$, the heat transfer term $\mathcal{Q}(T_g - T_d)$, and terms modeling the gas pressure gradient force exerted on the particles and its work, in the form $\vartheta_d \frac{\partial p_g}{\partial x}$, $\vartheta_d \frac{\partial p_g}{\partial x} u_d$.

The form of the contribution of the drag term in the energy equations, $D(u_g - u_d)u_d$, follows from the assumption (as in [75]) that the effects of drag dissipation are assigned completely to the heating of the gas. This is more clear if we write the equations for the specific internal energies:

$$\vartheta_g \rho_g \left( \frac{\partial \varepsilon_g}{\partial t} + u_g \frac{\partial \varepsilon_g}{\partial x} \right) = -p_g \frac{\partial}{\partial x}\left( \vartheta_g u_g + (1 - \vartheta_g)u_d \right) - D(u_g - u_d)^2 - \mathcal{Q}(T_g - T_d), \qquad (3.43a)$$

$$\vartheta_d \rho_d \left( \frac{\partial \varepsilon_d}{\partial t} + u_d \frac{\partial \varepsilon_d}{\partial x} \right) = \mathcal{Q}(T_g - T_d). \qquad (3.43b)$$

Only in the equation for the gas phase do we need to include a contribution $D(u_g - u_d)^2$. Let us remark that the effect of drag dissipation is of minor importance in comparison with heat conduction

between the phases [48], and for instance in the formulations adopted in [51, 150, 155] this contribution is neglected.

The nonconservative terms modeling exchange of momentum and energy related to the gas pressure gradient, namely $p_g \frac{\partial \vartheta_g}{\partial x}$, $p_g \frac{\partial}{\partial x}\left((1-\vartheta_g)u_d\right)$, $\vartheta_d \frac{\partial p_g}{\partial x}$, $\vartheta_d \frac{\partial p_g}{\partial x} u_d$, under the hypothesis $\vartheta_d \ll 1$ are small and give a weak coupling. They can be neglected, as in [176]. These nonconservative terms pose a mathematical difficulty when we wish to allow for discontinuous solutions of the two-phase system. An extensive mathematical analysis of the nonconservative system (3.19) without drag and heat transfer terms has been performed by Sainsaulieu in [175, 174]. The author gives a definition of shock waves solutions for the two-phase nonconservative system and derives explicit approximate jump conditions for these discontinuous solutions, showing that they are perturbations of order $\varepsilon = \frac{1}{\rho_d} \ll 1$ of the decoupled jump conditions of the homogeneous system.

### 3.3.3    The Mixture Speed of Sound

Gas flows carrying a particulate phase may exhibit a sound speed that is much lower than the sound speed of the pure gas. We here derive an expression for the speed of sound of the mixture of gas and particles, based on the model (3.19) with $\varphi \equiv 0$, under the assumption that momentum and energy exchange between the gas and dust occurs rapidly enough so that they are in mechanical and thermal equilibrium (*homogeneous flow* hypothesis). The result will be used in Chapter 7 (Section 7.4.1) for a numerical test with the algorithm we propose to model dusty gas flows.

We consider the propagation of small amplitude pressure waves (acoustic waves) against a steady background with constant velocities $u_{g0} = u_{d0} = 0$, constant densities $\rho_0 = \vartheta_{g0}\rho_{g0}$, $\beta_0 = \vartheta_{d0}\rho_d = (1-\vartheta_{g0})\rho_d$ (recall that $\rho_d = \text{const.}$), and constant gas pressure. We also assume that $c_{vd}\beta_0 \gg c_{vg}\rho_0$ so that the dust contains much more thermal energy than the gas. Since we are assuming the temperature equilibrates rapidly between the gas and dust and we are considering small perturbations about a constant state, it is then reasonable to assume that the dust acts as a heat reservoir that keeps the gas at a constant temperature as the acoustic wave propagates. We can then drop the corresponding source term and simply consider isothermal behaviour. The effective equation of state is then

$$p_g = c_{g,\text{isot}}^2 \, \rho_g \,, \quad c_{g,\text{isot}}^2 = R\bar{T}_g \,, \tag{3.44}$$

where $c_{g,\text{isot}}$ represents the isothermal sound speed of the pure gaseous phase and $\bar{T}_g$ denotes the constant temperature of the two-phase mixture. Under the above assumption of isothermal flow, and using (3.44), equations (3.19) give the reduced system

$$\frac{\partial}{\partial t}\left(\vartheta_g \rho_g\right) + \frac{\partial}{\partial x}\left(\vartheta_g \rho_g u_g\right) = 0 \,, \tag{3.45a}$$

$$\frac{\partial}{\partial t}\left(\vartheta_g \rho_g u_g\right) + \frac{\partial}{\partial x}\left(\vartheta_g \rho_g u_g^2\right) + c_{g,\text{isot}}^2 \vartheta_g \frac{\partial \rho_g}{\partial x} = -D(u_g - u_d) \,, \tag{3.45b}$$

$$\frac{\partial}{\partial t}\left((1-\vartheta_g)\rho_d\right) + \frac{\partial}{\partial x}\left((1-\vartheta_g)\rho_d u_d\right) = 0 \,, \tag{3.45c}$$

$$\frac{\partial}{\partial t}\left((1-\vartheta_g)\rho_d u_d\right) + \frac{\partial}{\partial x}\left((1-\vartheta_g)\rho_d u_d^2\right) + c_{g,\text{isot}}^2 (1-\vartheta_g)\frac{\partial \rho_g}{\partial x} + D(u_g - u_d) \,, \tag{3.45d}$$

where we have also used the algebraic constraint $\vartheta_g + \vartheta_d = 1$. Considering small perturbations with respect to background variables, we write

$$\rho_g = \rho_{g0} + \tilde{\rho}_g \qquad \text{and} \qquad \vartheta_g = \vartheta_{g0} + \tilde{\vartheta}_g \,. \tag{3.46}$$

Linearizing (3.45), and dividing the resulting continuity equations of the two phases by the corresponding background microscopic densities, we obtain

$$\frac{\vartheta_{g0}}{\rho_{g0}}\frac{\partial\tilde{\rho}_g}{\partial t} + \frac{\partial\tilde{\vartheta}_g}{\partial t} + \vartheta_{g0}\frac{\partial u_g}{\partial x} = 0\,, \tag{3.47a}$$

$$\vartheta_{g0}\rho_{g0}\frac{\partial u_g}{\partial t} + c_{g,\text{isot}}^2\,\vartheta_{g0}\frac{\partial\tilde{\rho}_g}{\partial x} = -D(u_g - u_d)\,, \tag{3.47b}$$

$$-\frac{\partial\tilde{\vartheta}_g}{\partial t} + (1 - \vartheta_{g0})\frac{\partial u_d}{\partial x} = 0\,, \tag{3.47c}$$

$$(1 - \vartheta_{g0})\rho_d\frac{\partial u_d}{\partial t} + c_{g,\text{isot}}^2\,(1 - \vartheta_{g0})\frac{\partial\tilde{\rho}_g}{\partial x} = D(u_g - u_d)\,. \tag{3.47d}$$

Adding now (3.47b) and (3.47d) eliminates the drag source term, and if we assume that this acts sufficiently fast that velocity perturbations satisfy $u_g = u_d \equiv u$, then the resulting equation along with the sum of (3.47a) and (3.47c) gives a reduced system of two equations for $\tilde{\rho}_g$ and $u$:

$$\frac{\vartheta_{g0}}{\rho_{g0}}\frac{\partial\tilde{\rho}_g}{\partial t} + \frac{\partial u}{\partial x} = 0\,, \tag{3.48a}$$

$$(\vartheta_{g0}\rho_{g0} + (1 - \vartheta_{g0})\rho_d)\frac{\partial u}{\partial t} + c_{g,\text{isot}}^2\frac{\partial\tilde{\rho}_g}{\partial x} = 0\,. \tag{3.48b}$$

This system has wave speeds $\pm c_\text{m}$ where

$$c_\text{m} = c_{g,\text{isot}}\sqrt{\frac{\rho_{g0}}{\vartheta_{g0}(\vartheta_{g0}\rho_{g0} + \vartheta_{d0}\rho_d)}} \tag{3.49}$$

is the mixture sound speed in the considered case of equilibrium flow. This expression can be derived more generally for the case in which the suspended phase is also compressible and governed by a non zero pressure law, see for example [202, 54].

Under the considered assumption of dilute dust phase, we can approximate $\vartheta_{g0} \approx 1$, and hence $\rho_{g0} \approx \rho_0$. Therefore, $c_\text{m} \approx c_{g,\text{isot}}\sqrt{\frac{\rho_0}{\rho_0+\beta_0}}$. This expression of the sound speed, $c'_\text{m} = c_{g,\text{isot}}\sqrt{\frac{\rho_0}{\rho_0+\beta_0}}$, is the result we can obtain directly with an analogous procedure to the one described above by neglecting in (3.19) the terms modeling momentum exchange due to the gas pressure gradient, which is again valid if $\vartheta_{g0} \approx 1$. This in particular suggests that neglecting pressure gradient terms in the hypothesis $\vartheta_d \ll 1$ still allows to model correctly the propagation of acoustic waves.

Note that $c_\text{m} < c_{g,\text{isot}} < c_g = \sqrt{\gamma R T_g}$, where $c_g$ is the isentropic pure gas sound speed (at same $T_g$), and, moreover, $c_\text{m}$ can be significantly lower than $c_{g,\text{isot}}$ and $c_g$ if $\beta_0$ is large compared to $\rho_0$.

Chapter 4

# HIGH RESOLUTION WAVE PROPAGATION METHODS

## 4.1 Godunov-Type Methods

For the numerical approximation of hyperbolic systems of conservation laws we consider Godunov-type schemes, that represent a particular class of finite volume methods. We will first focus on the one-dimensional case, i.e. system (2.5).

Let us consider a discretization in space and time with spatial interval $\Delta x$ and time step $\Delta t$. We define the discrete points $(x_i, t^n)$ by $x_i = i\Delta x$, $i \in \mathbb{Z}$, and $t^n = n\Delta t$, $n \in \mathbb{N}$. In the finite volume approach, the numerical solution $Q_i^n \in \mathbb{R}^m$ that we associate to the point $(x_i, t^n)$ is viewed as an approximation of the average of the exact solution $q(x,t)$ at time $t^n$ over the spatial cell $\mathcal{C}_i = (x_{i-1/2}, x_{i+1/2})$, $x_{i\pm1/2} = (i \pm 1/2)\Delta x$:

$$Q_i^n \simeq \frac{1}{\Delta x} \int_{\mathcal{C}_i} q(x, t^n)\, dx \equiv \bar{Q}_i^{\,n}\,. \tag{4.1}$$

We shall consider 3-point explicit schemes in conservation form, of the following type:

$$Q_i^{n+1} = Q_i^n - \frac{\Delta t}{\Delta x} \left[ F(Q_i^n, Q_{i+1}^n) - F(Q_{i-1}^n, Q_i^n) \right]\,, \tag{4.2}$$

where the function $F : \mathbb{R}^m \times \mathbb{R}^m \to \mathbb{R}^m$ is called *numerical flux*. The form (4.2) is very natural with the interpretation of $Q_i^n$ as in (4.1). In fact, since we know that every weak solution $q(x,t)$ satisfies the integral form of the conservation law (2.3), we can write

$$\int_{\mathcal{C}_i} q(x, t^{n+1})\, dx = \int_{\mathcal{C}_i} q(x, t^n)\, dx - \left[ \int_{t^n}^{t^{n+1}} f(q(x_{i+1/2}, t))\, dt - \int_{t^n}^{t^{n+1}} f(q(x_{i-1/2}, t))\, dt \right]. \tag{4.3}$$

Dividing by $\Delta x$ and using the cell average (4.1), we have

$$\bar{Q}_i^{\,n+1} = \bar{Q}_i^{\,n} - \frac{1}{\Delta x} \left[ \int_{t^n}^{t^{n+1}} f(q(x_{i+1/2}, t))\, dt - \int_{t^n}^{t^{n+1}} f(q(x_{i-1/2}, t))\, dt \right]. \tag{4.4}$$

Comparing this to (4.2), we see that the numerical flux function $F(Q_i^n, Q_{i+1}^n)$ plays the role of the average physical flux through $x_{i+1/2}$ over the time interval $[t^n, t^{n+1}]$:

$$F(Q_i^n, Q_{i+1}^n) \simeq \frac{1}{\Delta t} \int_{t^n}^{t^{n+1}} f(q(x_{i+1/2}, t))\, dt\,. \tag{4.5}$$

For *consistency* with the physical flux $f(q)$, we will in general require $F(w, w) = f(w)$, $\forall w$.

Godunov-type methods are based on solving Riemann problems between cell averages $Q_i^n$, $Q_{i+1}^n$ in order to define the numerical flux $F(Q_{i+1}^n, Q_i^n)$ associated to the interface at $x_{i+1/2}$. We can either compute the exact solution of the Riemann problem at each cell interface, as in the original Godunov's method [69], or we can use an approximate solution. A wide variety of *Approximate Riemann Solvers* has been proposed that can be applied with much less computational effort than the exact Riemann solver, and yet are in many cases equally effective. Let $q^*(x, t) = q_{\mathrm{R}}^*(\frac{x}{t}; Q_i^n, Q_{i+1}^n)$ denote the similarity

solution, either exact or approximate, for a Riemann problem with initial data $Q_i^n$ and $Q_{i+1}^n$. The numerical flux for this class of methods is defined as

$$F(Q_i^n, Q_{i+1}^n) = \frac{1}{\Delta t} \int_{t^n}^{t^{n+1}} f(q^*(x_{i+1/2}, t)) \, dt = q_R^*(0; Q_i^n, Q_{i+1}^{n+1}) \,. \tag{4.6}$$

### 4.1.1  Structure of the Approximate Riemann Solvers

The general structure of the class of approximate Riemann solver we are interested in consists of $M_w$ waves $\mathcal{W}^p \in \mathbb{R}^m$ propagating at some speeds $s^p \in \mathbb{R}$, $p = 1, 2, \cdots, M_w$ . For assigned values $q_\ell$ and $q_r$ for the left and right state of the Riemann problem, the vectors $\mathcal{W}^p$ represent the jump in $q$ across each wave and their sum must recover the total jump:

$$q_r - q_\ell = \sum_{p=1}^{M_w} \mathcal{W}^p \,. \tag{4.7}$$

Moreover, the following *conservation condition* needs to be satisfied:

$$f(q_r) - f(q_\ell) = \sum_{p=1}^{M_w} s^p \mathcal{W}^p \,. \tag{4.8}$$

For these solvers the numerical flux can be expressed as:

$$F(Q_i, Q_{i+1}) = f(Q_i) + \sum_{p=1}^{M_w} \left(s_{i+1/2}^p\right)^- \mathcal{W}_{i+1/2}^p = f(Q_{i+1}) - \sum_{p=1}^{M_w} \left(s_{i+1/2}^p\right)^+ \mathcal{W}_{i+1/2}^p \,, \tag{4.9}$$

where $s^+ = \max(s, 0)$, $s^- = \min(s, 0)$, and the subscript $(i + 1/2)$ indicates quantities computed for the Riemann problem at $x_{1+1/2}$. The updating formula (4.2) then takes the form of the following first-order upwind scheme:

$$Q_i^{n+1} = Q_i^n - \frac{\Delta t}{\Delta x} \left[ \sum_{p=1}^{M_w} \left(s_{i+1/2}^p\right)^- \mathcal{W}_{i+1/2}^p + \sum_{p=1}^{M_w} \left(s_{i-1/2}^p\right)^+ \mathcal{W}_{i-1/2}^p \right] \,. \tag{4.10}$$

Let us finally recall that the CFL stability condition [41, 42] must hold:

$$\text{Courant number} = \frac{\Delta t}{\Delta x} \max_p |s^p| \leq 1 \,, \qquad 1 \leq p \leq M_w \,. \tag{4.11}$$

### 4.1.2  The HLL Solver

The HLL solver was introduced by Harten, Lax, and van Leer in [78]. This solver consists in approximating the Riemann solution by two waves ($M_w = 2$ regardless of the dimension $m$ of the system), with some speed $a_\ell$ and $a_r$ chosen to approximate the minimum and maximum characteristic speed of the system. The solver is called HLLE when the definition of $a_\ell$ and $a_r$ proposed by Einfeldt [57] in the context of gas dynamics is used. Specifically, Einfeldt defines:

$$a_\ell = \min_p \left( \min \left( \lambda^p(q_\ell), \hat{\lambda}^p(q_\ell, q_r) \right) \right) \quad \text{and} \quad a_r = \max_p \left( \max \left( \lambda^p(q_r), \hat{\lambda}^p(q_\ell, q_r) \right) \right) \,, \tag{4.12}$$

where $\lambda^p(q)$ is the $p$-th eigenvalue of the Jacobian matrix $f'(q)$ of the system, and $\hat{\lambda}^p(q_\ell, q_r)$ is the $p$-th eigenvalue of a Roe linearization for the problem (see next section).

The waves for the HLL solver are

$$\mathcal{W}^1 = q_m - q_\ell \quad \text{and} \quad \mathcal{W}^2 = q_r - q_m \,, \tag{4.13}$$

where the intermediate state $q_m$ is determined by the conservation condition (4.8) as

$$q_m = \frac{a_r\, q_r - a_\ell\, q_\ell - [f(q_r) - f(q_\ell)]}{a_r - a_\ell}\,. \tag{4.14}$$

A disadvantage of this solver is that the full Riemann solution structure is approximated by only two waves based on the approximate speeds of the fastest and slowest wave in the system. For a system with more than two equations, as in the case of the Euler system, this in general will lead to a loss of resolution for waves traveling at intermediate speeds. However, this solver is very robust in problems where other more accurate solvers may suffer from the appearance of unphysical solutions (e.g. negative densities).

### 4.1.3   The Roe Solver

One of the most popular approximate Riemann solvers is due to Roe [169], and it has been extensively used. The idea is to determine an approximate Riemann solution by solving a linear system with a constant coefficient matrix $\hat{A} = \hat{A}(q_\ell, q_r)$, instead of the original nonlinear system (2.5).

DEFINITION 4.1  *The matrix $\hat{A}(q_\ell, q_r)$ is called a Roe linearization if it is endowed with the following properties:*

(i) *Hyperbolicity of the linearized system:*

   $\hat{A}(q_\ell, q_r)$ *has real eigenvalues and a corresponding complete set of eigenvectors;*

(ii) *Consistency:*           $\hat{A}(q_\ell, q_r) \to f'(\bar{q})$   *as*   $q_\ell, q_r \to \bar{q}$;

(iii) *Conservation condition:*

$$f(q_r) - f(q_\ell) = \hat{A}(q_\ell, q_r)\,(q_r - q_\ell)\,. \tag{4.15}$$

Denoting with $\{\hat{r}^p, \hat{\lambda}^p\}$ the eigenstructure of $\hat{A}$, and with $\alpha^p$ the coefficients of the projection of the jump $(q_r - q_\ell)$ onto the eigenvectors $\hat{r}^p$, the waves $\mathcal{W}^p$ and corresponding speeds $s^p$ that form the structure of the Roe solver are given by:

$$\mathcal{W}^p = \alpha^p \hat{r}^p \qquad \text{and} \qquad s^p = \hat{\lambda}^p\,, \quad p = 1, \cdots, M_w \equiv m\,. \tag{4.16}$$

The conservation condition (4.8) follows from the property (iii) above.

In [169] Roe suggests to take $\hat{A}$ in the form

$$\hat{A}(q_\ell, q_r) = A(\hat{q})\,, \qquad \hat{q} = \hat{q}(q_\ell, q_r)\,, \tag{4.17}$$

where $A(q) = f'(q)$ is the Jacobian matrix of the original system and $\hat{q} = \hat{q}(q_\ell, q_r)$ is an average state defined so that the properties $(i)$-$(iii)$ listed above will hold. In particular, Roe derives $\hat{A}(q_\ell, q_r)$ for the Euler equations of gas dynamics with the ideal polytropic gas law $p(\mathcal{E}, \rho) = (\gamma - 1)\mathcal{E}$. Focusing here on the one-dimensional case (2.10), for the considered equation of state the Jacobian matrix of the system (2.18) can be expressed as a function of the only two variables $u$ (velocity) and $H$ (specific total enthalpy). The linearization $\hat{A}(q_\ell, q_r)$ is then defined by Roe as the Jacobian matrix evaluated in an average state $(\hat{u}, \hat{H})$, which is determined by the conditions of Def. 4.1 as

$$\hat{u} = \frac{\sqrt{\rho_\ell}\, u_\ell + \sqrt{\rho_r}\, u_r}{\sqrt{\rho_\ell} + \sqrt{\rho_r}} \qquad \text{and} \qquad \hat{H} = \frac{\sqrt{\rho_\ell}\, H_\ell + \sqrt{\rho_r}\, H_r}{\sqrt{\rho_\ell} + \sqrt{\rho_r}}\,. \tag{4.18}$$

A well-known drawback of the Roe solver is that it may compute entropy-violating solutions. This happens when the true solution of the Riemann problem contains a transonic rarefaction, that is one for which $\lambda^p$ changes sign from negative to positive through the rarefaction fan, and the failure of the solver is caused by the approximation of this rarefaction by means of a single discontinuity. Several 'entropy fixes' have been proposed to address this problem, e.g. [76, 77, 55]. We will return on this topic in Chapter 5.

## 4.2  Wave Propagation Algorithms

A class of high resolution multidimensional *Wave Propagation Algorithms* for general time-dependent hyperbolic systems is described in [120], and implemented in the CLAWPACK software [115]. These methods are based on solving Riemann problems for waves and, in one dimension, use an updating formula of the form:

$$Q_i^{n+1} = Q_i^n - \frac{\Delta t}{\Delta x}\left(\mathcal{A}^+\Delta Q_{i-1/2} + \mathcal{A}^-\Delta Q_{i+1/2}\right) - \frac{\Delta t}{\Delta x}\left(\widetilde{F}_{i+1/2} - \widetilde{F}_{i-1/2}\right), \qquad (4.19)$$

where $\mathcal{A}^\pm\Delta Q_{i+1/2}$ are the left-going and right-going *fluctuations* resulting from the Riemann solution at the grid interface $x_{i+1/2}$, and $\widetilde{F}_{i+1/2}$ are *correction fluxes* yielding high resolution. For a hyperbolic system of conservation laws of the form (2.5), the fluctuations must satisfy the *conservation condition*

$$f(Q_{i+1}) - f(Q_i) = \mathcal{A}^-\Delta Q_{i+1/2} - \mathcal{A}^+\Delta Q_{i+1/2}. \qquad (4.20)$$

We stress that this class of methods can be applied also to equations that are not in conservation form (e.g. the advection equations (3.17e), (3.17f)), in which case there is no flux function $f(q)$, and the constraint (4.20) does not need to be satisfied.

We show in particular how schemes that are based on a decomposition of the form (4.7), and give the algorithm (4.10), enter in the framework of the wave propagation methods. Let us define:

$$\mathcal{A}^-\Delta Q_{i+1/2} = \sum_{p=1}^{M_w}\left(s_{i+1/2}^p\right)^-\mathcal{W}_{i+1/2}^p \quad \text{and} \quad \mathcal{A}^+\Delta Q_{i+1/2} = \sum_{p=1}^{M_w}\left(s_{i+1/2}^p\right)^+\mathcal{W}_{i+1/2}^p. \qquad (4.21)$$

Note that the quantity $\mathcal{A}^+\Delta Q_{i+1/2}$ measures the net effect of all right-going waves from $x_{i+1/2}$, while $\mathcal{A}^-\Delta Q_{i+1/2}$ measures the net effect of all left-going waves from this same interface. Using (4.21), the updating formula (4.10) takes the form (4.19) with $\widetilde{F}_{i+1/2} = 0$ :

$$Q_i^{n+1} = Q_i^n - \frac{\Delta t}{\Delta x}\left(\mathcal{A}^+\Delta Q_{i-1/2} + \mathcal{A}^-\Delta Q_{i+1/2}\right). \qquad (4.22)$$

This first-order method is then extended to high resolution by adding the term of the correction fluxes.

### 4.2.1  Second-Order Corrections

The second-order correction fluxes $\widetilde{F}_{i+1/2}$ are defined by

$$\widetilde{F}_{i+1/2} = \frac{1}{2}\sum_{p=1}^{M_w}|s_{i+1/2}^p|\left(1 - \frac{\Delta t}{\Delta x}|s_{i+1/2}^p|\right)\widetilde{\mathcal{W}}_{i+1/2}^p \qquad (4.23)$$

where $\widetilde{\mathcal{W}}_{i+1/2}^p$ is obtained by multiplying the wave $\mathcal{W}_{i+1/2}^p$ by a *limiter* function $\phi(\theta)$:

$$\widetilde{\mathcal{W}}_{i+1/2}^p = \phi(\theta_{i+1/2})\mathcal{W}_{i+1/2}^p. \qquad (4.24)$$

In the absence of limiters, (4.23) can be interpreted as arising from propagating a piecewise linear "correction wave", as described in [117, 122]. Limiter functions are needed to avoid oscillations near discontinuities, and they depend on a variable $\theta$ that measures the smoothness of the solution. The value of $\theta_{i+1/2}^p$ in (4.24) is obtained by comparing the wave $\mathcal{W}_{i+1/2}^p$ with the wave $\widetilde{\mathcal{W}}_{I+1/2}^p$ in the same family $p$ at the neighbouring Riemann problem in the upwind direction, i.e.

$$
I = \begin{cases} i - 1 & \text{if } s_{i+1/2}^p > 0, \\ i + 1 & \text{if } s_{i+1/2}^p < 0. \end{cases}
\tag{4.25}
$$

One approach to define $\theta_{i+1/2}^p$ is

$$
\theta_{i+1/2}^p = \frac{\widetilde{\mathcal{W}}_{I+1/2}^p \cdot \widetilde{\mathcal{W}}_{i+1/2}^p}{\widetilde{\mathcal{W}}_{i+1/2}^p \cdot \widetilde{\mathcal{W}}_{i+1/2}^p} \,.
\tag{4.26}
$$

Other methods can be used, as the one proposed by Liu and Lax in [111, 132].

We conclude this section by reporting some standard limiter functions:

$$
\text{Minmod:} \qquad \phi(\theta) = \max(0, \min(1, \theta))
\tag{4.27}
$$

$$
\text{Superbee:} \qquad \phi(\theta) = \max(0, \min(1, 2\theta), \min(2, \theta))
\tag{4.28}
$$

$$
\text{van Leer:} \qquad \phi(\theta) = \frac{\theta + |\theta|}{1 + \theta}
\tag{4.29}
$$

$$
\text{MC:} \qquad \phi(\theta) = \max(0, \min((1+\theta)/2, 2, 2\theta)) \,.
\tag{4.30}
$$

### 4.2.2 The F-Wave Formulation

The definition (4.21) of the fluctuations $\mathcal{A}^{\pm}\Delta Q_{i+1/2}$ is based on a decomposition of the jump in $q$ between the left and right state in the Riemann problem of the form (4.7). An alternative approach is to decompose the jump in $f$ into waves $\mathcal{Z}^p$, called $f$-waves:

$$
f(q_r) - f(q_\ell) = \sum_{p=1}^{M_w} \mathcal{Z}^p \,.
\tag{4.31}
$$

Assuming these waves $\mathcal{Z}^p$ are moving at some speeds $s^p$, we define the fluctuations directly from $\mathcal{Z}^p$ as:

$$
\mathcal{A}^{-}\Delta Q_{i+1/2} = \sum_{p:s_{i+1/2}^p<0}^{M_w} \mathcal{Z}_{i+1/2}^p \qquad \text{and} \qquad \mathcal{A}^{+}\Delta Q_{i+1/2} = \sum_{p:s_{i+1/2}^p>0}^{M_w} \mathcal{Z}_{i+1/2}^p \,,
\tag{4.32}
$$

where the subscript $(i + 1/2)$ refers to quantities resulting from the Riemann problem at the grid interface $x_{i+1/2}$. Moreover, in this framework, the high resolution correction fluxes are written as

$$
\widetilde{F}_{i+1/2} = \frac{1}{2} \sum_{p=1}^{M_w} \operatorname{sgn}\left(s_{i+1/2}^p\right) \left(1 - \frac{\Delta t}{\Delta x} \left|s_{i+1/2}^p\right|\right) \widetilde{\mathcal{Z}}_{i+1/2}^p \,.
\tag{4.33}
$$

If we have a set of $M_w$ waves $\mathcal{W}^p$ and speeds $s^p$ resulting from a decomposition in the jump in $q$ of the form (4.7), and satisfying the conservation condition (4.8), as for the HLL solver and the Roe solver of Sections 4.1.2 and 4.1.3, then we can formulate the corresponding scheme in terms of f-waves setting

$$
\mathcal{Z}^p = s^p \mathcal{W}^p, \quad 1 \le p \le M_w \,.
\tag{4.34}
$$

Note, on the other hand, that if we start with a decomposition of the jump in $f$ in f-waves $\mathcal{Z}^p$ of the form (4.32), given the speeds $s^p$ we can recover the waves $\mathcal{W}^p$ through the formula above only if the speeds are not zero.

An advantage of the f-wave approach is that using the condition (4.32) to define the $\mathcal{Z}^p$ guarantees that the method will be conservative when the fluctuations (4.32) are used. This is true for any linearization $\tilde{A}(q_\ell, q_r)$ of the Jacobian matrix $A(q) = f'(q)$ of the system, for instance the simple arithmetic average $\tilde{A}(q_\ell, q_r) = A\left(\frac{1}{2}(q_\ell + q_r)\right)$, whereas (4.8) may not be satisfied if the wave splitting is based on (4.7), unless $\tilde{A}(q_\ell, q_r)$ is chosen to be a special average such as the Roe average.

The f-wave formulation is also advantageous in the context of spatially-varying flux functions and problems with source terms. We will discuss these applications in Chapter 5, where a more general approach is explored, based on the simultaneous decomposition in waves of both the jump in $q$ and $f$. Useful applications of the f-wave approach will be also illustrated in Chapter 7 in presenting a numerical model for dusty gas flows.

## 4.3 Multidimensional Numerical Methods

We consider the numerical approximation of a two-dimensional hyperbolic system of conservation laws of the form

$$\frac{\partial q}{\partial t} + \frac{\partial f(q)}{\partial x} + \frac{\partial g(q)}{\partial y} = 0. \tag{4.35}$$

Let us assume a uniform Cartesian grid with space intervals $\Delta x$, $\Delta y$ in the $x$ and $y$ direction, respectively, and let us set $x_i = i\Delta x$, $y_j = j\Delta y$, $i, j \in \mathbb{Z}$. We will denote with $Q_{i,j}^n$ the approximate average of the solution $q(x, y, t)$ at time $t^n$ over the cell $\mathcal{C}_{i,j} = (x_{i-1/2}, x_{i+1/2}) \times (y_{j-1/2}, y_{j+1/2})$, $x_{i\pm1/2} = (i\pm1/2)\Delta x$, $y_{j\pm1/2} = (j\pm1/2)\Delta y$ :

$$Q_{i,j}^n \simeq \frac{1}{\Delta x \Delta y} \iint_{\mathcal{C}_i} q(x, y, t^n) \, dx \, dy. \tag{4.36}$$

### 4.3.1 Dimensional Splitting

A simple way to extend one-dimensional numerical methods to more space dimensions is to use *dimensional splitting*. A fractional-step method is applied to split the multidimensional problem into a sequence of one-dimensional problems. To solve (4.35), for example, we might alternate between solving $\partial q/\partial t + \partial f(q)/\partial x = 0$ and $\partial q/\partial t + \partial g(q)/\partial x = 0$. Given the initial cell values $Q_{i,j}^n$ at time $t^n$, we solve the first system along each row of cells $\mathcal{C}_{i,j}$ with $j$ fixed to update $Q_{i,j}^n$ to $Q_{i,j}^*$. Then, these values $Q_{i,j}^*$ are used as initial data to solve the second system along each column of cells $\mathcal{C}_{i,j}$ with $i$ fixed, which finally gives the approximate cell values $Q_{i,j}^{n+1}$ at time $t^{n+1}$.

### 4.3.2 Fully Discrete Flux-Differencing Methods

Let us consider the integral form of the system (4.35) given by:

$$\frac{d}{dt} \iint_{\mathcal{C}_{i,j}} q(x, y, t) dx \, dy = \int_{y_{j-1/2}}^{y_{j+1/2}} f(q(x_{i+1/2}, y, t)) dy - \int_{y_{j-1/2}}^{y_{j+1/2}} f(q(x_{i-1/2}, y, t)) \, dy$$

$$+ \int_{x_{i-1/2}}^{x_{i+1/2}} g(q(x, y_{j+1/2}, t)) \, dx - \int_{x_{i-1/2}}^{x_{i+1/2}} g(q(x, y_{j-1/2}, t)) \, dx. \tag{4.37}$$

If we integrate this expression from $t^n$ to $t^{n+1}$, we are led to a fully discrete flux-differencing method of the form

$$Q_{i,j}^{n+1} = Q_{i,j}^n - \frac{\Delta t}{\Delta x} \left[ F(Q_{i,j}^n, Q_{i+1,j}^n) - F(Q_{i-1,j}^n, Q_{i,j}^n) \right] - \frac{\Delta t}{\Delta y} \left[ G(Q_{i,j}^n, Q_{i,j+1}^n) - G(Q_{i,j-1}^n, Q_{i,j}^n) \right], \tag{4.38}$$

where the numerical fluxes $F(Q_{i,j}^n, Q_{i+1,j}^n)$ and $G(Q_{i,j}^n, Q_{i,j+1}^n)$ represent an approximation of the physical fluxes through the edges given by $x = x_{i+1/2}$, $y \in (y_{j-1/2}, y_{j+1/2})$ and $x \in (x_{i-1/2}, x_{i+1/2})$, $y = y_{j+1/2}$, respectively, over the time interval $[t^n, t^{n+1})$:

$$F(Q_{i,j}^n, Q_{i+1,j}^n) \simeq \frac{1}{\Delta t \Delta y} \int_{t^n}^{t^{n+1}} \int_{y_{j-1/2}}^{y_{j+1/2}} f(q(x_{i+1/2}, y, t)) \, dy \, dt \,, \tag{4.39a}$$

$$G(Q_{i,j}^n, Q_{i,j+1}^n) \simeq \frac{1}{\Delta t \Delta x} \int_{t^n}^{t^{n+1}} \int_{x_{i-1/2}}^{x_{i+1/2}} g(q(x, y_{j+1/2}, t)) \, dx \, dt \,. \tag{4.39b}$$

To define the numerical fluxes in (4.38), we can solve one-dimensional Riemann problems normal to each cell interface. If we perform this task by employing the approximate Riemann solvers described in Section 4.1.1, then, for the $F$ fluxes we have:

$$F(Q_{i,j}, Q_{i+1,j}) = f(Q_{i,j}) + \sum_{p=1}^{M_w} \left( s_{i+1/2,j}^{x,p} \right)^- \mathcal{W}_{i+1/2,j}^{x,p}$$

$$= f(Q_{i+1,j}) - \sum_{p=1}^{M_w} \left( s_{i+1/2,j}^{x,p} \right)^+ \mathcal{W}_{i+1/2,j}^{x,p} \,, \tag{4.40a}$$

where the set of $M_w$ waves $\mathcal{W}_{i+1/2,j}^{x,p}$ and speeds $s_{i+1/2,j}^{x,p}$ is obtained by solving a Riemann problem in the $x$-direction for the system $\partial q / \partial t + \partial f(q) / \partial x = 0$ with data $Q_{i,j}$, $Q_{i+1,j}$. Similarly, for the $G$ fluxes:

$$G(Q_{i,j}, Q_{i,j+1}) = g(Q_{i,j}) + \sum_{p=1}^{M_w} \left( s_{i+1/2,j}^{y,p} \right)^- \mathcal{W}_{i+1/2,j}^{y,p}$$

$$= g(Q_{i,j+1}) - \sum_{p=1}^{M_w} \left( s_{i+1/2,j}^{y,p} \right)^+ \mathcal{W}_{i+1/2,j}^{y,p} \,, \tag{4.40b}$$

where the set of $M_w$ waves $\mathcal{W}_{i,j+1/2}^{y,p}$ and speeds $s_{i,j+1/2}^{y,p}$ results from solving a Riemann problem in the $y$-direction for the system $\partial q / \partial t + \partial g(q) / \partial x = 0$ with data $Q_{i,j}$, $Q_{i,j+1}$.

We can write the algorithm in terms of fluctuations by setting

$$\mathcal{A}^{\pm} \Delta Q_{i+1/2,j} = \sum_{p=1}^{M_w} \left( s_{i+1/2,j}^{x,p} \right)^{\pm} \mathcal{W}_{i+1/2,j}^{x,p} \quad \text{and} \quad \mathcal{B}^{\pm} \Delta Q_{i,j+1/2} = \sum_{p=1}^{M_w} \left( s_{i,j+1/2}^{y,p} \right)^{\pm} \mathcal{W}_{i+1/2,j}^{y,p} \,. \tag{4.41}$$

We then obtain the following first-order upwind scheme:

$$Q_{i,j}^{n+1} = Q_{i,j}^n - \frac{\Delta t}{\Delta x} \left( \mathcal{A}^+ \Delta Q_{i-1/2,j} + \mathcal{A}^- \Delta Q_{i+1/2,j} \right) - \frac{\Delta t}{\Delta y} \left( \mathcal{B}^+ \Delta Q_{i,j-1/2} + \mathcal{B}^- \Delta Q_{i,j+1/2} \right) \,. \tag{4.42}$$

This method is typically stable only for Courant numbers up to $\frac{1}{2}$.

### 4.3.3  Multidimensional Wave Propagation Algorithms

The general form of the wave propagation algorithms for solving two-dimensional hyperbolic systems is

$$Q_{i,j}^{n+1} = Q_{i,j}^n - \frac{\Delta t}{\Delta x} \left( \mathcal{A}^+ \Delta Q_{i-1/2,j} + \mathcal{A}^- \Delta Q_{i+1/2,j} \right)$$

$$- \frac{\Delta t}{\Delta y} \left( \mathcal{B}^+ \Delta Q_{i,j-1/2} + \mathcal{B}^- \Delta Q_{i,j+1/2} \right)$$

$$- \frac{\Delta t}{\Delta x} \left( \widetilde{F}_{i+1/2,j} - \widetilde{F}_{i-1/2,j} \right) - \frac{\Delta t}{\Delta x} \left( \widetilde{G}_{i,j+1/2} - \widetilde{G}_{i,j-1/2} \right) \,, \tag{4.43}$$

where the quantities $\mathcal{A}^{\pm}\Delta Q$ and $\mathcal{B}^{\pm}\Delta Q$ represent fluctuations arising from Riemann problems in the $x$ and $y$ direction, respectively. The $\widetilde{F}$ and $\widetilde{G}$ fluxes are used to perform second order corrections, and also corrections for cross-derivative terms that arise in two dimensions and which did not appear in one dimension.

A method of the form (4.42), that is (4.43) with $\widetilde{F} = \widetilde{G} = 0$, is based on propagating waves normal to each interface. In reality the waves should propagate in a multidimensional manner and affect other cell averages besides those adjacent to the interface. This is accomplished by splitting each fluctuation $\mathcal{A}^{*}\Delta Q_{i+1/2,j}$ (and similarly $\mathcal{B}^{*}\Delta Q_{i,j+1/2}$) for $* = +$ and $-$ into two *transverse fluctuations* which will be denoted $\mathcal{B}^{+}\mathcal{A}^{*}\Delta Q_{i+1/2,j}$ (up-going) and $\mathcal{B}^{-}\mathcal{A}^{*}\Delta Q_{i+1/2,j}$ (down-going). This transverse decomposition of the fluctuations can be viewed as solving a second Riemann problem in the transverse direction, even though it is not based on left and right states as we normally interpret a Riemann solver. Let us assume, for example, that the waves and speeds resulting from solving Riemann problems in the normal direction are based on the eigenstructure of some linearized matrices $\tilde{A}$ and $\tilde{B}$ of $f'(q)$ and $g'(q)$, respectively. Then we compute the coefficients $\beta^{p}$ of the projection of $\mathcal{A}^{+}\Delta Q_{i+1/2,j}$ on the eigenvectors $r^{y,p}$ of $\tilde{B}$, $\mathcal{A}^{+}\Delta Q_{i+1/2,j} = \sum_{p=1}^{M_w} \beta^p r^{y,p}$, and we set

$$\mathcal{B}^{\pm}\mathcal{A}^{+}\Delta Q_{i+1/2,j} = \sum_{p=1}^{M_w} (\lambda^{p,y})^{\pm} \beta^p r^{y,p} \,, \tag{4.44}$$

where $\lambda^{p,y}$ are the eigenvalues of $\tilde{B}$.

The transverse fluctuations are used to update the four neighbouring $\widetilde{G}$ fluxes (and similarly $\widetilde{F}$ fluxes), which are initialized to zero, according to:

$$\widetilde{G}_{i+1,j+1/2} = \widetilde{G}_{i+1,j+1/2} - \frac{\Delta t}{2\Delta x}\mathcal{B}^{+}\mathcal{A}^{+}\Delta Q_{i+1/2,j} \,,$$

$$\widetilde{G}_{i+1,j-1/2} = \widetilde{G}_{i+1,j-1/2} - \frac{\Delta t}{2\Delta x}\mathcal{B}^{-}\mathcal{A}^{+}\Delta Q_{i+1/2,j} \,,$$

$$\widetilde{G}_{i,j+1/2} = \widetilde{G}_{i,j+1/2} - \frac{\Delta t}{2\Delta x}\mathcal{B}^{+}\mathcal{A}^{-}\Delta Q_{i+1/2,j} \,,$$

$$\widetilde{G}_{i,j-1/2} = \widetilde{G}_{i,j-1/2} - \frac{\Delta t}{2\Delta x}\mathcal{B}^{-}\mathcal{A}^{-}\Delta Q_{i+1/2,j} \,. \tag{4.45}$$

We remark that the transverse corrections terms have also the effect of improving the stability limit, allowing full Courant number 1, relative to the maximum wave speed in any direction.

Once the transverse corrections described above have been implemented, it is possible to achieve second-order accuracy by making one-dimensional flux corrections analogous to (4.23). Here we use waves and speeds computed in solving the Riemann problem normal to each interface. We perform corrections of the form:

$$\widetilde{F}_{i+1/2,j} = \frac{1}{2}\sum_{p=1}^{M_w} |s_{i+1/2,j}^{x,p}| \left(1 - \frac{\Delta t}{\Delta x}|s_{i+1/2,j}^{x,p}|\right) \widetilde{\mathcal{W}}_{i+1/2,j}^{x,p} \,, \tag{4.46}$$

where $\widetilde{\mathcal{W}}_{i+1/2,j}^{x,p}$ is a limited version of $\mathcal{W}_{i+1/2,j}^{x,p}$, obtained comparing $\mathcal{W}_{i+1/2,j}^{x,p}$ to $\mathcal{W}_{i-1/2,j}^{x,p}$ if $s_{i+1/2,j}^{x,p} > 0$, or to $\mathcal{W}_{i+3/2,j}^{x,p}$ if $s_{i+1/2,j}^{x,p} < 0$.

We can also propagate the second-order corrections in the transverse direction, this improving the stability properties and reducing spurious oscillations in many problems (see e.g. [119]). This is

accomplished by applying the routine that performs the splitting into transverse fluctuations to

$$\mathcal{A}^\pm \Delta Q_{i+1/2,j} \mp \sum_{p=1}^{M_w} \left| s_{i+1/2,j}^{x,p} \right| \left( 1 - \frac{\Delta t}{\Delta x} \left| s_{i+1/2,j}^{x,p} \right| \right) \widetilde{\mathcal{W}}_{i+1/2,j}^{x,p}, \tag{4.47}$$

instead of to $\mathcal{A}^\pm \Delta Q_{i+1/2,j}$.

### 4.4  The CLAWPACK Software

The software package CLAWPACK [115] (conservation law package) is a collection of Fortran routines that implement the wave propagation methods described in the previous sections. It solves hyperbolic systems of conservation laws and hyperbolic nonconservative systems as well. Systems with variable coefficients and problems with source terms can also be treated.

The software performs multidimensional computations on Cartesian grids and more generally on logically rectangular quadrilateral grids (curvilinear grids).

Moreover, the package includes adaptive mesh refinement versions (AMRCLAW) [13], and a MPI version in which the domain can be distributed among multiple processors.

We refer to [122] for a complete description of the algorithms implemented in the software.

Chapter 5

# RELAXATION SCHEMES AND THEIR RELATION TO APPROXIMATE RIEMANN SOLVERS

The idea of relaxation methods for systems of conservation laws is to approximate a system of the form (2.1) by solving a modified system with a relaxation source term that formally reduces to the original equations in the limit as the *relaxation time* $\tau \to 0^+$. Relaxation schemes have been extensively studied in the literature. We refer for example to [7], [26], [29], [70], [91], [99], [109], [130].

Considering here the one-dimensional case, a general form of *relaxation system* associated to the conservation law (2.5) is

$$\frac{\partial q}{\partial t} + \frac{\partial}{\partial x} g(q, v) = 0 \,, \tag{5.1a}$$

$$\frac{\partial v}{\partial t} + B(q, v) \frac{\partial q}{\partial x} + C(q, v) \frac{\partial v}{\partial x} = -\frac{1}{\tau} \left( v - v_{\text{eq}}(q) \right) \,, \tag{5.1b}$$

where $v \in \mathbb{R}^l$ is an additional vector variable whose equilibrium value for $\tau \to 0^+$ is $v_{\text{eq}}(q)$ and the function $g : \mathbb{R}^m \times \mathbb{R}^l \to \mathbb{R}^m$ is such that $g(q, v_{\text{eq}}(q)) = f(q)$. This function $g$ and the matrices $B \in \mathbb{R}^{l \times m}$ and $C \in \mathbb{R}^{l \times l}$ must be defined so that the homogeneous relaxation system is hyperbolic, and in general they will be chosen so that the new problem (5.1) is easier to solve than the original one. For instance, a linear relaxation system can be used to solve a nonlinear conservation law. The equations (5.1) formally recover the original conservation law in the *relaxation limit* $\tau \to 0^+$. A general necessary condition for convergence is the so-called *subcharacteristic condition* [131], which requires that the eigenvalues of the hyperbolic part of (5.1) span the characteristic speeds of the original problem.

One way to solve the relaxation system (5.1) is to is to employ a fractional step method. First, given the initial data $q^n$ and $v^n$ at time $t^n$, we apply some finite volume scheme to the homogeneous system

$$\frac{\partial q}{\partial t} + \frac{\partial}{\partial x} g(q, v) = 0 \,, \tag{5.2a}$$

$$\frac{\partial v}{\partial t} + B(q, v) \frac{\partial q}{\partial x} + C(q, v) \frac{\partial v}{\partial x} = 0 \,, \tag{5.2b}$$

for advancing the solution over a time step $\Delta t$. Let us denote $q^*$ and $v^*$ the updated variables we find through this step. Then we consider the solution over time $\Delta t$ of the ordinary differential equations

$$\frac{\partial q}{\partial t} = 0 \,, \tag{5.3a}$$

$$\frac{\partial v}{\partial t} = -\frac{1}{\tau} \left( v - v_{\text{eq}}(q) \right) \,. \tag{5.3b}$$

We can solve exactly the system above, obtaining:

$$q^{n+1} = q^* \,, \tag{5.4a}$$

$$v^{n+1} = v_{\text{eq}}(q^{n+1}) + e^{-\frac{\Delta t}{\tau}} \left( v^* - v_{\text{eq}}(q^{n+1}) \right) \,. \tag{5.4b}$$

Since we are only concerned with the equilibrium limit $\tau \to 0^+$, we simply set, instead of (5.4b),

$$v^{n+1} = v_{\text{eq}}(q^{n+1}) = v_{\text{eq}}(q^*) \,. \tag{5.5}$$

This is what is called *relaxed scheme* in [93]. Employing the equilibrium condition above allows us to ignore $v^*$, so that we don't need to update $v^n$ to $v^*$ in the first step. Here we are considering this special case of relaxation scheme in order to be able to relate it to approximate Riemann solvers, as we will explain in the next section.

In summary, our relaxation scheme consists of the following two steps:

ALGORITHM 5.1 (RELAXED SCHEME)
  1. Solve the hyperbolic system (5.2) to update $q^n$ to $q^{n+1}$.

  2. Set $v^{n+1} = v_{\text{eq}}(q^{n+1})$ (*equilibrium condition*).

## 5.1 Relaxation Schemes and Approximate Riemann Solvers

Relaxation methods based on the Algorithm 5.1 can result in the definition of a class of approximate Riemann solvers for the original system of conservation laws. This has been explored in our work [124], and much of this chapter is taken from that paper. Let us restrict here our analysis to a relaxation system in the following form, that slightly extends the one proposed by Jin and Xin in [93]:

$$\frac{\partial q}{\partial t} + \frac{\partial v}{\partial x} = 0 \,, \tag{5.6a}$$

$$\frac{\partial v}{\partial t} + D^2 \frac{\partial q}{\partial x} = -\frac{1}{\tau}(v - f(q)) \,, \tag{5.6b}$$

where $v \in \mathbb{R}^m$, and $D^2 \in \mathbb{R}^{m \times m}$ is a positive definite matrix. Note that in this case $l = m$, so that we are replacing the original $m$ conservation laws with $2m$ equations. Moreover, $g(q,v) = v$, $B = D^2$, $C = 0$, and $v_{\text{eq}}(q) = f(q)$. In [93] Jin and Xin choose $D^2$ to be a diagonal matrix with positive diagonal elements. We assume without loss of generality that $D$ itself has positive eigenvalues given by the pairs $\pm d^j$ for $j = 1, \cdots, m$. Then the matrix

$$\begin{bmatrix} 0 & I \\ D^2 & 0 \end{bmatrix} \tag{5.7}$$

appearing as the coefficient matrix on the left-hand side of (5.6) has $2m$ eigenvalues given by

$$s^{2j-1} = -d^j \qquad \text{and} \qquad s^{2j} = +d^j \tag{5.8}$$

with $2m$ eigenvectors

$$\theta^{2j-1} = \begin{bmatrix} z^j \\ -d^j z^j \end{bmatrix} \quad \text{and} \quad \theta^{2j} = \begin{bmatrix} z^j \\ +d^j z^j \end{bmatrix} \,, \tag{5.9}$$

for $j = 1, \cdots, m$. Note that, if $\lambda^j(q)$ denotes the $j$-th eigenvalue of $f'(q)$, the subcharacteristic condition for (5.6) reads

$$-d_{\max} \le \lambda^j(q) \le d_{\max} \,, \quad \forall j = 1, \cdots, m \,, \, \forall q \,, \tag{5.10}$$

where $d_{\max} = \max_j d^j$ is the spectral radius of $D$.

Let us now consider the solution of a Riemann problem for (5.6), by applying the Algorithm 5.1. Given the states $q_\ell$ and $q_r$, we compute $v_\ell = f(q_\ell)$ and $v_r = f(q_r)$. This corresponds to the equilibrium

condition that is imposed at each time step in the algorithm. We then solve a Riemann problem for the homogeneous system associated to (5.6) with initial data

$$\begin{bmatrix} q_\ell \\ f(q_\ell) \end{bmatrix}, \quad \begin{bmatrix} q_r \\ f(q_r) \end{bmatrix}. \tag{5.11}$$

The solution of this linear Riemann problem requires the decomposition

$$\begin{bmatrix} q_r - q_\ell \\ f(q_r) - f(q_\ell) \end{bmatrix} = \sum_{p=1}^{2m} \alpha^p \, \theta^p. \tag{5.12}$$

Once we have determined the scalar coefficients $\alpha^p$ by solving the system above, we can define

$$\mathcal{W}^{2j-1} = \alpha^{2j-1} \, z^j \qquad \text{and} \qquad \mathcal{W}^{2j} = \alpha^{2j} \, z^j, \tag{5.13}$$

for $j = 1, \cdots, m$. These $2m$ waves $\mathcal{W}^p \in \mathbb{R}^m$, $p = 1, \cdots, 2m$, together with the corresponding propagation speeds $s^p$ given in (5.8), are used to update the vector $q$. By virtue of step 2 in the algorithm, $v$ is simply reset through the equilibrium condition $v = v_{\mathrm{eq}}(q)$, thus we don't need to keep track of this variable. The relaxation process has disappeared, and we view the relaxation schemes as a way to update $q$. Note that by using (5.8),(5.9) and (5.13), from (5.12) we can write the jump in $q$ as

$$q_r - q_\ell = \sum_{p=1}^{2m} \mathcal{W}^p, \tag{5.14}$$

which is the form of the decomposition (4.7) (with $M_w = 2m$) that characterizes the structure of the approximate Riemann solvers presented in Section 4.1.1. Also, from (5.12), the jump in the flux satisfies

$$f(q_r) - f(q_\ell) = \sum_{p=1}^{2m} s^p \mathcal{W}^p, \tag{5.15}$$

which corresponds to the conservation condition (4.8) with $M_w = 2m$.

In conclusion, the relaxation scheme has led to the definition of an approximate Riemann solver for the original system of $m$ conservation laws consisting of the $2m$ waves $\mathcal{W}^p$ in (5.13) with the speeds $s^p$ given in (5.8).

### 5.1.1 Diagonal Matrix D

For the case of a diagonal matrix $D = \mathrm{diag}(d^1, \ d^2, \ldots, \ d^m)$ as used by Jin and Xin in [93], we have $z^j = e^j$, the $j$th unit vector. The elements $d^j$ of $D$ must be chosen so that the subcharacteristic condition (5.10) is satisfied. For the Euler equations, Jin and Xin choose them as some approximations to the eigenvalues $u - c$, $u$, and $u + c$ of the Jacobian matrix (where $u$ is the velocity and $c$ the sound speed).

Note that when $z^j = e^j$, the decomposition (5.12) splits into $m$ decoupled $2 \times 2$ problems of the form

$$\begin{bmatrix} q_r^j - q_\ell^j \\ v_r^j - v_\ell^j \end{bmatrix} = \alpha^{2j-1} \begin{bmatrix} 1 \\ -d^j \end{bmatrix} + \alpha^{2j} \begin{bmatrix} 1 \\ d^j \end{bmatrix} \tag{5.16}$$

involving only the $j$th component of the vector $q$ and the $j$th component of the flux vector $v = f(q)$. Solving this system gives

$$\alpha^{2j-1} = \frac{1}{2d^j} (d^j (q_r^j - q_\ell^j) - (v_r^j - v_\ell^j)), \tag{5.17a}$$

$$\alpha^{2j} = \frac{1}{2d^j} (d^j (q_r^j - q_\ell^j) + (v_r^j - v_\ell^j)). \tag{5.17b}$$

When applied to the Euler equations, for example, the density and its flux are split into one pair of waves with speeds $\pm d^1$, the momentum is split into a second pair of waves with speeds $\pm d^2$, and the energy is split into a third pair of waves with speeds $\pm d^3$. The splitting of each component is done in such a way that conservation is maintained, which is guaranteed by the manner in which the flux differences are split along with the components of $q_r - q_\ell$ so that (5.15) is satisfied. In the next section we will show that this can be viewed as a generalization of the HLL Riemann solver.

## 5.2 Relation to the HLL Solver

Let us consider the HLL solver introduced in Section 4.1.2, and assume for the moment that $a_\ell = -a_r$ with $a_r > 0$. Then this is equivalent to the relaxation Riemann solver described in the previous section if we take $D$ to be the diagonal matrix $D = a_r I$, so that

$$s^{2j-1} = -d^j = a_\ell \quad \text{and} \quad s^{2j} = d^j = a_r. \tag{5.18}$$

Then the $j$th system (5.16) splits the $j$th component of $q_r - q_\ell$ into 2 waves propagating at speeds $a_\ell$ and $a_r$. After doing this for all $m$ components we obtain $2m$ waves, each carrying a jump in only one component of $q$. But $m$ of these waves travel at the same speed $a_\ell$ and the other $m$ at speed $a_r$ and so we can lump these together into 2 waves, which then must be the HLL waves (4.13) since both approaches are conservative. We can verify directly that these are the same by using the solution (5.17). The left-going wave carries a jump $\alpha^{2j-1}$ in the $j$th component and so the intermediate state $q_m$ in (4.14) has $j$th component

$$
\begin{aligned}
q_m^j &= q_\ell^j + \alpha^{2j-1} = \frac{1}{2d^j}(d^j(q_r^j + q_\ell^j) - (v_r^j - v_\ell^j)) \\
&= \frac{1}{2}(q_r^j + q_\ell^j) - \frac{1}{2d^j}(f(q_r^j) - f(q_\ell^j)).
\end{aligned} \tag{5.19}
$$

Since $d^j = a_r = -a_\ell$ we have $2d^j = a_r - a_\ell$ and this agrees with the $j$th component of (4.14).

We thus see that the relaxation scheme in the case $D = dI$ amounts to using the HLL Riemann solver with $a_\ell = -d$ and $a_r = d$. Let $\lambda^j(q)$ denote the $j$th eigenvalue of the Jacobian matrix $f'(q)$. If we choose

$$d = \max_{1 \le j \le m} \left( \max(|\lambda^j(q_\ell)|, \ |\lambda^j(q_r)|) \right) \tag{5.20}$$

as an upper bound on the characteristic speeds (assuming the system is genuinely nonlinear) and then apply the first-order upwind method together with this approximate Riemann solver, the resulting method is simply Rusanov's method, as discussed in [194], for example. This method is also known as the Local Lax–Friedrichs method. If we choose $d = \Delta x/\Delta t$, an upper bound on all possible wave speeds provided the CFL condition is satisfied for the grid being used, then this method reduces to the classical Lax–Friedrichs method. We note in passing that the Local and classical Lax–Friedrichs methods can be extended to second-order accuracy to obtain the central schemes of Nessyahu & Tadmor [157] and Kurganov & Tadmor [103] respectively, and connections between these methods and relaxation schemes are briefly discussed in the introduction to [103].

If $D$ is diagonal but the diagonal elements $d^j$ are not equal (as in the choice of Jin and Xin [93]), we can view the relaxation scheme as a generalization of the HLL solver in which separate speeds $a_r^j = -a_\ell^j = d^j$ are chosen for each component of the vector $q$. It is not clear that this generalization will be an improvement, however, since in coupled systems of conservation laws we do not expect information in different components of $q$ to propagate at different speeds. Rather, it is different eigencomponents of $q$ (based on the eigenvectors of $f'(q)$) which propagate at different speeds. This suggests that a more substantial improvement might be made by replacing the unit vectors $z^j = e^j$ used in deriving HLL

from the decomposition (5.12) by some approximations to the eigenvectors of $f'(q)$. Generalizations of this form will be pursued in the following sections.

First we present a generalization of the relaxation scheme that agrees with the more general HLL method in the case when $a_\ell \neq -a_r$. Rather than using a matrix of the form (5.7), consider a relaxation system

$$\frac{\partial q}{\partial t} + \frac{\partial v}{\partial x} = 0, \tag{5.21a}$$

$$\frac{\partial v}{\partial t} - (D_\ell D_r)\frac{\partial q}{\partial x} + (D_\ell + D_r)\frac{\partial v}{\partial x} = -\frac{1}{\tau}(v - f(q)), \tag{5.21b}$$

with

$$D_\ell = \operatorname{diag}(a_\ell) \quad \text{and} \quad D_r = \operatorname{diag}(a_r). \tag{5.22}$$

The coefficient matrix appearing in this system,

$$\begin{bmatrix} 0 & I \\ -D_\ell D_r & D_\ell + D_r \end{bmatrix}, \tag{5.23}$$

has eigenvalues

$$s^{2j-1} = a_\ell \qquad \text{and} \qquad s^{2j} = a_r \tag{5.24}$$

and eigenvectors

$$\theta^{2j-1} = \begin{bmatrix} e^j \\ a_\ell\, e^j \end{bmatrix} \quad \text{and} \quad \theta^{2j} = \begin{bmatrix} e^j \\ a_r\, e^j \end{bmatrix}, \tag{5.25}$$

for $j = 1, \cdots, m$. Note that if $a_\ell = -a_r$ then the matrix (5.23) reduces to (5.7). Using the vectors (5.25) in the decomposition (5.12) gives the HLL solver for arbitrary $a_\ell$ and $a_r$.

### 5.3 Relaxation Riemann Solvers

The analysis of the relation between relaxation schemes and Riemann solvers has led us to introduce a general class of approximate Riemann solvers which allows as many as $2m$ waves in the resulting solution. The idea is to decompose both the jump in $q$ and the jump in the flux $f$ simultaneously, in the form:

$$\begin{bmatrix} q_r - q_\ell \\ f(q_r) - f(q_\ell) \end{bmatrix} = \alpha^1 \begin{bmatrix} w^1 \\ \phi^1 \end{bmatrix} + \cdots + \alpha^{2m} \begin{bmatrix} w^{2m} \\ \phi^{2m} \end{bmatrix}, \tag{5.26}$$

where the vectors $w^p, \phi^p \in \mathbb{R}^m$ must be chosen in some manner, together with speeds $s^p$, $p = 1, \cdots, 2m$. In general, the definition of the speeds $s^p$ must satisfy proper stability criteria, that from the relaxation method's viewpoint correspond to the subcharacteristic condition.

Once we have determined the scalar coefficients $\alpha^1, \alpha^2, \cdots, \alpha^{2m}$ by solving the $2m \times 2m$ system (5.26) (provided the vectors $[w^p, \phi^p]^{\mathrm{T}}$ are linearly independent), the waves needed for updating $q$ are then

$$\mathcal{W}^p = \alpha^p w^p, \quad p = 1, 2, \cdots, 2m, \tag{5.27}$$

with speeds $s^p$. We will refer to this solver as a *relaxation Riemann solver*, based on the considerations in the previous sections. Note also that conservation requires:

$$\sum_{p=1}^{2m} \alpha^p\, \phi^p = \sum_{p=1}^{2m} s^p \mathcal{W}^p, \tag{5.28}$$

and a sufficient condition for satisfying this equality is to define

$$\phi^p = s^p\, w^p. \tag{5.29}$$

With this choice conservation will be always guaranteed, no matter how the $w^p$ and $s^p$ are defined. This is accomplished by introducing more degrees of freedom ($2m$ rather than $m$) and requiring that the jump in $f$ is decomposed in a manner consistent with the jump in $q$. Note that (5.29) is reminiscent of the Rankine-Hugoniot jump conditions relating the jump in $f$ across a shock to the jump in $q$.

We have seen that the Jin and Xin relaxation scheme and the HLL solver correspond to defining $w^{2j-1} = w^{2j} = e^j$, $j = 1,\ 2,\ \ldots,\ m$, in the decomposition (5.26). However, as already noticed, it is attractive instead to define the vectors $w^p$ as some approximations to the eigenvectors of the Jacobian matrix $f'(q)$ near $q_\ell$ and $q_r$. Let $\{\tilde{r}^j\}_{1 \le j \le m}$ denote a set of $m$ linearly independent vectors approximating the eigenvectors $\{r^j\}_{1 \le j \le m}$ of $f'(q)$, and let us associate to $\tilde{r}^j$ two distinct speeds $s_\ell^j$, $s_r^j$, $j = 1, \cdots, m$. Then we can define an approximate Riemann solver based on the decomposition (5.26) with the choice

$$\left[ \begin{array}{c} w^{2j-1} \\ \phi^{2j-1} \end{array} \right] = \left[ \begin{array}{c} \tilde{r}^j \\ s_\ell^j \tilde{r}^j \end{array} \right] \qquad \text{and} \qquad \left[ \begin{array}{c} w^{2j} \\ \phi^{2j} \end{array} \right] = \left[ \begin{array}{c} \tilde{r}^j \\ s_r^j \tilde{r}^j \end{array} \right]. \qquad (5.30)$$

This decomposition arises naturally in the process of solving the $2m \times 2m$ linear system appearing in a relaxation scheme based on a relaxation system of the form (5.21) with

$$D_\ell = \tilde{R}\, S_\ell\, \tilde{R}^{-1} \qquad \text{and} \qquad D_r = \tilde{R}\, S_r\, \tilde{R}^{-1}\,, \qquad (5.31a)$$

where

$$S_\ell = \text{diag}(s_\ell^j) \qquad \text{and} \qquad S_r = \text{diag}(s_r^j)\,, \qquad (5.31b)$$

and $\tilde{R} = [\tilde{r}^1, \cdots, \tilde{r}^m]$. Since we assume $s_\ell^j \ne s_r^j$, then the coefficient matrix (5.23) is diagonalizable and the vectors appearing in (5.30) are the eigenvectors. In the following sections we will discuss some possible definitions of $\tilde{r}^j$, $s_\ell^j$, $s_r^j$. In particular, we will consider the choice $\tilde{r}^j = \hat{r}^j$, where $\hat{r}^j$, $j = 1, \cdots, m$, are the eigenvectors of the Roe matrix (see Section 4.1.3), and explore in this connection the relation with the Roe solver.

To conclude, we remark that the added flexibility of specifying $2m$ waves rather than $m$ also allows some interesting new possibilities in deriving approximate Riemann solvers. In Sections 5.8 and 5.9 we will look at possible applications to conservation laws with discontinuous coefficients and with source terms.

## 5.4   Relation to the Roe Solver

One obvious choice for the vectors $\tilde{r}^j$ in (5.30) is to use the eigenvectors $\hat{r}^j$ of the Roe matrix $\hat{A}$ satisfying (4.15). If we choose two distinct speeds $s_\ell^j \ne s_r^j$, since the $\hat{r}^j$ for $j = 1,\ 2,\ \ldots,\ m$ are linearly independent, it follows that the full set of $2m$ vectors given by (5.30) will span $\mathbb{R}^{2m}$, and a decomposition of the form (5.26) can always be performed to define an approximate Riemann solution.

It turns out that we can also choose $s_\ell^j = s_r^j$ provided that we define this value to be $\hat{\lambda}^j$, the $j$th eigenvalue of the matrix $\hat{A}$. In this case the two vectors in (5.30) are identical and there are only $m$ distinct vectors in (5.26),

$$\left[ \begin{array}{c} q_r - q_\ell \\ f(q_r) - f(q_\ell) \end{array} \right] = \hat{\alpha}^1 \left[ \begin{array}{c} \hat{r}^1 \\ \hat{\lambda}^1 \hat{r}^1 \end{array} \right] + \cdots + \hat{\alpha}^m \left[ \begin{array}{c} \hat{r}^m \\ \hat{\lambda}^m \hat{r}^m \end{array} \right]. \qquad (5.32)$$

This $2m \times m$ linear system has a unique solution $\hat{\alpha} \in \mathbb{R}^m$ in spite of the fact that it appears to be overdetermined. The particular vector on the left hand side of (5.32) lies in the span of these $m$ vectors since $\hat{r}^j$ and $\hat{\lambda}^j$ come from the Roe matrix $\hat{A}$ satisfying (4.15). In fact, we can simply solve

$$q_r - q_\ell = \hat{\alpha}^1 \hat{r}^1 + \cdots + \hat{\alpha}^m \hat{r}^m \qquad (5.33)$$

as one usually does with the Roe solver and then

$$f(q_r) - f(q_\ell) = \hat{\alpha}^1 \hat{\lambda}^1 \hat{r}^1 + \cdots + \hat{\alpha}^m \hat{\lambda}^m \hat{r}^m \tag{5.34}$$

will automatically be satisfied by (4.15), as is easily seen if we multiply (5.33) by $\hat{A}$.

## 5.5 Entropy Fixes

As mentioned in Section 4.1.3, a failing of the Roe solver is that it can lead to entropy-violating shocks. This typically happens if the true Riemann solution contains a transonic rarefaction wave in some family, say the $k$th family, with characteristic speeds that increase from negative to positive values through the rarefaction fan. This means that information in the $k$th family should travel partly to the left and partly to the right and affect cell averages on both sides. The Roe solver approximates every wave by a single discontinuity propagating at a speed given by an eigenvalue of $\hat{A}$, and in the transonic rarefaction case $\hat{\lambda}^k \approx 0$ typically and the proper spreading does not occur. An entropy fix is often used to address this problem. One possibility proposed by Harten and Hyman [77] (see also [118]) is to replace the single wave $\hat{\alpha}^k \hat{r}^k$ in this case by a pair of waves $\alpha_\ell^k \hat{r}^k$ and $\alpha_r^k \hat{r}^k$ propagating at speeds $s_\ell^k < 0 < s_r^k$ that are chosen to approximate the characteristic speeds at each edge of the rarefaction fan. The total wave strength should be the same, so we need

$$\alpha_\ell^k + \alpha_r^k = \hat{\alpha}^k, \tag{5.35}$$

and to maintain conservation we also require

$$\alpha_\ell^k s_\ell^k + \alpha_r^k s_r^k = \hat{\alpha}^k \hat{\lambda}^k. \tag{5.36}$$

This gives a linear system of two equations to solve for $\alpha_\ell^k$ and $\alpha_r^k$, yielding

$$\alpha_\ell^k = \frac{\hat{\alpha}^k s_r^k - \hat{\lambda}^k}{s_r^k - s_\ell^k} \qquad \text{and} \qquad \alpha_r^k = \frac{\hat{\lambda}^k - \hat{\alpha}^k s_\ell^k}{s_r^k - s_\ell^k}. \tag{5.37}$$

Exactly this same method can be derived by using a relaxation Riemann solver of the form (5.26), which we now take to be of the special form

$$\begin{bmatrix} q_r - q_\ell \\ f(q_r) - f(q_\ell) \end{bmatrix} = \alpha_\ell^1 \begin{bmatrix} \hat{r}^1 \\ s_\ell^1 \hat{r}^1 \end{bmatrix} + \alpha_r^1 \begin{bmatrix} \hat{r}^1 \\ s_r^1 \hat{r}^1 \end{bmatrix} + \cdots + \alpha_\ell^m \begin{bmatrix} \hat{r}^m \\ s_\ell^m \hat{r}^m \end{bmatrix} + \alpha_r^m \begin{bmatrix} \hat{r}^m \\ s_r^m \hat{r}^m \end{bmatrix}. \tag{5.38}$$

Here we are allowing each wave speed $\hat{\lambda}^j$ to be replaced by a pair of speeds $s_\ell^j$ and $s_r^j$. If we take $s_\ell^j = s_r^j = \hat{\lambda}^j$ for every $j$ then this reduces to the original Roe solver with each vector repeated twice. This system will have infinitely many solution since any $\alpha_\ell^j$ and $\alpha_r^j$ satisfying

$$\alpha_\ell^j + \alpha_r^j = \hat{\alpha}^j \tag{5.39}$$

provides a solution, where $\hat{\alpha}^j$ are the Roe coefficients in (5.32). For any such choice of $\alpha_\ell^j$ and $\alpha_r^j$ we essentially have the original Roe solver — we've simply replaced one wave by two waves propagating at the same speed and adding up to the original wave.

If the $k$th family has a transonic rarefaction, however, then we can choose $s_\ell^k < 0 < s_r^k$ (while still taking $s_\ell^j = s_r^j = \hat{\lambda}^j$ for $j \neq k$) and the decomposition (5.38) results in the Roe solver with the entropy fix described above. As in the discussion of the HLL method in Section 5.2, including $\Delta f$ in the decomposition (5.38) ensures that conservation is maintained and leads to the same coefficients $\alpha_\ell^k$ and $\alpha_r^k$ as in (5.37).

### 5.6 Generalized Roe Solvers

Let us consider $s_\ell^j \neq s_r^j$ in each family, while still using in (5.30) the eigenvectors $\hat{r}^j$ of the Roe matrix and thus a decomposition of the form (5.38). One possible choice might be

$$s_\ell^j = \lambda^j(q_\ell), \qquad s_r^j = \lambda^j(q_r), \tag{5.40}$$

for $j = 1, 2, \ldots, m$. This definition would automatically give spreading across any rarefaction wave, including transonic ones. On the other hand if $\lambda^j(q_\ell) > \lambda^j(q_r)$ then the $j$th wave in the true Riemann solution is presumably a shock, but we would be approximating it by two waves. We can still solve the system (5.38). The state that arises in the approximate solution between these two waves can be viewed as an approximation to the value that would be found by averaging an overturned compression wave as in Brenier's transport-collapse method [19] or the large time step method of [116]. This also has similarities to the method developed by Engquist & Osher [58] for scalar problems and Osher & Solomon [161] for systems, often called the Osher solver in general. In this approach only the integral curves of the eigenvectors are used to compute an approximate Riemann solution, so that rarefaction waves and overturned compression waves are used in every family. Hence (5.38) with the choice (5.40) might be viewed as an approximation to the Osher solver based on Roe averages. Perhaps a closer connection can be made with a different choice of eigenvectors and speeds in (5.38).

Note that if $s_\ell^j$ and $s_r^j$ have the same sign then the generalization proposed in this section does not really change the contribution from the $j$th family to the numerical solution, at least not at the level of a first-order upwind method based on these waves. This is because the two waves in this family affect only one of the neighboring cell averages and might as well be lumped into a single wave. We can combine them as

$$\alpha_l^j \begin{bmatrix} \hat{r}^j \\ s_\ell^j \hat{r}^j \end{bmatrix} + \alpha_r^j \begin{bmatrix} \hat{r}^j \\ s_r^j \hat{r}^j \end{bmatrix} = \beta^j \begin{bmatrix} \hat{r}^j \\ s^j \hat{r}^j \end{bmatrix}, \tag{5.41}$$

for some choice of $\beta^j$ and $s^j$, where $s^j$ should then be used as the speed of this lumped wave. We can easily solve for the required values:

$$\beta^j = \alpha_l^j + \alpha_r^j \qquad \text{and} \qquad s^j = \frac{\alpha_l^j s_\ell^j + \alpha_r^j s_r^j}{\alpha_l^j + \alpha_r^j}. \tag{5.42}$$

On the other hand, we know there is a unique decomposition of $q_r - q_\ell$ into the eigenvectors $\hat{r}^j$ with the coefficients $\hat{\alpha}^j$, and from this we can deduce that in fact $\beta^j = \hat{\alpha}^j$ and also that $s^j = \hat{\lambda}^j$, the corresponding Roe velocity.

It is only in the transonic case that something different is obtained by the more general choice (5.40). For a transonic rarefaction this gives a standard entropy fix, as already discussed. For a transonic shock this would introduce additional dissipation. This may also be desirable in some cases, since the lack of dissipation in shocks for which $\hat{\lambda}^k \approx 0$ is also known to cause numerical difficulties, such as nonphysical oscillations near slowly moving shocks. The addition of more dissipation in this case is one approach to improving solutions in this case. See for example [8], [52], [92], [98].

A further generalization of this solver is obtained by using vectors $\tilde{r}^j$ in (5.30) that are not the eigenvectors of the Roe matrix. This may be useful for problems where a Roe average satisfying (4.15) is not available, and instead one wishes to use a simpler average such as $\hat{A} = f'\left(\frac{1}{2}(q_\ell + q_r)\right)$. By taking the $\hat{r}^j$ in (5.38) to be the eigenvectors of this matrix and choosing some reasonable values for $s_l^j$ and $s_r^j$, for example (5.40), it is possible to obtain consistent decompositions of $q_r - q_\ell$ and $f(q_r) - f(q_\ell)$ in terms of these $2m$ waves. Moreover, we can merge each pair of waves into a single wave using (5.41) with $\beta^j$ and $s^j$ defined by (5.42) if desired (typically in all but the transonic rarefaction case). We then

have a decomposition into $m$ waves,

$$q_r - q_\ell = \sum_{j=1}^{m} \beta^j \hat{r}^j \tag{5.43}$$

and set of speeds $s^j$ for which

$$f(q_r) - f(q_\ell) = \sum_{j=1}^{m} s^j \beta^j \hat{r}^j \tag{5.44}$$

holds. This mimics an important property of the Roe solver that is useful in wave-propagation implementations (see Section 4.2).

One possible application of this idea would be to use the Roe eigenvectors coming from a simpler but related system of equations as an approximation. This could be useful for problems where a Roe matrix cannot be found directly.

### 5.7   The Roe Solver as a Relaxation Scheme

The Roe solver and the generalization presented in the previous section can be viewed in the context of relaxation schemes using the connection introduced in Sections 5.1, 5.3. This may be useful in analyzing the Roe scheme. As already noticed, the decomposition (5.38) can be considered as arising form a relaxation system of the form (5.21) with the matrices $D_\ell$, $D_r$ as in (5.31) and with the choice $\tilde{R} = \hat{R}$, the matrix of Roe eigenvectors. For the original Roe scheme $s_\ell^j = s_r^j = \hat{\lambda}^j$ for all $j$. In this case $D_\ell = D_r = \hat{A}$ and the coefficient matrix (5.23) reduces to

$$\begin{bmatrix} 0 & I \\ -\hat{A}^2 & 2\hat{A} \end{bmatrix}. \tag{5.45}$$

This matrix is defective: each eigenvalue $\hat{\lambda}^j$ has algebraic multiplicity 2 but geometric multiplicity 1 and there are only $m$ distinct vectors in (5.38) as already discussed.

Normally a relaxation system of the form (5.6) or (5.21) yields a solution $q(x,t)$ which may converge to the solution of the original conservation law as $\tau \to 0$, but will not agree with this solution for $\tau > 0$. Instead, it approximates the solution to a viscous conservation law of the form

$$\frac{\partial q}{\partial t} + \frac{\partial f(q)}{\partial x} = \tau \frac{\partial}{\partial x} \left( B(q) \frac{\partial q}{\partial x} \right) + \mathcal{O}(\tau^2), \tag{5.46}$$

where the viscosity matrix $B(q)$ can be determined by a Chapman-Enskog expansion [29], [131]. The structure of this viscosity matrix can play a role in determining whether the correct entropy-satisfying solution is obtained in the limit $\tau \to 0$, see for example [15], [16], [68], [134]. For a relaxation system with the coefficient matrix (5.45), we find that

$$B(q) = -\hat{A}^2 + 2\hat{A}f'(q) - (f'(q))^2. \tag{5.47}$$

Note that if $q_\ell \approx q_r$ then $\hat{A} \approx f'(q)$ and the viscosity matrix vanishes in the case of equality. Moreover, even when there is a large jump between $q_\ell$ and $q_r$ it is possible that this relaxation system will reproduce an exact weak solution to the original conservation law even when $\tau > 0$, as if there were no viscosity. This happens in the special case when we consider a Riemann problem between states $q_\ell$ and $q_r$ that satisfy the Rankine-Hugoniot jump condition for some scalar value $s$,

$$f(q_r) - f(q_\ell) = s(q_r - q_\ell). \tag{5.48}$$

Suppose we solve the relaxation system

$$\frac{\partial q}{\partial t} + \frac{\partial v}{\partial x} = 0 \,, \tag{5.49a}$$

$$\frac{\partial v}{\partial t} - \hat{A}^2 \frac{\partial q}{\partial x} + 2\hat{A}\frac{\partial v}{\partial x} = -\frac{1}{\tau}\left(v - f(q)\right) \tag{5.49b}$$

with this Riemann initial data $q_\ell$, $q_r$ and $v_\ell = f(q_\ell)$, $v_r = f(q_r)$ and with the matrix $\hat{A}$ chosen to be the Roe matrix for this data (and frozen at this value even if $q$ and $v$ evolve). Then the property (4.15) of the Roe matrix implies that $q_r - q_\ell$ is an eigenvector of $\hat{A}$, proportional to $\hat{r}^k$ for some $k$, and that $s = \hat{\lambda}^k$ is the corresponding eigenvalue. It follows that

$$q(x,t) = q(x - \hat{\lambda}^k t, 0) \tag{5.50a}$$

$$v(x,t) = v(x - \hat{\lambda}^k t, 0) = f(q(x,t)) \tag{5.50b}$$

is the solution to the relaxation system (5.49) for any value of $\tau$. The jump discontinuity simply propagates with speed $\hat{\lambda}^k$ and since $v \equiv f(q)$, the source term vanishes. This is a weak solution of the original conservation law in this case, though it may not satisfy the entropy condition. If the discontinuity should spread into a rarefaction wave, the relaxation system will instead produce the expansion shock.

Of course if this relaxation system is now used numerically as part of a relaxation scheme, then numerical viscosity may be added when the linear system is solved numerically. But in the case $\hat{\lambda}^k = 0$ it is possible that no smearing is introduced, as for example in Roe's first-order method which produces entropy-violating solutions in the transonic case. It is well known that this is caused by a lack of numerical viscosity, which has been extensively analyzed by other means, but it is interesting to observe that this phenomenon is connected with a relaxation system which itself lacks viscosity and produces entropy-violating weak solutions even in the case when the data is not transonic. It is also interesting to note that the viscosity matrix (5.47) generally fails to be positive definite. In fact if $\hat{A}$ and $f'(q)$ commute then $B(q) = -(\hat{A} - f'(q))^2$ is negative definite.

Note that adding an entropy fix to Roe's method, as described in Sections 5.5 and 5.6, changes the relaxation system to one of the more general form (5.21). The entropy-violating weak solution is no longer an exact solution, as we have explicitly added spreading of this wave.

## 5.8   Discontinuous Flux Functions

As one example of how a relaxation Riemann solver with $2m$ waves might prove useful, consider a conservation law with a spatially varying flux function $f(q, x)$. One way to solve this problem numerically is to use a finite-volume method with the flux function discretized so that the $i$th grid cell has a flux function $f_i(q)$ associated with it. At a cell interface we must then solve a Riemann problem with data $q_\ell$, $q_r$ and two different flux functions $f_\ell(q)$ and $f_r(q)$. When $f_\ell$ and $f_r$ are nonlinear, determining the exact Riemann solution for this situation may be nontrivial, e.g, [63], [101], [113], [195].

One natural way to use (5.26) might be to compute two sets of eigenvectors and eigenvalues using the two Jacobian matrices $f'_\ell(q_\ell)$ and $f'_r(q_r)$. Call these $\lambda^j_\ell, r^j_\ell$ and $\lambda^j_r, r^j_r$. These could be used to define $2m$ vectors for use in (5.26). This does not seem to be a good idea in general, however. Often both $\lambda^j_\ell$ and $\lambda^j_r$ will have the same sign, indicating what direction the $j$th wave is propagating. Suppose these are both positive, for example, indicating that this wave is propagating into the cell on the right, where the flux function is $f_r(q)$. Then the eigenvector $r^j_r$ may be a useful component in the decomposition, but $r^j_\ell$ may be completely irrelevant.

Instead, it is useful to observe that the Riemann solution must typically involve a stationary discontinuity in $q$ (moving at speed 0) at the interface, between two values $q_\ell^*$ and $q_r^*$ related via

$$f_\ell(q_\ell^*) = f_r(q_r^*). \tag{5.51}$$

This is required because the flux must be continuous at the interface. This suggests that the Riemann solver should include $m$ waves that allow jumps in each of the $m$ components of $q$ and combine to give no jump in $f$. If we also have some $m$ vectors $r^j$ and speeds $s^j$ (for $j = 1, 2, \ldots, m$) that represent the propagating waves we expect the Riemann solution to contain, then we can look for a decomposition of the form

$$\begin{bmatrix} q_r - q_\ell \\ f_r(q_r) - f_\ell(q_\ell) \end{bmatrix} = \alpha^1 \begin{bmatrix} r^1 \\ s^1 r^1 \end{bmatrix} + \cdots + \alpha^m \begin{bmatrix} r^m \\ s^m r^m \end{bmatrix} + \alpha^{m+1} \begin{bmatrix} e^1 \\ 0 \end{bmatrix} + \cdots + \alpha^{2m} \begin{bmatrix} e^m \\ 0 \end{bmatrix}. \tag{5.52}$$

The hard part in general may be to determine a suitable choice for $r^j$ and $s^j$.

We illustrate this for one simple example, the variable-coefficient advection equation

$$\frac{\partial q}{\partial t} + \frac{\partial}{\partial x}(a(x)q) = 0, \tag{5.53}$$

where $a(x) > 0$ everywhere. The Riemann problem with data $q_\ell$, $q_r$ and speeds $a_\ell, a_r$ has flux functions $f_\ell(q) = a_\ell q$ and $f_r(q) = a_r q$. Physically this might model the density of items traveling on a system of conveyer belts, at the junction between two belts moving at different speeds. The exact solution of this Riemann problem is

$$q(x,t) = \begin{cases} q_\ell & \text{if } x/t < 0, \\ q^* & \text{if } 0 < x/t < a_r, \\ q_r & \text{if } x/t > a_r, \end{cases} \tag{5.54}$$

where

$$q^* = \frac{a_\ell q_\ell}{q_r}, \tag{5.55}$$

as determined by the requirement that $a_\ell q_\ell = a_r q^*$ so that the flux is continuous.

Applying the decomposition (5.52) with $m = 1$ to this simple problem yields the correct Riemann solution if we take $r^1 = 1$ and $s^1 = a_r$. We have

$$\begin{bmatrix} q_r - q_\ell \\ a_r q_r - a_\ell q_\ell \end{bmatrix} = \alpha^1 \begin{bmatrix} 1 \\ a_r \end{bmatrix} + \alpha^2 \begin{bmatrix} 1 \\ 0 \end{bmatrix}. \tag{5.56}$$

Solving for $\alpha^1, \alpha^2$ yields

$$\alpha^1 = \frac{q_r - a_\ell q_\ell}{a_r} = q_r - q^* \qquad \text{and} \qquad \alpha^2 = \frac{a_\ell q_\ell}{a_r} - q_r = q^* - q_\ell, \tag{5.57}$$

where $q^*$ is given by (5.55). These waves propagate with speeds $s^1 = a_r$ and $s^2 = 0$ and so the exact solution (5.54) is achieved.

Another standard way to approach this variable-flux problem is to view $a(x)$ as a second variable in a system of two equations

$$\frac{\partial}{\partial t} \begin{bmatrix} q \\ a \end{bmatrix} + \frac{\partial}{\partial x} \begin{bmatrix} aq \\ 0 \end{bmatrix} = 0. \tag{5.58}$$

This is now a nonlinear system of two conservation laws in which both fields are linearly degenerate (but there is no longer a spatially-varying coefficient). The flux Jacobian is

$$\begin{bmatrix} a & q \\ 0 & 0 \end{bmatrix}, \tag{5.59}$$

with eigenvalues $\lambda^1 = 0$, $\lambda^2 = a$, and eigenvectors

$$r^1 = \begin{bmatrix} q \\ -a \end{bmatrix}, \qquad r^2 = \begin{bmatrix} 1 \\ 0 \end{bmatrix}. \tag{5.60}$$

Solving the Riemann problem for this system again gives the solution (5.54).

Notice that attempting to use a Roe solver for the system (5.58) (as might be desired for more complicated problems of this type) would be less successful than the simple Riemann solver proposed in (5.56). The Roe matrix for the system (5.58) is given by

$$\hat{A} = \begin{bmatrix} \hat{a} & \hat{q} \\ 0 & 0 \end{bmatrix}, \tag{5.61}$$

where $\hat{a} = \frac{1}{2}(a_\ell + a_r)$ and $\hat{q} = \frac{1}{2}(q_\ell + q_r)$, so the Roe solver uses the decomposition

$$\begin{bmatrix} q_r - q_\ell \\ a_r q_r - a_\ell q_\ell \end{bmatrix} = \hat{\alpha}^1 \begin{bmatrix} \hat{q} \\ -\hat{a} \end{bmatrix} + \hat{\alpha}^2 \begin{bmatrix} 1 \\ 0 \end{bmatrix}. \tag{5.62}$$

This does not give the exact Riemann solution since the propagation speed $\hat{a}$ of the moving wave is not the correct speed $a_r$ unless $a_\ell = a_r$.

For the simple scalar linear problem (5.53) there are many ways to determine the exact solution, as we have just illustrated. For more general nonlinear systems with discontinuous fluxes some sort of approximate Riemann solver must be used. We hope that the relaxation Riemann solvers might provide a better starting point than augmented systems of the form (5.58).

There is a simplification of the relaxation Riemann solver (5.52) that arises naturally in an implementation based on the wave-propagation method of Section 4.2 and which leads to the so-called *f-wave* formulation introduced in Section 4.2.2. Since the waves numbered $m + 1$ through $2m$ are viewed as being stationary at the interface we have $s^{m+1} = \cdots = s^{2m} = 0$ and these waves do not contribute to the fluctuations (4.21) or to the correction fluxes (4.23). Hence we only need to determine the coefficients $\alpha^1$, ..., $\alpha^m$. These can be determined by considering only the lower part of the system in (5.52), i.e.,

$$f_r(q_r) - f_\ell(q_\ell) = \alpha^1 s^1 r^1 + \cdots + \alpha^m s^m r^m, \tag{5.63}$$

which is a linear system of $m$ equations for the $m$ unknowns $\alpha^1$, ..., $\alpha^m$. Note that this is similar to the standard Riemann solver based on the decomposition

$$q_r - q_\ell = \sum_{p=1}^{M_w} \alpha^p r^p, \tag{5.64}$$

but we decompose the jump in $f$ into eigencomponents rather than the jump in $q$. This makes sense since there is no jump in $f$ across the stationary interface and so the full jump $f_r(q_r) - f_\ell(q_\ell)$ can be split into pieces corresponding to propagating waves, whereas $q$ has an unknown jump across the interface. This is consistent with standard Riemann solvers in the case of a single flux function, at least in some cases. For a linear constant coefficient system with $f(q) = Aq$, or for Roe's method based on a matrix $\hat{A}$ satisfying (4.15), performing the decomposition (5.63) would result in exactly the same coefficients $\alpha^p$ as performing the decomposition (5.64).

Approximate Riemann solvers based on splitting the jump in $f$ have been first studied numerically for various applications by Bale, LeVeque, Mitran and Rossmanith in [10]. This work started directly from (5.63) and only later was the connection with relaxation schemes realized.

### 5.9  Source Terms

Let us now consider a conservation law

$$\frac{\partial q}{\partial t} + \frac{\partial f(q)}{\partial x} = \psi \qquad (5.65)$$

with a source term $\psi$. One common approach to solving this equation is to use a fractional step method, alternating between solving the homogeneous conservation law and the ordinary differential equation (ODE) $\frac{\partial q}{\partial t} = \psi$. This leads to inaccuracy in some cases, for example if the solution is nearly in steady state with $\frac{\partial f(q)}{\partial x} \approx \psi$ and we wish to study the propagation of small disturbances on this background state (see the discussion in [121], for example).

Another approach is to somehow incorporate $\psi$ into the solution of Riemann problems. One way to do this is to discretize the source terms as a sum of delta function singularities with strength proportional to the cell size $\Delta x$ at the cell interfaces, so that the effect of the source is concentrated at these points. This approach is taken by Jenny and Müller [89] in their *Rankine-Hugoniot Riemann solver*, for example. In this case we must solve a more general Riemann problem of the form

$$\frac{\partial q}{\partial t} + \frac{\partial f(q)}{\partial x} = \Psi \delta(x) \qquad (5.66)$$

where $\Psi = \Delta x\, \psi_{\ell,r}$ is the strength of the delta function at this interface and the data $q_\ell, q_r$ comes from the cells to the left and right. The solution to this Riemann problem consists of propagating waves satisfying the usual Rankine-Hugoniot jump conditions away from $x/t = 0$ (where the source term vanishes) along with jumps in $q$ across $x/t = 0$ that satisfy

$$f(q_r^*) - f(q_\ell^*) = \Psi \,. \qquad (5.67)$$

This is similar to (5.51) but now the flux is not continuous at the interface because of the singular source. This suggests that we use a Riemann solver analogous to (5.52) but with the source term included,

$$\begin{bmatrix} q_r - q_\ell \\ f(q_r) - f(q_\ell) - \Psi \end{bmatrix} = \alpha^1 \begin{bmatrix} r^1 \\ s^1 r^1 \end{bmatrix} + \cdots + \alpha^m \begin{bmatrix} r^m \\ s^m r^m \end{bmatrix} + \alpha^{m+1} \begin{bmatrix} e^1 \\ 0 \end{bmatrix} + \cdots + \alpha^{2m} \begin{bmatrix} e^m \\ 0 \end{bmatrix}. \qquad (5.68)$$

As in the wave-propagation implementation of methods based on (5.51), we only need $\alpha^1, \ldots, \alpha^m$ and these can be obtained by solving the smaller $m \times m$ system

$$f(q_r) - f(q_\ell) - \Psi = \alpha^1 s^1 r^1 + \cdots + \alpha^m s^m r^m \,, \qquad (5.69)$$

and then using

$$\mathcal{W}^p = \alpha^p r^p \qquad (5.70)$$

as the $p$th wave in the wave propagation algorithm of Section 4.2. Again, this corresponds to the f-wave approach introduced in Section 4.2.2.

Note that a numerical steady state will be maintained by this method. Suppose that the cell averages $Q_i^n$ and source terms at the interfaces $\psi_{i-1/2}^n$ satisfy

$$\frac{f(Q_i^n) - f(Q_{i-1}^n)}{\Delta x} = \psi_{i-1/2}^n \qquad (5.71)$$

at time $t^n$. Then the left-hand side of (5.69) will be zero and hence $\alpha^p = 0$ for $p = 1, 2, \ldots, m$. All waves $\mathcal{W}^p$ arising from each modified Riemann problem will then have zero strength and a wave-propagation algorithm will reduce to giving $Q_i^{n+1} = Q_i^n$.

If the solution does not satisfy (5.71) exactly but is close to a steady state, then it is the deviation from steady state that is used to define the waves in the approximate Riemann solution. This is similar in spirit to the quasi-steady wave-propagation algorithm proposed in [121]. In that algorithm the delta function singularities were placed at cell centers rather than cell interfaces, however, and a new set of Riemann problems at these points was introduced to cancel out the source terms. An algorithm based on (5.69) is easier to implement than the one proposed in [121], and preliminary results indicate that it may also be more robust when the solution deviates further from steady state.

Chapter 6

# PRESSURE LINEARIZATION METHOD FOR THE COMPUTATION OF REAL FLUIDS

## 6.1 Introduction

We consider the numerical solution of the compressible Euler equations (2.10) with a general convex equation of state (EOS) $p = p(\mathcal{E}, \rho)$ in the framework of finite volume schemes.

In the literature, research has been done to extend classical methods designed for ideal polytropic gases to real gases. Some extensions to the real fluid case of either flux-vector splitting or flux-difference splitting schemes can be found for instance in [36, 53, 64, 65, 71, 128, 143, 201].

A distinct approach is the method by Coquel and Perthame [39], who introduce the idea of *energy relaxation* and propose a general formulation for extending some classical schemes for ideal polytropic gases to the case of general pressure laws. Numerical results based on this method are reported in [84]. Moreover in [144] the energy relaxation theory is applied to high-order WENO schemes.

In the same spirit of [39], here we develop a method based on the linearization of the equation of state that defines a general and simple procedure for constructing a Godunov-type finite volume method for the computation of real fluids. By reinterpreting our scheme as a relaxation method, we then find close similarity with the energy relaxation approach.

The original starting point for the idea of performing a linerization of the pressure law was the desire to construct a framework that could be advantageous in the computation of real multicomponent flows. Many existing methods for multifluid flows are restricted to equations of state linear in the thermodynamic variable $\mathcal{E}$ [3, 4, 178, 74, 182], and the task of defining a multifluid model guaranteeing pressure equilibrium at material interfaces is more difficult for equations of state of general form. Some recent successful work in this direction can be found for instance in [177, 179, 184, 5]. We will dedicate the last sections of this chapter to the discussion of the extension of the pressure linearization method to the multifluid case.

## 6.2 Pressure Linearization Algorithm

Our approach for the solution of the Euler equations (2.10) with a general pressure law $p = p(\mathcal{E}, \rho)$ is based on the replacement of the original equation of state with one that is linear in the selected thermodynamic variables $\mathcal{E}, \rho$:

$$p^{\mathrm{L}} = \bar{\kappa}\mathcal{E} + \bar{\chi}\rho + \beta \,, \tag{6.1}$$

with values $\bar{\kappa}$, $\bar{\chi}$, $\beta$ locally defined for each cell of the computational domain. This linearized equation of state is employed in the *evolution step* of a Godunov-type finite volume method, when we construct the structure of the solution (waves and speeds) that is used to update the vector $q = [\rho, m, E]^{\mathrm{T}}$ of the conserved variables. We then return to the original EOS $p = p(\mathcal{E}, \rho)$ to define the updated values of the pressure $p$ in the *projection step*.

Assuming $\bar{\kappa}$, $\bar{\chi}$, $\beta$ frozen at some values, the speed of sound corresponding to the pressure law (6.1) is given by (see (2.15))

$$c^{\mathrm{L}} = \sqrt{\bar{\kappa}h^{\mathrm{L}} + \bar{\chi}} \,, \tag{6.2}$$

with $h^{\mathrm{L}} = (\mathcal{E} + p^{\mathrm{L}})/\rho$.

Let us consider a discretization with cells indexed in space by $i \in \mathbb{Z}$, and in time by $n \in \mathbb{N}$. The following *consistency condition* for the pressure must hold in each cell:

$$p(\mathcal{E}_i^n, \rho_i^n) = \bar{\kappa}_i^n \mathcal{E}_i^n + \bar{\chi}_i^n \rho_i^n + \beta_i^n \,. \tag{6.3}$$

This equality ensures consistency also for the enthalpy $h_i^n = (\mathcal{E}_i^n + p(\mathcal{E}_i^n, \rho_i^n))/\rho_i^n = (h^{\mathrm{L}})_i^n$. In order to guarantee a correct approximation of the propagation speeds of the problem, we then require that the speed of sound associated in each cell to $p^{\mathrm{L}}$, that is $(c^{\mathrm{L}})_i^n = \sqrt{\bar{\kappa}_i^n h_i^n + \bar{\chi}_i^n}$, is the same as we would obtain from the original EOS. To this aim, we define $\bar{\kappa}_i^n$ and $\bar{\chi}_i^n$ as the cell values of the thermodynamic derivatives (2.14):

$$\bar{\kappa}_i^n = \kappa(\mathcal{E}_i^n, \rho_i^n) \qquad \text{and} \qquad \bar{\chi}_i^n = \chi(\mathcal{E}_i^n, \rho_i^n) \,, \quad \forall \, i, \, n \,. \tag{6.4}$$

The consistency condition (6.3) then determines uniquely $\beta_i^n$:

$$\beta_i^n = p(\mathcal{E}_i^n, \rho_i^n) - \bar{\kappa}_i^n \mathcal{E}_i^n - \bar{\chi}_i^n \rho_i^n \,. \tag{6.5}$$

Geometrically, in the coordinate space $(\mathcal{E}, \rho, p)$, we are locally approximating the graph of the function $p(\mathcal{E}, \rho)$ at the point $(\mathcal{E}_i^n, \rho_i^n, p(\mathcal{E}_i^n, \rho_i^n))$ with the tangent plane at this point.

The problem we now face in the evolution step consists of solving the Euler equations with a linear pressure law with parameters $\bar{\kappa}$, $\bar{\chi}$ and $\beta$ varying in the computational domain. This is analogous to a multifluid problem where the flow composition is described by the three variables $\bar{\kappa}$, $\bar{\chi}$ and $\beta$. Therefore, we solve our problem by constructing a multifluid model, requiring in particular the addition of transport equations governing the dynamics of the flow composition. For instance, we could simply add advection equations for the quantities $\bar{\kappa}$, $\bar{\chi}$ and $\beta$:

$$\frac{\partial \bar{\kappa}}{\partial t} + u \frac{\partial \bar{\kappa}}{\partial x} = 0 \,, \tag{6.6a}$$

$$\frac{\partial \bar{\chi}}{\partial t} + u \frac{\partial \bar{\chi}}{\partial x} = 0 \,, \tag{6.6b}$$

$$\frac{\partial \beta}{\partial t} + u \frac{\partial \beta}{\partial x} = 0 \,. \tag{6.6c}$$

Instead of the above formulation, we will adopt the Shyue-type multifluid model described in Section 3.2.3. Hence, we select as material variables

$$\psi = \frac{1}{\bar{\kappa}} \,, \qquad \eta = \frac{\bar{\chi}}{\bar{\kappa}} \,, \quad \text{and} \quad \mu = \frac{\beta}{\bar{\kappa}} \,, \tag{6.7}$$

and we describe their dynamics by a set of advection equations, with the one for $\eta$ in conservative form:

$$\frac{\partial \psi}{\partial t} + u \frac{\partial \psi}{\partial x} = 0 \,, \tag{6.8a}$$

$$\frac{\partial}{\partial t}(\eta\rho) + \frac{\partial}{\partial x}(\eta\rho u) = 0 \,, \tag{6.8b}$$

$$\frac{\partial \mu}{\partial t} + u \frac{\partial \mu}{\partial x} = 0 \,. \tag{6.8c}$$

Note that (6.6) are mathematically equivalent to (6.8). In the context of genuine multifluid problems the formulation (6.7), (6.8) is derived in order to guarantee pressure equilibrium at material interfaces, and it is based on updating the pressure through the mixture equation of state $p = \frac{1}{\psi}(\mathcal{E} + \eta\rho + \mu)$, as in (3.18). Here in the projection step we will employ the original equation of state to update the pressure,

and not the linearized one, so until this point there is no special need of adopting (6.7), (6.8). However, aiming to extend our method to the actual multifluid case, and for other reasons that will be clear later in the chapter (Sect. 6.7, 6.8), we wish to use a formulation which is already in the framework of multifluid models.

To summarize, the system that we solve in the evolution step of the chosen Godunov-type finite volume scheme reads:

$$\frac{\partial q}{\partial t} + \frac{\partial}{\partial x} f^{\text{L}}(q, \psi, \eta\rho, \mu) = 0 \,, \tag{6.9a}$$

$$\frac{\partial}{\partial t}(\eta\rho) + \frac{\partial}{\partial x}(\eta\rho u) = 0 \,, \tag{6.9b}$$

$$\frac{\partial \psi}{\partial t} + u\frac{\partial \psi}{\partial x} = 0 \,, \tag{6.9c}$$

$$\frac{\partial \mu}{\partial t} + u\frac{\partial \mu}{\partial x} = 0 \,, \tag{6.9d}$$

where

$$q = \begin{bmatrix} \rho \\ m \\ E \end{bmatrix}, \qquad f^{\text{L}}(q, \psi, \eta\rho, \mu) = \begin{bmatrix} m \\ \dfrac{m^2}{\rho} + p^{\text{L}} \\ \dfrac{m}{\rho}(E + p^{\text{L}}) \end{bmatrix}, \tag{6.9e}$$

and $p^{\text{L}}$ is expressed as

$$p^{\text{L}} = p^{\text{L}}(\mathcal{E}, \psi, \eta\rho, \mu) = \frac{1}{\psi}(\mathcal{E} + \eta\rho + \mu) \,. \tag{6.9f}$$

In the solution of the system above, we associate to the pressure law (6.9f) the speed of sound (6.2), that in terms of $\psi$, $\eta$ is given by

$$c^{\text{L}} = \sqrt{\frac{h^{\text{L}}}{\psi} + \frac{\eta}{\psi}} \,. \tag{6.10}$$

This definition assumes frozen conditions for the quantities $\eta$, $\psi$, $\mu$.

Our algorithm consists of the following steps:

ALGORITHM 6.1 (PLM)

(*i*) Given $q^n$, we compute $\psi^n$, $(\eta\rho)^n$ and $\mu^n$ through (6.7), by using the local values of the thermo-dynamic derivatives (6.4) and the consistency condition (6.5). With these initial values at time $t^n$ we solve the new system (6.9) by a Godunov-type finite volume method to obtain the updated vector of the conserved variables $q^{n+1}$.

(*ii*) We update the pressure through the original EOS:

$$p^{n+1} = p(\mathcal{E}^{n+1}, \rho^{n+1}) \,. \tag{6.11}$$

Note that, since in (*ii*) we just need the updated values of the vector $q = (\rho, m, E)^{\text{T}}$, and not those of the other variables, we do not have to track $\psi$, $\eta\rho$ and $\mu$. Therefore, in the implementation of our method we can work with vectors with the same dimension as $q$, that is with a number of components equal to the number of equations of the original Euler system. However, the additional equations (6.8) affect the definition of the structure of the solution that is used to update the vector $q$.

The Algorithm 6.1 above defines a simple and general procedure to solve the Euler equations for real fluids, and can be applied to extend some classical schemes designed for a restricted class of equations of state to the case of more general pressure laws.

In the framework of Godunov-type methods, we observe that the general underlying approximation of our approach consists of considering the thermodynamic derivatives $\kappa(\mathcal{E}, \rho)$ and $\chi(\mathcal{E}, \rho)$ frozen across the acoustic waves of each local Riemann problem, and allowing them to be discontinuous only across the contact wave. We refer to Fig. 3.1 in Chapter 3, where the Riemann solution of the Shyue-type model system is illustrated.

Note that if we apply our method to a Godunov-type scheme that is exact on isolated contact discontinuities we will maintain this property, since the quantities $\psi$, $\eta$ and $\mu$ are simply advected with the flow.

In Section 6.4 we will specialize our approach to the Roe solver.

### 6.2.1 Two-Dimensional System

In two dimensions, the system (6.9) takes the form

$$\frac{\partial q}{\partial t} + \frac{\partial}{\partial x} f^{\text{L}}(q, \psi, \eta\rho, \mu) + \frac{\partial}{\partial y} g^{\text{L}}(q, \psi, \eta\rho, \mu) = 0, \tag{6.12a}$$

$$\frac{\partial}{\partial t}(\eta\rho) + \frac{\partial}{\partial x}(\eta\rho u) + \frac{\partial}{\partial y}(\eta\rho v) = 0, \tag{6.12b}$$

$$\frac{\partial \psi}{\partial t} + u\frac{\partial \psi}{\partial x} + v\frac{\partial \psi}{\partial y} = 0, \tag{6.12c}$$

$$\frac{\partial \mu}{\partial t} + u\frac{\partial \mu}{\partial x} + v\frac{\partial \mu}{\partial y} = 0, \tag{6.12d}$$

where

$$q = \begin{bmatrix} \rho \\ \rho u \\ \rho v \\ E \end{bmatrix}, \quad f^{\text{L}}(q, \psi, \eta\rho, \mu) = \begin{bmatrix} \rho u \\ \rho u^2 + p^{\text{L}} \\ \rho uv \\ u(E + p^{\text{L}}) \end{bmatrix}, \quad g^{\text{L}}(q, \psi, \eta\rho, \mu) = \begin{bmatrix} \rho v \\ \rho uv \\ \rho v^2 + p^{\text{L}} \\ v(E + p^{\text{L}}) \end{bmatrix}, \tag{6.12e}$$

with $E = \mathcal{E} + \frac{1}{2}\rho(u^2 + v^2)$ and $p^{\text{L}} = p^{\text{L}}(\mathcal{E}, \psi, \eta\rho, \mu)$, as in (6.9f).

## 6.3 Relaxation Method

We now illustrate how the basic formulation of our approach can be interpreted as a relaxation method.

Let us consider here a simpler version of system (6.9), obtained by assuming a linear pressure law of the form (6.1) with fixed constant values $\bar{\kappa} > 0$ and $\bar{\chi}$ in the whole computational domain, hence $\bar{\kappa}_i^n = \bar{\kappa}$, $\bar{\chi}_i^n = \bar{\chi}$, $\forall i$, $n$. Then $\beta$ is the only variable for which we need to add a transport equation, and the evolution problem of our method can be formulated more simply as:

$$\frac{\partial q}{\partial t} + \frac{\partial}{\partial x} f^{\text{L}}(q, \beta) = 0, \tag{6.13a}$$

$$\frac{\partial \beta}{\partial t} + u\frac{\partial \beta}{\partial x} = 0, \tag{6.13b}$$

where

$$f^{\mathrm{L}}(q,\beta) = \begin{bmatrix} m \\ \dfrac{m^2}{\rho} + p^{\mathrm{L}} \\ \dfrac{m}{\rho}(E + p^{\mathrm{L}}) \end{bmatrix}, \tag{6.13c}$$

with (6.1):

$$p^{\mathrm{L}} = p^{\mathrm{L}}(\mathcal{E}, \rho, \beta) = \bar{\kappa}\mathcal{E} + \bar{\chi}\rho + \beta. \tag{6.13d}$$

The pressure linearization algorithm based on (6.13) reads:

ALGORITHM 6.2 (PLM-$\beta$)

(i) Given $q^n$, we compute $\beta^n$ through the consistency condition

$$\beta^n = p(\mathcal{E}^n, \rho^n) - \bar{\kappa}\mathcal{E}^n - \bar{\chi}\rho^n. \tag{6.14}$$

With these initial values $q^n$, $\beta^n$, we solve (6.13) by a given Godunov-type finite volume method over a time step $\Delta t$ to obtain the updated vector $q^{n+1}$.

(ii) We update the pressure by using the original EOS:

$$p^{n+1} = p(\mathcal{E}^{n+1}, \rho^{n+1}). \tag{6.15}$$

Similarly to what we have observed for Algorithm 6.1, we don't need to track the variable $\beta$ in step (i) of the algorithm above, since only $q^{n+1}$ is needed to update the pressure in (ii). The value of $\beta$ is reset every time step by using the consistency condition (6.14).

Now consider (6.13) with a relaxation source term for the second equation:

$$\frac{\partial q}{\partial t} + \frac{\partial}{\partial t} f^{\mathrm{L}}(q, \beta) = 0, \tag{6.16a}$$

$$\frac{\partial \beta}{\partial t} + u \frac{\partial \beta}{\partial x} = -\frac{1}{\tau}(\beta - \beta_{\mathrm{eq}}(\mathcal{E}, \rho)), \tag{6.16b}$$

where $\tau > 0$ is the *relaxation time* and $\beta_{\mathrm{eq}}(\mathcal{E}, \rho)$ is defined by the equality

$$p(E, \rho) = \bar{\kappa}\mathcal{E} + \bar{\chi}\rho + \beta_{\mathrm{eq}}(\mathcal{E}, \rho). \tag{6.16c}$$

Formally, when $\tau \to 0^+$ (*equilibrium limit*), $\beta = \beta_{\mathrm{eq}}$, so that we recover the Euler system (2.10) with the original EOS, since $p^{\mathrm{L}}(\mathcal{E}, \rho, \beta_{\mathrm{eq}}(\mathcal{E}, \rho)) = p(\mathcal{E}, \rho)$. Under proper stability conditions that we will discuss later, the solution of the relaxation system (6.16), in the limit $\tau \to 0^+$, can provide an approximation for the Euler equations (2.10).

As we have seen in Chapter 5, one way to solve (6.16) is to employ a fractional step method. First, we apply some finite volume scheme to the corresponding homogeneous system for advancing the solution over a time step $\Delta t$. Given the initial data $q^n$ and $\beta^n$, let us denote by $q^*$ and $\beta^*$ the updated variables that we obtain through this step. Then we consider the solution over time $\Delta t$ of the equations that result from (6.16) setting the spatial gradients to zero:

$$\frac{\partial q}{\partial t} = 0, \tag{6.17a}$$

$$\frac{\partial \beta}{\partial t} = -\frac{1}{\tau}(\beta - \beta_{\mathrm{eq}}(\mathcal{E}, \rho)). \tag{6.17b}$$

We can solve exactly this system, obtaining:

$$q^{n+1} = q^*\,, \tag{6.18a}$$

$$\beta^{n+1} = \beta_{\text{eq}}(\mathcal{E}^{n+1}, \rho^{n+1}) + e^{-\Delta t/\tau}\left(\beta^* - \beta_{\text{eq}}(\mathcal{E}^{n+1}, \rho^{n+1})\right)\,. \tag{6.18b}$$

Since we are only concerned with the equilibrium limit $\tau \to 0^+$, we simply set, instead of (6.18b),

$$\beta^{n+1} = \beta_{\text{eq}}(\mathcal{E}^{n+1}, \rho^{n+1})\,. \tag{6.19}$$

Employing the equilibrium condition above allows us to ignore $\beta^*$, so that we don't need to update $\beta^n$ to $\beta^*$ in the first step. In summary, our relaxation scheme consists of:

(i) Update $q^n$ to $q^{n+1}$ by solving the homogeneous relaxation system (that is (6.13)). We observe that this step amounts to considering the *frozen conditions limit* $\tau \to \infty$. Therefore it is appropriate here to employ the *frozen speed of sound* $c^{\text{L}}$ given by (6.2), whose definition considers the nonequilibrium variable $\beta$ held constant.

(ii) Set $\beta^{n+1} = \beta_{\text{eq}}(\mathcal{E}^{n+1}, \rho^{n+1})$ *(equilibrium limit $\tau \to 0^+$).*

Note that step (ii) implies the computation of the updated value of the pressure $(p^{\text{L}})^{n+1}$ by means of the original EOS since

$$(p^{\text{L}})^{n+1} = p^{\text{L}}(\mathcal{E}^{n+1}, \rho^{n+1}, \beta^{n+1}) = p^{\text{L}}(E^{n+1}, \rho^{n+1}, \beta_{\text{eq}}(\mathcal{E}^{n+1}, \rho^{n+1})) = p(\mathcal{E}^{n+1}, \rho^{n+1})\,, \tag{6.20}$$

through (6.16c). It is then clear that the relaxation scheme (i)-(ii) defined above is equivalent to the Algorithm 6.2. We conclude that the basic formulation of our pressure linearization approach can be viewed as a relaxation method, providing a formal mathematical validation of our scheme.

The interpretation as a relaxation scheme shows that there is a close similarity with the *energy relaxation* approach of Coquel and Perthame [39]. These authors introduce a relaxation system for approximating the Euler equations with a general pressure law $p(\varepsilon, \rho)$, based on a decomposition of the internal specific energy in the form $\varepsilon = \varepsilon_1 + \varepsilon_2$. The energy $\varepsilon_1$ is associated with a a simpler pressure law $p_1(\varepsilon_1, \rho)$, chosen in the form of the ideal polytropic gas EOS, $p_1 = (\gamma_1 - 1)\rho\,\varepsilon_1$, and the energy $\varepsilon_2$ is advected by the flow. The advection of $\beta$ in our basic model (6.13), and correspondingly the advection of $\mu = \frac{\beta}{\bar{\kappa}}$ in (6.9), can be considered analogous to the advection of $\varepsilon_2$ in [39]. However, in our method we keep the energy $\mathcal{E}$ as one thermodynamic variable to which our simpler linear pressure law $p^{\text{L}}$ is associated.

An original feature of our approach is the addition of the three equations (6.8) for the parameters $\psi$, $\eta\rho$, $\mu$ of the linear EOS (6.9f), taking them from the framework of multifluid models. In particular, this formulation allows us to naturally construct a scheme that uses values of $\psi$, $\eta\rho$, $\mu$ locally defined in each cell of the computational domain, so that optimal values can be assigned to these quantities. Moreover, our formulation is suitable for some important extensions that will be detailed in the following.

### 6.3.1 First Order Asymptotic Approximation

We here derive the first order approximation of (6.16), which gives a stability criterion on the possible values that can be assigned to $\bar{\kappa}$ and $\bar{\chi}$. Adopting a common technique [28, 131, 81, 93, 149, 39], we use an asymptotic expansion of the Chapman–Enskog type, which in the present case reads:

$$\beta = \beta_{\text{eq}} + \tau\,\beta_d + \mathcal{O}(\tau^2)\,, \tag{6.21}$$

where $\beta_d$ denotes the first order correction for $\beta$. By using the definition (6.16c) of $\beta_{\mathrm{eq}}$, we then have:

$$p^{\mathrm{L}}(\mathcal{E}, \rho, \beta) = p(\mathcal{E}, \rho) + \tau \beta_d + \mathcal{O}(\tau^2)\,, \tag{6.22}$$

and hence

$$f^{\mathrm{L}}(q, \beta) = f(q) + \tau \begin{bmatrix} 0 \\ \beta_d \\ u\beta_d \end{bmatrix} + \mathcal{O}(\tau^2)\,. \tag{6.23}$$

Introducing (6.23) in (6.16a), we obtain, up to $\mathcal{O}(\tau)$,

$$\frac{\partial q}{\partial t} + \frac{\partial f(q)}{\partial x} = -\tau \frac{\partial}{\partial x} \begin{bmatrix} 0 \\ \beta_d \\ u\,\beta_d \end{bmatrix}\,, \tag{6.24}$$

while using (6.21) in (6.16b) we get, neglecting higher order terms,

$$-\beta_d = \frac{\partial \beta_{\mathrm{eq}}}{\partial t} + u\,\frac{\partial \beta_{\mathrm{eq}}}{\partial x}\,. \tag{6.25}$$

Computing now from (6.16c) (assuming smooth solutions)

$$\begin{aligned}
\frac{\partial \beta_{\mathrm{eq}}}{\partial t} &= (\kappa - \bar{\kappa}) \frac{\partial \mathcal{E}}{\partial t} + (\chi - \bar{\chi}) \frac{\partial \rho}{\partial t}\,, \\
\frac{\partial \beta_{\mathrm{eq}}}{\partial x} &= (\kappa - \bar{\kappa}) \frac{\partial \mathcal{E}}{\partial x} + (\chi - \bar{\chi}) \frac{\partial \rho}{\partial t}\,,
\end{aligned} \tag{6.26}$$

formula (6.25) gives

$$-\beta_d = (\kappa - \bar{\kappa}) \left( \frac{\partial \mathcal{E}}{\partial t} + u\,\frac{\partial \mathcal{E}}{\partial x} \right) + (\chi - \bar{\chi}) \left( \frac{\partial \rho}{\partial t} + u\,\frac{\partial \rho}{\partial x} \right)\,. \tag{6.27}$$

From (6.16a) we also derive

$$\begin{aligned}
\frac{\partial \rho}{\partial t} + u\,\frac{\partial \rho}{\partial x} &= -\rho\,\frac{\partial u}{\partial x}\,, \\
\frac{\partial \mathcal{E}}{\partial t} + u\,\frac{\partial \mathcal{E}}{\partial x} &= -(\mathcal{E} + p)\,\frac{\partial u}{\partial x}\,,
\end{aligned} \tag{6.28}$$

with the last equality valid up to higher order terms. Therefore we obtain:

$$\begin{aligned}
-\beta_d &= \rho \left[ (\bar{\kappa} - \kappa)\frac{\mathcal{E} + p}{\rho} + (\bar{\chi} - \chi) \right] \frac{\partial u}{\partial x} \\
&= \rho \left[ \bar{\kappa} h + \bar{\chi} - (\kappa h + \chi) \right] \frac{\partial u}{\partial x} \\
&= \rho \left[ (c^{\mathrm{L}})^2 - c^2 \right] \frac{\partial u}{\partial x}\,,
\end{aligned} \tag{6.29}$$

where in the last term we have used the speed of sound corresponding to the linear equation of state $p^{\mathrm{L}}$, $c^{\mathrm{L}} = \sqrt{\bar{\kappa} h + \bar{\chi}}$. By introducing the last result in (6.24), we finally find the first order approximation of the relaxation system (6.16):

$$\frac{\partial q}{\partial t} + \frac{\partial f(q)}{\partial x} = \tau \frac{\partial}{\partial x} \begin{bmatrix} 0 \\ \rho\,[(c^{\mathrm{L}})^2 - c^2]\,\dfrac{\partial u}{\partial x} \\ \rho\,[(c^{\mathrm{L}})^2 - c^2]\,u\,\dfrac{\partial u}{\partial x} \end{bmatrix}\,. \tag{6.30}$$

In order to have a nonnegative diffusion matrix, we deduce from (6.30) that a stability criterion is

$$c^{\mathrm{L}} \geq c \, . \tag{6.31}$$

The above relation represents a *subcharacteristic condition* [131] for the problem, expressing the requirement that the speed of sound $c^{\mathrm{L}}$ of the homogeneous relaxation system is at least as large as the speed of sound $c$ of the original Euler equations.

Even if we could always choose $\bar{\kappa}$ and $\bar{\chi}$ such that (6.31) is satisfied, we need indeed to set these parameters so that $c^{\mathrm{L}}$ is close to $c$, in order to minimize the numerical diffusion. In this sense, the local definition (6.4) of $\bar{\kappa}$ and $\bar{\chi}$ that we have proposed in the formulation of our method in Section 6.2 is an optimal choice, since it guarantees locally the same speed of sound as we would have from the original EOS, and (6.31) is satisfied in each cell in the equality limit.

Note that in our scheme we can also employ global constant parameters $\bar{\kappa}$ and $\bar{\chi}$ satisfying the subcharacteristic condition (6.31) to avoid the computation of the derivatives of the pressure, thus following the idea of [39]. In this case there would be the difficulty of estimating appropriately the global values $\bar{\kappa}$ and $\bar{\chi}$, and in general we would have the drawback of a larger numerical diffusion. However, the possibility of adopting global parameters gives further flexibility to our method, in particular when we do not have a pressure law in explicit form, or whenever we wish to reduce as much as possible the computational cost.

### 6.4  Application to the Roe Method

We illustrate in this section how our approach applies to the Roe method [169]. We will call the resulting scheme PLM-Roe (Pressure Linearization Method applied to Roe's method).

Consider the system (6.9), which here we rewrite compacting together the equations in conservative form, by introducing the vector of the conserved variables $q_{\mathrm{C}}$ and the corresponding flux function $f_{\mathrm{C}}^{\mathrm{L}}$:

$$
\begin{aligned}
\frac{\partial q_{\mathrm{C}}}{\partial t} + \frac{\partial}{\partial x} f_{\mathrm{C}}^{\mathrm{L}}(q_{\mathrm{C}}, \psi, \mu) &= 0 \, , \\
\frac{\partial \psi}{\partial t} + u \frac{\partial \psi}{\partial x} &= 0 \, , \\
\frac{\partial \mu}{\partial t} + u \frac{\partial \mu}{\partial x} &= 0 \, ,
\end{aligned}
\tag{6.32a}
$$

where

$$
q_{\mathrm{C}} = \left[ \begin{array}{c} q \\ \eta \rho \end{array} \right] \qquad \text{and} \qquad f_{\mathrm{C}}^{\mathrm{L}}(q_{\mathrm{C}}, \psi, \mu) = \left[ \begin{array}{c} f^{\mathrm{L}}(q, \psi, \eta \rho, \mu) \\ (\eta \rho)\, u \end{array} \right] \, . \tag{6.32b}
$$

We can express the system above in a fully quasi-linear form as follows:

$$
\frac{\partial z}{\partial t} + A^{\mathrm{L}}(z) \frac{\partial z}{\partial x} = 0 \, , \tag{6.33a}
$$

where

$$
z = [\rho, m, E, \eta \rho, \psi, \mu]^{\mathrm{T}} \, , \tag{6.33b}
$$

and the matrix $A^{\mathrm{L}}(z)$ is given by:

$$
A^{\mathrm{L}}(z) = \begin{bmatrix}
0 & 1 & 0 & 0 & 0 & 0 \\[2mm]
\dfrac{1}{\psi}\dfrac{u^2}{2} - u^2 & \left(2 - \dfrac{1}{\psi}\right)u & \dfrac{1}{\psi} & \dfrac{1}{\psi} & -\dfrac{\zeta}{\psi^2} & \dfrac{1}{\psi} \\[3mm]
u\left(\dfrac{1}{\psi}\dfrac{u^2}{2} - H\right) & H - \dfrac{1}{\psi}u^2 & \left(1 + \dfrac{1}{\psi}\right)u & \dfrac{1}{\psi}u & -\dfrac{\zeta}{\psi^2}u & \dfrac{1}{\psi}u \\[3mm]
-\eta u & \eta & 0 & u & 0 & 0 \\[2mm]
0 & 0 & 0 & 0 & u & 0 \\[2mm]
0 & 0 & 0 & 0 & 0 & u
\end{bmatrix}, \tag{6.33c}
$$

where we have defined

$$
\zeta \equiv \mathcal{E} + \eta\rho + \mu. \tag{6.33d}
$$

Following the approach of Roe [169], we solve Riemann problems at interfaces between neighbouring cell averages with a linearized version of the system (6.33). The problem we have at each cell interface takes the form:

$$
\frac{\partial z}{\partial t} + \hat{A}^{\mathrm{L}}(z_\ell, z_r)\frac{\partial z}{\partial x} = 0,
$$

$$
z(x,0) = \begin{cases} z_\ell & \text{for } x \text{ to the left of the interface}, \\ z_r & \text{for } x \text{ to the right of the interface}, \end{cases} \tag{6.34}
$$

where $\hat{A}^{\mathrm{L}}(z_\ell, z_r)$ is a constant coefficient matrix that is locally defined depending on the values of the initial data $z_\ell$ and $z_r$ of the Riemann problem. Extending Roe's idea, we define the matrix $\hat{A}^{\mathrm{L}}$ as the original matrix $A^{\mathrm{L}}$ evaluated in an average state $(\hat{u}, \hat{H}, \hat{\eta}, \hat{\psi}, \hat{\zeta})$, involving those variables explicitly appearing in $A^{\mathrm{L}}$:

$$
\hat{A}^{\mathrm{L}} = A^{\mathrm{L}}(\hat{u}, \hat{H}, \hat{\eta}, \hat{\psi}, \hat{\zeta}). \tag{6.35}
$$

Let us introduce here the following operator, which we will use frequently hereafter, producing the difference between the right and left value of its argument:

$$
\Delta(\cdot) \equiv (\cdot)_r - (\cdot)_\ell. \tag{6.36}
$$

In order to obtain a method guaranteeing the conservation of the quantities in $q_{\mathrm{C}}$, we need to satisfy the condition (iii) of Def. 4.1, which in this case reads:

$$
\Delta f_{\mathrm{C}}^{\mathrm{L}} = \{\hat{A}^{\mathrm{L}}\Delta z\}_{1 \le i \le 4}, \tag{6.37}
$$

where we recall that $f_{\mathrm{C}}^{\mathrm{L}}$ is the flux function associated to $q_{\mathrm{C}}$ (see (6.32)). As we will detail in the next section, we can ensure the above property by defining the average variables as follows:

$$
\hat{u} = \frac{\sqrt{\rho_\ell}\, u_\ell + \sqrt{\rho_r}\, u_r}{\sqrt{\rho_\ell} + \sqrt{\rho_r}}, \tag{6.38a}
$$

$$
\hat{H} = \frac{\sqrt{\rho_\ell}\, H_\ell + \sqrt{\rho_r}\, H_r}{\sqrt{\rho_\ell} + \sqrt{\rho_r}}, \tag{6.38b}
$$

$$
\hat{\eta} = \frac{\sqrt{\rho_\ell}\, \eta_\ell + \sqrt{\rho_r}\, \eta_r}{\sqrt{\rho_\ell} + \sqrt{\rho_r}}, \tag{6.38c}
$$

$$
\hat{\psi} = \frac{\psi_\ell\, \psi_r}{\tilde{\psi}}, \tag{6.38d}
$$

where

$$\tilde{\psi} = \frac{\sqrt{\rho_\ell}\,\psi_\ell + \sqrt{\rho_r}\,\psi_r}{\sqrt{\rho_\ell} + \sqrt{\rho_r}}\,, \tag{6.38e}$$

and

$$\hat{\zeta} = \frac{\psi_\ell\,\psi_r}{\tilde{\psi}^2}\tilde{\zeta}\,, \tag{6.38f}$$

with

$$\tilde{\zeta} = \frac{\sqrt{\rho_\ell}\,\zeta_\ell + \sqrt{\rho_r}\,\zeta_r}{\sqrt{\rho_\ell} + \sqrt{\rho_r}}\,. \tag{6.38g}$$

Moreover, the average speed of sound associated to $(\hat{u}, \hat{H}, \hat{\eta}, \hat{\psi}, \hat{\zeta})$ is given by:

$$\hat{c} = \sqrt{\frac{1}{\hat{\psi}}\left(\hat{H} - \frac{\hat{u}^2}{2}\right) + \frac{\hat{\eta}}{\hat{\psi}}}\,. \tag{6.39}$$

With (6.33c), (6.35), (6.38), the definition of the matrix $\hat{A}^{\mathrm{L}}$ is complete. The eigenvalues of $\hat{A}^{\mathrm{L}}$ are found to be:

$$\hat{\lambda}^1 = \hat{u} - \hat{c}, \qquad \hat{\lambda}^2 = \hat{\lambda}^3 = \hat{\lambda}^4 = \hat{\lambda}^5 = \hat{u}\,, \qquad \hat{\lambda}^6 = \hat{u} + \hat{c}\,, \tag{6.40}$$

and the matrix of the corresponding right eigenvectors takes the form:

$$\hat{R} = [\hat{r}^1, \cdots, \hat{r}^6] = \begin{bmatrix} 1 & 1 & 0 & 0 & 0 & 1 \\ \hat{u} - \hat{c} & \hat{u} & 0 & 0 & 0 & \hat{u} + \hat{c} \\ \hat{H} - \hat{u}\hat{c} & \hat{H} - \hat{\psi}\hat{c}^2 & -1 & \frac{\hat{\zeta}}{\hat{\psi}} & -1 & \hat{H} + \hat{u}\hat{c} \\ \hat{\eta} & \hat{\eta} & 1 & 0 & 0 & \hat{\eta} \\ 0 & 0 & 0 & 1 & 0 & 0 \\ 0 & 0 & 0 & 0 & 1 & 0 \end{bmatrix}. \tag{6.41}$$

The solution of the linear problem (6.34) consists of six discontinuities propagating at constant speed. The jump across the $p$-th discontinuity is a multiple through a coefficient $\alpha^p$ of the eigenvector $\hat{r}^p$ of $\hat{A}^{\mathrm{L}}$, and propagates at a velocity given by the corresponding eigenvalue $\hat{\lambda}^p$. The total jump $z_r - z_\ell$ is then recovered by the sum:

$$\sum_{p=1}^{6} \alpha^p\,\hat{r}^p = z_r - z_\ell\,. \tag{6.42}$$

By solving the linear system above for the coefficients $\alpha^p$, we obtain:

$$\alpha^2 = \frac{1}{\hat{\psi}\,\hat{c}^2}\left[(\hat{H} - \hat{u}^2 + \hat{\eta})\,\Delta z_1 + \hat{u}\,\Delta z_2 - \Delta z_3 - \Delta z_4 + \frac{\hat{\zeta}}{\hat{\psi}}\,\Delta z_5 - \Delta z_6\right], \tag{6.43a}$$

$$\alpha^6 = \frac{1}{2\,\hat{c}}\left[\Delta z_2 + (\hat{c} - \hat{u})\,\Delta z_1 - \hat{c}\,\alpha^2\right], \tag{6.43b}$$

$$\alpha^1 = \Delta z_1 - \alpha^2 - \alpha^6\,, \tag{6.43c}$$

$$\alpha^3 = -\hat{\eta}\,\Delta z_1 + \Delta z_4\,, \tag{6.43d}$$

$$\alpha^4 = \Delta z_5\,, \tag{6.43e}$$

$$\alpha^5 = \Delta z_6\,. \tag{6.43f}$$

These coefficients can be also rewritten as:

$$\alpha^1 = \frac{\Delta p - \hat{\rho}\,\hat{c}\,\Delta u}{2\,\hat{c}^2}\,, \tag{6.44a}$$

$$\alpha^2 = \Delta\rho - \frac{\Delta p}{\hat{c}^2}\,, \tag{6.44b}$$

$$\alpha^3 = \hat{\rho}\,\Delta\eta\,, \tag{6.44c}$$

$$\alpha^4 = \Delta\psi\,, \tag{6.44d}$$

$$\alpha^5 = \Delta\mu\,, \tag{6.44e}$$

$$\alpha^6 = \frac{\Delta p + \hat{\rho}\,\hat{c}\,\Delta u}{2\,\hat{c}^2}\,, \tag{6.44f}$$

where

$$\hat{\rho} \equiv \sqrt{\rho_\ell}\,\sqrt{\rho_r}\,. \tag{6.44g}$$

We remarked in Section 6.2 that in our algorithm we don't have to track in time the variables $\psi$, $\eta\rho$, $\mu$, since these quantities are reset each time step, and we only need to update the vector $q$. This implies that the last three rows of the right eigenvectors matrix $\hat{R}$ (6.41) are not employed in the construction of the solution of each local Riemann problem. On the other hand, the added equations governing $\psi$, $\eta\rho$, $\mu$ have the effect of introducing new waves propagating at speed $\hat{u}$ used in the updating of $q$, and, moreover, they play a role in the determination of the average quantities that define $\hat{A}^{\mathrm{L}}$.

In summary, our method leads to the construction of an approximate Riemann solver that uses six waves $\mathcal{W}^p \in \mathbb{R}^3$ and corresponding speeds $s^p$ given by:

$$\mathcal{W}^p = \alpha^p \{\hat{r}^p\}_{1 \le i \le 3}\,, \qquad s^p = \hat{\lambda}^p\,, \quad p = 1, \ldots, 6\,. \tag{6.45}$$

In the implementation of this solver we can then sum together the waves propagating with the same speed $\hat{\lambda}^2 = \hat{\lambda}^3 = \hat{\lambda}^4 = \hat{\lambda}^5 = \hat{u}$ to define a single wave $\sum_{p=2}^{5} \mathcal{W}^p$ associated to $\hat{u}$, thus reducing the total number of waves to three.

We observe that if a Riemann problem for the original system (6.33) consists of a single contact discontinuity, that is, $u_\ell = u_r = u$ and $p_\ell = p_r = p$, we have $\alpha^1 = \alpha^6 = 0$. Hence, the solution of the corresponding linear problem (6.34) involves a single jump across a discontinuity propagating at speed $\hat{u} = u$, so that, by conservation, we recover the exact solution. However, except in the case the original EOS is linear (as for the ideal polytropic gas or the stiffened gas EOS), with our method we lose the well known property of the classical Roe solver of exactly capturing single shock waves. Nevertheless, due to the compressive nature of the shocks, the discrete shock profiles result sharply resolved, as we can observe from the numerical experimentation.

To conclude, we recall that a Roe's linearization is not uniquely determined when a general equation of state is considered. Several formulations of Roe's method for real gases [71, 128, 143, 201] can be described as linearizations in quasi-Jacobian form [146], where the original average state $(\hat{u}, \hat{H})$ of Roe is augmented by additional unknowns, namely the thermodynamic pressure derivatives (with respect to a pair of independent thermodynamic variables). Our approach shares some similarity with this class of methods, since we determine an extended average state $(\hat{u}, \hat{H}, \hat{\eta}, \hat{\psi}, \hat{\zeta})$ that involves quantities related to the pressure derivatives. Note that we can regard $1/\hat{\psi}$ and $\hat{\eta}/\hat{\psi}$ as the averages corresponding to the thermodynamic derivatives $\kappa(\mathcal{E}, \rho) = \frac{\partial p(\mathcal{E}, \rho)}{\partial \mathcal{E}}$ and $\chi(\mathcal{E}, \rho) = \frac{\partial p(\mathcal{E}, \rho)}{\partial \rho}$, respectively.

### 6.4.1   Average Quantities

We look for average values $\hat{u}$, $\hat{H}$, $\hat{\eta}$, $\hat{\psi}$ and $\hat{\zeta}$ such that the matrix $\hat{A}^{\mathrm{L}} = A^{\mathrm{L}}(\hat{u}, \hat{H}, \hat{\eta}, \hat{\psi}, \hat{\zeta})$ satisfies the property (6.37).

First, let us introduce some identities that we will use in the following. If for a given quantity $a$ we define

$$\tilde{a} \equiv \frac{\sqrt{\rho_\ell}\, a_\ell + \sqrt{\rho_r}\, a_r}{\sqrt{\rho_\ell} + \sqrt{\rho_r}} \qquad \text{and} \qquad \underset{\sim}{a} \equiv \frac{\sqrt{\rho_r}\, a_\ell + \sqrt{\rho_\ell}\, a_r}{\sqrt{\rho_\ell} + \sqrt{\rho_r}}, \tag{6.46}$$

it is straightforward to prove the equalities:

$$\Delta(ab) = \tilde{a}\,\Delta b + \underset{\sim}{b}\,\Delta a\,, \tag{6.47a}$$

$$\Delta\left(\frac{1}{a}\right) = -\frac{\Delta a}{a_\ell\, a_r}\,, \tag{6.47b}$$

$$\left(\widetilde{\frac{1}{a}}\right) = \frac{1}{a_\ell\, a_r}\, \underset{\sim}{a}\,, \tag{6.47c}$$

for any choice of $a$, $b \in \mathbb{R}$. We also rewrite here the form of the EOS of our problem, as given in (6.9f),

$$p^{\mathrm{L}}(\mathcal{E}, \psi, \eta\rho, \mu) = \frac{1}{\psi}(\mathcal{E} + \eta\rho + \mu)\,, \tag{6.48}$$

and we note that, since the consistency condition (6.3) holds in each cell, we have $p_\ell^{\mathrm{L}} = p_\ell$ and $p_r^{\mathrm{L}} = p_r$, hence $\Delta p^{\mathrm{L}} = \Delta p$. Consider now the equations given by the condition (6.37). We immediately see that the first one reduces to the identity $\Delta m = \Delta m$. The second relation reads, after a rearrangement of the terms:

$$\Delta p + \frac{\hat{\zeta}}{\hat{\psi}^2} - \frac{1}{\hat{\psi}}\left[\Delta\mathcal{E} + \Delta(\eta\rho) + \Delta\mu\right] = \left(\frac{1}{2\hat{\psi}} - 1\right)\left[\Delta(\rho u^2) + \hat{u}^2\,\Delta\rho - 2\hat{u}\,\Delta(\rho u)\right]. \tag{6.49}$$

In order to satisfy the above equation, a natural choice is to impose that both the left and right member vanishes, therefore we obtain:

$$\Delta p = -\frac{\hat{\zeta}}{\hat{\psi}^2}\Delta\psi + \frac{1}{\hat{\psi}}\Delta\zeta\,, \tag{6.50}$$

where we have used $\zeta = \mathcal{E} + \eta\rho + \mu$, and

$$\Delta\rho u^2 + \hat{u}^2\,\Delta\rho = 2\hat{u}\Delta(\rho u)\,. \tag{6.51}$$

Assume that we can define $\hat{\psi}$ and $\hat{\zeta}$ such that the equality (6.50) holds. Through the relation (6.47a), an easy computation shows that we can satisfy (6.51) by defining $\hat{u}$ as we anticipated in (6.38a), that is $\hat{u} = \tilde{u}$. Let us now consider the third equation of (6.37), that can be written, rearranging properly the terms,

$$\Delta(\rho u H) = \frac{\hat{u}}{2\hat{\psi}}\left[\hat{u}^2\,\Delta\rho - 2\hat{u}\Delta(\rho u) + \Delta(\rho u^2)\right] \tag{6.52}$$

$$+ \hat{u}\left\{-\frac{\hat{\zeta}}{\hat{\psi}^2}\Delta\psi + \frac{1}{\hat{\psi}}\left[\Delta\mathcal{E} + \Delta(\eta\rho) + \Delta\mu\right]\right\}$$

$$+ \hat{u}\Delta E + \hat{H}\Delta(\rho u) - \hat{u}\hat{H}\Delta\rho\,. \tag{6.53}$$

Using (6.50) and (6.51), together with the relation $\rho\,H = E + p$, we obtain

$$\Delta(\rho u H) = -\hat{u}\hat{H}\Delta\rho + \hat{H}\Delta(\rho u) + \hat{u}\Delta(\rho H)\,, \tag{6.54}$$

which is satisfied if $\hat{H}$ is defined as in (6.38b), $\hat{H} = \tilde{H}$, as it is easily proved by using (6.47a). Then, the fourth equation of (6.37) gives:

$$\Delta(\eta\rho u) = -\hat{\eta}\hat{u}\Delta\rho + \hat{\eta}\Delta(\rho u) + \hat{u}\Delta(\rho\eta)\,, \tag{6.55}$$

so that we determine $\hat{\eta}$ as given in (6.38c), $\hat{\eta} = \tilde{\eta}$. The final step consists in finding average quantities $\hat{\psi}$ and $\hat{\zeta}$ such that the relation (6.50) is satisfied. From the EOS (6.48) we have, by using the equality (6.47a),

$$\Delta p = \left[\tilde{\mathcal{E}} + (\tilde{\eta\rho}) + \tilde{\mu}\right]\Delta\left(\frac{1}{\psi}\right) + \left(\frac{1}{\tilde{\psi}}\right)\Delta(\mathcal{E} + \eta\rho + \mu)\,. \tag{6.56}$$

Then, employing (6.47b) and (6.47c), together with $\zeta = \mathcal{E} + \eta\rho + \mu$, we obtain

$$\Delta p = -\frac{\tilde{\zeta}}{\psi_\ell\,\psi_r}\Delta\psi + \frac{\tilde{\psi}}{\psi_\ell\,\psi_r}\Delta\zeta\,. \tag{6.57}$$

The comparison of the relation above with (6.50) leads to set

$$\frac{1}{\hat{\psi}} = \frac{\tilde{\psi}}{\psi_\ell\,\psi_r} \qquad \text{and} \qquad \frac{\hat{\zeta}}{\hat{\psi}^2} = \frac{\tilde{\zeta}}{\psi_\ell\,\psi_r}\,, \tag{6.58}$$

so that we get

$$\hat{\psi} = \frac{\psi_\ell\,\psi_r}{\tilde{\psi}} \qquad \text{and} \qquad \hat{\zeta} = \frac{\psi_\ell\,\psi_r}{\tilde{\psi}^2}\tilde{\zeta}\,, \tag{6.59}$$

as previously reported in (6.38).

### 6.4.2  Two Dimensions

The PLM-Roe is extended to two dimensions by first rewriting the two-dimensional system (6.12) in the fully quasi-linear form $\frac{\partial z}{\partial t} + A^{\mathrm{L}}(z)\frac{\partial z}{\partial x} + B^{\mathrm{L}}(z)\frac{\partial z}{\partial y} = 0$, and then considering Roe linearizations $\hat{A}^{\mathrm{L}}$ and $\hat{B}^{\mathrm{L}}$ for the matrices $A^{\mathrm{L}}(z)$ and $B^{\mathrm{L}}(z)$, respectively. With an analogous procedure as in the one-dimensional case, we define:

$$\hat{A}^{\mathrm{L}} = A^{\mathrm{L}}(\hat{u}, \hat{v}, \hat{H}, \hat{\eta}, \hat{\psi}, \hat{\zeta}) \qquad \text{and} \qquad \hat{B}^{\mathrm{L}} = B^{\mathrm{L}}(\hat{u}, \hat{v}, \hat{H}, \hat{\eta}, \hat{\psi}, \hat{\zeta})\,, \tag{6.60}$$

and the average state $(\hat{u}, \hat{v}, \hat{H}, \hat{\eta}, \hat{\psi}, \hat{\zeta})$ is determined as in (6.38), together with the average for $v$:

$$\hat{v} = \frac{\sqrt{\rho_\ell}\,v_\ell + \sqrt{\rho_r}\,v_r}{\sqrt{\rho_\ell} + \sqrt{\rho_r}}\,. \tag{6.61}$$

The average sound speed is then given by

$$\hat{c} = \sqrt{\frac{1}{\hat{\psi}}\left(\hat{H} - \frac{\hat{u}^2 + \hat{v}^2}{2}\right) + \frac{\hat{\eta}}{\hat{\psi}}}\,. \tag{6.62}$$

## 6.5 Numerical Experiments

We present a selection of numerical results obtained with the PLM-Roe scheme developed in the previous section. Moreover, an entropy fix [76, 77] has been added in the implementation of the method in the form described in [118].

We report below some equations of state that we have used in our experiments.

*Ideal Polytropic Gas*

An ideal polytropic gas (thermally and calorically perfect gas) is defined by the thermodynamic relations:

$$p = \rho R T\,, \qquad \text{and} \qquad \varepsilon = c_v T\,, \quad c_v = \text{const.}\,, \tag{6.63}$$

where $R$ is the gas constant and $c_v$ the heat coefficient at constant volume. The gas constant $R$ is given by $\frac{\mathcal{R}}{M_w}$, where $\mathcal{R}$ is the universal gas constant, and $M_w$ the molecular weight of the gas.

The pressure as a function of the thermodynamic variables $\mathcal{E}$ and $\rho$ takes the form

$$p(\mathcal{E}, \rho) = (\gamma - 1)\,\mathcal{E}\,, \tag{6.64}$$

where $\gamma > 1$ is the adiabatic exponent [138] of the gas, and is related to $R$ and $c_v$ through $\gamma - 1 = \frac{R}{c_v}$.

*Stiffened gas EOS*

The *stiffened gas* EOS is often used to model liquids and solids at high pressure, and it has the form

$$p(\mathcal{E}, \rho) = (\gamma - 1)\,\mathcal{E} - \gamma\,\pi\,, \tag{6.65}$$

where the parameters $\gamma$ and $\pi$ depend on the considered material (e.g. $\gamma = 4.4$, $\pi = 6 \times 10^8\,Pa$ to model water under high pressure). This pressure law is sometimes called Tammann EOS [31].

*Van der Waals EOS*

The van der Waals equation of state [200] can be written as

$$p(\mathcal{E}, \rho) = \frac{R}{c_v} \left( \frac{\mathcal{E} + a\,\rho^2}{1 - \rho\,b} \right) - a\rho^2\,, \tag{6.66}$$

where $R$ is the gas constant, $c_v$ the specific heat at constant volume, and the coefficients $a$ and $b$ take into account the effects of the intermolecular cohesive forces and the finite size of the molecules, respectively. The internal energy is related to the temperature through $\varepsilon = c_v T$.

*Two-Molecular Vibrating Gas*

We consider an equation of state modeling a thermally perfect, calorically imperfect two-molecular vibrating gas,

$$p(\mathcal{E}, \rho) = \rho R T \left( \frac{\mathcal{E}}{\rho} \right)\,, \tag{6.67a}$$

where the temperature is given by the implicit equation

$$\frac{\mathcal{E}}{\rho} = c_v^{tr}\,T + \frac{\alpha\,\Theta_{vib}}{e^{\frac{\Theta_{vib}}{T}} - 1}\,. \tag{6.67b}$$

The parameters in the relations above will be set in our numerical experiments as $R = 287.086\,J\,kg^{-1}K^{-1}$ (specific gas constant), $c_v = R/(\gamma^{tr} - 1)$ with $\gamma^{tr} = 1.4$, $\Theta_{vib} = 10^3 K$, and $\alpha = R$. These values are chosen to model air.

We employ Newton's iterative method to compute the temperature by means of (6.67b), for given values of $\mathcal{E}$ and $\rho$.

*Osborne EOS*

A quite general equation of state has been developed by R. K. Osborne at the Los Alamos Scientific Laboratory [167], and can be written in the form

$$p(\mathcal{E}, \rho) = \frac{1}{\mathcal{E}_0 + \phi_0} \left\{ \xi(a_1 + a_2\xi) + \mathcal{E}_0[b_0 + \xi(b_1 + b_2\xi) + \mathcal{E}_0(c_0 + c_1\xi)] \right\}, \qquad (6.68)$$

where $\mathcal{E}_0 = \rho_0\varepsilon$ and $\xi = (\rho/\rho_0 - 1)$. We choose the parameters in (6.68) as the typical values for water, $\rho_0 = 10^{-2} kg\,m^{-3}$, $a_1 = 3.84 \times 10^{-4} J^{-2} m^{-6}$, $a_2 = 1.756 \times 10^{-3} J^{-2} m^{-6}$, $b_0 = 1.312 \times 10^{-2} J\,m^{-3}$, $b_1 = 6.265 \times 10^{-2} J\,m^{-3}$, $b_2 = 0.2133\,J\,m^{-3}$, $c_0 = 0.5132$, $c_1 = 0.6761$, and $\phi_0 = 2 \times 10^{-2} J\,m^{-3}$.

### 6.5.1 One-dimensional Tests

All the numerical examples presented here involve the solution of Riemann shock tube problems, in which the initial data consist of two constant states separated by a diaphragm.

In all the experiments second order corrections have been applied, employing the van Leer limiter function (4.29).

For each test we use the results computed on a fine grid of 2000 cells as a reference solution. This will be marked by a solid line in all the figures.

EXPERIMENT 6.2. *Stiffened Gas EOS.*

We compute the solution for a shock-tube problem considered in [86, 61] for the stiffened gas EOS. The computational domain is the interval $[0, 1]\,m$, and the initial interface is located at $x = 0.5\,m$. The density, velocity and pressure of the left and right state are given in Table 6.1. The parameters in the EOS (6.65) are defined as $\gamma = 7.15$ and $\pi = 3 \times 10^8\,Pa$.

The exact solution for this test consists of a sonic rarefaction wave, a contact discontinuity, and a right-going shock wave with Mach number $M_s = 2.6$.

Although for this EOS, that is linear in $\mathcal{E}$, our method reduces to the classical Roe scheme, we present this test to validate our approach. The results obtained with 100 grid cells are shown in Figure 6.1. The implementation of an entropy fix (as in [164]) allows us to compute correctly the sonic rarefaction wave.

Table 6.1: Initial data for Experiment 6.2.

| state | $\rho\ [kg\,m^{-3}]$ | $u\ [m\,s^{-1}]$ | $p\ [Pa]$ |
|-------|----------------------|------------------|-----------|
| left  | $1.0 \times 10^3$    | $2.0 \times 10^3$ | $5.0 \times 10^8$ |
| right | $1.0 \times 10^3$    | $2.0 \times 10^3$ | $1.0 \times 10^6$ |
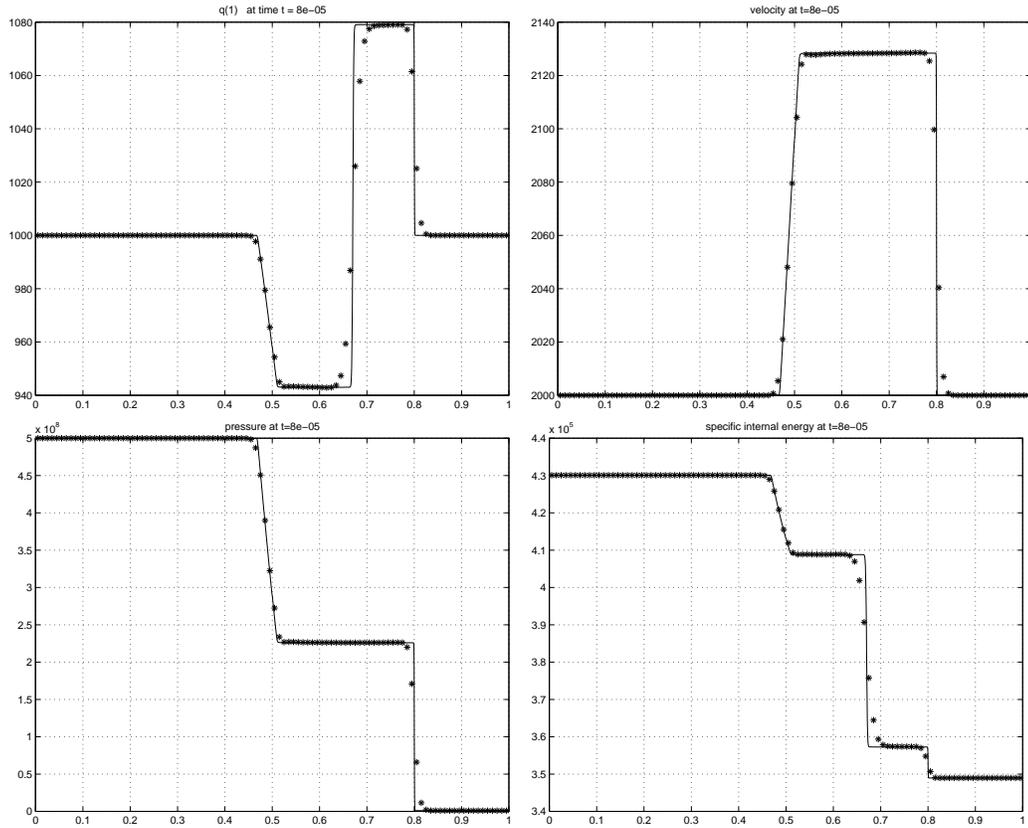
Figure 6.1: Experiment 6.2. Stiffened gas EOS. Density, velocity, pressure and specific internal energy at time $t = 8.0 \times 10^{-5} s$. Number of grid cells = 100. CFL = 0.9.

EXPERIMENT 6.3. *Van der Waals Gas.*

We solve a shock tube problem taken from [114]. We employ the van der Waals EOS (6.66) with parameters modeling water given by $R = 461.5 \, J/(kg \, K)$, $c_v = 1401.88 \, J/(kg \, K)$, $a = 1684.54 \, m^6 Pa/kg^2$, and $b = 0.001692 \, m^3/kg$. The computational domain is the interval $[0, 1] \, m$, and the initial interface is located at $x = 0.5 \, m$, as in the previous experiment. The left and right states, expressed in terms of density, velocity, and pressure, are specified in Table 6.2.

The exact solution of this problem consists of a rarefaction wave moving to the left, a contact discontinuity and a shock wave moving to the right. Figure 6.2 shows the results for this test with 100 grid cells.

Table 6.2: Initial data for Experiment 6.3.

| state | $\rho \, [kg \, m^{-3}]$ | $u \, [m \, s^{-1}]$ | $p \, [Pa]$ |
|---|---|---|---|
| left | 200.0 | 0.0 | $3.5 \times 10^7$ |
| right | 117.0 | 0.0 | $1.95 \times 10^7$ |
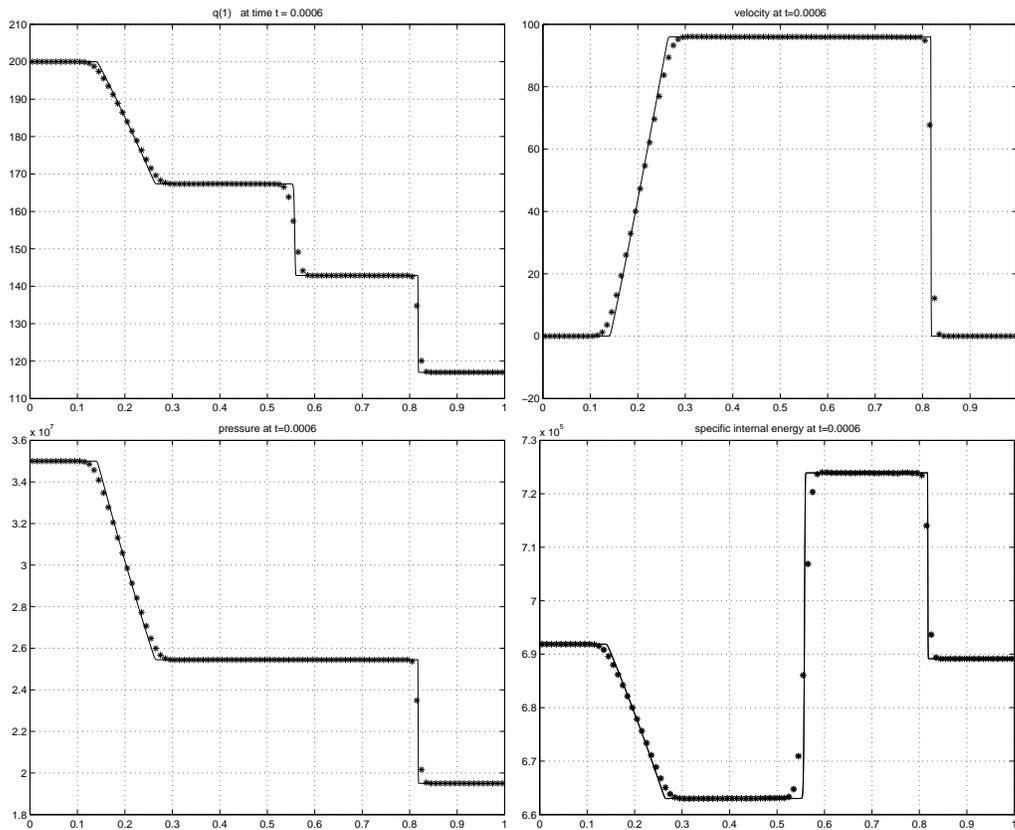
Figure 6.2: Experiment 6.3. Van der Waals gas. Density, velocity, pressure and specific internal energy at time $t = 0.6 \times 10^{-3}\, s$. Number of grid cells = 100. CFL = 0.9.

EXPERIMENT 6.4. *Two-molecular Vibrating Gas and Osborne model.*

We consider a shock-tube problem proposed in [144] for both the two-molecular vibrating gas model and the Osborne model. The computational domain is the interval $[-10, 10]\, m$, and the initial interface is located at $x = 0$. The values for the left and right state expressed in terms of density, velocity and internal energy are given in Table 6.3.

This experiment represents a version of the experiment by Lax [110], and its exact solution involves a left-going rarefaction wave, a contact discontinuity, and a right-going shock wave. Figure 6.3 and 6.4 show the results for this test with the two-molecular vibrating gas EOS and the Osborne EOS, respectively. The number of grid cells used is 200.

Table 6.3: Initial data for Experiment 6.4.

| state | $\rho\ [kg\, m^{-3}]$ | $u\ [m\, s^{-1}]$ | $\varepsilon\ [J\, kg^{-1}]$ |
|-------|-----------------------|-------------------|------------------------------|
| left  | 0.066                 | 0.0               | $7.22 \times 10^6$           |
| right | 0.030                 | 0.0               | $1.44 \times 10^6$           |
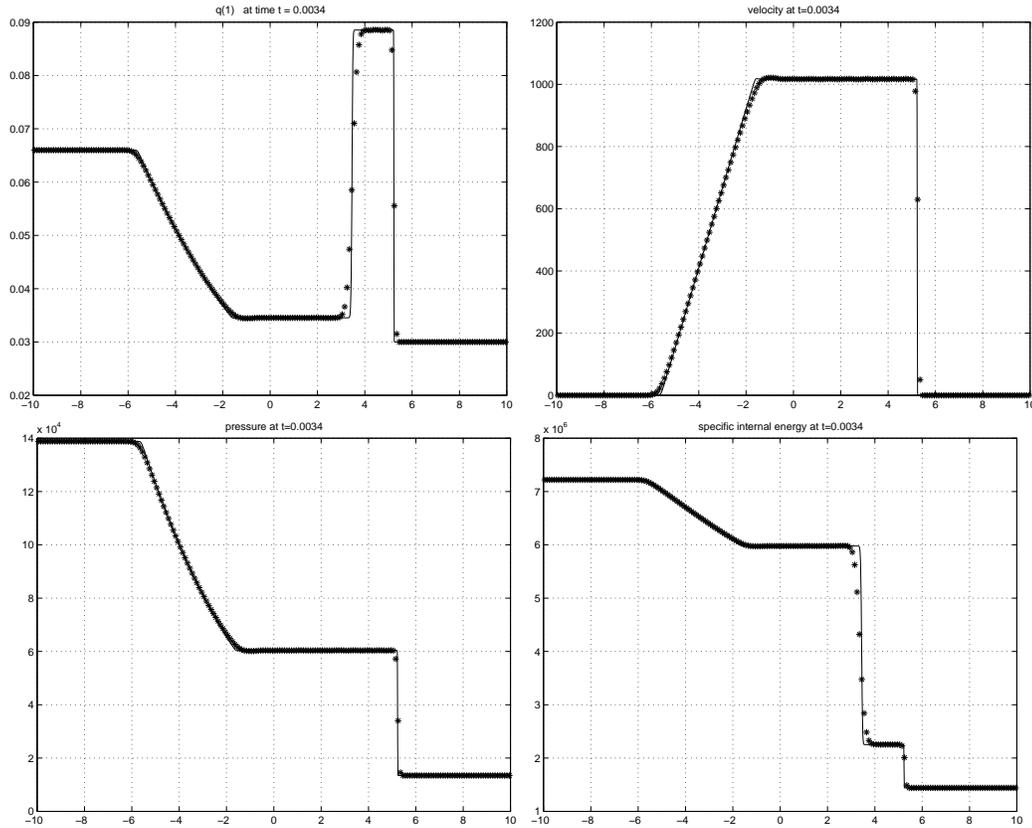
Figure 6.3: Experiment 6.4. Two-molecular vibrating gas. Density, velocity, pressure and specific internal energy at time $t = 0.0034\,s$. Number of grid cells $= 200$. CFL $= 0.9$.

### 6.5.2  Two-Dimensional test

EXPERIMENT 6.5. *Double-Mach Reflection.*

We consider the reflection of a planar shock wave by an oblique surface. This problem is well known in the literature, and has generated a large amount of analytical, computational and experimental work. We refer the reader especially to [36, 37] for a detailed description of the test, and to [47, 66] for some experimental results.

The problem involves a Mach 10 shock in air that initially makes a $60°$ angle with a reflecting wall. The undisturbed air ahead of the shock has density $\rho = 1.4\,kg\,m^{-3}$ and pressure $p = 1.0 \times 10^5 Pa$. The computational domain is defined by $0 \leq x \leq 4$ and $0 \leq y \leq 1$, and the reflecting wall lies along its bottom, beginning at $x = 1/6$. The shock makes a $60°$ angle with the $x$-axis and extends to the top of the domain at $y = 1$. On the left-hand boundary and on the short region from $x = 0$ to $x = 1/6$ along the bottom boundary, we impose the exact post-shock condition. The flow values along the top boundary, at $y = 1$, are set to describe the exact motion of the Mach 10 shock. Finally, on the right-hand boundary, at $x = 4$, we assign zero gradients.

Following [144], we compute the solution for this test with both the ideal polytropic gas EOS (6.64), with $\gamma = 1.4$, and the two-vibrating gas model (6.67). We use the two-dimensional wave propagation algorithms described in Section 4.3 of Chapter 4, including the transverse fluctuations terms. Moreover, second order corrections have been applied by using the van Leer limiter function (4.29).
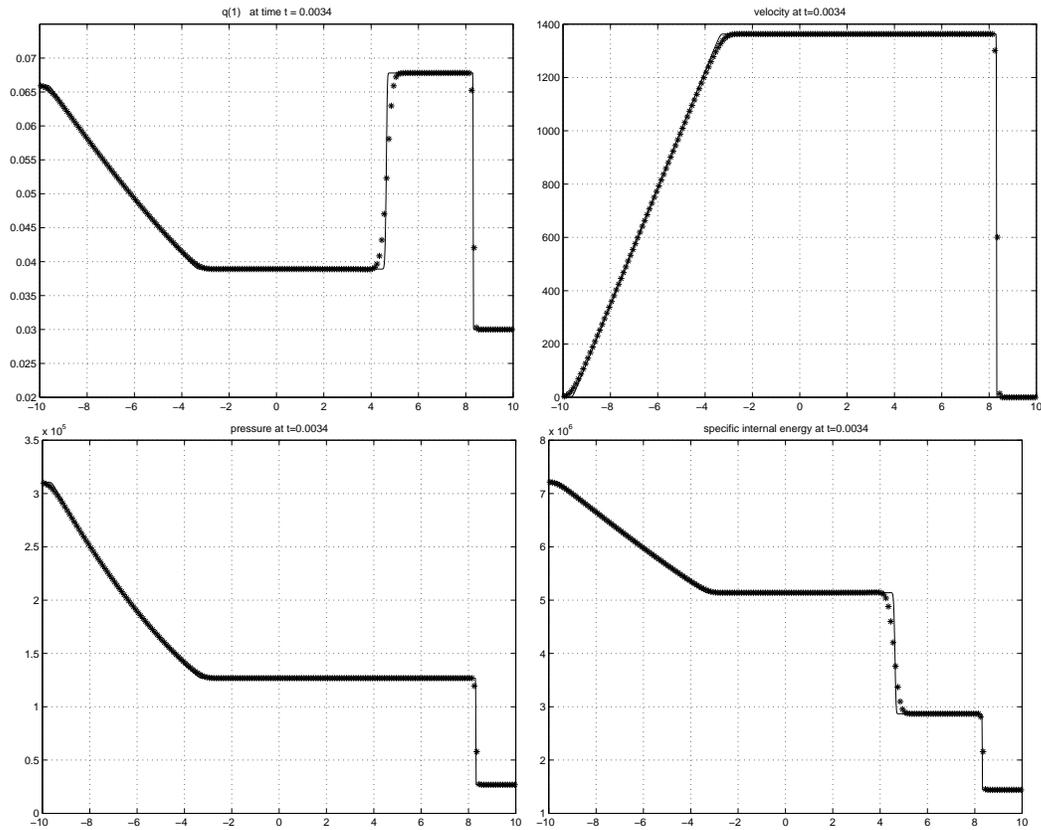
Figure 6.4: Experiment 6.4. Osborne model. Density, velocity, pressure and specific internal energy at time $t = 0.0034\,s$. Number of grid cells = 200. CFL = 0.9.

The results obtained with a $480 \times 120$ mesh are displayed in Figure 6.5. The comparison with the experimental work of [66] shows that our scheme is able to capture the distinguishing features related to the different form of the equation of state. In particular, we observe that in the calculation with the two-vibrating molecular gas the main shock is less curved at the compression corner, and that the Mach stem near the wall is pushed forward by the jet.
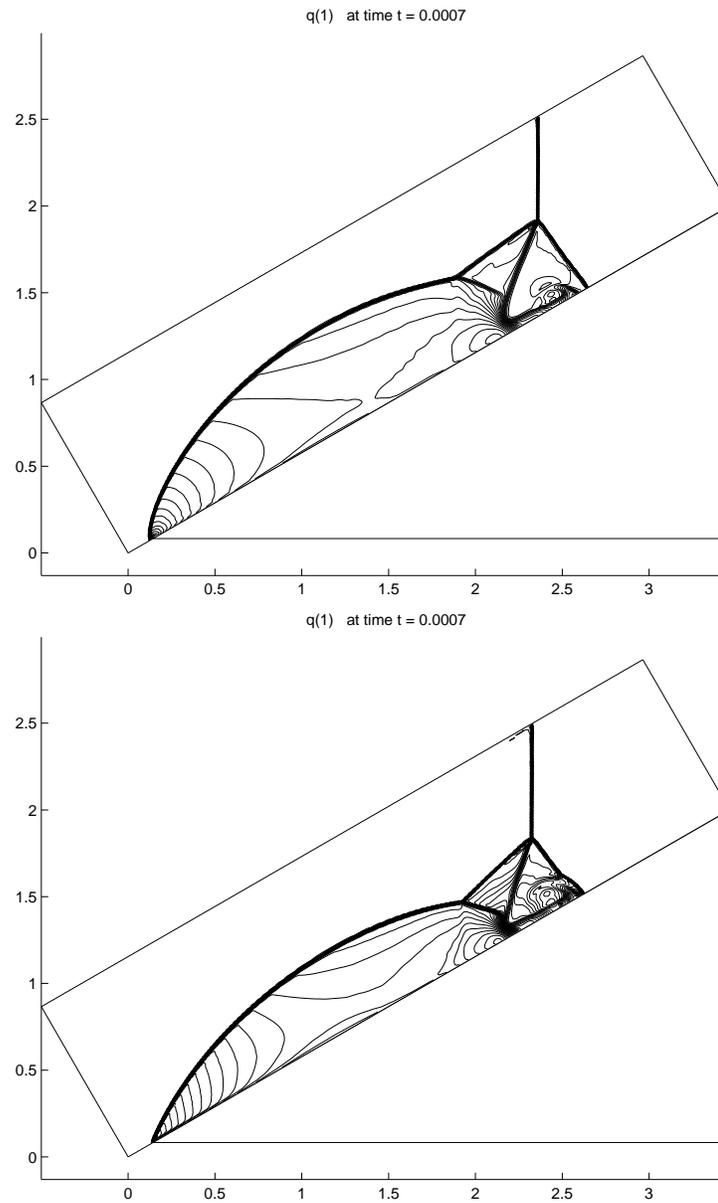
Figure 6.5: Experiment 6.5: Double-Mach Reflection. Above: Ideal Polytropic Gas. Below: Two-molecular vibrating gas. Density contours at $t = 0.7 \times 10^{-3}\,s$. Number of grid cells in the $x$ direction: $480$; in the $y$ direction: 120. CFL $= 0.9$.

### 6.6 Intrinsic Difficulties of the Flow Description based on Cell Discretization

When in a finite volume method we derive quantities from the selected primary variables, some inconsistencies with the correct physical behaviour may arise as a consequence of the discrete cell-based description of the solution. In particular, when we solve the flow equations by using an Eulerian conservative formulation, the pressure updated through the conserved variables may develop oscillations at contact interfaces. We remark that this difficulty not only appears in multicomponent problems, but also in the case of single-component flows for a general pressure law. However, in the special case of the ideal polytropic gas equation of state (6.64) or the stiffened gas EOS (6.65) the equilibrium of the pressure for single fluids is maintained, as we will discuss in the following.

Let us consider a cell-based discretization of a one-dimensional single-component fluid flow. For any physical quantity $\zeta(x,t)$, at fixed time $t$ we assign to each cell $\mathcal{C}$ a value $\zeta_c(t)$. A natural choice for cell values, in particular for quantities that are conserved, is the average over the cell:

$$\bar{\zeta}_c(t) = \frac{1}{|\mathcal{C}|} \int_{\mathcal{C}} \zeta(x,t)\, dx \,. \tag{6.69}$$

We select the vector $q = [\rho, m, E]^{\mathrm{T}}$ as the primary variables that describe the flow, so that we characterize the flow conditions in each cell at time $t$ with the averages $\bar{\rho}_c$, $\bar{m}_c$, $\bar{E}_c$. Assume now we wish to derive another physical quantity $\alpha$ which is related to the the primary variables through a function $\varphi$, i.e. $\alpha = \varphi(q)$. It is clear that only if $\varphi$ is linear in $q$ the evaluation of $\varphi$ in the average state $\bar{q}_c$ will produce the average of $\alpha$ over the cell, that is $\bar{\alpha}_c$. In general, we will instead have $\varphi(\bar{q}_c) = \tilde{\alpha}_c \neq \bar{\alpha}_c$. This simple mathematical observation is basilar in understanding the problem of pressure oscillations generated at contact interfaces in numerical computations.

#### 6.6.1 Contact Discontinuities

We focus on the situation in which a contact discontinuity is present in the flow. We assume uniform flow conditions on each side of this discontinuity, denoting the corresponding quantities with the subscripts $\ell$ and $r$, for the left and right state, respectively. Across the contact discontinuity, the flow velocity $u$ and the pressure $p$ remain constant,

$$u_\ell = u_r \equiv u^{\mathrm{c}} \quad \text{and} \quad p_\ell = p_r \equiv p^{\mathrm{c}} \,, \tag{6.70}$$

while the other quantities in general will have a jump. In particular, we consider the description of the flow conditions for the cell inside which the contact discontinuity is located. We denote with $\mathcal{C}_\ell$ and $\mathcal{C}_r$ the portions of the cell $\mathcal{C}$ on the left and on the right of the discontinuity, and we introduce the corresponding cell fractions

$$\xi_\ell \equiv \frac{|\mathcal{C}_\ell|}{|\mathcal{C}|}, \qquad \text{and} \qquad \xi_r \equiv \frac{|\mathcal{C}_r|}{|\mathcal{C}|} = 1 - \xi_\ell \,. \tag{6.71}$$

The average $q$ in the cell with the discontinuity can be written:

$$\bar{q}_c = \frac{1}{|\mathcal{C}|} \int_{\mathcal{C}_\ell} q_\ell \, dx + \frac{1}{|\mathcal{C}|} \int_{\mathcal{C}_r} q_r \, dx \tag{6.72}$$

$$= q_\ell \xi_\ell + q_r \xi_r \,.$$

Note that $\bar{m}_c = m_\ell \xi_\ell + m_r \xi_r = \bar{\rho}_c u^{\mathrm{c}}$. Let us now derive some quantity $\alpha = \varphi(q)$ by evaluating the average state $\bar{q}_c$ that describes the flow conditions in the cell, and use this to define a cell value $\tilde{\alpha} = \varphi(\bar{q}_c)$ for $\alpha$. If we wish to compute the velocity, $\alpha = u$, then we have

$$\tilde{u}_c = \frac{\bar{m}_c}{\bar{\rho}_c} = \frac{\bar{\rho}_c u^{\mathrm{c}}}{\bar{\rho}_c} = u^{\mathrm{c}} \,. \tag{6.73}$$

Thus, when deriving the velocity from the conserved variables, we are able to obtain the correct constant value of the physical velocity across the contact discontinuity.

For the internal energy per unit volume $\mathcal{E}$, we then have:

$$\tilde{\mathcal{E}}_c \;=\; \bar{E}_c - \frac{1}{2}\frac{(\bar{m}_c)^2}{\bar{\rho}_c} = \bar{E}_c - \frac{1}{2}\bar{\rho}_c(u^c)^2 \tag{6.74}$$

$$= \left[E_\ell - \frac{1}{2}\rho_\ell(u^c)^2\right]\xi_\ell + \left[E_r - \frac{1}{2}\rho_r(u^c)^2\right]\xi_r = \bar{\mathcal{E}}_c \,.$$

This result could also have been deduced directly by noticing that if $u$ is constant then $\mathcal{E}$ is a linear function of $\rho$ and $E$.

We now consider the pressure $p$, expressed by the equation of state

$$p(\mathcal{E},\rho) = p\left(E - \frac{m^2}{\rho},\rho\right) \equiv \Pi(q)\,. \tag{6.75}$$

Let us define $\tilde{p}_c \equiv \Pi(\bar{q}_c)$. By the above derivation (6.74) for $\mathcal{E}$, we have

$$\tilde{p}_c = p(\bar{\mathcal{E}}_c, \bar{\rho}_c)\,. \tag{6.76}$$

For a general function $p(\mathcal{E},\rho)$, we will have $p(\bar{\mathcal{E}}_c, \bar{\rho}_c) \neq p^c$, therefore the cell value $\tilde{p}_c = \Pi(\bar{q}_c)$ does not provide a consistent description of the pressure in correspondence of the contact discontinuity. However, in the special case of $p$ linear in $\mathcal{E}$ and $\rho$, as for an ideal polytropic gas or a stiffened gas, we correctly obtain $p(\bar{\mathcal{E}}_c, \bar{\rho}_c) = \bar{p}_c = p^c$ so that the constant value of the pressure across the contact discontinuity is preserved in the discrete representation.

As an example of a nonlinear equation of state, we consider here the van der Waals law (6.66) (the nonlinearity is in $\rho$ only):

$$p(\mathcal{E},\rho) = \frac{R}{c_v}\left(\frac{\mathcal{E} + a\,\rho^2}{1 - \rho\,b}\right) - a\rho^2\,. \tag{6.77}$$

It is useful to plot the isobaric curves for a given EOS in the plane $(\rho, \mathcal{E})$ to observe the difference between the case of a linear pressure law and a nonlinear one in the presence of a contact discontinuity within a cell. Let $\rho_\ell$, $\mathcal{E}_\ell$ and $\rho_r$, $\mathcal{E}_r$ be the left and right values of the density and the internal energy per unit volume across the discontinuity. By assumption, they satisfy $p(\mathcal{E}_\ell,\rho_\ell) = p(\mathcal{E}_r,\rho_r) \equiv p^c$, this meaning that the points $(\rho_\ell, \mathcal{E}_\ell)$ and $(\rho_r, \mathcal{E}_r)$ lie on the same isobaric curve with value $p^c$.

The pressure cell value $\tilde{p}_c \equiv \Pi(\bar{q}_c) = p(\bar{\mathcal{E}}_c, \bar{\rho}_c)$ will be equal to $p^c$ only if the point $(\bar{\rho}_c, \bar{\mathcal{E}}_c)$ lies on the same isobaric curve of $(\rho_\ell, \mathcal{E}_\ell)$ and $(\rho_r, \mathcal{E}_r)$. By virtue of (6.72) and (6.74) this point $(\bar{\rho}_c, \bar{\mathcal{E}}_c)$ is located on the straight line connecting $(\rho_\ell, \mathcal{E}_\ell)$ and $(\rho_r, \mathcal{E}_r)$. If the pressure law is linear in $\mathcal{E}$, $\rho$, then the isobaric curves are straight lines, hence we will always have $\tilde{p}_c = p(\bar{\mathcal{E}}_c, \bar{\rho}_c) = p^c$. See Figure 6.6 for a graphical description of this situation.

On the other hand, for a general EOS, the isobaric lines have varying curvature, and the point $(\bar{\rho}_c, \bar{\mathcal{E}}_c)$ in general will not lie on the curve $p = p^c$, that is $p(\bar{\mathcal{E}}_c, \bar{\rho}_c) \neq p^c$. Figure 6.7 shows the occurrence of this situation for the van der Waals equation of state (6.77), with the values for $R$, $c_v$, $a$, $b$ used in Experiment 6.3. Note also that the point $(\bar{\rho}_c, \bar{\mathcal{E}}_c)$ could lie below the critical isobaric line and below the critical isothermal line (dotted lines in the figure), that is, this point may not represent a physical state for the gas.

From this discussion we conclude that the definition of the pressure cell value based on $\bar{q}_c$ in general does not provide an appropriate description of the flow in the presence of a contact discontinuity. In the continuous description case, under the hypothesis of local thermodynamic equilibrium, the equation of state gives the value of the pressure as a function of $\mathcal{E}$ and $\rho$ everywhere *except* at the point of the discontinuity itself. In the discrete cell-based representation, the definition $\tilde{p}_c = \Pi(\bar{q}_c)$ relies on the

implicit assumption that each cell can be treated as a system in thermodynamic equilibrium at the average values $\bar{\mathcal{E}}_c$, $\bar{\rho}_c$. This hypothesis is appropriate for cells corresponding to smoothly-varying flow conditions, but not for cells containing contact discontinuities. Thus, inconsistencies with the real physical situation may arise.



PSfrag replacements
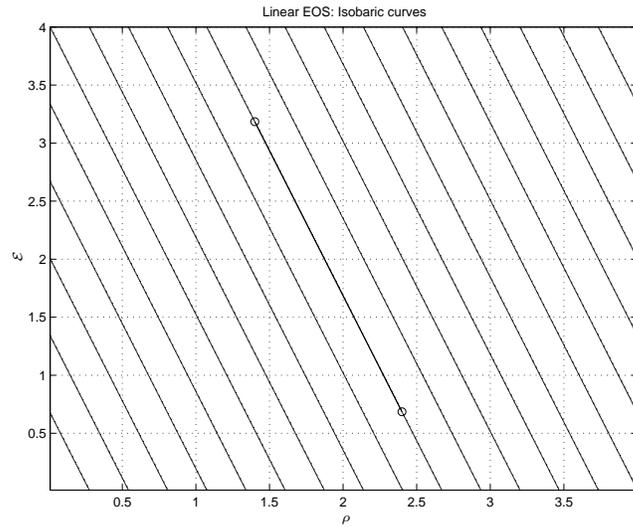
Figure 6.6: Isobaric curves for a linear EOS in the plane $(\rho, \mathcal{E})$. The circles represent two possible states across a contact discontinuity.



PSfrag replacements
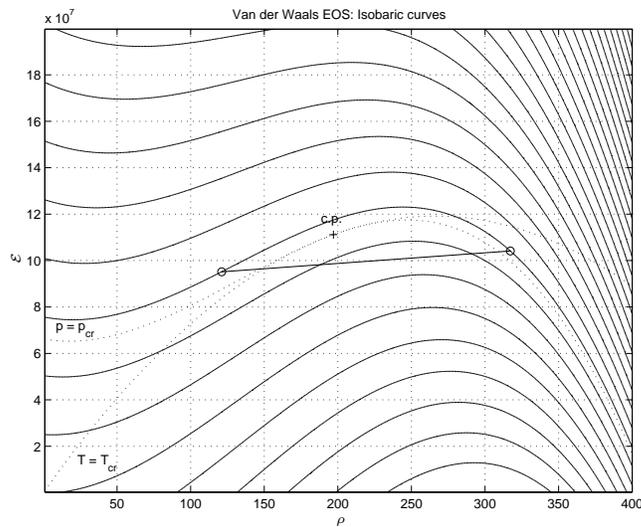
Figure 6.7: Van der Waals isobaric curves in the plane $(\rho, \mathcal{E})$. The dotted lines indicate the critical isobaric curve and the critical isothermal curve; the point denoted with + corresponds to the critical point of the gas. The two circles represent two possible states across a contact discontinuity.

*Multifluid Flows*

If we consider multifluid flows, then the pressure is also expressed as a function of additional variables that describe the flow composition.

Let us consider a mixture equation of state linear in $\mathcal{E}$ and $\rho$, in the form (3.4):

$$p = \bar{\kappa}\mathcal{E} + \bar{\chi}\rho + \beta \,, \tag{6.78}$$

where $\bar{\kappa}$, $\bar{\chi}$, $\beta$ are the material-dependent parameters. To be able to recover the correct constant value of the pressure across contact interfaces in the discrete cell-based representation, we need to select properly the material quantities that augment the vector of the primary variables $q$ with which we describe the flow conditions. We can easily see that if we select $(q, \psi, (\eta\rho), \mu)$ as the extended vector of the primary variables, where

$$\psi = \frac{1}{\bar{\kappa}} \,, \qquad \eta = \frac{\bar{\chi}}{\bar{\kappa}} \,, \quad \text{and} \quad \mu = \frac{\beta}{\bar{\kappa}} \,, \tag{6.79}$$

then we can properly compute the physical pressure $p^c$. To demonstrate this, first, let us rewrite the pressure law (6.78) in terms of (6.79):

$$p = \frac{1}{\psi}(\mathcal{E} + (\eta\rho) + \mu) \equiv \Pi(q, \psi, \eta\rho, \mu) \,. \tag{6.80}$$

The pressure cell value defined as $\tilde{p}_c = \Pi(\bar{q}_c, \bar{\psi}_c, \overline{(\eta\rho)}_c, \bar{\mu}_c)$ gives:

$$
\begin{aligned}
\tilde{p}_c &= \frac{1}{\bar{\psi}_c}(\bar{\mathcal{E}}_c + \overline{(\eta\rho)}_c + \bar{\mu}_c) \tag{6.81} \\[2mm]
&= \frac{(\mathcal{E}_\ell + (\eta\rho)_\ell + \mu_\ell)\xi_\ell + (\mathcal{E}_r + (\eta\rho)_r + \mu_r)\xi_r}{\psi_\ell \xi_\ell + \psi_r \xi_r} \\[2mm]
&= \frac{p^c \psi_\ell \xi_\ell + p^c \psi_r \xi_r}{\psi_\ell \xi_\ell + \psi_r \xi_r} = p^c \,.
\end{aligned}
$$

The result above explains further the formulation (3.12), (3.17) of the Shyue-type multifluid model described in Section 3.2.3.

### 6.6.2 Two-Dimensional Case

In two dimensions, in which case $q = [\rho, \rho u, \rho v, E]^{\mathrm{T}}$, we encounter further difficulties since the tangential velocity may vary across contact discontinuities (*slip lines*). Let us consider again $u_\ell = u_r \equiv u^c$, $p_\ell = p_r \equiv p^c$, but $v_\ell \neq v_r$. Since here the kinetic energy $\mathcal{K}$ consists of the contributions of both $u$ and $v$, $\mathcal{K} = \frac{1}{2}\rho(u^2 + v^2)$, the derivation of the cell value of $\mathcal{E}$ from the conserved variables does not produce in general $\bar{\mathcal{E}}_c$, differently from the result in (6.74). Therefore the equality (6.76) and the consequent discussion do not hold anymore. Note that if we consider $\mathcal{K}^t = \frac{1}{2}\rho v^2$ as an additional primary variable, then the computation of $\tilde{\mathcal{E}}_c$ from $[\bar{\rho}_c, (\bar{\rho u})_c, \bar{E}_c, \bar{\mathcal{K}^t}_c]^{\mathrm{T}}$, still gives:

$$
\begin{aligned}
\tilde{\mathcal{E}}_c &= \bar{E}_c - \frac{1}{2}\bar{\rho}_c (u^c)^2 - \bar{\mathcal{K}^t}_c \tag{6.82} \\[2mm]
&= \left[E_\ell - \frac{1}{2}\rho_\ell(u^c)^2 - \mathcal{K}_\ell^t\right]\xi_\ell + \left[E_r - \frac{1}{2}\rho_r(u^c)^2 - \mathcal{K}_r^t\right]\xi_r = \bar{\mathcal{E}}_c \,.
\end{aligned}
$$

## 6.7 Pressure Oscillations in Conservative Finite Volume Methods

The difficulties in the discrete cell-based description of a fluid flow described in the previous section will inevitably reflect on the numerical solution of the flow equations by finite volume methods, which are

based on a cell discretization. A conservative method for the Euler equations that updates the pressure by using the vector $q$ of the conserved quantities, that is through $p(\mathcal{E}, \rho) = p\left(E - \frac{1}{2}\frac{m^2}{\rho}\right) \equiv \Pi(q)$, may fail to preserve the invariance of the pressure across contact discontinuities. Clearly, the Pressure Linearization Method will suffer from these difficulties.

As expected from the previous discussion, in the case of an ideal polytropic gas, and more generally for any equation of state linear in $\mathcal{E}$ and $\rho$, no oscillations appear in the numerical solution. However, the numerical experimentation shows that spurious oscillations may arise for pressure laws with nonlinearities in $\mathcal{E}$ or $\rho$. Note that the erroneous fluctuations of the pressure contaminate the entire solution field (e.g. density and velocity). We show this problem by presenting some numerical tests.

### 6.7.1   Numerical Experiments

We present some numerical results for a gas governed by the van der Waals equation of state (6.77) with the parameters $R$, $c_v$, $a$ and $b$ used for the Experiment 6.3.

The computations have been performed both by the PLM-Roe and by the method of Roe extended to real gases by using the approach of Glaister [64] (see also [201]). These two methods give the same type of numerical solution, hence just the results obtained with the latter approach will be plotted. In each experiment we have used a grid of 100 cells, and no second order corrections have been applied.

EXPERIMENT 6.6. *Moving contact discontinuity.*

We consider an experiment proposed in [61], consisting of a moving contact discontinuity. The density, velocity, and pressure of the left and right state are given in Table 6.4.

As we can see from Figure 6.8, oscillations arise around the contact discontinuity.

Table 6.4: Initial data for Experiment 6.6.

| state | $\rho$ $[kg\,m^{-3}]$ | $u$ $[m\,s^{-1}]$ | $p$ $[Pa]$ |
|---|---|---|---|
| left | 1.0 | 100.0 | $1.0 \times 10^5$ |
| right | 10.0 | 100.0 | $1.0 \times 10^5$ |

EXPERIMENT 6.7. *Shock Tube Problem.*

We solve a Riemann shock tube problem tested in [114, 61, 21], with the left and right state specified in Table 6.5. The computational domain is the interval $[0, 1]$ $m$, and the initial interface is located at $x = 0.5\ m$.

The exact solution of this problem consists of a rarefaction wave moving to the left, a contact discontinuity and a shock wave moving to the right. The results are displayed in Figure 6.9, where we use as a reference solution (solid line) the results obtained on a fine grid with a modified version of the PLM that will be introduced in Section 6.8.

We can see from the plots that two methods used for the computation, both based on the standard updating of the pressure through the vector of the conserved variables, are not able to preserve the invariance of the pressure and the velocity across the contact discontinuity.

We recall that in the Experiment 6.2 with the van der Waals EOS, performed by the PLM-Roe, no oscillations were observed around the contact discontinuity (Fig. 6.2).

This difference can be explained by observing in the plane $(\rho, \mathcal{E})$ the location of the points characterizing the exact solution of the two examples. In Figure 6.10 we denote the left and right states of the Riemann problem with the lowercase letters l and r, and the left and right states across the contact

Table 6.5: Initial data for Experiment 6.7.

| state | $\rho \; [kg\, m^{-3}]$ | $u \; [m\, s^{-1}]$ | $p \; [Pa]$ |
|-------|------------------------|---------------------|-------------|
| left  | 333.0 | 0.0 | $3.7311358 \times 10^{7}$ |
| right | 111.0 | 0.0 | $2.1770768 \times 10^{7}$ |
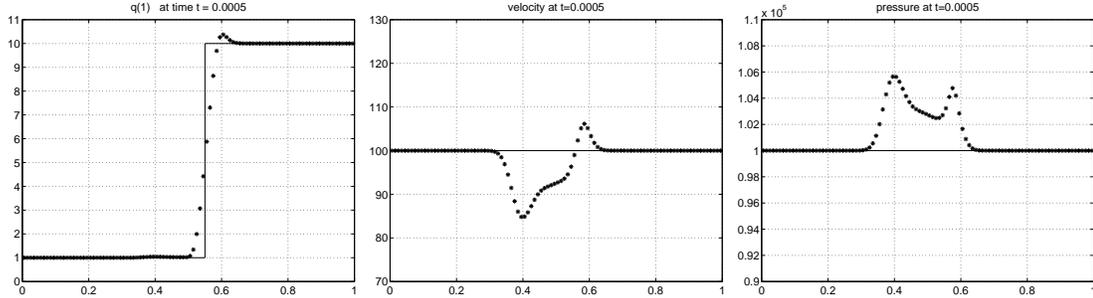


Figure 6.8: Experiment 6.5. Van der Waals gas. Density, velocity, and pressure at time $t = 0.5 \times 10^{-3}\, s$. Number of grid cells $= 100$. CFL $= 0.9$. Results obtained by a Roe-type method with standard updating of the pressure. Solid line: exact solution.
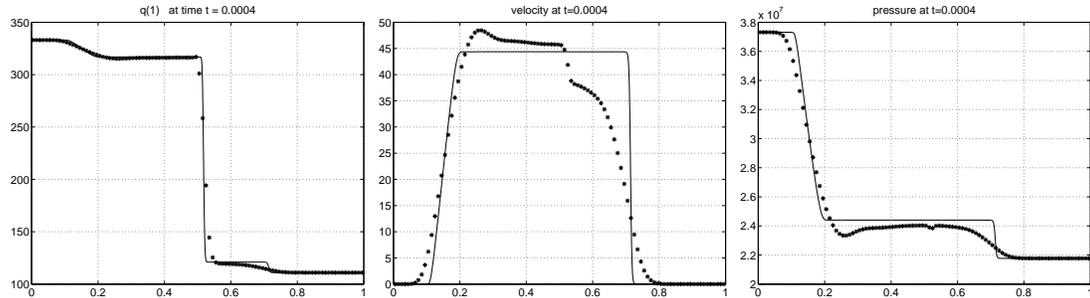


Figure 6.9: Experiment 6.6. Van der Waals gas. Density, velocity, and pressure at time $t = 0.4 \times 10^{-3}\, s$. Number of grid cells $= 100$. CFL $= 0.9$. Results obtained by a Roe-type method with standard updating of the pressure.

discontinuity with the uppercase letters L and R. Moreover, circles $\circ$ refers to Experiment 6.2, while stars $*$ to Experiment 6.6.

Observing the location of the states across the contact discontinuity, we can see that for test 6.2 the isobaric curve through these states is well approximated by the straight line connecting the two points. Therefore, in view of the analysis of Section 6.6, the pressure computed from the cell values of $\rho$ and $\mathcal{E}$ will be a good approximation of the physical constant value of the pressure across the contact discontinuity. On the other hand, the isobaric curve through the states across the discontinuity for test 6.6 departs noticeably from the straight line connecting the two points. Hence, we expect difficulties in the computation of the pressure.
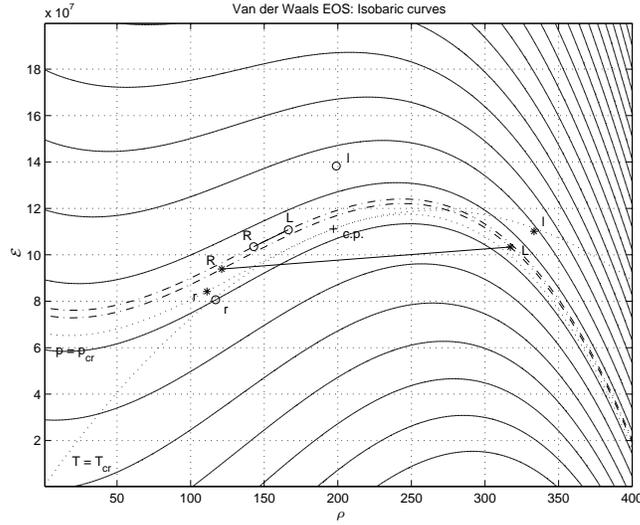
Figure 6.10: Points corresponding in the plane $(\rho, \mathcal{E})$ to the exact solution of Experiment 6.3 ($\circ$) and Experiment 6.7 ($*$).

## 6.8  Modified PLM

The numerical results reported in the previous section confirm that to avoid pressure oscillations we need to abandon the updating of the pressure through $p = \Pi(q)$ around contact discontinuities. Still, we would like to maintain the conservative form of the Euler system, without turning to either primitive formulations or hybrid ones (see for instance the approaches of Karni [96, 97] for multifluid flows).

We propose here a natural modification (in one dimension) of the Pressure Linearization Method that allows to preserve pressure equilibrium at contact interfaces.

In the evolution step we maintain the system (6.9) of the original PLM. The formulation is then augmented by an advection equation for a tracer variable $\vartheta$ that locates the contact discontinuity:

$$\frac{\partial \vartheta}{\partial t} + u\,\frac{\partial \vartheta}{\partial x} = 0\,. \tag{6.83}$$

The variable $\vartheta$ is initialized to zero and one on opposite sides of a known initial discontinuity (either shock or contact wave) in the flow field.

As the solution evolves, far from the contact discontinuity ($\vartheta = 0$ or $\vartheta = 1$, up to a tolerance) we still update the pressure through $p(\mathcal{E}, \rho)$, as in the original PLM. Otherwise, in the cells where the contact discontinuity is spread ($0 < \vartheta < 1$), we update the pressure by exploiting the linear EOS (6.9f),

$$p^{\mathrm{L}} = p^{\mathrm{L}}(\mathcal{E}, \psi, \eta\rho, \mu) = \frac{1}{\psi}(\mathcal{E} + \eta\rho + \mu)\,, \tag{6.84}$$

which corresponds to the mixture equation of state of the Shyue-type multifluid model (3.17) on which we have built our method.

Everywhere in the computational domain, both away from the contact interface and around it, the variables $\eta$, $\psi$, $\mu$ are defined locally every time step through the same relations of the standard approach:

$$\psi_i^{n_0} = \frac{1}{\bar{\kappa}_i^n}\,, \qquad \eta_i^{n_0} = \frac{\bar{\chi}_i^n}{\bar{\kappa}_i^n}\,, \tag{6.85}$$

where

$$\bar{\kappa}_i^n = \kappa(\mathcal{E}_i^n, \rho_i^n), \quad \bar{\chi}_i^n = \chi(\mathcal{E}_i^n, \rho_i^n), \tag{6.86}$$

and $\mu$ is reset locally to $\mu_i^{n_0}$ by using the following generalized form of the consistency condition (6.3):

$$p_i^n = \frac{1}{\psi^{n_0}} \left( \mathcal{E}_i^n + \eta_i^{n_0} \rho^n + \mu_i^{n_0} \right). \tag{6.87}$$

which must hold independently of the updating procedure used to define $p_i^n$. Note that in the above relations we have added a subscript 0 to the superscript $n$ in the notation for the re-initialized quantities $\eta$, $\psi$, $\mu$ at time $t^n$, to underline that these quantities have been reset before performing the evolution step, and to avoid confusion in the description of the algorithm in the following.

Each time step the local values (6.85) give the initial data at time $t^n$ that we use to evolve the transport equations (6.9b), (6.9c) (6.9d) for $\eta$, $\psi$, $\mu$, which we rewrite here for clearness:

$$\frac{\partial}{\partial t}(\eta\rho) + \frac{\partial}{\partial x}(\eta\rho u) = 0, \tag{6.88a}$$

$$\frac{\partial \psi}{\partial t} + u \frac{\partial \psi}{\partial x} = 0, \tag{6.88b}$$

$$\frac{\partial \mu}{\partial t} + u \frac{\partial \mu}{\partial x} = 0. \tag{6.88c}$$

The values of $(\eta\rho)$, $\psi$, $\mu$ that we compute at time $t^{n+1}$ by solving these equations will be then used only in those cells where the pressure is updated through (6.84).

Here the idea is to exploit the following property of the formulation of the Shyue-type model (3.17), when it is solved by a Godunov-type scheme that is exact on isolated contact discontinuities (like the PLM-Roe):

PRESSURE EQUILIBRIUM PRESERVATION PROPERTY
*If for an interface-only problem at time $t^n$ we satisfy in each cell of the computational domain*

$$p^c = p_i^n = \frac{1}{\psi_i^n}(\mathcal{E}_i^n + (\eta\rho)_i^n + \mu_i^n), \tag{6.89}$$

*then, the updating of the pressure through*

$$p_i^{n+1} = \frac{1}{\psi_i^{n+1}}(\mathcal{E}_i^{n+1} + (\eta\rho)_i^{n+1} + \mu_i^{n+1}), \tag{6.90}$$

*where $\psi_i^{n+1}$, $(\eta\rho)_i^{n+1}$, $\mu_i^{n+1}$ come from the solution of the transport equations (6.88), guarantees pressure equilibrium at time $t^{n+1}$, that is $p_i^{n+1} = p^c$, $\forall i$.*

To prove the result above, let us consider the solution of an interface-only problem by means of a Godunov-type scheme that is exact on isolated contact discontinuities. By hypothesis, at the initial time $t^n$ we have $u_i^n = u^c = $ constant, and $p_i^n = p^c = $ constant, $\forall i$. We will assume without loss of generality that $u^c > 0$.

The updating of the density $\rho$ gives:

$$\rho_i^{n+1} = \rho_i^n + \frac{\Delta t}{\Delta x} u^c (\rho_{i-1}^n - \rho_i^n) = \xi \rho_{i-1}^n + (1 - \xi)\rho_i^n, \tag{6.91}$$

where we have defined $\xi \equiv \frac{\Delta t}{\Delta x} u^c$. Similarly, for the momentum $m$ we obtain:

$$m_i^{n+1} = m_i^n + \frac{\Delta t}{\Delta x}(u^c)^2(\rho_{i-1}^n - \rho_i^n) = u^c[\xi \rho_{i-1}^n + (1 - \xi)\rho_i^n]. \tag{6.92}$$

Thus, we derive the velocity as

$$u_i^{n+1} = \frac{m_i^{n+1}}{\rho_i^{n+1}} = u^c ,\tag{6.93}$$

which shows that the method preserves the invariance of $u$. Computing now the updated value of the total energy $E$,

$$E_i^{n+1} = \xi E_{i-1}^n + (1-\xi)\, E_i^n ,\tag{6.94}$$

we find that the internal energy $\mathcal{E}$ is updated as:

$$\mathcal{E}_i^{n+1} = E_i^{n+1} - \frac{1}{2}\frac{(m_i^{n+1})^2}{\rho_i^{n+1}} = \xi\mathcal{E}_{i-1}^n + (1-\xi)\,\mathcal{E}_i^n .\tag{6.95}$$

It is then easy to see that the variables $(\eta\rho)$, $\psi$, and $\mu$ are all updated by the same formula that we have obtained for $\rho$ and $\mathcal{E}$, i.e. $\alpha_i^{n+1} = \xi\alpha_{i-1}^n + (1-\xi)\,\alpha_i^n$, for $\alpha = (\eta\rho), \psi, \mu$. Hence, the updating of the pressure through (6.84) gives:

$$
\begin{aligned}
p^{n+1} &= \frac{1}{\psi_i^{n+1}}(\mathcal{E}_i^{n+1} + (\eta\rho)_i^{n+1} + \mu_i^{n+1}) & (6.96)\\[2mm]
&= \frac{\xi(\mathcal{E}_{i-1}^n + (\eta\rho)_{i-1}^n + \mu_{i-1}^n) + (1-\xi)(\mathcal{E}_i^n + (\eta\rho)_i^n + \mu_i^n)}{\xi\psi_{i-1}^n + (1-\xi)\psi_i^n}\\[2mm]
&= \frac{\xi p^c\psi_{i-1}^n + (1-\xi)p^c\psi_i^n}{\xi\psi_{i-1}^n + (1-\xi)\psi_i^n} = p^c .
\end{aligned}
$$

Therefore, pressure equilibrium is maintained. $\qquad\square$

Note the similarity of (6.96) with the result (6.81) of Section 6.6.1.

The equations (6.88a), (6.88b) express the advection of the thermodynamic derivatives $\kappa(\mathcal{E}, \rho)$ and $\chi(\mathcal{E}, \rho)$ in each local Riemann problem. In an interface-only problem this exactly describes the actual dynamics of the pressure derivatives, since the internal energy $\mathcal{E}$ and the density $\rho$ are advected with the flow. However, in the general case, when also acoustic waves may be present, $\kappa(\mathcal{E}, \rho)$ and $\chi(\mathcal{E}, \rho)$ are no longer simply governed by advection equations. Our approach, based on (6.88a), (6.88b), considers the pressure derivatives frozen across shocks and rarefactions. Despite this approximation, the numerical experimentation performed shows that the method is effective also when acoustic waves are present. See also related discussion in Section 6.9 for possible improvements.

We summarize here the modified algorithm:

ALGORITHM 6.3 (MODIFIED PLM)

(i) Given $q^n$, $p^n$, we compute $\psi^{n_0}$, $(\eta\rho)^{n_0} = \eta^{n_0}\rho^n$ and $\mu^{n_0}$ as in (6.85), (6.86), (6.87). With these initial values at time $t^n$ we solve the system (6.9) and, moreover, the additional advection equation (6.83) by a given Godunov-type method that is exact on isolated contact discontinuities. We thus obtain the updated vector of the conserved variables $q^{n+1}$ and the updated quantities $\psi^{n+1}$, $(\eta\rho)^{n+1}$, $\mu^{n+1}$, $\vartheta^{n+1}$.

(ii) Updating of the pressure:

      ○ If $\vartheta^{n+1} = 0$ or $\vartheta^{n+1} = 1$ (up to a tolerance) then we update the pressure through the original EOS:

$$p^{n+1} = p(\mathcal{E}^{n+1}, \rho^{n+1}) .\tag{6.97}$$

○ If instead $0 < \vartheta^{n+1} < 1$ then we update the pressure through (6.84):

$$p^{n+1} = p^{\mathrm{L}}(\mathcal{E}^{n+1}, (\eta\rho)^{n+1}, \psi^{n+1}, \mu^{n+1}) = \frac{1}{\psi^{n+1}} \left( \mathcal{E}^{n+1} + (\eta\rho)^{n+1} + \mu^{n+1} \right). \qquad (6.98)$$

Differently from Algorithm 6.1, note that in this case we need the updated values of $\eta\rho$, $\psi$, $\mu$ to be used in (6.98), though these quantities are re-initialized every time step.

### 6.8.1  Modified PLM-Roe

In the evolution step the modified version of the PLM-Roe uses the same formulation of the original method, that is the Roe linearization $\hat{A}^{\mathrm{L}}$ defined in (6.33c), (6.35), and the corresponding eigenstructure. However, differently from the standard scheme, we now employ the full structure of the matrix $\hat{R}$ of the eigenvectors (see (6.41)), since we need the updated values of $\eta\rho$, $\psi$, $\mu$. Moreover, we add the equation (6.83) for the tracer, which is linearized as $\partial\vartheta/\partial t + \hat{u}\,\partial\vartheta/\partial x = 0$, where $\hat{u}$ is the Roe average velocity defined in (6.38a).

### 6.8.2  Numerical Results

We now perform the Experiments 6.6 and 6.7 of Section 6.7.1 by using the modified PLM-Roe. As we can observe from Figures 6.11 and 6.12, the scheme is able to preserve the invariance of $u$, $p$ across contact discontinuities.
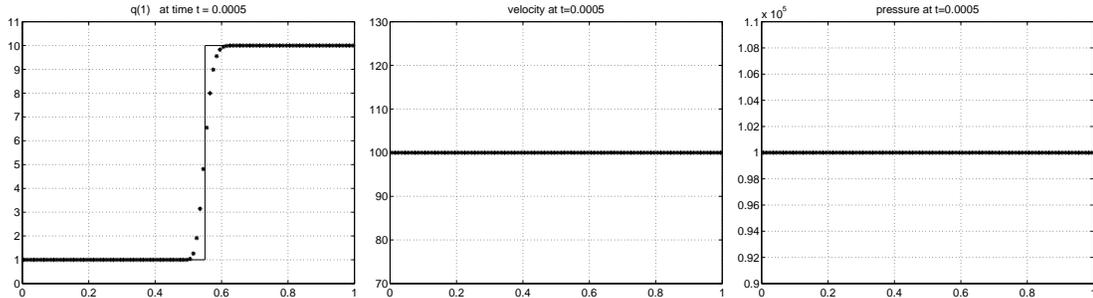


Figure 6.11: Experiment 6.6. Density, velocity, and pressure at $t = 0.5 \times 10^{-3}\,s$. Number of grid cells $= 100$. CFL $= 0.9$. Results obtained by the modified PLM-Roe.
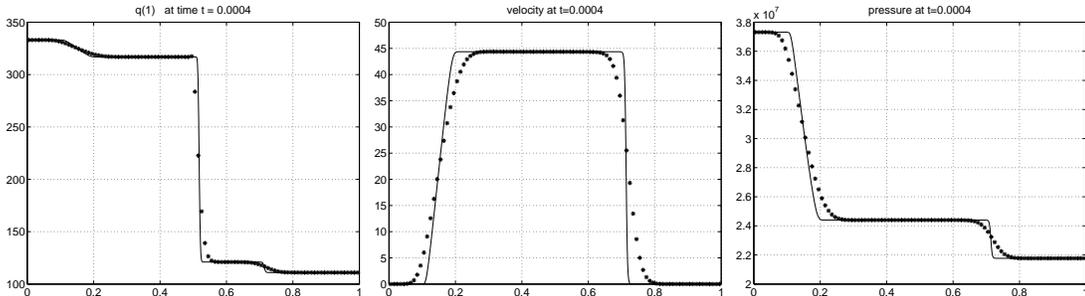


Figure 6.12: Experiment 6.7. Density, velocity, and pressure at $t = 0.4 \times 10^{-3}\,s$. Number of grid cells $= 100$; CFL $= 0.9$. Results obtained by the modified PLM-Roe. Solid line: solution computed with the same method on a grid of 2000 cells.

### 6.9    Multifluid Pressure Linearization Method

We now describe how our Pressure Linearization Method can be extended to genuine multifluid flows. Let us consider two pure fluids $k = 1, 2$ separated by some interface. We will denote the corresponding quantities with the subscripts 1 and 2. In the evolution step we employ again the formulation (6.9) of the PLM. As in the modified PLM, we then add an advection equation for a quantity that locates the material interface, which in this context is chosen to be the volume fraction of one component. Considering here the volume fraction $\vartheta_1$ of fluid 1, we add:

$$\frac{\partial \vartheta_1}{\partial t} + u \frac{\partial \vartheta_1}{\partial x} = 0 \,. \tag{6.99}$$

Given $\vartheta_1$, we can then compute $\vartheta_2 = 1 - \vartheta_1$.

Far from material interfaces we still update the pressure by using the equation of state of the species that occupies the considered region, while around contact interfaces we update the pressure by using the linear EOS (6.84). Again, we would like to exploit the pressure equilibrium preservation property of the Shyue-type multifluid model (3.17) discussed in Section 6.8.

Let us now describe how we can define in the multifluid case the quantities $(\eta\rho)_i^{no}$, $\psi_i^{no}$, $\mu_i^{no}$ that represent the initial data at time $t^n$ of the equations (6.88).

We need to introduce a mixture model for the region where the material interface is numerically spread, which should recover the single-component case in the regions where a single fluid is present. Following a standard approach, the mixture density $\rho$ and the mixture energy $\mathcal{E}$ are defined by the volume averages

$$\rho = \sum_{k=1}^{2} \vartheta_k \rho_k \qquad \text{and} \qquad \mathcal{E} = \sum_{k=1}^{2} \vartheta_k \mathcal{E}_k \,. \tag{6.100}$$

For coherence with the equations (6.88a), (6.88b), we then define $(\rho\eta)$ and $\psi$ for the mixture as follows:

$$(\eta\rho) = \sum_{k=1}^{2} \eta_k (\vartheta\rho)_k \,, \qquad \psi = \sum_{k=1}^{2} \psi_k \vartheta_k \,, \tag{6.101a}$$

with

$$\eta_k = \frac{\chi_k}{\kappa_k} \qquad \psi_k = \frac{1}{\kappa_k} \,, \quad k = 1, 2 \,, \tag{6.101b}$$

where

$$\kappa_k = \kappa_k(\mathcal{E}_k, \rho_k) \qquad \text{and} \qquad \chi_k = \chi_k(\mathcal{E}_k, \rho_k) \,, \quad k = 1, 2 \,, \tag{6.101c}$$

are the thermodynamic derivatives corresponding to each component. The relations above require the knowledge of the partial densities $(\vartheta\rho)_k$ and the individual densities and energies $\rho_k$, $\mathcal{E}_k$. Therefore, we need additional relations to complete the description of the mixture. Our approach consists in augmenting the formulation with:

(1) Conservation equation for the partial density $(\vartheta\rho)_1$:

$$\frac{\partial}{\partial t} ((\vartheta\rho)_1) + \frac{\partial}{\partial x} ((\vartheta\rho)_1 u) = 0 \,. \tag{6.102}$$

Through this we obtain the values of $(\vartheta\rho)_1$ and $(\vartheta\rho)_2 = \rho - (\vartheta\rho)_1$ to be used in (6.101a). Moreover, the equation (6.102) allows us to estimate the individual densities of the two fluids as

$$\rho_1 = \frac{(\vartheta\rho)_1}{\vartheta_1} \quad \text{and} \quad \rho_2 = \frac{\rho - (\vartheta\rho)_1}{1 - \vartheta_1} \,. \tag{6.103}$$

The relations above are used for the fluid $k$ only when $\vartheta_k \neq 0$. Practically, in the implementation of the numerical scheme, we use them for $a \leq \vartheta_k < 1$, $a = 0.5$. For $0 \leq \vartheta_k < a$, $\rho_k$ is set equal to the value found in correspondence of $\vartheta_k = 0.5$. Alternatively, a fixed constant value can be assigned (for instance the initial value of $\rho_k$ in the region where $\vartheta_k = 1$ in a shock-tube problem).

(2) *Isobaric condition*:

$$p_1 = p_2 = p \,. \tag{6.104}$$

Having obtained the densities $\rho_k$, $k = 1, 2$ as in (6.103), this isobaric condition allows us to determine the individual energies:

$$\mathcal{E}_k = \mathcal{E}_k(p, \rho_k)\,, \quad k = 1, 2 \,. \tag{6.105}$$

Hence, the individual thermodynamic derivatives in (6.101c) are evaluated as

$$\kappa_k = \kappa_k(\mathcal{E}_k(p, \rho_k), \rho_k) \quad \text{and} \quad \chi_k = \chi_k(\mathcal{E}_k(p, \rho_k), \rho_k)\,, \quad k = 1, 2 \,. \tag{6.106}$$

Though these relations are valid in general for $\vartheta_k \in [0, 1]$, in the implementation of the method if $\vartheta_1 = 0$ or 1 (pure fluid) we use (6.101c) for convenience.

At each initial time $t^n$ we know the cell value of the pressure $p_i^n$, so we can define $(\eta \rho)^{n_0} = \eta^{n_0} \rho^n$ and $\psi^{n_0}$ through (6.101), (6.106). We then determine $\mu^{n_0}$ through the generalized consistency condition:

$$p_i^n = \frac{1}{\psi^{n_0}} \left( \mathcal{E}_i^n + (\eta \rho)_i^{n_0} + \mu_i^{n_0} \right) \,. \tag{6.107}$$

Let us write here the complete system of equations that is used in the evolution step of the method:

$$\frac{\partial q}{\partial t} + \frac{\partial}{\partial x} f^{\mathrm{L}}(q, \psi, \eta \rho, \mu) = 0 \,, \tag{6.108a}$$

$$\frac{\partial}{\partial t}(\eta \rho) + \frac{\partial}{\partial x}(\eta \rho u) = 0 \,, \tag{6.108b}$$

$$\frac{\partial \psi}{\partial t} + u \frac{\partial \psi}{\partial x} = 0 \,, \tag{6.108c}$$

$$\frac{\partial \mu}{\partial t} + u \frac{\partial \mu}{\partial x} = 0 \,, \tag{6.108d}$$

$$\frac{\partial \vartheta_1}{\partial t} + u \frac{\partial \vartheta_1}{\partial x} = 0 \,, \tag{6.108e}$$

$$\frac{\partial}{\partial t}((\vartheta \rho)_1) + \frac{\partial}{\partial x}((\vartheta \rho)_1 u) = 0 \,, \tag{6.108f}$$

where

$$q = \begin{bmatrix} \rho \\ m \\ E \end{bmatrix}\,, \qquad f^{\mathrm{L}}(q, \psi, \eta \rho, \mu) = \begin{bmatrix} m \\ \dfrac{m^2}{\rho} + p^{\mathrm{L}} \\ \dfrac{m}{\rho}(E + p^{\mathrm{L}}) \end{bmatrix}\,, \tag{6.108g}$$

and $p^{\text{L}}$ is expressed again as

$$p^{\text{L}} = p^{\text{L}}(\mathcal{E}, \psi, \eta\rho, \mu) = \frac{1}{\psi}(\mathcal{E} + \eta\rho + \mu). \tag{6.108h}$$

The speed of sound is given by the same formula as in the original PLM:

$$c^{\text{L}} = \sqrt{\frac{h^{\text{L}}}{\psi} + \frac{\eta}{\psi}}, \tag{6.109}$$

where now $\psi$ and $\eta = \frac{(\eta\rho)}{\rho}$ are defined by (6.101a).

To summarize, the algorithm of the multifluid Pressure Linearization Method is:

ALGORITHM 6.4 (MULTIFLUID PLM)

$(i)$ Given $q^n$, $p^n$, $\vartheta_1^n$, $(\vartheta\rho)_1^n$, we compute $\psi^{n_0}$, $(\eta\rho)^{n_0} = \eta^{n_0}\rho^n$ and $\mu^{n_0}$ as in (6.101), (6.106), (6.107). With these initial values at time $t^n$, we solve the system (6.108) by a Godunov-type method that is exact on isolated contact discontinuities. We thus obtain the updated vector of the conserved variables $q^{n+1}$ and the updated quantities $\psi^{n+1}$, $(\eta\rho)^{n+1}$, $\mu^{n+1}$, $\vartheta_1^{n+1}$, $(\vartheta\rho)_1^{n+1}$.

$(ii)$ Updating of the pressure:

○ If $\vartheta_1^{n+1} = 0$ or $\vartheta_1^{n+1} = 1$ (up to a tolerance $\epsilon$), then we update the pressure through the EOS of the fluid whose volume fraction is 1:

$$p^{n+1} = p_k(\mathcal{E}^{n+1}, \rho^{n+1}), \quad k = \begin{cases} 1 & \text{if } \vartheta_2^{n+1} = 1 - \vartheta_1^{n+1} = 0, \\ 2 & \text{if } \vartheta_1^{n+1} = 0. \end{cases} \tag{6.110}$$

○ If instead $0 < \vartheta_1^{n+1} < 1$, then we update the pressure through (6.108h):

$$p^{n+1} = p^{\text{L}}(\mathcal{E}^{n+1}, (\eta\rho)^{n+1}, \psi^{n+1}, \mu^{n+1}) = \frac{1}{\psi^{n+1}}(\mathcal{E}^{n+1} + (\eta\rho)^{n+1} + \mu^{n+1}). \tag{6.111}$$

In our implementation we have used a tolerance $\epsilon = 10^{-7}$.

As already noted for the modified PLM, the employment of the transport equations (6.108b), (6.108c) amounts to simply advect the pressure derivatives. This models the exact physical evolution of $\kappa$ and $\chi$ just for interface-only problems, in which both the density $\rho$ and the internal energy per unit volume $\mathcal{E}$ are convected by the flow. However, the thermodynamic derivatives in the more general case vary through the acoustic waves, and their dynamics is not simply governed by advection equations. As a first version of the method we let this approximation, which we expect nonetheless to produce reliable results at least when the thermodynamic derivatives have not large variations with $\mathcal{E}$ and $\rho$, as it is often the case in many practical problems. Let us mention that in [177] an analogous approximation is considered in problems involving fluids governed by the Cochran–Chan EOS. Possible improvements of the method are under study. One possibility is to replace the advection equations by more complex equations that better approximate the true dynamics of the pressure derivatives in the general case, and that reduce to advection equations in interface-only problems. An approach of this type has been specialized by Shyue to fluids governed by the van der Waals [183] and by the Mie–Grüneisen equations of state [184].

### 6.9.1   Multifluid PLM-Roe

The fully quasi-linear form of the augmented PLM system (6.108) is

$$\frac{\partial z_a}{\partial t} + A_a^{\text{L}}(z_a) \frac{\partial z_a}{\partial x} = 0, \tag{6.112a}$$

where

$$z_a = [\rho, m, E, \eta\rho, \psi, \mu, \vartheta_1, (\vartheta\rho)_1]^{\mathrm{T}} ,  \qquad (6.112b)$$

and the matrix $A_a^{\mathrm{L}}(z_a)$ is given by:

$$A_a^{\mathrm{L}}(z_a) = \begin{bmatrix}
0 & 1 & 0 & 0 & 0 & 0 & 0 & 0 \\
\dfrac{1}{\psi}\dfrac{u^2}{2} - u^2 & \left(2-\dfrac{1}{\psi}\right)u & \dfrac{1}{\psi} & \dfrac{1}{\psi} & -\dfrac{\zeta}{\psi^2} & \dfrac{1}{\psi} & 0 & 0 \\
u\left(\dfrac{1}{\psi}\dfrac{u^2}{2}-H\right) & H-\dfrac{1}{\psi}u^2 & \left(1+\dfrac{1}{\psi}\right)u & \dfrac{1}{\psi}u & -\dfrac{\zeta}{\psi^2}u & \dfrac{1}{\psi}u & 0 & 0 \\
-\eta u & \eta & 0 & u & 0 & 0 & 0 & 0 \\
0 & 0 & 0 & 0 & u & 0 & 0 & 0 \\
0 & 0 & 0 & 0 & 0 & u & 0 & 0 \\
0 & 0 & 0 & 0 & 0 & 0 & u & 0 \\
-\phi u & \phi & 0 & 0 & 0 & 0 & 0 & u
\end{bmatrix}, \qquad (6.112c)$$

where $\zeta = \mathcal{E} + \eta\rho + \mu$, and $\phi = \frac{(\vartheta\rho)_1}{\rho}$. Following an analogous procedure as in Section 6.4 for the PLM-Roe, we define the Roe linearization $\hat{A}_a^{\mathrm{L}}$ as

$$\hat{A}_a^{\mathrm{L}} = A_a^{\mathrm{L}}(\hat{u}, \hat{H}, \hat{\eta}, \hat{\psi}, \hat{\zeta}, \hat{\phi}) , \qquad (6.113)$$

where the average quantities $(\hat{u}, \hat{H}, \hat{\eta}, \hat{\psi}, \hat{\zeta})$ are obtained as in (6.38) by imposing the conservation condition for the first four conservative equations of the system, and the average $\hat{\phi}$ is then determined as

$$\hat{\phi} = \frac{\sqrt{\rho_\ell}\,\phi_\ell + \sqrt{\rho_r}\,\phi_r}{\sqrt{\rho_\ell}+\sqrt{\rho_r}} , \qquad (6.114)$$

through the conservation condition for the equation for $(\vartheta\rho)_1$ . The eigenvalues of $\hat{A}_a^{\mathrm{L}}$ are

$$\hat{\lambda}^1 = \hat{u} - \hat{c}, \qquad \hat{\lambda}^2 = \hat{\lambda}^3 = \hat{\lambda}^4 = \hat{\lambda}^5 = \hat{\lambda}^6 = \hat{\lambda}^7 = \hat{u} , \qquad \hat{\lambda}^8 = \hat{u} + \hat{c}, \qquad (6.115)$$

and the matrix of the corresponding right eigenvectors takes the form:

$$\hat{R} = \left[\hat{r}^1, \cdots, \hat{r}^8\right] = \begin{bmatrix}
1 & 1 & 0 & 0 & 0 & 0 & 0 & 1 \\
\hat{u}-\hat{c} & \hat{u} & 0 & 0 & 0 & 0 & 0 & \hat{u}+\hat{c} \\
\hat{H}-\hat{u}\hat{c} & \hat{H}-\hat{\psi}\hat{c}^2 & -1 & \frac{\hat{\zeta}}{\hat{\psi}} & -1 & 0 & 0 & \hat{H}+\hat{u}\hat{c} \\
\hat{\eta} & \hat{\eta} & 1 & 0 & 0 & 0 & 0 & \hat{\eta} \\
0 & 0 & 0 & 1 & 0 & 0 & 0 & 0 \\
0 & 0 & 0 & 0 & 1 & 0 & 0 & 0 \\
0 & 0 & 0 & 0 & 0 & 1 & 0 & 0 \\
\hat{\phi} & \hat{\phi} & 0 & 0 & 0 & 0 & 1 & \hat{\phi}
\end{bmatrix}. \qquad (6.116)$$

The coefficients $\alpha^p$, $p = 1, \cdots, 8$, of the projection of the jump of $z_{a,r} - z_{a,\ell}$ onto the set of eigenvectors $\hat{r}^p$, i.e. $z_{a,r} - z_{a,\ell} = \sum_{p=1}^{8} \alpha^p \, \hat{r}^p$, are:

$$\alpha^2 = \frac{1}{\hat{\psi}\,\hat{c}^2} \left[ (\hat{H} - \hat{u}^2 + \hat{\eta})\,\Delta z_1 + \hat{u}\,\Delta z_2 - \Delta z_3 - \Delta z_4 + \frac{\hat{\zeta}}{\hat{\psi}}\,\Delta z_5 - \Delta z_6 \right], \qquad (6.117\text{a})$$

$$\alpha^8 = \frac{1}{2\,\hat{c}} \left[ \Delta z_2 + (\hat{c} - \hat{u})\,\Delta z_1 - \hat{c}\,\alpha^2 \right], \qquad (6.117\text{b})$$

$$\alpha^1 = \Delta z_1 - \alpha^2 - \alpha^8, \qquad (6.117\text{c})$$

$$\alpha^3 = -\hat{\eta}\,\Delta z_1 + \Delta z_4, \qquad (6.117\text{d})$$

$$\alpha^4 = \Delta z_5, \qquad (6.117\text{e})$$

$$\alpha^5 = \Delta z_6, \qquad (6.117\text{f})$$

$$\alpha^6 = \Delta z_7, \qquad (6.117\text{g})$$

$$\alpha^7 = -\hat{\phi}\,\Delta z_1 + \Delta z_8, \qquad (6.117\text{h})$$

where the average sound speed $\hat{c}$ has the same expression as in (6.39), and $z_p$ denotes the $p$-th component of $z_a$, $p = 1, \cdots, 8$. The coefficients above can also be expressed as:

$$\alpha^1 = \frac{\Delta p - \hat{\rho}\,\hat{c}\,\Delta u}{2\,\hat{c}^2}, \qquad (6.118\text{a})$$

$$\alpha^2 = \Delta\rho - \frac{\Delta p}{\hat{c}^2}, \qquad (6.118\text{b})$$

$$\alpha^3 = \hat{\rho}\,\Delta\eta, \qquad (6.118\text{c})$$

$$\alpha^4 = \Delta\psi, \qquad (6.118\text{d})$$

$$\alpha^5 = \Delta\mu, \qquad (6.118\text{e})$$

$$\alpha^6 = \Delta\vartheta_1, \qquad (6.118\text{f})$$

$$\alpha^7 = \hat{\rho}\,\Delta(\vartheta\rho)_1, \qquad (6.118\text{g})$$

$$\alpha^8 = \frac{\Delta p + \hat{\rho}\,\hat{c}\,\Delta u}{2\,\hat{c}^2}, \qquad (6.118\text{h})$$

where $\hat{\rho} \equiv \sqrt{\rho_\ell}\,\sqrt{\rho_r}$.

The structure of the solver consists of the eight waves and speeds

$$\mathcal{W}^p = \alpha^p \hat{r}^p, \qquad s^p = \hat{\lambda}^p, \quad p = 1, \ldots, 8. \qquad (6.119)$$

As in the PLM-Roe, we can then sum together waves propagating at the same speed $\hat{u}$.

*Modification of the Average Advection Velocity*

Difficulties may arise with the structure above of the multifluid solver in relation to the employment of the nonconservative advection equations for $\psi$, $\mu$, $\vartheta_1$, linearized by using the Roe average $\hat{u}$. In fact,

these quantities do not travel at a correct speed in presence of acoustic waves, and they are not in phase with the conservative variables. Inaccuracies then may appear in the solution, as for instance overshoots in the density. This is particularly evident for example in a Riemann problem for which the initial states have the same velocity $u_\ell = u_r = 0$, but different pressures and densities. Then the Roe average velocity is $\hat{u} = 0$, so that the quantities $\psi$, $\mu$, $\vartheta_1$ remain steady, though in reality a contact wave is starting moving with a nonzero speed.

These difficulties suggested us to linearize the nonconservative advection equations by adopting an average velocity $\tilde{u}$ in general different from $\hat{u}$, which could better approximate the interface speed. We remark that this does not affect the conservation property of the scheme.

In particular, we propose to adopt the following definition, which corresponds to the contact wave velocity computed for the acoustic solver described for instance in [194]:

$$\tilde{u} = \frac{\rho_\ell c_\ell u_\ell + \rho_r c_r u_r}{\rho_\ell c_\ell + \rho_r c_r} - \frac{p_r - p_\ell}{\rho_\ell c_\ell + \rho_r c_r}\,, \tag{6.120}$$

where $c_\ell$, $c_r$ are the sound speeds corresponding to the left and right state, respectively:

$$c_{\ell,r} = \sqrt{\frac{h_{\ell,r}}{\psi_{\ell,r}} + \frac{\eta_{\ell,r}}{\psi_{\ell,r}}}\,. \tag{6.121}$$

Note that for interface-only problems we have $\hat{v} = \hat{u}$. Formula (6.120) in particular gives a nonzero speed when the initial states have the same zero velocity but different pressures, so that the interface speed is modeled more appropriately. An ideal definition of $\tilde{u}$ is still subject of investigation, but the one proposed here improved the results of our numerical experiments.

The form of the waves for this modified solver is still the one given in (6.119), but now the corresponding speeds are

$$s^1 = \hat{u} - \hat{c}\,, \qquad s^2 = s^3 = s^4 = \hat{u}\,, \qquad s^5 = s^6 = s^7 = \tilde{u}\,, \qquad s^8 = \hat{u} + \hat{c}\,. \tag{6.122}$$

Here we can then define a single wave $\sum_{p=2}^{4} \mathcal{W}^p$ corresponding to $\hat{u}$ and a single wave $\sum_{p=5}^{7} \mathcal{W}^p$ for $\tilde{u}$, thus reducing the total number of waves to four.

### 6.9.2  Note on Two-Dimensional Problems

In two-dimensional interface problems (*slip line* problems) strong pressure oscillations can be generated even by schemes that preserve pressure equilibrium in the one-dimensional case.

Approaches to overcome this difficulty have been suggested for instance in [178, 183]. The idea is to add a transport equation for the tangential kinetic energy $\mathcal{K}^t = \frac{1}{2}\rho v^2$ with the form:

$$\frac{\partial \mathcal{K}^t}{\partial t} + \frac{\partial}{\partial x}\left(\mathcal{K}^t u\right) = 0\,. \tag{6.123}$$

The value of $\mathcal{K}^t$ computed through this equation is used to update the internal energy that then updates the pressure as

$$\mathcal{E} = E - \frac{1}{2}\frac{m^2}{\rho} - \mathcal{K}^t\,. \tag{6.124}$$

In this connection we refer to the brief discussion in Section 6.6.2.

Here we didn't implement a modification of this type, since in problems where there are not strong shear flows moving along the interfaces we can still obtain results with no spurious pressure oscillations without using this correction.

### 6.10   Numerical Experiments

We consider a selection of numerical tests taken from the literature and present results obtained with the multifluid PLM approach.

Second order corrections have been applied for these tests limiting the waves componentwise by means of the minmod limiter function (4.27).

#### 6.10.1   One-Dimensional Tests

EXPERIMENT 6.8. *Gas-Liquid Shock Tube.*

We consider a shock tube problem originally proposed in [183], and tested also in [5]. It involves a liquid phase modeled by the stiffened gas EOS on the left of the domain, and a van der Waals gas on the right. The parameters of the stiffened gas EOS (6.65) are here $\gamma = 4.4$ and $\pi = 6 \times 10^8\, Pa$, while the parameters of the van der Waals law (6.66) are set as: $\frac{R}{c_v} = \gamma - 1$, $\gamma = 1.4$, $a = 5\, m^6 Pa/kg^2$, and $b = 10^{-3}\, m^3/kg$.

The computational domain is the interval $[0, 1]\, m$ and the initial diaphragm is located at $x = 0.7\, m$. The initial data in terms of the density, velocity, and pressure are reported in Table 6.6.

The solution of this problem consists of a left-going rarefaction, a right-going contact discontinuity, and a shock wave. Figure 6.13 shows the results obtained with a grid of 300 cells. These results are similar to those reported in [183, 5].

Table 6.6: Initial data for Experiment 6.8.

| state | EOS | $\rho\ [kg\,m^{-3}]$ | $u\ [m\,s^{-1}]$ | $p\ [Pa]$ |
|---|---|---|---|---|
| left | stiffened gas | $10^3$ | 0 | $10^9$ |
| right | van der Waals | 50 | 0 | $10^5$ |

EXPERIMENT 6.9. *Interface-Shock Interaction.*

We consider a problem, again taken from [183], which consists of a left-going Mach 1.422 shock wave interacting with a stationary material interface. The computational domain is the interval $[0, 1]$ $m$, and the shock wave is initially located at $x = 0.5\, m$ in a region of pure stiffened gas that extends in the interval $(0.4, 1]\, m$. At $x = 0.4\, m$ there is initially an interface between the stiffened gas and a van der Waals gas. The parameters used for the equations of state of the two materials are the same of Experiment 6.8. The initial conditions for the problem are described in Table 6.7.

After the interaction, the structure of the solution consists of a transmitted shock wave, an interface, and a reflected rarefaction wave. Results with 500 grid cells are shown in Figure 6.14. Again there is good agreement with the results in [183, 5].

Table 6.7: Initial data for Experiment 6.9.

| domain | state | EOS | $\rho\ [kg\,m^{-3}]$ | $u\ [m\,s^{-1}]$ | $p\ [Pa]$ |
|---|---|---|---|---|---|
| $0 < x < 0.4$ | left | Van der Waals | 1.2 | 0 | $10^5$ |
| $0.4 < x < 0.5$ | middle (pre-shock) | Stiffened Gas | $10^3$ | 0 | $10^5$ |
| $0.5 < x < 1.$ | right (post-shock) | Stiffened Gas | $1.23 \times 10^3$ | $-432.69$ | $10^9$ |
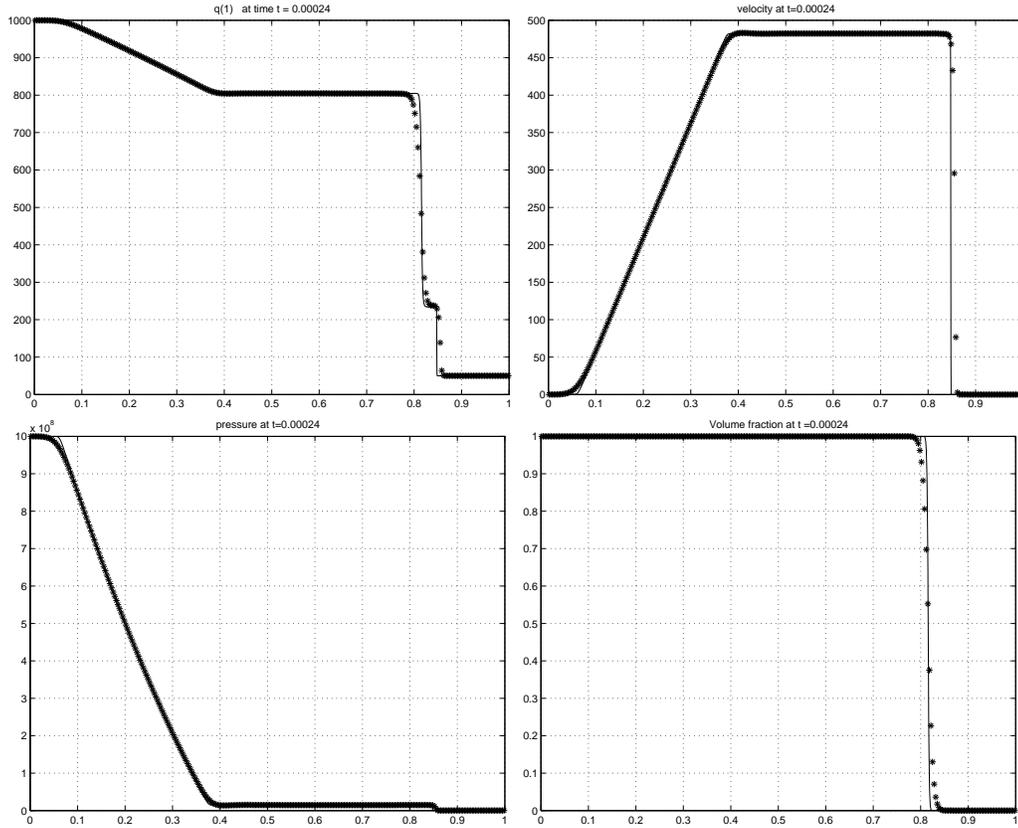
Figure 6.13: Experiment 6.8. Density, velocity, pressure and volume fraction at time $t = 0.24 \times 10^{-3}\,s$. Number of grid cells = 300. CFL = 0.5. Solid line: Reference solution computed with 3000 grid cells.

*Mie–Grüneisen EOS*

The Mie–Grüneisen equation of state can be written as:

$$p(\mathcal{E}, \rho) = \Gamma(\rho)(\mathcal{E} + \rho \varepsilon_{\mathrm{ref}}(\rho)) + p_{\mathrm{ref}}(\rho)\,, \qquad (6.125)$$

where $\Gamma(\rho)$ is the so-called Grüneisen coefficient and $p_{\mathrm{ref}}(\rho)$, $\varepsilon_{\mathrm{ref}}(\rho)$ express a reference pressure and specific internal energy, respectively.

Many pressure laws can be written in this form, as for instance the stiffened gas EOS (6.65), with $\Gamma = \gamma - 1$, $\varepsilon_{\mathrm{ref}} = 0$ and $p_{\mathrm{ref}} = -\gamma\pi$.

Here we consider two particular equations of state with the form (6.125), which have been extensively used to model gaseous or solid explosives and solid metals under high pressure: the Jones–Wilkins–Lee (JWL) EOS [112], and the Cochran–Chan EOS [35]. Below we write the expression of $\Gamma(\rho)$, $\varepsilon_{\mathrm{ref}}(\rho)$, $p_{\mathrm{ref}}(\rho)$ for these two examples and we report the values of the parameters used in the numerical tests presented in the following.
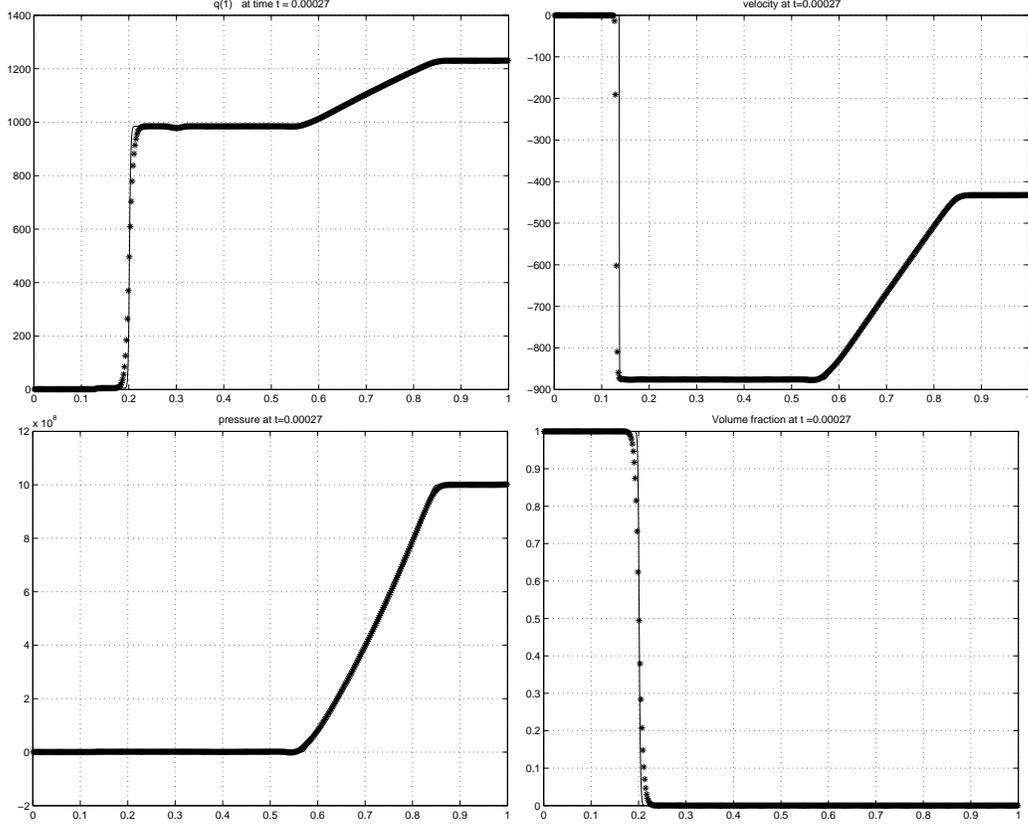
Figure 6.14: Experiment 6.9. Density, velocity, pressure and volume fraction at time $t = 0.27 \times 10^{-3} \, s$. Number of grid cells = 500. CFL = 0.5. Solid line: Reference solution computed with 3000 grid cells.

*Jones–Wilkins–Lee Equation of State*

$$\Gamma(\rho) = \Gamma_0 \, , \qquad\qquad (6.126a)$$

$$\varepsilon_{\mathrm{ref}}(\rho) = \frac{a}{r_1 \rho_0} e^{-r_1 \frac{\rho_0}{\rho}} + \frac{b}{r_2 \rho_0} e^{-r_2 \frac{\rho_0}{\rho}} - \varepsilon_0 \qquad\qquad (6.126b)$$

$$p_{\mathrm{ref}}(\rho) = a e^{-r_1 \frac{\rho_0}{\rho}} + b e^{-r_2 \frac{\rho_0}{\rho}} \, . \qquad\qquad (6.126c)$$

*Cochran–Chan Equation of State*

$$\Gamma(\rho) = \Gamma_0 \, , \qquad\qquad (6.127a)$$

$$\varepsilon_{\mathrm{ref}}(\rho) = -\frac{a}{(1 - w_1)\rho_0} \left[ \left( \frac{\rho_0}{\rho} \right)^{1-w_1} - 1 \right] + \frac{b}{(1 - w_2)\rho_0} \left[ \left( \frac{\rho_0}{\rho} \right)^{1-w_2} - 1 \right] - c_v T_0 \qquad\qquad (6.127b)$$

$$p_{\mathrm{ref}}(\rho) = a \left( \frac{\rho_0}{\rho} \right)^{-w_1} - b \left( \frac{\rho_0}{\rho} \right)^{-w_2} \, . \qquad\qquad (6.127c)$$

Table 6.8: Material properties for the JWL equation of state modeling explosive.

| Parameter | Value (Explosive) | Units |
|-----------|-------------------|-------|
| $\rho_0$ | 1840 | $[kg/m^3]$ |
| $\Gamma_0$ | 0.25 | |
| $a$ | $854.5 \times 10^9$ | $[Pa]$ |
| $b$ | $20.5 \times 10^9$ | $[Pa]$ |
| $r_1$ | 4.6 | |
| $r_2$ | 1.35 | |
| $\varepsilon_0$ | 0 | $[J/kg]$ |

Table 6.9: Material properties for the Cochran–Chan EOS modeling copper and explosive.

| Parameter | Copper | Explosive | Units |
|-----------|--------|-----------|-------|
| $\rho_0$ | 8900 | 1840 | $[kg/m^3]$ |
| $\Gamma_0$ | 2 | 0.93 | |
| $a$ | $1.4567 \times 10^{11}$ | $1.287 \times 10^{10}$ | $[Pa]$ |
| $b$ | $1.4775 \times 10^{11}$ | $1.342 \times 10^{10}$ | $[Pa]$ |
| $w_1$ | 2.994 | 1.994 | |
| $w_2$ | 4.1 | 3.1 | |
| $c_v$ | 393 | 1087 | $[J/(kg\,K)]$ |
| $T_0$ | 300 | 300 | $[K]$ |

EXPERIMENT 6.10. *Impact Problem.*

We solve a problem originally proposed in [177], consisting of a copper plate impacting under atmospheric conditions on a solid explosive considered as an inert material. The copper (on the left) has an initial velocity of 1500 $m/s$, while the explosive (on the right) is at rest.

The two materials are both modeled by the Cochran–Chan EOS (6.127), but with different values of the material-dependent parameters, which we report in Table 6.9. In Table 6.10 we summarize the initial conditions of the experiment. The computational domain is the interval $[0,1]$ $m$, and the initial interface is at $x = 0.5$ $m$.

The exact solution of this problem consists of two shocks moving in opposite directions, and a material interface in between. The numerical solution obtained with our method on a grid of 100 cells is displayed in Figure 6.15. We can notice that no spurious pressure oscillations appear at the material interface, and moreover, by comparison with the exact solution shown in [177], we observe that the waves move at the correct speed.

Table 6.10: Initial data for Experiment 6.10.

| state | EOS | $\rho\ [kg\,m^{-3}]$ | $u\ [m\,s^{-1}]$ | $p\ [Pa]$ |
|-------|-----|----------------------|-------------------|-----------|
| left | Cochran–Chan (copper) | $8.9 \times 10^3$ | $1.5 \times 10^3$ | $10^5$ |
| right | Cochran–Chan (explosive) | $1.84 \times 10^3$ | 0.0 | $10^5$ |
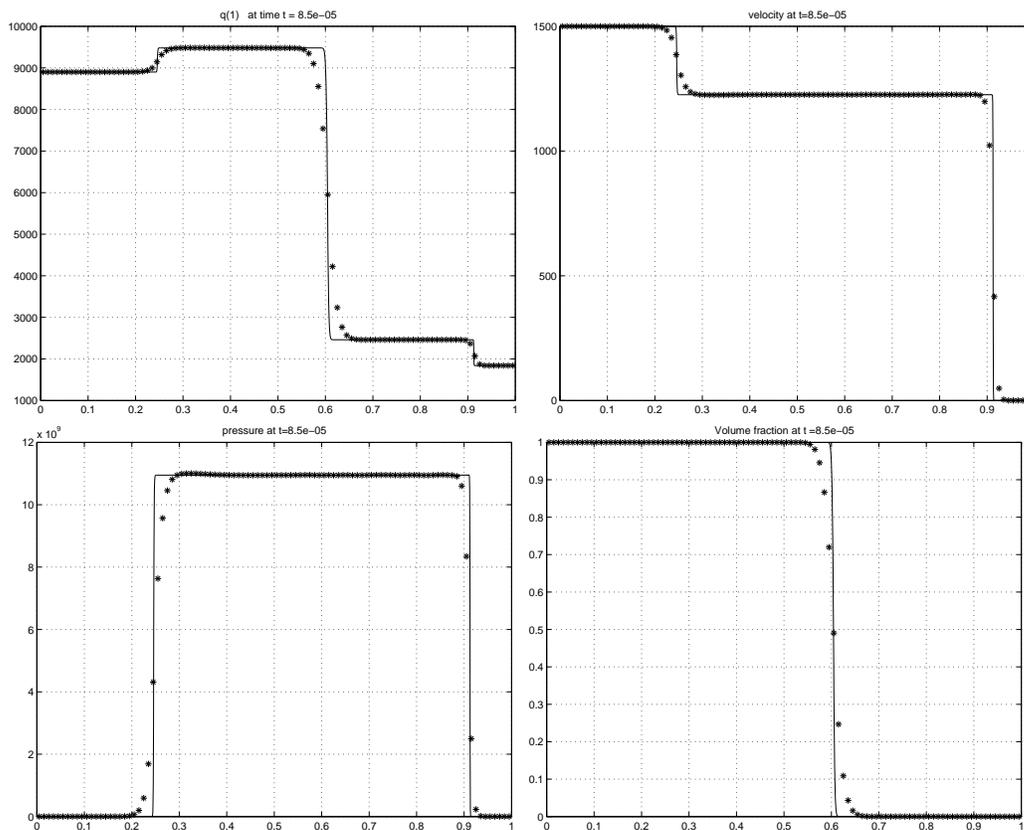
Figure 6.15: Experiment 6.10. Density, velocity, pressure and volume fraction at time $t = 0.85 \times 10^{-6}\, s$. Number of grid cells = 100. CFL = 0.5. Solid line: Reference solution computed with 2000 grid cells.

EXPERIMENT 6.11.

We consider another example taken from [177], involving the interaction of gaseous detonation products with a copper plate. Copper is modeled by the Cochran–Chan equation of state, as in the previous example, while the detonation products are governed by the JWL EOS (6.126) with the parameters reported in Table 6.8. The domain is again $[0, 1]\, m$ with an initial interface located at $x = 0.5\, m$. The initial conditions in terms of the density, velocity, pressure are given in Table 6.11.

Table 6.11: Initial data for Experiment 6.11.

| state | EOS | $\rho\ [kg\,m^{-3}]$ | $u\ [m\,s^{-1}]$ | $p\ [Pa]$ |
|-------|-----|----------------------|------------------|-----------|
| left | JWL (detonation products) | $2.48537 \times 10^3$ | 0.0 | $3.7 \times 10^{10}$ |
| right | Cochran–Chan (copper) | $8.9 \times 10^3$ | 0.0 | $10^5$ |

The solution of this problem consists of a left-going rarefaction, an interface, and a right-going shock. Results obtained with 100 grid cells are shown in Figure 6.16. Good agreement can be observed with the results reported in [177, 184].
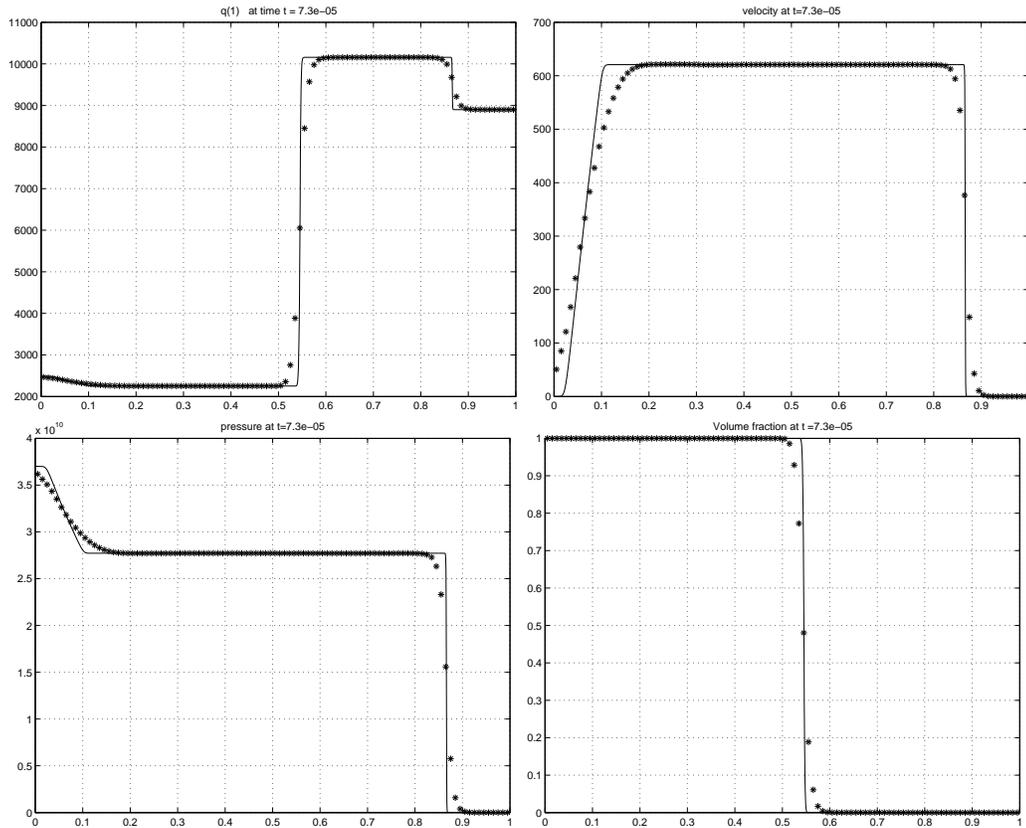
Figure 6.16: Experiment 6.11. Density, velocity, pressure and volume fraction at time $t = 0.73 \times 10^{-6} \, s$. Number of grid cells $= 100$. CFL $= 0.5$. Solid line: Reference solution computed with 2000 grid cells.

### 6.10.2  Two-Dimensional Test

We perform a test with the two-dimensional version of our multifluid Pressure Linearization Method. We use the wave-propagation formulation described in 4.3 of Chapter 4, including transverse fluctuations terms and high-resolution corrections (componentwise minmod limiter).

EXPERIMENT 6.12. *Shock-Bubble Interaction*

We simulate the interaction of a shock wave with a gas bubble. This is a classical problem in the literature, which has been extensively studied both experimentally [73, 87] and numerically, e.g. [165, 74, 183]. It is also of practical importance in many applications, as for instance the study of shock-induced enhancement of mixing [137].

Following the work of Shyue [183], here we consider a two-dimensional version of the previous Experiment 6.9. A left-going Mach 1.422 planar shock wave traveling initially in a liquid, modeled by the stiffened gas EOS, interacts with a van der Waals gas bubble. The computational domain is the rectangle $[0, 1.2] \times [-0.5, 0.5] \, m^2$, and the shock wave is initially located at $x_s = 0.95 \, m$. The bubble initially has center in $(x_0, y_0) = (0.7 \, m, 0)$ and it has radius $r = 0.2 \, m$. The parameters used for the equations of state of the two materials are the same of Experiment 6.9. On the upper and lower boundary we impose reflecting conditions, while on the left and right side we use zeroth-order extrapolation. Figure 6.17 and Table 6.12 describe the initial conditions of the problem.

Results obtained with a $240 \times 200$ mesh and CFL $= 0.9$ are displayed in Figures 6.18 and 6.19. In Figure 6.18 the solution for the density (left) and the pressure (middle) is illustrated by showing the
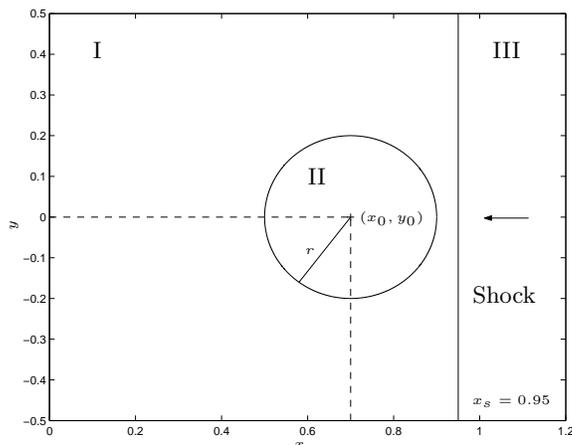
Figure 6.17: Experiment 6.12. Shock-bubble interaction.

Table 6.12: Initial data for Experiment 6.12.

| domain | EOS | $\rho \ [kg \, m^{-3}]$ | $u \ [m \, s^{-1}]$ | $p \ [Pa]$ |
|--------|-----|------------------------|---------------------|------------|
| I | Stiffened Gas (pre-shock) | $10^3$ | 0 | $10^5$ |
| II | Van der Waals (Bubble) | 1.2 | 0 | $10^5$ |
| III | Stiffened Gas (post-shock) | $1.23 \times 10^3$ | $-432.69$ | $10^9$ |

gradient of these quantities. For the density, this corresponds to the Schlieren visualization technique used in physical experiments. In the same figure we also show (on the left) the volumetric fraction of the gas component together with the velocity field. In Figure 6.19 cross-sectional plots of the solution at $y = 0$ are reported. Comparing our results with the work of [183, 5] we find very good agreement.

### 6.10.3   Conclusions

The numerical experimentation demonstrates the efficiency of our method, and in particular its property of guaranteeing pressure equilibrium at material interfaces.

   The main advantage of our approach with respect to some of the existing work on multifluid flows, e.g. Saurel and Abgrall [178], Abgrall and Karni [4], Shyue [182, 183, 184], is its general and flexible structure that allows the application of the method to arbitrary equations of state. The method of Allaire et al. [5] can also be applied to general pressure laws. However, for general equations of state it requires the solution by some type of iterative method of a nonlinear algebraic equation, expressing an isobaric condition between the two considered fluids.

   Instead, the procedure of our approach is very general, and the specific information needed for each species are the governing pressure law and the expressions of the thermodynamic derivatives. This information could be possibly given in a tabulated form, instead of in an analytical form.

   Work is still in progress to improve the robustness of the method in the case of large density and energy ratios.

   Note finally that the multifluid algorithm recovers the modified PLM algorithm 6.3, hence it represents a flexible tool for the computation of both single-component and multi-component real fluids with the ability of avoiding the occurrence of spurious pressure oscillations.

89
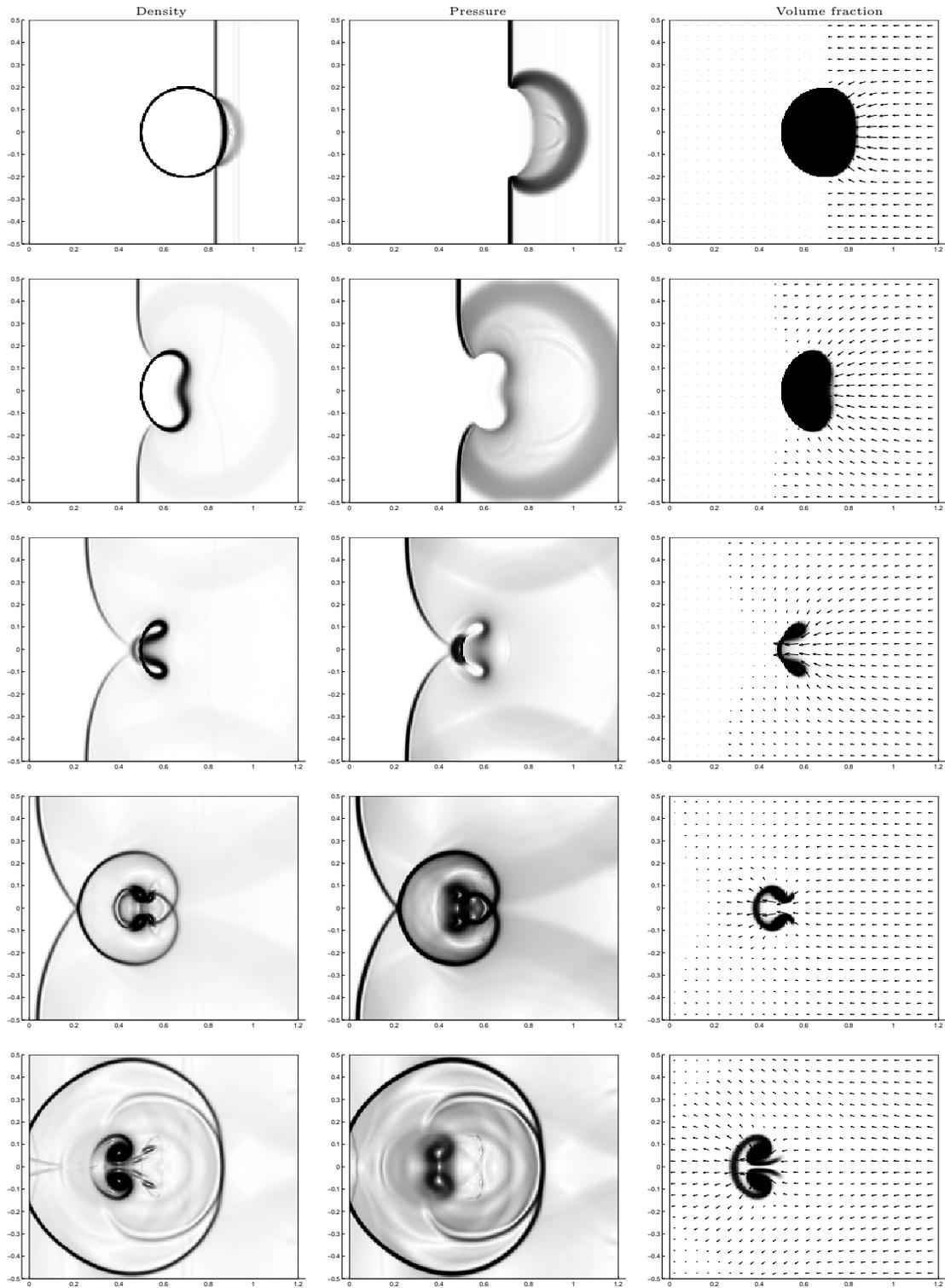


Figure 6.18: Experiment 6.12. Density, pressure, volume fraction at $t = 1, 2, 3, 4, 5 \times 10^{-4}$ $s$.

90
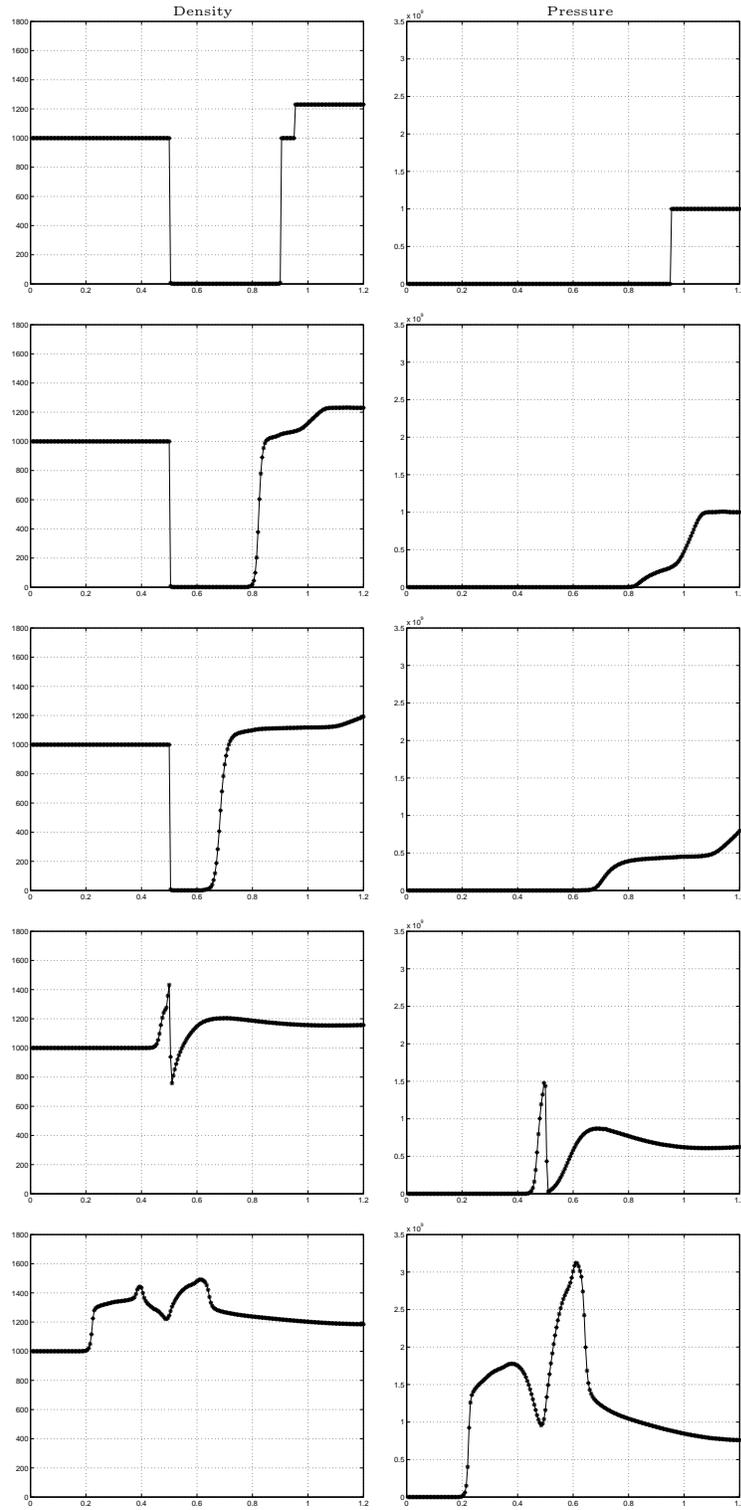


Figure 6.19: Experiment 6.12. Density and pressure along $y = 0$ at $t = 0, 1, 2, 3, 4 \times 10^{-4}$ $s$.

Chapter 7

# PHYSICAL AND NUMERICAL MODELING OF DUSTY GAS FLOWS

## 7.1 Physical Model

We consider a two-phase flow composed of solid particles suspended in a gaseous phase. Particle-laden gas flows, also called dusty gas flows, arise in many applications, from industrial processes to geophysical flows. One particular application, which was the original motivation for our work, is the study of volcanic ash plumes and pyroclastic flows. Chapter 8 will be dedicated to the description of applications of the dusty flow model presented here to volcanic phenomena.

We describe the thermo-fluid dynamics of the dusty gas by the physical model introduced in Section 3.3, assuming $\varphi \equiv 0$ (*pressureless* particulate phase), and neglecting the coupling terms related to the gas pressure gradient, in virtue of the assumption $\vartheta_d \ll 1$. The model is extended here to three dimensions, and gravity effects are taken into account. Subscripts g and d refer to the gas and dust phase, respectively, and the nomenclature used is summarized in Table 7.1. The equations expressing the conservation of mass, momentum and total energy for the two phases are:

$$\frac{\partial \rho}{\partial t} + \nabla \cdot (\rho \mathcal{V}_g) = 0 \,, \tag{7.1a}$$

$$\frac{\partial}{\partial t} (\rho \mathcal{V}_g) + \nabla \cdot (\rho \mathcal{V}_g \otimes \mathcal{V}_g + pI) = \rho \mathfrak{g} - D(\mathcal{V}_g - \mathcal{V}_d) \,, \tag{7.1b}$$

$$\frac{\partial E}{\partial t} + \nabla \cdot ((E+p)\mathcal{V}_g) = \rho \mathcal{V}_g \cdot \mathfrak{g} - D(\mathcal{V}_g - \mathcal{V}_d) \cdot \mathcal{V}_d - \mathcal{Q}(T_g - T_d) \,, \tag{7.1c}$$

$$\frac{\partial \beta}{\partial t} + \nabla \cdot (\beta \mathcal{V}_d) = 0 \,, \tag{7.1d}$$

$$\frac{\partial}{\partial t} (\beta \mathcal{V}_d) + \nabla \cdot (\beta \mathcal{V}_d \otimes \mathcal{V}_d) = \beta \mathfrak{g} + D(\mathcal{V}_g - \mathcal{V}_d) \,, \tag{7.1e}$$

$$\frac{\partial \Omega}{\partial t} + \nabla \cdot (\Omega \mathcal{V}_d) = \beta \mathcal{V}_d \cdot \mathfrak{g} + D(\mathcal{V}_g - \mathcal{V}_d) \cdot \mathcal{V}_d + \mathcal{Q}(T_g - T_d) \,. \tag{7.1f}$$

Coupling between the conservation laws of gas and dust occurs through the source terms modeling inter-phase drag and heat transfer.

### 7.1.1 Closure Relations

We summarize here the closure relations of system (7.1), already written in Section 3.3. Moreover we give specific expressions for the drag function D and heat transfer function Q taken from [150, 155], [102].

*Gas Thermodynamic Relations*

$$p_g = (\gamma - 1)\rho_g \varepsilon_g \,, \qquad \varepsilon_g = c_{vg} T_g \,, \quad \gamma, c_{vg} = \text{constant} \,. \tag{7.2}$$

*Dust energy relation*

$$\varepsilon_d = c_{vd} T_d \,, \quad c_{vd} = \text{constant} \,. \tag{7.3}$$

Table 7.1: Nomenclature.

$\vartheta_g$, $\vartheta_d$ = volume fractions, $\vartheta_g + \vartheta_d = 1$, $\vartheta_d \ll 1$;
$\rho_g$, $\rho_d$ = material microscopic mass densities ($\rho_d$ = constant);
$\rho = \vartheta_g \rho_g$ = gas macroscopic density;
$\beta = \vartheta_d \rho_d$ = dust macroscopic density (concentration);
$p_g$ = gas pressure, $p = \vartheta_g p_g$;
$\mathcal{V}_g = (u_g, v_g, w_g)^{\mathrm{T}}$, $\mathcal{V}_d = (u_d, v_d, w_d)^{\mathrm{T}}$ = vectorial velocities;
$\varepsilon_g$, $\varepsilon_d$ = specific internal energies;
$e_g = \varepsilon_g + \frac{1}{2}|\mathcal{V}_g|^2$, $e_d = \varepsilon_d + \frac{1}{2}|\mathcal{V}_d|^2$ = specific total energies;
$E = \vartheta_g \rho_g e_g$, $\Omega = \vartheta_d \rho_d e_d$ = total energies per unit volume;
$T_g$, $T_d$ = temperatures;
$R$ = gas constant;
$\gamma = c_{pg}/c_{vg}$ = gas specific heats ratio;
$c_{vd}$ = dust specific heat;
$\mu$ = gas dynamic viscosity;
$\kappa_g$ = gas thermal conductivity;
$\mathfrak{g} = (0, 0, -g)$ = gravity acceleration ($z$ direction);
$D$ = drag function;
$d$ = dust particle diameter;
$C_{\mathrm{d}}$ = drag coefficient;
$\mathcal{Q}$ = heat transfer function;
$Re$ = Reynolds number;
$Nu$ = Nusselt number;
$Pr$ = Prandtl number.

*Drag Function*

$$D = \frac{3}{4} C_{\mathrm{d}} \frac{\beta \rho}{\rho_d d} |u_g - u_d|, \tag{7.4}$$

where $d$ is the dust particle diameter, and $C_{\mathrm{d}}$ the drag coefficient, which we express as

$$C_{\mathrm{d}} = \begin{cases} \frac{24}{Re}\left(1 + 0.15 Re^{0.687}\right) & \text{if } Re < 1000, \\ 0.44 & \text{if } Re \geq 1000. \end{cases} \tag{7.5}$$

Above

$$Re = \frac{\rho\, d |\mathcal{V}_g - \mathcal{V}_d|}{\mu}, \tag{7.6}$$

is the Reynolds number, with $\mu$ denoting the dynamic viscosity of the gas.

*Heat Transfer Function*

$$\mathcal{Q} = \frac{Nu\, 6\kappa_g \beta}{\rho_d d^2}, \tag{7.7}$$

where $Nu$ is the Nusselt number, which we take in the form

$$Nu = 2 + 0.65 Re^{1/2} Pr^{1/3}. \tag{7.8}$$

Here

$$Pr = \frac{c_{pg}\mu}{\kappa_g} \tag{7.9}$$

is the Prandtl number, $\kappa_g$ denotes the gas thermal conductivity, and $c_{pg}$ the gas specific heat at constant pressure.

## 7.2 Numerical Method

We neglect for the moment the gravity source terms whose numerical treatment will be illustrated in Section 7.3. System (7.1) can be written in compact form without gravity as:

$$\frac{\partial q}{\partial t} + \nabla \cdot \mathbb{F}(q) = \psi(q),$$
(7.10a)

where

$$q = \begin{bmatrix} \rho \\ \rho \mathcal{V}_g \\ E \\ \beta \\ \rho \mathcal{V}_d \\ \Omega \end{bmatrix}, \quad \mathbb{F}(q) = \begin{bmatrix} \rho \mathcal{V}_g \\ \rho \mathcal{V}_g \otimes \mathcal{V}_g + pI \\ (E+p)\mathcal{V}_g \\ \rho \mathcal{V}_d \\ \rho \mathcal{V}_d \otimes \mathcal{V}_d \\ \Omega \mathcal{V}_d \end{bmatrix}, \quad \psi(q) = \begin{bmatrix} 0 \\ -D(\mathcal{V}_g - \mathcal{V}_d) \\ -D(\mathcal{V}_g - \mathcal{V}_d)\mathcal{V}_d - \mathcal{Q}(T_g - T_d) \\ 0 \\ D(\mathcal{V}_g - \mathcal{V}_d) \\ D(\mathcal{V}_g - \mathcal{V}_d)\mathcal{V}_d + \mathcal{Q}(T_g - T_d) \end{bmatrix}.$$
(7.10b)

Numerically, we solve the system above by using a fractional step technique, in which we alternate between solving the homogeneous hyperbolic system

$$\frac{\partial q}{\partial t} + \nabla \cdot \mathbb{F}(q) = 0$$
(7.11)

and the system of ordinary differential equations

$$\frac{\partial q}{\partial t} = \psi(q).$$
(7.12)

### 7.2.1 Hyperbolic Portion

To solve the homogeneous hyperbolic portion of system (7.10), we use the wave propagation algorithms based on Riemann solvers presented in Chapter 4, adopting in particular the f-wave formulation described in Section 4.2.2. The use of the f-wave approach is advantageous for the gas phase when we add gravity (see Section 7.3), and for the dust phase it helps to simplify the treatment of the nonstrictly hyperbolic Riemann solution.

We describe here the numerical scheme used in the one-dimensional case. The method is extended to two and three space dimensions by employing the algorithms illustrated in Section 4.3. System (7.11) in one space dimension along the $x$ coordinate takes the form $\frac{\partial q}{\partial t} + \frac{\partial f(q)}{\partial x} = 0$, and partitioning $q$ and $f$ in quantities corresponding to gas and dust we can write these equations as

$$\frac{\partial}{\partial t} \begin{bmatrix} q_g \\ q_d \end{bmatrix} + \frac{\partial}{\partial x} \begin{bmatrix} f_g(q_g) \\ f_d(q_d) \end{bmatrix} = \begin{bmatrix} 0 \\ 0 \end{bmatrix},$$
(7.13a)

with

$$q_g = \begin{bmatrix} \rho \\ \rho u_g \\ E \end{bmatrix}, \quad f_g(q_g) = \begin{bmatrix} \rho u_g \\ \rho u_g^2 + p \\ (E+p)u_g \end{bmatrix}, \quad q_d = \begin{bmatrix} \beta \\ \beta u_d \\ \Omega \end{bmatrix}, \quad f_d(q_d) = \begin{bmatrix} \beta u_d \\ \beta u_d^2 \\ \Omega u_d \end{bmatrix},$$
(7.13b)

where $E = \rho\varepsilon_g + \frac{1}{2}\rho u_g^2$, $\Omega = \beta\varepsilon_d + \frac{1}{2}\rho u_d^2$, and $p = (\gamma - 1)\rho\varepsilon_g$. As already discussed in Section 3.3.1, the homogeneous hyperbolic equations decouple into two separate systems for the gas phase and the dust phase, thus we can treat the two sets of equations independently.

*7.2.2   Gas Phase*

For the gas phase we have the set of equations

$$\frac{\partial q_g}{\partial t} + \frac{\partial f_g(q_g)}{\partial x} = 0, \tag{7.14}$$

which is the standard Euler system of gas dynamics for an ideal polytropic gas. Numerically, we solve these equations by employing the Roe solver [169] presented in Section 4.1.3. The Roe linearization $\hat{A}(q_{g,\ell}, q_{g,r})$ is given by the matrix (3.30) evaluated in the Roe average state $(\hat{u}_g, \hat{H})$, defined by (see (4.18))

$$\hat{u}_g = \frac{\sqrt{\rho_\ell}\, u_{g,\ell} + \sqrt{\rho_r}\, u_{g,r}}{\sqrt{\rho_\ell} + \sqrt{\rho_r}} \qquad \text{and} \qquad \hat{H} = \frac{\sqrt{\rho_\ell}\, H_\ell + \sqrt{\rho_r}\, H_r}{\sqrt{\rho_\ell} + \sqrt{\rho_r}}. \tag{7.15}$$

The approximate Riemann solution is based on the eigenvectors of the Roe matrix

$$\hat{r}_g^1 = \begin{bmatrix} 1 \\ \hat{u}_g - \hat{c}_g \\ \hat{H} - \hat{u}_g \hat{c}_g \end{bmatrix}, \quad \hat{r}_g^2 = \begin{bmatrix} 1 \\ \hat{u}_g \\ \frac{\hat{u}_g^2}{2} \end{bmatrix}, \quad \hat{r}_g^3 = \begin{bmatrix} 1 \\ \hat{u}_g + \hat{c}_g \\ H + \hat{u}_g \hat{c}_g \end{bmatrix}, \tag{7.16}$$

and its eigenvalues

$$\hat{\lambda}_g^1 = \hat{u}_g - \hat{c}_g, \qquad \hat{\lambda}_g^2 = \hat{u}_g, \qquad \hat{\lambda}_g^3 = \hat{u}_g + \hat{c}_g. \tag{7.17}$$

Here, the average sound speed is given, as standard, by

$$\hat{c}_g = \sqrt{(\gamma - 1)\left(\hat{H} - \frac{\hat{u}_g^2}{2}\right)}. \tag{7.18}$$

In the f-wave approach, for the Riemann problem at $x_{i-1/2}$ between states $Q_{g,i-1}$, $Q_{g,i}$ we decompose

$$f_g(Q_{g,i}) - f_g(Q_{g,i-1}) = \sum_{p=1}^{3} \mathcal{Z}_{g,i-1/2}^p, \tag{7.19}$$

where each f-wave $\mathcal{Z}_{g,i-1/2}^p$ is taken as a scalar multiple of $\hat{r}_{g,i-1/2}^p$,

$$\mathcal{Z}_{g,i-1/2}^p = \xi_{i-1/2}^p \hat{r}_{g,i-1/2}^p, \quad p = 1, \cdots, 3. \tag{7.20}$$

The coefficients $\xi_{i-1/2}^p$ are found to be (omitting here all the grid indexes)

$$\xi^2 = \frac{\gamma - 1}{\hat{c}_g^2}\left[(\hat{H} - \hat{u}_g^2)\,\Delta f_{g,1} + \hat{u}\,\Delta f_{g,2} - \Delta f_{g,3}\right], \tag{7.21a}$$

$$\xi^3 = \frac{1}{2\,\hat{c}}\left[\Delta f_{g,2} + (\hat{c} - \hat{u})\,\Delta f_{g,1} - \hat{c}\,\xi^2\right], \tag{7.21b}$$

$$\xi^1 = \Delta f_{g,1} - \xi^2 - \xi^3, \tag{7.21c}$$

where we have used the notation $\Delta f_g = (\Delta f_{g,1}, \Delta f_{g,2}, \Delta f_{g,3})^{\mathrm{T}} = f_g(Q_{g,i}) - f_g(Q_{g,i-1})$. The f-waves $\mathcal{Z}_{g,i-1/2}^p$ in (7.20) together with corresponding speeds $s_{i-1/2}^p = \hat{\lambda}_{g,i-1/2}^p$, $p = 1, \cdots, 3$ are the quantities we use to define the fluctuations (4.32) and the correction fluxes (4.33) which enter in the wave propagation updating formula (4.19).

*7.2.3   Dust Phase*

For the dust phase we have the non strictly hyperbolic pressureless equations

$$\frac{\partial q_d}{\partial t} + \frac{\partial f_d(q_d)}{\partial x} = 0 \,. \tag{7.22}$$

One numerical approach to solve this system is to replace it by the strictly hyperbolic system (3.34), (3.26b) with a small pressure perturbation $\varphi(\beta)$. Let us assume for instance the isothermal law (3.23), $\varphi = a^2\beta$, with $a$ small. Similarly to the scheme described for the gas phase, we can determine a Roe linearization $\hat{A}_d$ of the diagonalizable Jacobian matrix $A_d$ in (3.35) (with $X$, $Y_1$, $Y_2$, $c_d$ as in (3.38)) and define an algorithm based on the the flux decomposition

$$f_d(Q_{d,i}) - f_g(Q_{d,i-1}) = \sum_{p=1}^{3} \mathcal{Z}_{d,i-1/2}^p \,, \tag{7.23}$$

where $\mathcal{Z}_{d,i-1/2}^p$ is taken as a scalar multiple of the Roe eigenvector $\hat{r}_{d,i-1/2}$,

$$\mathcal{Z}_{d,i-1/2}^p = \zeta_{i-1/2}^p \hat{r}_{d,i-1/2}^p \,, \quad p = 1, \cdots, 3 \,. \tag{7.24}$$

For $\varphi = a^2\beta$ the Roe matrix $\hat{A}_d$ has eigenvectors

$$\hat{r}_d^1 = \begin{bmatrix} 1 \\ \hat{u}_d - a \\ \hat{e}_d - a(\hat{u}_d - a) \end{bmatrix} , \quad \hat{r}_d^2 = \begin{bmatrix} 0 \\ 0 \\ 1 \end{bmatrix} , \quad \hat{r}_d^3 = \begin{bmatrix} 1 \\ \hat{u}_d + a \\ \hat{e}_d + a(\hat{u}_d + a) \end{bmatrix} , \tag{7.25}$$

with eigenvalues

$$\hat{\lambda}_d^1 = \hat{u}_d - a \,, \qquad \hat{\lambda}_d^2 = \hat{u}_d \,, \qquad \hat{\lambda}_d^3 = \hat{u}_d + a \,, \tag{7.26}$$

where $\hat{u}_d$ is the Roe average as in (3.42), and

$$\hat{e}_d = \frac{\sqrt{\beta_\ell}e_{d,\ell} + \sqrt{\beta_r}e_{d,r}}{\sqrt{\beta_\ell} + \sqrt{\beta_r}} \,. \tag{7.27}$$

The coefficients $\zeta^p$ of the projection of the flux jump $\Delta f_d$ onto $\hat{r}_d^p$ are

$$\zeta^1 = \frac{1}{2a}\left[(\hat{u}_d + a)\,\Delta f_{d,1} - \Delta f_{d,2}\right] \,, \tag{7.28a}$$

$$\zeta^2 = [-\hat{e}_d + (\hat{u}_d^2 - a^2)]\Delta f_{d,1} - \hat{u}_d\Delta f_{d,2} + \Delta f_{d,3} \,, \tag{7.28b}$$

$$\zeta^3 = \frac{1}{2a}\left[(-\hat{u}_d + a)\,\Delta f_{d,1} + \Delta f_{d,2}\right] \,. \tag{7.28c}$$

A drawback of such a solver is that it may suffer from the appearance of nonphysical states, e.g. states with negative densities. Moreover, poor results are typically obtained when applying second order corrections when the common value of the density of the two intermediate states of the Riemann problem is large in comparison to the values of the left and right states .

   We adopt instead the more efficient method for the pressureless equations proposed in [123]. This approach allows to model robustly vacuum states and to perform efficiently high resolution corrections. The structure of the scheme is based on the features of the Riemann solution of the pressureless system. Recalling the discussion in Section 3.3.1, the solution to a Riemann problem at $x_{i-1/2}$ between states $Q_{d,i-1}$ and $Q_{d,i}$ can consists of either a pair of waves with vacuum between if $u_{d,i-1} < u_{d,i}$, or a single delta-shock if $u_{d,i-1} > u_{d,i}$, which propagates at speed

$$\hat{u}_{d,i-1/2} = \frac{\sqrt{\beta_{i-1}}u_{d,i-1} + \sqrt{\beta_i}u_{d,i}}{\sqrt{\beta_{i-1}} + \sqrt{\beta_i}} \,. \tag{7.29}$$

In the wave propagation framework a single wave is generally used in either case with magnitude $\mathcal{W}_{d_i-1/2} = Q_{d,i} - Q_{d,i-1}$ and speed $\hat{u}_{d,i-1/2}$. The only time two waves are used is if $u_{d,i-1} < 0 < u_{d,i}$, in which case they are propagating in opposite directions at speeds $u_{d,i-1}$, $u_{d,i}$ with vacuum state between. Then we take $\mathcal{W}^1_{d_i-1/2} = -Q_{d,i-1}$ and $\mathcal{W}^2_{d_i-1/2} = Q_{d,i}$. We note in passing that the same wave structure in this case would be obtained by applying the HLL solver of Section 4.1.2 with $a_\ell = u_{d,\ell}$, $a_r = u_{d,r}$. In fact we can see that the intermediate state in (4.14) results to be $q_m = 0$.

The solver is ultimately developed in the f-wave form. With this approach we consider the flux decomposition

$$f_d(Q_{d,i}) - f_d(Q_{d,i-1}) = \mathcal{Z}^1_{d,i-1/2} + \mathcal{Z}^2_{d,i-1/2}, \tag{7.30}$$

and define the f-waves through the following algorithm:
If $u_{d,i-1} < 0 < u_{d,i}$, set

$$
\begin{aligned}
\mathcal{Z}^1_{d,i-1/2} &= -f_d(Q_{d,i-1}), & s^1_{d,i-1/2} &= u_{d,i-1}, \\
\mathcal{Z}^2_{d,i-1/2} &= f_d(Q_{d,i}), & s^2_{d,i-1/2} &= u_{d,i}.
\end{aligned} \tag{7.31}
$$

Otherwise, compute speed $\hat{u}_{d,i-1/2}$ by (7.29), and set:

$$
\begin{aligned}
\text{if } u_{d,i-1/2} < 0: \quad &\mathcal{Z}^1_{d,i-1/2} = f_d(Q_{d,i}) - f_d(Q_{d,i-1}), & s^1_{d,i-1/2} &= \hat{u}_{d,i-1/2}, \\
&\mathcal{Z}^2_{d,i-1/2} = 0, & s^2_{d,i-1/2} &= \hat{u}_{d,i-1/2}, \\
\text{if } u_{d,i-1/2} \geq 0: \quad &\mathcal{Z}^1_{d,i-1/2} = 0, & s^1_{d,i-1/2} &= \hat{u}_{d,i-1/2}, \\
&\mathcal{Z}^2_{d,i-1/2} = f_d(Q_{d,i}) - f_d(Q_{d,i-1}), & s^2_{d,i-1/2} &= \hat{u}_{d,i-1/2}.
\end{aligned} \tag{7.32}
$$

Limiters are applied to these waves as explained in Sections (4.2.1), (4.2.2). The f-wave formulation of the solver is more robust and accurate in general than would be a standard wave propagation implementation based on waves $\mathcal{W}^p$, and in particular f-waves work better in high resolution correction terms.

### 7.2.4 Drag and Heat Transfer Source Terms

As already mentioned, we use a fractional step technique to treat the drag and heat transfer source terms. We thus consider the numerical solution of the system of ordinary differential equations (7.12):

$$\frac{\partial \rho}{\partial t} = 0, \tag{7.33a}$$

$$\frac{\partial}{\partial t}(\rho \mathcal{V}_g) = -A|\mathcal{V}_g - \mathcal{V}_d|(\mathcal{V}_g - \mathcal{V}_d), \tag{7.33b}$$

$$\frac{\partial E}{\partial t} = -A|\mathcal{V}_g - \mathcal{V}_d|(\mathcal{V}_g - \mathcal{V}_d) \cdot \mathcal{V}_d - \mathcal{Q}(T_g - T_d), \tag{7.33c}$$

$$\frac{\partial \beta}{\partial t} = 0, \tag{7.33d}$$

$$\frac{\partial}{\partial t}(\beta \mathcal{V}_d) = A|\mathcal{V}_g - \mathcal{V}_d|(\mathcal{V}_g - \mathcal{V}_d), \tag{7.33e}$$

$$\frac{\partial \Omega}{\partial t} = A|\mathcal{V}_g - \mathcal{V}_d|(\mathcal{V}_g - \mathcal{V}_d) \cdot \mathcal{V}_d + \mathcal{Q}(T_g - T_d), \tag{7.33f}$$

where we have defined

$$A = \frac{3}{4}C_d \frac{\beta \rho}{\rho_d d}. \tag{7.34}$$

In many problems of interest mechanical and thermal equilibrium is reached quickly, and the time scale for the processes related to the drag and to the heat transfer is much smaller than the time scale of the wave-propagation behaviour determined by the (homogeneous) hyperbolic part of the system. In particular, the fastest time scale corresponds to the heat transfer processes. Therefore, the system with the source terms (7.1) is typically stiff, and an explicit solver is not appropriate to treat the corresponding system of ODEs (7.33). In fact, it would be necessary to use a very small time step to resolve the fast processes, and it would be practically impossible to simulate the propagation of waves over distances of physical interest. Trying to use for instance a simple explicit Euler scheme can lead to negative energies, if the time step is not small enough to resolve the fastest time scale.

Here we propose a semi-analytical solver, which exploits the exact solution of the system of ODEs with the drag and heat transfer contributions considered separately. First we solve the ODEs arising from the drag terms over a time step $\Delta t$, and then we solve the ODEs for heat transfer.

### 7.2.5 Drag

For the drag terms we have the system of ordinary differential equations

$$\frac{\partial \rho}{\partial t} = 0\,, \tag{7.35a}$$

$$\frac{\partial}{\partial t}\left(\rho \mathcal{V}_g\right) = -A|\mathcal{V}_g - \mathcal{V}_d|(\mathcal{V}_g - \mathcal{V}_d)\,, \tag{7.35b}$$

$$\frac{\partial E}{\partial t} = -A|\mathcal{V}_g - \mathcal{V}_d|(\mathcal{V}_g - \mathcal{V}_d)\cdot \mathcal{V}_d\,, \tag{7.35c}$$

$$\frac{\partial \beta}{\partial t} = 0\,, \tag{7.35d}$$

$$\frac{\partial}{\partial t}\left(\beta \mathcal{V}_d\right) = A|\mathcal{V}_g - \mathcal{V}_d|(\mathcal{V}_g - \mathcal{V}_d)\,, \tag{7.35e}$$

$$\frac{\partial \Omega}{\partial t} = A|\mathcal{V}_g - \mathcal{V}_d|(\mathcal{V}_g - \mathcal{V}_d)\cdot \mathcal{V}_d\,, \tag{7.35f}$$

with initial data $\rho^0$, $(\rho \mathcal{V}_g)^0$, $E^0$, $\beta^0$, $(\beta \mathcal{V}_d)^0$, $\Omega^0$ at time $t^0$ coming from the hyperbolic solver. We look for the solution of the system above over a time step $\Delta t$. Equations (7.35a), (7.35d) clearly have the solution

$$\rho(t^0 + \Delta t) = \rho^0 \quad \text{and} \quad \beta(t^0 + \Delta t) = \beta^0\,. \tag{7.36}$$

We assume that the Reynolds number is constant in time, so that the drag coefficient is equal to its initial value, $C_{\mathrm{d}} = C_{\mathrm{d}}^0$. From this and through (7.36), it follows that $A$ is constant in time and equal to

$$A^0 = \frac{3}{4}C_{\mathrm{d}}^0 \frac{\beta^0 \rho^0}{\rho_d d}\,. \tag{7.37}$$

Then, we can write the equations (7.35b), (7.35e) for the momentum of the two phases as

$$\frac{\partial \rho^0 \mathcal{V}_g}{\partial t} = -A^0|\mathcal{V}_g - \mathcal{V}_d|(\mathcal{V}_g - \mathcal{V}_d)\,, \tag{7.38a}$$

$$\frac{\partial \beta^0 \mathcal{V}_d}{\partial t} = A^0|\mathcal{V}_g - \mathcal{V}_d|(\mathcal{V}_g - \mathcal{V}_d)\,. \tag{7.38b}$$

Subtracting these equations divided by the corresponding densities, gives:

$$\frac{\partial}{\partial t}\left(\mathcal{V}_g - \mathcal{V}_d\right) = -A^0\left(\frac{1}{\rho^0} + \frac{1}{\beta^0}\right)|\mathcal{V}_g - \mathcal{V}_d|(\mathcal{V}_g - \mathcal{V}_d)\,. \tag{7.39}$$

Let us now define

$$\mathcal{S} = |\mathcal{V}_g - \mathcal{V}_d| \,. \tag{7.40}$$

Differentiating this relation with respect to the time, we obtain:

$$\frac{\partial \mathcal{S}}{\partial t} = \frac{1}{\mathcal{S}} (\mathcal{V}_g - \mathcal{V}_d) \cdot \frac{\partial}{\partial t} (\mathcal{V}_g - \mathcal{V}_d) \,. \tag{7.41}$$

Then, using (7.39),

$$\frac{\partial \mathcal{S}}{\partial t} = -A^0 \xi_D^0 \mathcal{S}^2 \,, \tag{7.42}$$

where we have introduced

$$\xi_D = \frac{1}{\rho} + \frac{1}{\beta} \,. \tag{7.43}$$

The solution of the ordinary differential equation (7.42) with the initial data $\mathcal{S}^0$ is:

$$\mathcal{S}(t^0 + \Delta t) = \frac{\mathcal{S}^0}{A^0 \, \xi_D^0 \, \mathcal{S}^0 \Delta t + 1} \,. \tag{7.44}$$

Using this result in (7.39) we find the solution for $(\mathcal{V}_g - \mathcal{V}_d)$ as

$$(\mathcal{V}_g - \mathcal{V}_d)(t^0 + \Delta t) = \frac{\mathcal{V}_g^0 - \mathcal{V}_d^0}{A^0 \xi_D^0 |\mathcal{V}_d^0 - \mathcal{V}_d^0| \Delta t + 1} \,. \tag{7.45}$$

Introducing (7.44), (7.45) in the momentum equations (7.35b, (7.35e) and integrating, we finally obtain:

$$(\rho \mathcal{V}_g)(t^0 + \Delta t) = (\rho \mathcal{V}_g)^0 + \frac{\mathcal{V}_g^0 - \mathcal{V}_d^0}{\xi_D^0} \left[ \frac{1}{A^0 \xi_D^0 |\mathcal{V}_g^0 - \mathcal{V}_d^0| \Delta t + 1} - 1 \right] \,, \tag{7.46a}$$

$$(\beta \mathcal{V}_d)(t^0 + \Delta t) = (\beta \mathcal{V}_d)^0 - \frac{\mathcal{V}_g^0 - \mathcal{V}_d^0}{\xi_D^0} \left[ \frac{1}{A^0 \xi_D^0 |\mathcal{V}_g^0 - \mathcal{V}_d^0| \Delta t + 1} - 1 \right] \,. \tag{7.46b}$$

Once the momentum equations have been solved, we can use the form of the energy equations to calculate the corresponding changes in energy of each phase. The right hand side of (7.35f) corresponds exactly to the change in kinetic energy of the dust corresponding to the change in momentum, and hence the internal energy of the dust remains constant in this step. The dust energy $\Omega$ is simply updated by the change in kinetic energy $\Delta \mathcal{K}_d$ resulting from the momentum update:

$$\Omega(t^0 + \Delta t) = \Omega^0 + \Delta \mathcal{K}_d \,, \tag{7.47a}$$

where $\Delta \mathcal{K}_d = \mathcal{K}_d(t^0 + \Delta t) - \mathcal{K}_d^0$, and $\mathcal{K}_d = \frac{1}{2} \beta |\mathcal{V}_d|^2$ denotes the dust kinetic energy per unit volume.

The right hand side of the gas energy equation (7.35c) is just the negative of the right hand side of (7.35f), as required by conservation of total energy. Hence the gas energy $E$ is updated by the negative of the update to $\Omega$ calculated above, in order to leave the total energy unchanged:

$$E(t^0 + \Delta t) = E^0 - \Delta \mathcal{K}_d \,. \tag{7.47b}$$

This energy change models both the the change in kinetic energy in the gas and also a change in internal energy due to drag dissipation and the resulting heating of the gas.

To conclude this section, it is interesting to write the expression of the solution for the velocities, which can be obtained from (7.46) dividing by the corresponding macroscopic densities, and rearranging the terms:

$$\mathcal{V}_g(t^0 + \Delta t) = \mathcal{V}_{eq} + \frac{\mathcal{V}_g^0 - \mathcal{V}_{eq}}{A^0 \xi_D^0 |\mathcal{V}_g^0 - \mathcal{V}_d^0| \Delta t + 1} \,, \tag{7.48a}$$

$$\mathcal{V}_d(t^0 + \Delta t) = \mathcal{V}_{eq} + \frac{\mathcal{V}_d^0 - \mathcal{V}_{eq}}{A^0 \xi_D^0 |\mathcal{V}_g^0 - \mathcal{V}_d^0| \Delta t + 1} \,, \tag{7.48b}$$

where

$$\mathcal{V}_{\text{eq}} = \frac{\rho^0 \mathcal{V}_g^0 + \mathcal{V}_d^0 \beta^0}{\rho^0 + \beta^0} \tag{7.49}$$

is the equilibrium velocity. If the drag relaxation time is small compared to $\Delta t$, the velocities $\mathcal{V}_g$ and $\mathcal{V}_d$ approach $\mathcal{V}_{\text{eq}}$ within the time step.

### 7.2.6   Heat Transfer

We now look for the solution of the system of ODEs for heat transfer:

$$\frac{\partial \rho}{\partial t} = 0 \,, \tag{7.50a}$$

$$\frac{\partial}{\partial t}(\rho \mathcal{V}_g) = 0 \,, \tag{7.50b}$$

$$\frac{\partial E}{\partial t} = -\mathcal{Q}(T_g - T_d) \,, \tag{7.50c}$$

$$\frac{\partial \beta}{\partial t} = 0 \,, \tag{7.50d}$$

$$\frac{\partial}{\partial t}(\beta \mathcal{V}_d) = 0 \,, \tag{7.50e}$$

$$\frac{\partial \Omega}{\partial t} = \mathcal{Q}(T_g - T_d) \,, \tag{7.50f}$$

with initial data $\rho^0$, $\beta^0$, $(\rho \mathcal{V}_g)^0$, $(\rho \mathcal{V}_d)^0$, $E^0$, $\Omega^0$ coming from the result of applying drag terms, as described above. Clearly, the solution of (7.50a), (7.50b), (7.50d), (7.50e) is

$$\rho(t^0 + \Delta t) = \rho^0 \,, \quad \beta(t^0 + \Delta t) = \beta^0 \,, \quad (\rho \mathcal{V}_g)(t^0 + \Delta t) = (\rho \mathcal{V}_g)^0 \,, \quad (\beta \mathcal{V}_d)(t^0 + \Delta t) = (\beta \mathcal{V}_d)^0 \,. \tag{7.51}$$

It follows that the Reynolds and Nusselt number are constant, hence $\mathcal{Q}$ is constant and equal to its initial value $\mathcal{Q}^0$:

$$\mathcal{Q}^0 = \frac{Nu^0 \, 6\kappa_g \beta^0}{\rho_d d^2} \,. \tag{7.52}$$

Then we can write the energy equations (7.50c), (7.50f) as:

$$\frac{\partial \rho^0 \varepsilon_g}{\partial t} = -\mathcal{Q}^0(T_g - T_d) \,, \tag{7.53a}$$

$$\frac{\partial \beta^0 \varepsilon_d}{\partial t} = \mathcal{Q}^0(T_g - T_d) \,. \tag{7.53b}$$

By using $\varepsilon_g = c_{vg} T_g$, $\varepsilon_d = c_{vd} T_d$, where $c_{vg}$, $c_{vd}$ are the specific heats at constant volume, we obtain:

$$\frac{\partial T_g}{\partial t} = -\frac{1}{\rho^0 c_{vg}} \mathcal{Q}^0(T_g - T_d) \,, \tag{7.54a}$$

$$\frac{\partial T_d}{\partial t} = \frac{1}{\beta^0 c_{vd}} \mathcal{Q}^0(T_g - T_d) \,. \tag{7.54b}$$

Subtracting the two equations above gives:

$$\frac{\partial}{\partial t}(T_g - T_d) = -\mathcal{Q}^0 \left( \frac{1}{\rho^0 c_{vg}} + \frac{1}{\beta^0 c_{vd}} \right)(T_g - T_d) \,. \tag{7.55}$$

The solution of this ordinary differential equation is:

$$(T_g - T_d)(t^0 + \Delta t) = (T_g^0 - T_d^0)e^{-\mathcal{Q}^0 \xi_\mathcal{Q}^0 \Delta t}, \tag{7.56}$$

where

$$\xi_\mathcal{Q} = \frac{1}{\rho c_{vg}} + \frac{1}{\beta c_{vd}}. \tag{7.57}$$

Introducing the above result in the equations for the total energy, we obtain

$$\frac{\partial E}{\partial t} = -\mathcal{Q}^0 (T_g^0 - T_d^0)e^{-\mathcal{Q}^0 \xi_\mathcal{Q}^0 \Delta t}, \tag{7.58a}$$

$$\frac{\partial \Omega}{\partial t} = \mathcal{Q}^0 (T_g^0 - T_d^0)e^{-\mathcal{Q}^0 \xi_\mathcal{Q}^0 \Delta t}, \tag{7.58b}$$

and the integration of these equations finally gives:

$$E(t^0 + \Delta t) = E^0 + \frac{T_g^0 - T_d^0}{\xi_\mathcal{Q}^0} \left[ e^{-\mathcal{Q}^0 \xi_\mathcal{Q}^0 \Delta t} - 1 \right], \tag{7.59a}$$

$$\Omega(t^0 + \Delta t) = \Omega^0 - \frac{T_g^0 - T_d^0}{\xi_\mathcal{Q}^0} \left[ e^{-\mathcal{Q}^0 \xi_\mathcal{Q}^0 \Delta t} - 1 \right]. \tag{7.59b}$$

Let us also report here the expression of the solution for the temperature for each phase:

$$T_g(t^0 + \Delta t) = T_{\text{eq}} + (T_g^0 - T_{\text{eq}})e^{-\mathcal{Q}^0 \xi_\mathcal{Q}^0 \Delta t}, \tag{7.60a}$$

$$T_d(t^0 + \Delta t) = T_{\text{eq}} + (T_d^0 - T_{\text{eq}})e^{-\mathcal{Q}^0 \xi_\mathcal{Q}^0 \Delta t}, \tag{7.60b}$$

where

$$T_{\text{eq}} = \frac{\rho^0 c_{vg} T_g^0 + \beta^0 c_{vd} T_d^0}{\rho^0 c_{vg} + \beta^0 c_{vd}} \tag{7.61}$$

is the equilibrium temperature. In the numerical solution of many problems of interest the thermal relaxation time is very small compared to $\Delta t$, and the temperatures approach the equilibrium value $T_{\text{eq}}$ within a time step.

### 7.2.7 Time Scales

As already noticed, time scales for mechanical and thermal relaxation are very small compared to the time scales of the wave-propagation behaviour of interest, and especially thermal equilibrium is approached very fast.

Let us focus first on characteristic times for mechanical equilibrium. Based on (7.45), the time $t_D^c$ that would be necessary to reach equilibrium if the process would occur at a constant rate given by its value at $t^0$ is

$$t_D^c = \frac{1}{A \xi_D^0 |\mathcal{V}_d^0 - \mathcal{V}_d^0|}. \tag{7.62}$$

The time $\bar{t}_D$ needed to reduce the velocity difference to $1/100$ of the initial value, i.e. such that $|\mathcal{V}_g - \mathcal{V}_d| = \frac{1}{100}|\mathcal{V}_g^0 - \mathcal{V}_d^0|$ is then:

$$\bar{t}_D = K t_D^c, \quad K = 99. \tag{7.63}$$

Considering now the heat transfer processes, in view of equation (7.56), the characteristic time for thermal equilibrium is

$$t_\mathcal{Q}^c = \frac{1}{\mathcal{Q} \xi_\mathcal{Q}}. \tag{7.64}$$

The time $\bar{t}_{\mathcal{Q}}$ needed to reduce the temperature difference to $1/100$ of the initial value, i.e. such that $(T_g - T_d) = \frac{1}{100}(T_g^0 - T_d^0)$ is then

$$\bar{t}_{\mathcal{Q}} = B\frac{1}{\mathcal{Q}\xi_{\mathcal{Q}}} = Bt_{\mathcal{Q}}^c\,, \quad B = \ln(100) = 4.6\,. \tag{7.65}$$

We quantify these time scale by considering some example values for the quantities involved that are in the typical ranges of the applications of interest (see Chapter 8 on volcanic applications). Here we assume $\rho^0 = 1.225\,kg\,m^{-3}$, $p^0 = 10^5\,Pa$, $T_g^0 = \frac{p^0}{\rho^0 R} = 284.43\,K$, $T_d^0 = 1200\,K$, $\rho_d = 2300\,kg\,m^{-3}$, $\vartheta_d = 0.01$, and $|\mathcal{V}_g^0 - \mathcal{V}_d^0| = 70\,m/s$. The physical parameters used are those in Table 8.1 in Chapter 8.

Table 7.2 shows the corresponding values of $\bar{t}_D$ and $\bar{t}_{\mathcal{Q}}$ for two values of the particle diameter, $d = 10\,\mu m$, and $d = 200\,\mu m$. The diameter $d$ affects noticeably the time scales as can be understood examining (7.37) and (7.52).

These relaxation time scales are small compared to the time period needed in our applications to study propagation of waves over distances of physical interest. For instance, in problems of pyroclastic dispersion dynamics phenomena are studied over spatial domains of the order of kilometers during periods of the order of minutes.

In the numerical simulation of these phenomena we do not want to take a time step $\Delta t$ of the order of the mechanical or thermal relaxation time scale. Rather, we want to use a time step based on the CFL restriction for the hyperbolic problem, that is $\Delta t = \mathcal{O}(\Delta x/s_{\max})$, where $s_{\max}$ is the maximum speed in absolute value related to the hyperbolic portion of the model equations. As a rough approximation, let us assume $s_{\max}$ equal to the gas sound speed at the temperature $T_g^0$ assumed above, which is $c_g \approx 338\,m/s$. Space intervals in our computations are typically in the range 10 to $30\,m$. Taking for instance $\Delta x = 15\,m$ we obtain $\Delta t \approx 0.04\,s$. If drag and heat transfer processes are characterized by the time scales in Table 7.2, then thermal relaxation occurs within $\Delta t$, and also mechanical relaxation for the smaller value of the particle diameter $d$.

However, let us remark that, although it is true that in great part of the spatial domain where we numerically study these phenomena velocities and temperatures of the two phases relax towards the equilibrium value very fast, the situation is different in regions around shocks. Due to the large inertia of solid particles, this solid phase keeps a higher velocity than the gaseous phase across shocks, and a nonequilibrium region forms. In this case relaxation does not occur in a time step, so it is important to use an ODE solver such as the one presented that allows to model both fast and slow interphase processes.

Table 7.2: Example of time scales for mechanical and thermal relaxation.

| $d\ [\mu m]$ | $\bar{t}_D\ [s]$ | $\bar{t}_{\mathcal{Q}}\ [s]$ |
|---|---|---|
| 10 | $1.5255 \times 10^{-3}$ | $4.5704 \times 10^{-5}$ |
| 200 | $8.1379 \times 10^{-2}$ | $8.9151 \times 10^{-3}$ |

## 7.3   Gravity Source Terms

We now consider the two-phase system (7.1) including also the gravity source terms. The gravity term for the dust equations is handled in the fractional step procedure along with the source terms for drag and heat transfer. Since the mass is constant over a time step in solving the corresponding system
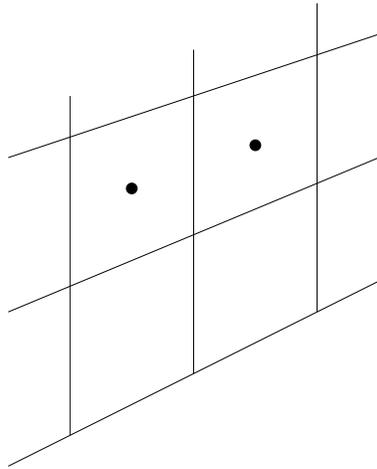
Figure 7.1: A two dimensional mapped grid fitted to surface topography.

of ODEs, the momentum equations are easily solved by modifying $\beta \mathcal{V}_d$ by $\mathfrak{g}\beta\Delta t$, which corresponds to a modification of the vertical momentum component only, since $\mathfrak{g} = (0, 0, -g)^{\mathrm{T}}$ acts in the vertical direction. The energy is then adjusted to reflect the change in kinetic energy $\Delta\mathcal{K}_d$ (as in (7.47a)).

A special numerical treatment is adopted for the gravity term of the gas phase, based on the approach described in section 5.9, which incorporates the effect of the source term into the solution of the Riemann problem. As already noted, this method is more accurate than the fractional step splitting technique in modeling perturbations from a steady state. This approach is used here for the gas gravity since in the application problems we are interested in the dusty gas fluid motion is relative to an atmosphere in hydrostatic balance.

Therefore, accounting for gravity, in place of (7.19), for each Riemann problem at the interface $(i-1/2)$ we decompose into f-waves the sum of the gas flux jump and the gravity contribution $-\Psi_{i-1/2}$ as

$$f_g(Q_{g,i}) - f_g(Q_{g,i-1}) - \Psi_{i-1/2} = \sum_{p=1}^{3} \mathcal{Z}_{g,i-1/2}^{p}. \tag{7.66}$$

The contribution $\Psi_{i-1/2}$ arising from the gas gravity source term

$$\psi_g(q_g) = (0, -g\rho_g, -g\rho_g u_g)^{\mathrm{T}}, \tag{7.67}$$

where here in general $u_g$ represents the gas velocity normal to the interface of the Riemann problem we are solving, is defined as

$$\Psi_{i-1/2} = \frac{1}{2}(\psi_g(Q_{g,i-1}) + \psi_g(Q_{g,i}))\Delta z_{i-1/2}, \tag{7.68}$$

where $\Delta z_{i-1/2} = z_i - z_{i-1}$ is the difference in the vertical coordinate of the centroids of the two cells adjacent to this interface $(i-1/2)$. In the hydrostatic case $u_{g,i} = u_{g,i-1} = 0$ and $\Delta f_g = (0, \Delta p, 0)^{\mathrm{T}}$. We expect the jump in pressure between the cell averages to approximately equal $-\frac{1}{2}g(\rho_{g,i-1} + \rho_{g,i})\Delta z_{i-1/2}$, and this cancellation occurs before the waves are generated for use in the hyperbolic solver, so that hydrostatic balance is maintained.

For applications to volcanic flows we will use a mapped grid that conforms to the ground surface, of the type shown in Figure 7.1 in two dimensions (blown up near the surface). A quadrilateral logically rectangular grid is used in which the horizontal grid lines are interpolated between the surface topography and a fixed upper elevation, while the vertical grid lines are still vertical. Riemann problems arising

from the hyperbolic portion of the equations are solved in directions normal to physical cell interfaces using the algorithms described so far. It is important to note that the gravitational source term will generally come into every Riemann problem on the grid, even those in the $x$-direction that are normal to a vertical cell interface (e.g., between the two cells whose centroids are marked by dots in the figure). Since gravity does not act normal to this interface, one might be tempted to drop the source term in this normal Riemann solver. However, the difference in elevation $\Delta z$ of the cell centroids means that there will be a pressure difference in the steady state solution that must be cancelled by the source term, and this is effectively taken into account by means of (7.68).

## 7.4   One-dimensional Experiments

We present results of two numerical experiments in one spatial dimension with no gravity, obtained by applying the numerical method described in the previous sections for the dusty gas model (7.1). Second order corrections are performed in the solution of the hyperbolic portion of the system by using the MC limiter (4.30) for the gas equations, and the minmod limiter (4.27) for the dust equations.

Results of multidimensional computations including gravity effects will be presented in Chapter 8, in the context of simulation of volcanic processes.

### 7.4.1   Sound Speed Test

We perform a test to show that our numerical model is able to simulate the propagation of acoustic waves at the expected sound speed of the mixture, assuming here that the drag and heat transfer equilibrate velocities and temperatures of gas and dust on a much faster time scale than the acoustic wave propagation. Note that we will not assume in general equilibrium between the two phases in our numerical method, but we now show that solving the coupled system handling the source terms by a fractional step approach is successful even in this limit.

We recall that under the equilibrium assumption the mixture sound speed, as derived in Section 3.3.3, is given by

$$c_{\mathrm{m}} = c_{g,\mathrm{isot}} \sqrt{\frac{\rho_g}{\vartheta_g \rho_{\mathrm{m}}}}, \qquad (7.69)$$

where $c_{g,\mathrm{isot}} = \sqrt{RT_g}$ and the mixture density is $\rho_{\mathrm{m}} = \vartheta_g \rho_g + \vartheta_d \rho_d = \rho + \beta$.

We model the propagation of a small amplitude pressure waves in a (one dimensional) steady region containing a mixture of gas and dust with constant flow variables, denoted in the following with the subscript 0. We consider an initial pressure perturbation described by the Gaussian function

$$p(x) = p_0 + \tilde{p}\, e^{-0.0001 x^2}, \qquad \tilde{p} = \frac{1}{100}\, p_0. \qquad (7.70)$$

The data of the steady background state are set as $p_0 = 10^5$ Pa, $u_{g0} = u_{d0} = 0$, $T_{g,0} = T_{d,0} = 1200$ K, $\rho_0 = 1$ Kg/m$^3$, $\vartheta_{d,0} = 0.01$, and physical parameters of the two phases are those reported in table 8.1 (Chapter 8). For these data equation (7.69) gives $c_{\mathrm{m}} = 65.2$ m/s.

In Figure 7.2 we display the result of the computation performed in the spatial domain $[-5000, 5000]$ m with 2000 cells and CFL $= 0.9$. The figure shows the evolution of the pressure profile from $t = 0$ to 60 s, with plots at intervals of 10 s. The initial perturbation (7.70) breaks into two waves propagating symmetrically in opposite directions. As time evolves, each of the two pulses decays to an acoustic wave propagating at the sound speed corresponding to the background state of the fluid mixture. We estimate the velocity of each pulse simply considering two positions (corresponding to the pressure pulse peak) at two different times. For instance, referring to Figure 7.2, we consider the positions $x_A = 3250$ m and $x_B = 3900$ m reached at times $t_A = 50$ s and $t_B = 60$ s, respectively. We then evaluate the numerical sound speed as $c_{\mathrm{m}}^{\mathrm{num}} \approx (x_B - x_A)/(t_B - t_A) = 65$ m/s. This agrees

approximately with the expected value of $c_\mathrm{m}$ reported above. Note that the isothermal and isentropic sound speed of the pure gas would be $c_{g,\mathrm{isot}} = 316.2$ m/s and $c_g = 374.1$ m/s, respectively, which are much greater than $c_\mathrm{m}$.
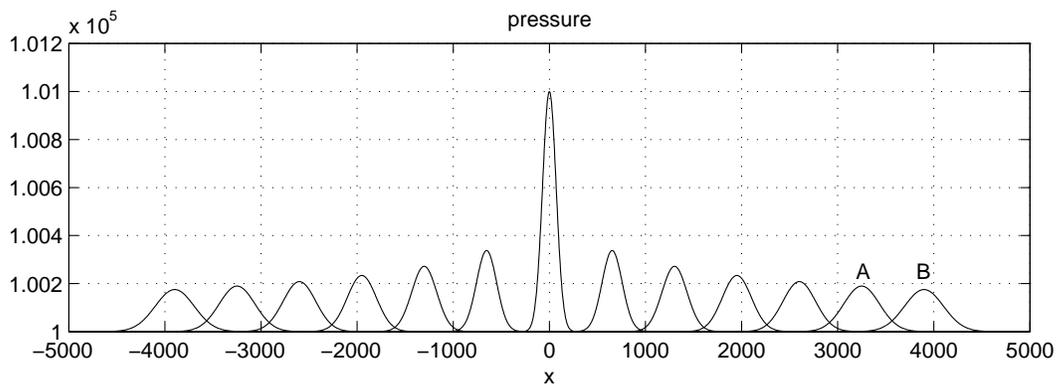


Figure 7.2: Sound speed experiment. Pressure perturbation as time evolves from $t = 0$ to $t = 60$ s (plots every 10 s).

### 7.4.2 Shock Tube Experiment

We simulate a shock tube experiment that has been studied numerically by Saito in [176], and was originally considered in [142]. It involves high-pressure and high-density pure air ($\gamma = 1.4$) in the driver section, and air laden with solid particles at room conditions in the driven section. As in [176], an extremely small amount of dust is assumed here in the driver section for numerical reasons. Dimensionless initial data are reported in Table 7.3. Flow variables are normalized by using as reference density $\rho_\mathrm{ref}$, reference pressure $p_\mathrm{ref}$, and reference temperature $T_\mathrm{ref}$ the values for air at room conditions. Moreover, the reference velocity is defined as $u_\mathrm{ref} = \sqrt{\frac{p_\mathrm{ref}}{\rho_\mathrm{ref}}}$.

Table 7.3: Initial data for Saito's experiment.

| variable | driver section | driven section |
|---|---|---|
| $p/p_\mathrm{ref}$ | 10.0 | 1.0 |
| $\rho/\rho_\mathrm{ref}$ | 10.0 | 1.0 |
| $\beta/\rho_\mathrm{ref}$ | 0.0001 | 1.0 |
| $u_g/u_\mathrm{ref}$ | 0.0 | 0.0 |
| $u_d/u_\mathrm{ref}$ | 0.0 | 0.0 |
| $T_g/T_\mathrm{ref}$ | 1.0 | 1.0 |
| $T_d/T_\mathrm{ref}$ | 1.0 | 1.0 |

Only for this experiment we adopt the definitions of the drag coefficient, Prandtl number, and gas viscosity that are used in [176]. These differ from the relations we typically employ, and which have been reported in Section (7.1.1). Here:

$$C_\mathrm{d} = 0.46 + 28\,Re^{-0.85}\,, \tag{7.71}$$

and the Prandtl number is assumed to be a constant, $Pr = 0.75$. The gas dynamic viscosity $\mu$ varies with the temperature $T$ based on (see [28])

$$\mu = 1.71 \times 10^{-5} \left( \frac{T}{273} \right)^{0.77}. \tag{7.72}$$

Moreover, the dust particle diameter needed to compute the Reynolds number is $d = 10 \, \mu$m, and the dust and gas heat coefficients at constant volume are assumed to be equal, with a dimensionless value given by $1/(\gamma - 1)$.

Following [176], we solve dimensionless equations, which are normalized by using $\ell = \frac{4\rho_d d}{3\rho_{\text{ref}}}$ as a characteristic length, and $\tau = \frac{\ell}{u_{\text{ref}}}$ as a characteristic time. The computational domain is the interval $[0, 100]$, and the diaphragm is located at $x = 50$ units. We use 1000 cells (as in [176]) and CFL $= 0.9$.

Results of the computations at normalized time units $= 5$, 10, and 30 are displayed in figures 7.3, 7.4, 7.5, respectively, together with results corresponding to the case of pure gas in both the driver and driven sections for comparison.

The structure of the solution of this shock tube problem involves a left-going rarefaction wave, a contact discontinuity, and a right-going shock wave. In particular, the presence of the particulate phase leads to the development of a partially dispersed shock wave, characterized by a frozen shock in the gas followed by a relaxation region. This is formed since dust particles cannot follow any abrupt change in the gas due to their large inertia. As described in [176], the gas loses energy due to the interaction with particles, and the shock front decelerates, as we can observe by comparing the shock position of the dusty gas solution with the one of the pure gas case. Moreover, the deceleration of the shock wave induces a compression behind the shock front that leads to a higher value of the pressure with respect to that of the pure gas [176].

As time progresses, the structure of the solution tends to a stationary configuration characterized by an equilibrium region around the contact surface, and relaxation regions of constant width behind the rarefaction and shock wave. This stationary state can be observed in Figure 7.5, where in particular we can notice the equilibrium zones from the velocity and temperature profiles.

The results presented here agree well with those reported by Saito in [176], which are validated by the author by comparison with pseudo-stationary solutions obtained through numerical integration of the steady conservation equations. The numerical method of Saito is based on an operator splitting technique that uses the Harten [76] and Yee [212] scheme for the gas phase and a semi-analytical approach for the dust phase. An inaccuracy in our results, not observed in [176], is the appearance of oscillations in the computed dust temperature in correspondence of the contact surface. These arise only when second order corrections are performed, and they decrease with mesh refinement. We remark that oscillations are generated in the process of deriving the dust temperature from the internal energy per unit volume, dividing this by the computed dust density. No oscillations appear in the dust energy (and in all the conserved variables), as shown in Figure 7.6. Note also that this inaccuracy does not affect the computation process. In fact, in the updating of the energies through (7.59) we actually don't need the dust temperature itself, but the product $\beta T_d$, as we can see by rewriting the term $\frac{T_g^0 - T_d^0}{\xi_Q^0}$ as $\frac{\rho c_{vg} c_{vd}}{\rho c_{vg} + \beta c_{vd}}(\beta T_g^0 - \beta T_d^0)$. This is also consistent with the form of the heat transfer source term, which can be rewritten as $\mathcal{Q}(T_g - T_d) = \mathcal{Q}'(\beta T_g - \beta T_d)$, where $\mathcal{Q}' = \frac{Nu \, 6\kappa_g}{\rho_d d^2}$. The fact that in the results of Saito this difficulty does not arise can be explained by considering that his algorithm for the dust phase uses the dust temperature as a primary variable, whereas in our case the dust temperature is derived from the conserved variables.
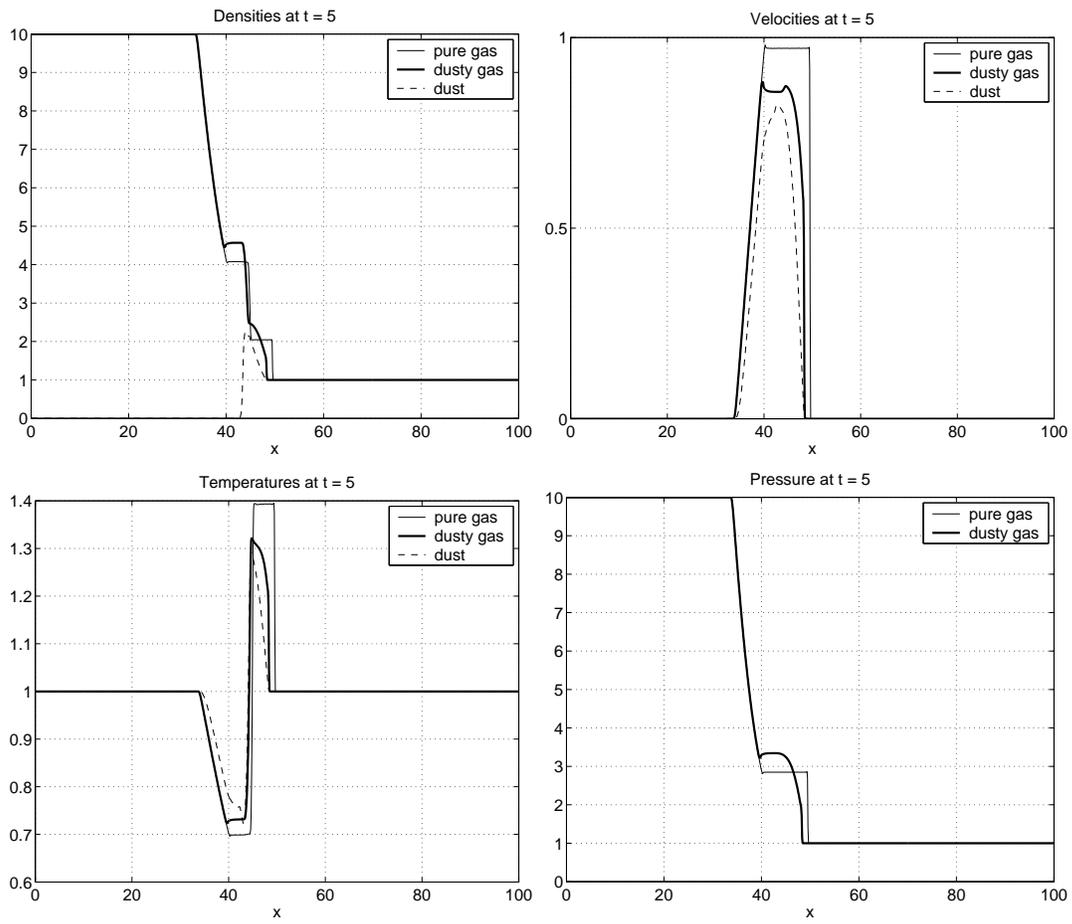
Figure 7.3: Saito's experiment. Densities, velocities, temperatures, and pressure at $t = 5$.
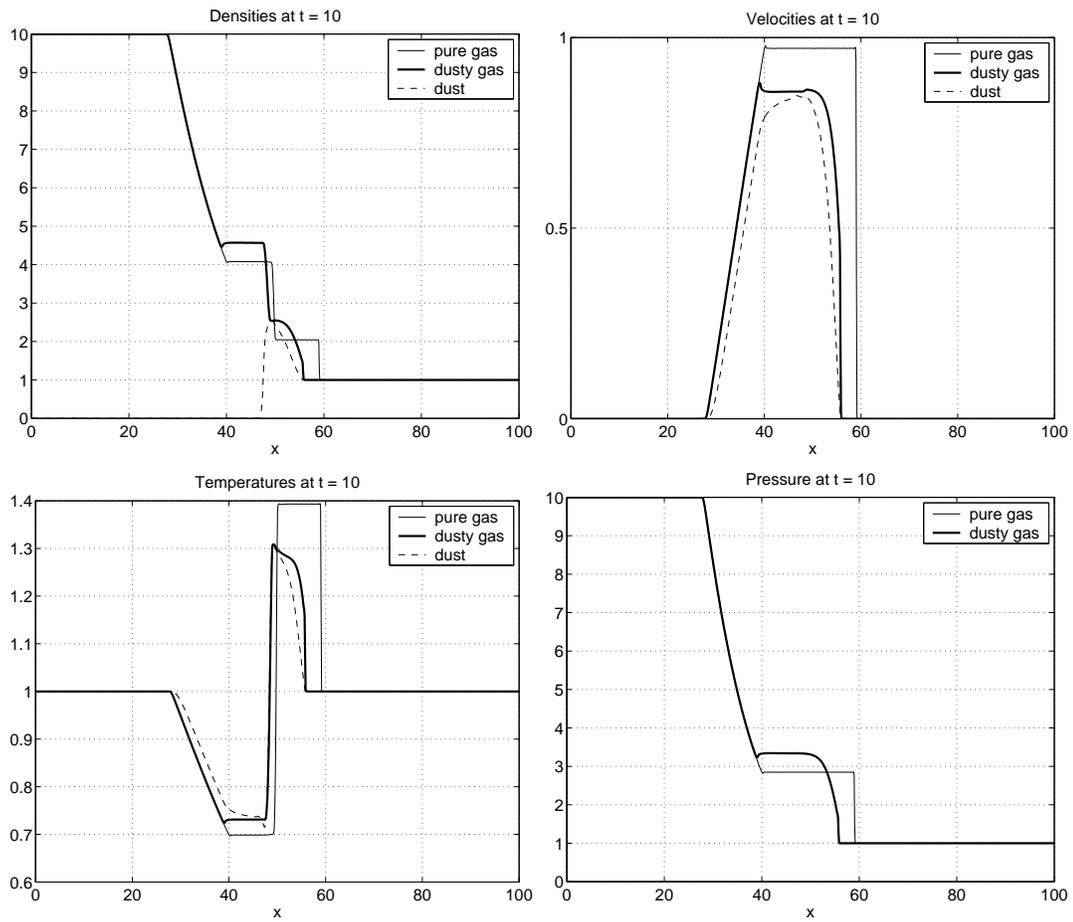
Figure 7.4: Saito's experiment. Densities, velocities, temperatures, and pressure at $t = 10$.
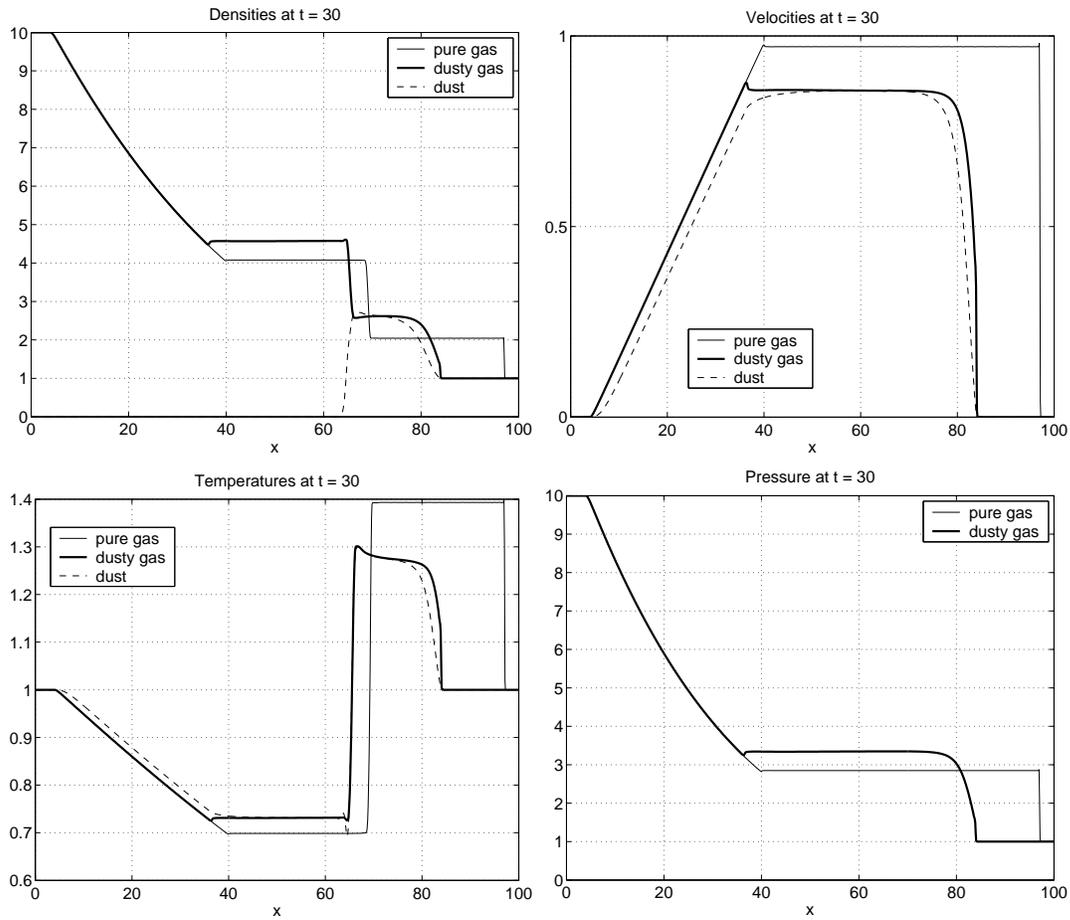
Figure 7.5: Saito's experiment. Densities, velocities, temperatures, and pressure at $t = 30$.
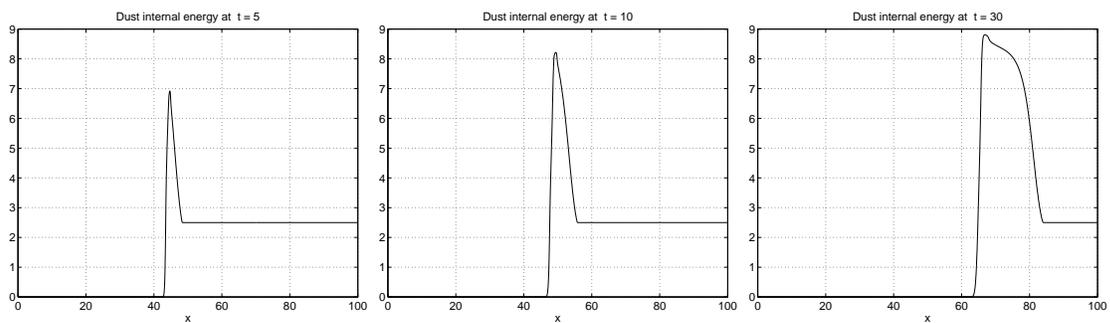


Figure 7.6: Saito's experiment. Dust internal energy per unit volume at $t = 5, 10, 30$.

Chapter 8

# SIMULATION OF EXPLOSIVE VOLCANIC ERUPTIONS

## *8.1 Theoretical and Numerical Models of Explosive Volcanic Eruptions*

Explosive volcanic events are characterized by the injection in the atmosphere of a mixture of gas and pyroclastic material at high velocity and high temperature. The eruptive mixture is the result of gas exsolution and magma fragmentation processes occurring during the magma ascent along the conduit. Steam can also be released as a consequence of the interaction of magma with underground aquifers. When the eruptive mixture enters into the atmosphere, it can evolve into a buoyant plume called Plinian column, or collapse and form pyroclastic flows on the ground surface, depending on the heating and the entrainment of air.

Since the mid-1970s, notable work has been dedicated to the physical description of these volcanic processes. The first theoretical studies on the dynamics of eruption columns were made in 1976 by Sparks and Wilson [185] and in 1978 by Sparks et al. [186], who presented models of generation and emplacement of pyroclastic flows caused by column collapse. The development in the following years of many one-dimensional steady state and homogeneous flow theoretical models [181, 205, 208, 46, 210, 23], accompanied by analogue laboratory experimentation [203, 83, 25, 100, 211], allowed the explanation of important aspects of the physical behaviour of volcanic plumes and pyroclastic flows. Among the various works, for instance Denlinger in 1984 presented a model for the generation of ash clouds from pyroclastic flows by employing the boundary layer theory [46], and applied this model to the 1980 eruption at Mount St. Helens (USA). In the context of Plinian eruptions, steady state and single-phase plume theory models such as those of Wilson and Walker [205] of 1987 and the one of Woods [208] of 1988 have been formulated to study in particular the conditions that lead to the generation of a buoyant plume through air entrainment, in an attempt to predict the buoyant or collapsing nature of the eruption column.

Although important, theoretical formulations are based on very simplified assumptions, and in particular they are unable to describe time-dependent processes, nonequilibrium effects and multidimensional phenomena.

A fundamental progress in the analysis of explosive volcanism has been achieved with the development of numerical multi-phase models. Early numerical studies of volcanic processes were made in 1984 by researchers at the Los Alamos Laboratory (Wohletz et al. [206]), who employed a two-dimensional transient two-phase flow model to simulate caldera-forming eruptions. The simulations modeled both processes in the magma chamber and the eruption dynamics in the atmospheric domain. Further work was performed at Los Alamos in the following years, beginning with the contributions of Valentine and Wohletz in 1989 [197, 196] and 1990 [207]. In these works the processes occurring in the magma chamber were not considered, and steady state conditions were assumed at the volcanic vent. The approach used by these researchers was based on the physical and numerical two-phase model of Harlow and Amsden [75] (1975). The flow dynamics here is described by the equations of mass, momentum and internal energy for the two phases (gas and pyroclastic particles in these volcanic applications). Drag, heat transfer, gravity, and exchange of momentum and energy related to the gas pressure gradient are taken into account, as well as gas viscous effects that are modeled by a stress tensor in the momentum and energy equations. The numerical algorithm used to solve the governing equations is based on a technique known as Implicit MultiField method (IMF). Main features of this method are the implicit

treatment of the momentum exchange term, and the employment of an iterative procedure for pressure, which is corrected until mass conservation is satisfied up to a residual. First codes that implemented this IMF approach were the KACHINA program [6] (Amsden and Harlow, 1974), and the KACHINA with Fully Implicit Exchange (K-FIX), the latter developed at Los Alamos in 1977 by Rivard and Torrey [168] to model the interaction of water and steam in a nuclear reactor. These codes and following versions (e.g. DASH code) were then used by Wohletz and co-workers in volcanology.

Important aspects of the thermo-fluid dynamics of eruption columns were demonstrated by the numerical simulations obtained by two-phase modeling, and especially the transient behaviour of the gas-pyroclasts mixture. Valentine and Wohletz in [197] studied in particular the physical conditions at the volcanic vent that generate Plinian or collapsing columns. The numerical experiments involved a hot mixture of gas (treated as a single-component ideal gas) and solid particles entering an atmosphere stratified in pressure and temperature. The domain adopted was two-dimensional with an axisymmetric configuration. Additional results were obtained by Valentine et al. in [198] and [199]. In the latter work these authors studied in particular the effects of the presence of a caldera rim.

Further progress in the numerical modeling of volcanic plumes and pyroclastic flows was realized by Dobran et al. [51] in 1993 and Neri and Dobran [150] in 1994. The previous model by Valentine and Wohletz [207] was extended to consider a two-component gas phase, made of water vapor and atmospheric air, and to model the dense gas particle regime (granular flow) according to a kinetic theory description. The numerical method used was again based on the model of Harlow and Amsden [75], and the implementing program belonged to the family of "FIX" codes developed from the K-FIX code of [168]. Several numerical experiments were performed on a two-dimensional axisymmetric domain with different steady state vent conditions to study in particular the influence of eruption parameters on the dynamics of eruption columns [150]. These simulations provided further insights in the study of volcanic processes, highlighting once more the unsteady behaviour that may characterize collapsing columns. In particular the results of the simulations showed columns exhibiting sustained oscillations of fountain heights and flow properties, flow instabilities producing the so-called phoenix clouds, which rise on the top of the pyroclastic flow, columns of transitional type between Plinian and collapsing (suspended flows).

Many other studies of volcanic phenomena based on the first multiphase model of Dobran, Neri and Macedonio [51] were developed by the same authors or co-workers. For instance the companion papers [162, 156] focus on the role of magma composition and water content in pyroclastic dispersion dynamics. The initial model of [51] has also been extended to account for particles of different sizes. In [151] a first extension to two particulate phases was introduced. This model was then used for example in [154] to study the mass partition between convective and collapsing transport systems, which is important especially in the interpretation of field deposits. The most recent version (2001) of this model and its implementing code (PDAC, Pyroclastic Dispersion Analysis Code) is described by Neri et al. in [153, 155]. Here a mixture of generic $N$ different particulate phases is considered. Accounting for particles of various size and microscopic density is important in order to be able to describe elutriation processes, that is the separation of particles of different size and density under the concurrent action of convective fluid motion and gravity forces. Recent applications of this model to existing active volcanoes include a study for pyroclastic flow hazard assessment of Vesuvius (Italy) [160, 192], and modeling of the transient dynamics of the Volcanian explosions occurred at Soufrière Hills Volcano, Montserrat, in 1997 [32] (all works of 2002). An original aspect of the latter work is the attempt to combine the simulation of explosive conduit evacuation and pyroclastic dispersal.

Other recent work (2004) on the simulation of Plinian clouds and pyroclastic flows and surges has been performed by Dartevelle [43] and Dartevelle et al. [44], by using a numerical code, MFIX, Multiphase Flow with Interphase Exchange [190], that was developed at the National Energy Technology Laboratory and Oak Ridge National Laboratory for studying fluid-solid systems, on the basis of the

Table 8.1: Physical parameters for the two phases.

| Quantity | Value | Unit |
|:---:|:---|:---|
| $R$ | 287.0 | J/(kg K) |
| $\gamma$ | 1.4 | |
| $c_{vd}$ | $1.3 \cdot 10^3$ | J/(kg K) |
| $\mu$ | $\mu = 10^{-5}$ | Pa s |
| $\kappa_g$ | 0.05 | W/(m K) |

K-FIX code of [168]. The MFIX code has been modified and extended over the years [189], and recently adapted by Dartevelle and co-workers to geophysical applications ((G)MFIX). The MFIX program is currently used also by J. Dufek and G. W. Bergantz in the context of rhyolitic conduit eruptions [56].

There is an extensive literature on volcanic processes and the brief list of works presented here is by no means exhaustive. Our aim was to introduce the subject of explosive volcanic eruptions and describe some of the contributions that have given us the guidelines for our work. Some additional literature specifically related to overpressured volcanic jets and decompression phase will be discussed in Section 8.5. Good reviews on volcanologic modeling, which have helped us in writing part of this introductory section, can be found for instance in [152, 50, 209]. Let us mention to conclude some work on volcanic ash tracking [180] and simulation of volcanic plumes on the large scale [158, 79], and other recent studies on pyroclastic flows [22].

## 8.2   Application of the Dusty Gas Flow Model

We apply the dusty gas flow model presented in Chapter 7 with the aim of simulating some of the processes that characterize explosive volcanic events. Indeed, the original motivation for the development of the two-phase flow model (7.1) was the numerical study of volcanic phenomena. The eruption mixture in this framework is described as a two-phase flow made of gas and solid particles of a single size. In particular, the gas phase is assumed to be dry air (no water vapor content). Some of the the physical parameters adopted for the two phases are reported in Table 8.1.

As we have seen, our model accounts for inter-phase drag, heat transfer, and gravity. To start our work in this application area, our aim was to keep the model as simple as possible while still allowing the simulation of some important features of volcanic columns. In particular, we neglect viscosity within the gas phase and effects of turbulence. As noted in [100, 197], viscosity plays essentially no role in the eruption dynamics. The Reynolds number of these flows is very large, $Re \sim 10^{10}$ to $10^{12}$, showing that viscous forces are negligible with respect to inertial forces. In [197] it is also shown that viscous forces are negligible with respect to buoyancy forces and thermodynamic (pressure) forces. However, the fact that the Reynolds number is very large indicates that turbulence is likely in these flows. In modeling the first stages of explosive volcanic eruptions (as considered here) when compressibility effects are the predominant ones we consider the omission of this contribution a reasonable approximation.

### 8.2.1   Software

We solve the system of equations (7.1) by employing the numerical techniques detailed in Chapter 7. As already discussed, for the hyperbolic portion of the system we use the wave propagation methods as implemented in the CLAWPACK software. The basic Fortran routines of this package have been adapted and extended to our model.

In particular, I implemented the two-phase model on quadrilateral grids with adaptive mesh refinement, and on three-dimensional Cartesian grids. Computations have been mainly performed in two space dimensions with an axisymmetric configuration. Results of some preliminary work in three dimensions are also reported.

## 8.3  Numerical Simulations

We present results of two sets of simulations on which we have focused our computational work. In the first set we test the performance of our model in describing the dynamics of pyroclastic dispersion in the atmosphere and the sensitivity to the variation of some eruption parameters that influence such processes. In the second set of experiments we study the fluid-dynamic structures of overpressured volcanic jets and in particular the different wave patterns that may develop depending on the crater geometry. For all the simulations the general set-up of the problem is the same and described below.

### 8.3.1  Initial and Boundary Conditions

We consider the injection of a hot supersonic particle-laden gas from a volcanic vent into a cooler atmosphere (e.g. [207, 51, 150, 151, 154, 156, 155]). Initially, a standard atmosphere vertically stratified in pressure and temperature is set all over the domain. At the vent, the gas pressure, the velocities and temperatures of the two phases, and the dust volumetric fraction are assumed to be fixed and constant.

The ground boundary is modeled as a free-slip reflector. For two-dimensional experiments, an axisymmetric configuration of the flow is used, and system (7.1) is rewritten in cylindrical coordinates. Analogously to the result shown for the standard Euler equations in Section 2.4.3, we obtain a new set of equations with the same form of (7.1) on the left-hand side, but with an additional geometric source term on the right-hand side. This additional source term is treated numerically with an operator splitting technique and by employing a Runge–Kutta solver for the corresponding system of ODEs to be solved in time. In this two-dimensional axisymmetric configuration, half of the volcanic vent, of diameter $D_v$, is located in the lower left-hand corner of the computational domain, the symmetry axis is modeled as a free-slip reflector, while the upper and right-hand edges of the domain are free flow boundaries and all the variables gradients are set to zero.

For three-dimensional experiments we have performed our simulations in an octant, collocating a quarter of the vent in a corner. The sides of the octant adjacent to the vent location are modeled again as free-slip reflectors and the other two lateral sides and the upper edge of the computational domain are free-flow boundaries.

## 8.4  Pyroclastic Dispersion Dynamics

As observed in Section 8.1, volcanic columns produced by explosive events can exhibit a different pyroclastic dispersal behaviour. The interaction between the hot particulate-laden jet and the atmosphere may produce a buoyant plume (Plinian column) or a collapsing column, depending on the heating and entrainment of air. Collapsing columns present the general behaviour illustrated in Figure 8.1 [150], consisting of the generation of a fountain above the vent, a recirculation region of pyroclastic material, and pyroclastic flows spreading laterally. Moreover, plumes buoyantly rise above the flow. There are several parameters that control the behaviour of the column and in particular material ejected with low density, high temperature and velocity, and small ratio of jet area to jet volume favor the development of a buoyant column (Dobran [49]).

As already mentioned, Neri and Dobran in [150] investigated numerically the influence of eruption parameters on the thermofluid dynamics of volcanic columns by adopting a two-phase model based on [75]. The results obtained by these authors on the different behaviour of eruption columns as

a function of vent diameter $D_v$ and exit velocity $v_v$ of the erupting mixture are shown in Figure 8.2. These results correspond to a particle diameter $d = 10\,\mu m$, a microscopic particle density $\rho_d = 2300\,kg/m^3$, a vent pressure $p_v = 0.1\,MPa$, a vent temperature $T_v = 1200\,K$, and a water vapor content of 0.8 wt %. The circles in this figure represent collapsing columns that display steady or quasi-steady state conditions after a few minutes of transient fountain building; the triangles refer to collapsing columns with oscillatory behaviour of flow properties in the fountain and pyroclastic flow even after a period of fountain building; squares represent columns at the transition between collapsing and Plinian (suspended flows) that may change their behaviour during the eruption. Moreover, the region between the short dashed lines indicates the presence of sustained oscillations, and the cross-hatched zones indicate the gradual transition between the various regions. An important conclusion of the study in [150] is that there is no clear separation boundary between the buoyant and collapsing columns.

Here we report a selection of results from a set of simulations that we have performed with data taken from this work of Neri and Dobran. The aim is to observe how sensitive our model is to parameters that influence pyroclastic dispersion processes and to see how it compares with the results in [150]. The physical model assumed in this work is more complex than ours, and takes into account several effects that we neglect. Among these, viscosity of the gas, turbulence, water vapor content, exchange of momentum and energy between the two phases related to the gas pressure gradient, and the dense regime for the particulate phase. Despite the simplifications of our model, we will see that we are able to capture some of the relevant features of the various eruption styles that have been described in [150].
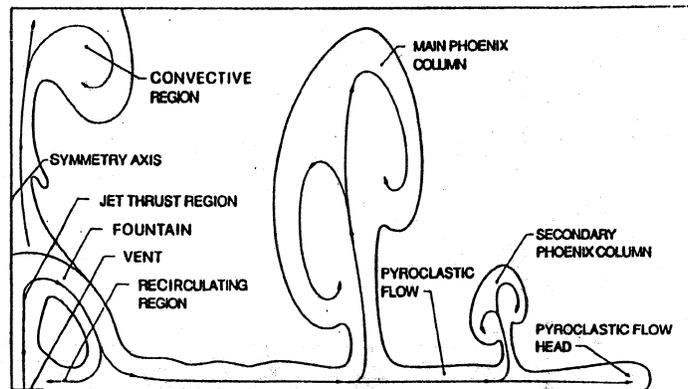


Figure 8.1: Characteristic features of a collapsing column. (From Neri and Dobran [150], reproduced with the courteous permission of AGU).

### 8.4.1   Numerical Simulations

*Vent Conditions*

The gas and dust phase are assumed to be in thermal and mechanical equilibrium at the vent, that is, they have the same temperature $T_v$ and the same exit velocity $v_v$. Different values of vent diameters $D_v$ and velocities $v_v$ are considered, while the other variables describing the vent conditions are kept fixed, and are assumed equal to those corresponding to the results of Figure 8.2. The only difference with that set of data is that we do not consider the water vapor content. In [150] the authors observe
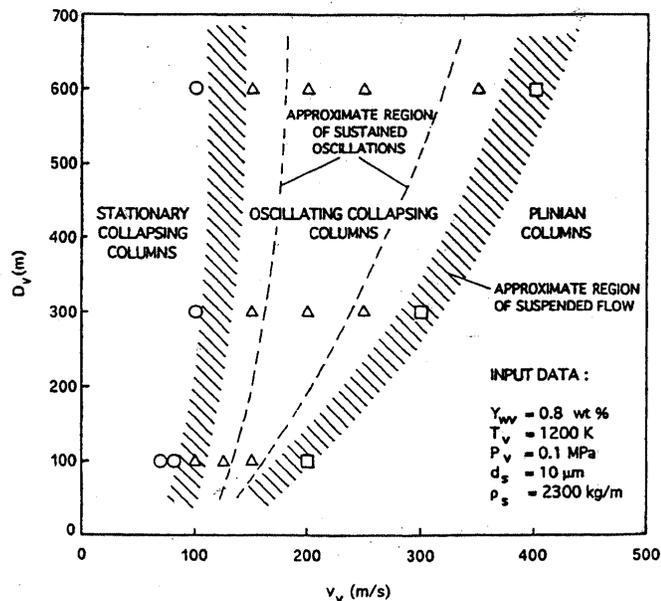
Figure 8.2: Regions characterized by different types of eruption columns as a function of vent diameter $D_v$ and exit velocity $v_v$. (From Neri and Dobran [150], reproduced with the courteous permission of AGU).

that the effect of an increase of the water content is a shifting to the left of the divided cross-hatched region in Figure 8.2 between the Plinian and oscillating collapsing columns.

Data are summarized in Table 8.2 (subscript $v$ refers to the vent), together with the physical properties assumed for the dust. We maintain the same nomenclature as in [150] for the simulations. Simulations with the same letter are characterized by the same diameter. Note that for this set of experiments the vent pressure is balanced with the atmospheric pressure at the vent exit. Moreover, vent conditions are supersonic relative to the eruptive mixture, and they are representative of jet conditions after its decompression in the volcanic crater (see related discussion in Section 8.5).

Table 8.2: Vent conditions for the set of simulations used to study pyroclastic dispersion dynamics.

| Simulation | $D_v$ [m] | $v_v$ [m/s] | $p_{g,v}$ [MPa] | $T_v$ [K] | $\vartheta_{d,v}$ | $d$ [$\mu$m] | $\rho_d$ [kg/m$^3$] |
|---|---|---|---|---|---|---|---|
| A2 | 100 | 80 | 0.1 | 1200 | 0.01 | 10 | 2300 |
| A6 | 100 | 200 | 0.1 | 1200 | 0.01 | 10 | 2300 |
| B3 | 300 | 200 | 0.1 | 1200 | 0.01 | 10 | 2300 |
| B5 | 300 | 300 | 0.1 | 1200 | 0.01 | 10 | 2300 |

*Simulation A2: Stationary Collapsing Column.*

Figure 8.3 shows the evolution of the eruptive mixture as computed for simulation A2, characterized by $D_v = 100\,\mathrm{m}$ and $v_v = 80\,\mathrm{m/s}$. In agreement with [150], we can recognize the typical features of a collapsing volcanic column, that is, fountain building above the volcanic vent, radially spreading pyroclastic flow, material recycling from the collapsed column back into the fountain, and rising of ash plumes from the pyroclastic flow. At about $10\,\mathrm{s}$ and $400\,\mathrm{m}$ above the vent the two-phase flow jet loses its vertical thrust, and begins to form a collapsing column. After the collapsed column has hit the ground, material starts being recycled into the fountain. As the time evolves the impact distance from the vent decreases and the column tends to stabilize with a steady narrow shape (as already observed in [150]).

In Figure 8.4 we display results computed on two different grid resolutions (cell size $=10$ m on the left, and cell size $=5$ m on the right). We can see that a smaller cell size produces a longer run-out of the pyroclastic flow and a smaller thickness, but there is no notable difference in the fountain height and in the dynamics of the collapse. The significant difference in the location of the flow head on the ground can be in part related to the type of free-slip boundary condition used, though the same effect of the grid resolution has been observed also in [51], where a no slip boundary condition is employed.

In Figure 8.5 we highlight the features of the recirculation region displaying a contour plot of the dust density together with the gas velocity vector field, as computed on the finest grid.

Figure 8.6 shows three-dimensional results for the same eruption. Though the mesh used is very coarse, and in particular anisotropic effects are produced as a consequence of the poor discretization of the circular vent on the Cartesian grid, there is qualitative agreement with the two-dimensional results with axisymmetry.

Relating our results with those in [150], first of all we have seen that the type of stationary collapsing column we observe is consistent with the data in Figure 8.2. Moreover, our plots of physical quantities are in agreement with those reported in [150]. In particular, the column height and the column impact distance are comparable. There is a difference in the length of the run-out of the pyroclastic flow, which is larger in our computations. This is not surprising, since we use a free slip boundary condition on the ground, whereas in [150] a no slip condition is used (consistently with their model that has viscous terms).

*Simulation A6: Transitional/Plinian Column.*

Figure 8.7 shows the results for Simulation A6, which has the same vent diameter $D_v = 100\,\mathrm{m}$ as A2, but a greater exit velocity, $v_v = 200\,\mathrm{m/s}$. The increase in the jet velocity, keeping $D_v$ fixed, produces a much more buoyant column, which in this case appears of transitional/Plinian type. This column reaches a height of about $2200\,\mathrm{m}$, and then begins to form a radially suspended flow from which some material rises buoyantly. Later, the suspended flow is reduced and the eruptive mixture develops as a buoyant column. Again, our results are consistent with the data in Figure 8.2, which indicate an eruption on the right edge of the transition region between collapsing and Plinian regimes for the considered values of diameter and exit velocity. In this case, omitting the water vapor content does not seem to influence the column style, at least in the the first minutes of the process. Moreover, our plots show qualitative agreement with those displayed in [150] for the same simulation, and in particular the column height is about the same.
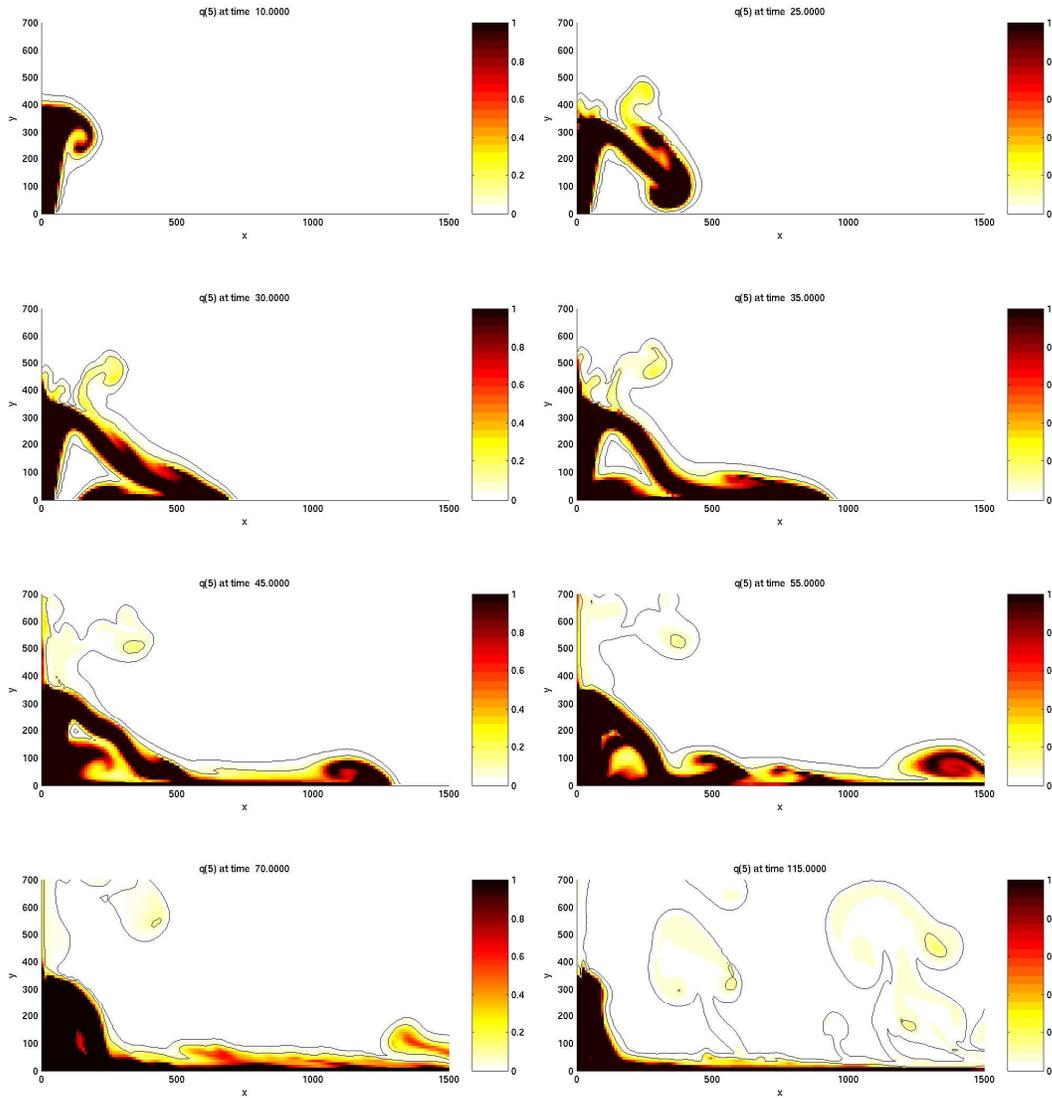
Figure 8.3: Simulation A2. Collapsing column. Dust density at time $t = 10$, 25, 30, 35, 45, 55, 70, 115 s. Computational domain: 3000 m $\times$ 3000 m. Cell size = 10 m ($300 \times 300$ cells). Contour values = $10^{[-4:1:0]}$ [kg/m$^3$].
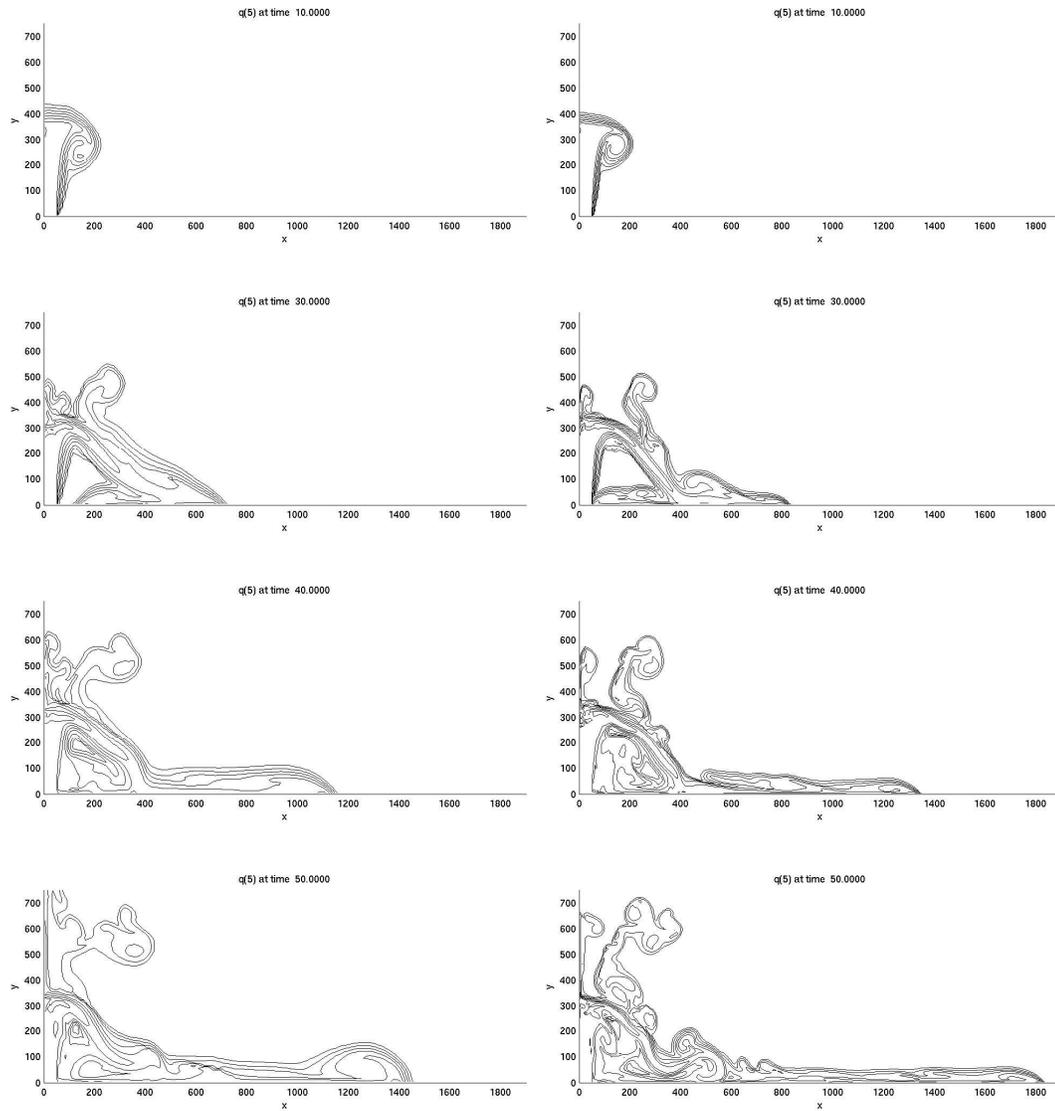
Figure 8.4: Simulation A2. Comparison between two different grid resolutions. Dust density at time $t = 10, 30, 40, 50$ s. Left: $\Delta x = 10\,m$, Right: $\Delta x = 5\,m$. Contour values $= 10^{[-5:.5:2]}$ [kg/m$^3$].
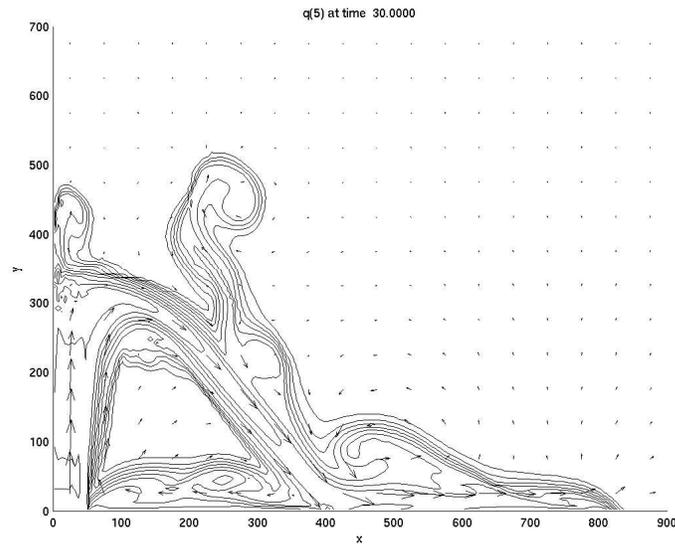
Figure 8.5: Simulation A2. Dust density contours and gas velocity vector field at $t = 30$ s. Contour values $= 10^{[-5:.4:2]}$ [kg/m$^3$]. Computational domain: 2000 m $\times$ 1000 m. Cell size $= 5$ m ($400 \times 200$ cells).
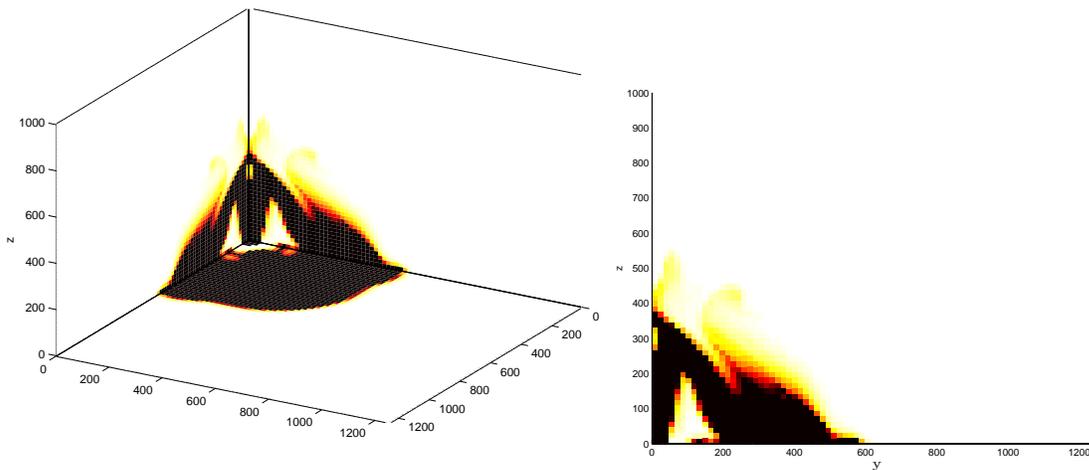


Figure 8.6: Simulation A2. Dust density at time $t = 30$ s. Right: $x$-slice.
Computational domain: octant with $80 \times 80 \times 64$ cells (uniform grid). Cell size $= 15.7$ m. CFL $= 0.9$.
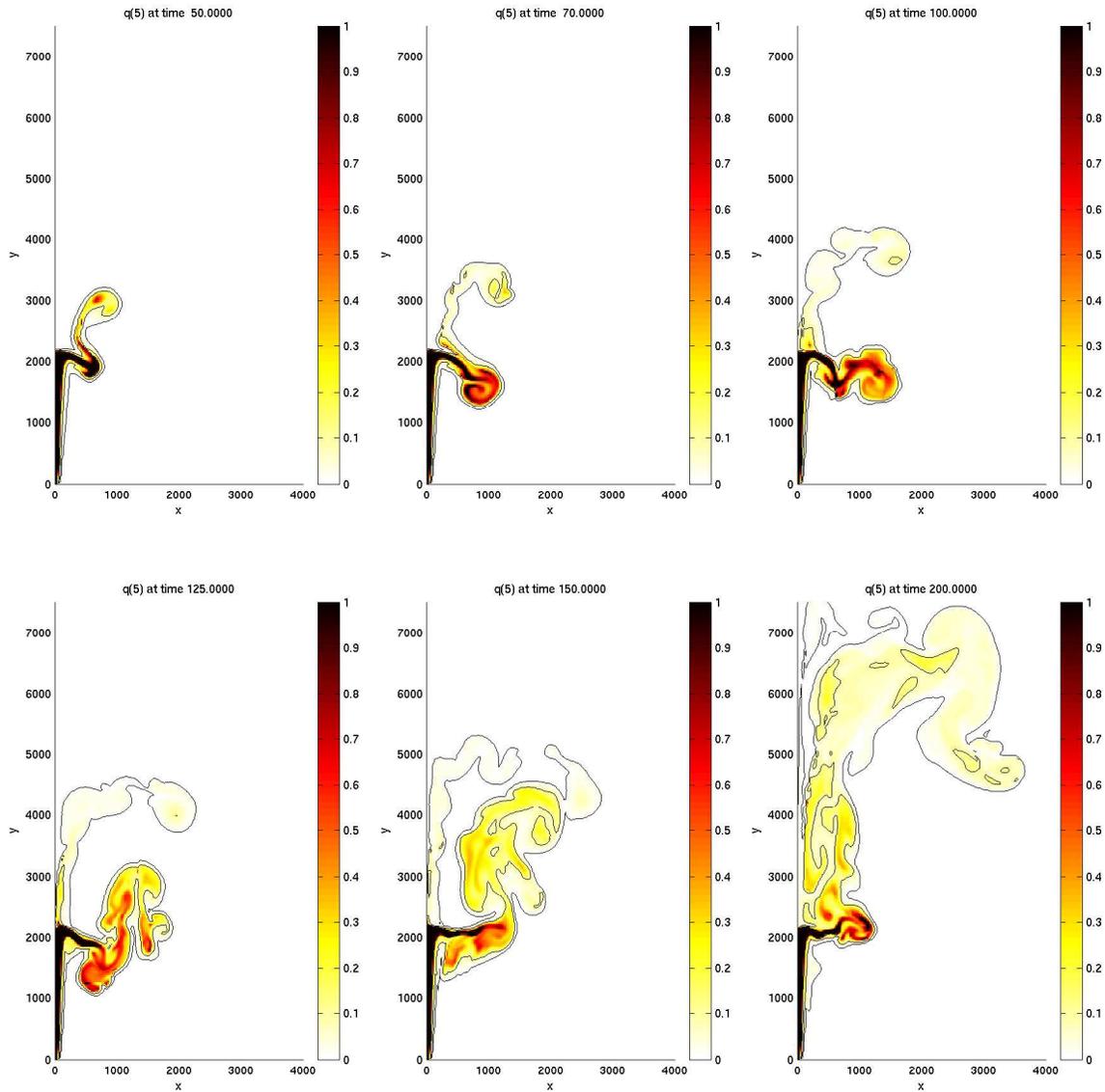
Figure 8.7: Simulation A6. Dust density at time $t = 50, 70, 100, 125, 150, 170$ s. Contour values $= 10^{[-5:1:0]}$ [kg/m$^3$]. Computational domain: 5000 m $\times$ 9000 m. Cell size $= 25$ m ($200 \times 360$ cells).

*Simulation B3: Oscillating Collapsing Column.*

In Figure 8.8 we display some results for Simulation B3. Here the exit velocity is the same as in Simulation A6, $v_v = 200\,\mathrm{m/s}$, but the vent diameter is increased to $300\,\mathrm{m}$. Differently from A6, we observe a collapse of the column, with some of the typical features already noted for A2: recirculation region, pyroclastic flow spreading on the ground, and plumes rising above it. However, differently from A2, in this case the eruption mixture exhibits a strongly unsteady character, with oscillations of the collapse height (also at later times, here not shown). This behaviour agrees with Figure 8.2, where the point corresponding to this simulation is located in the middle of the region of oscillating collapsing columns, and with other observations in [150].
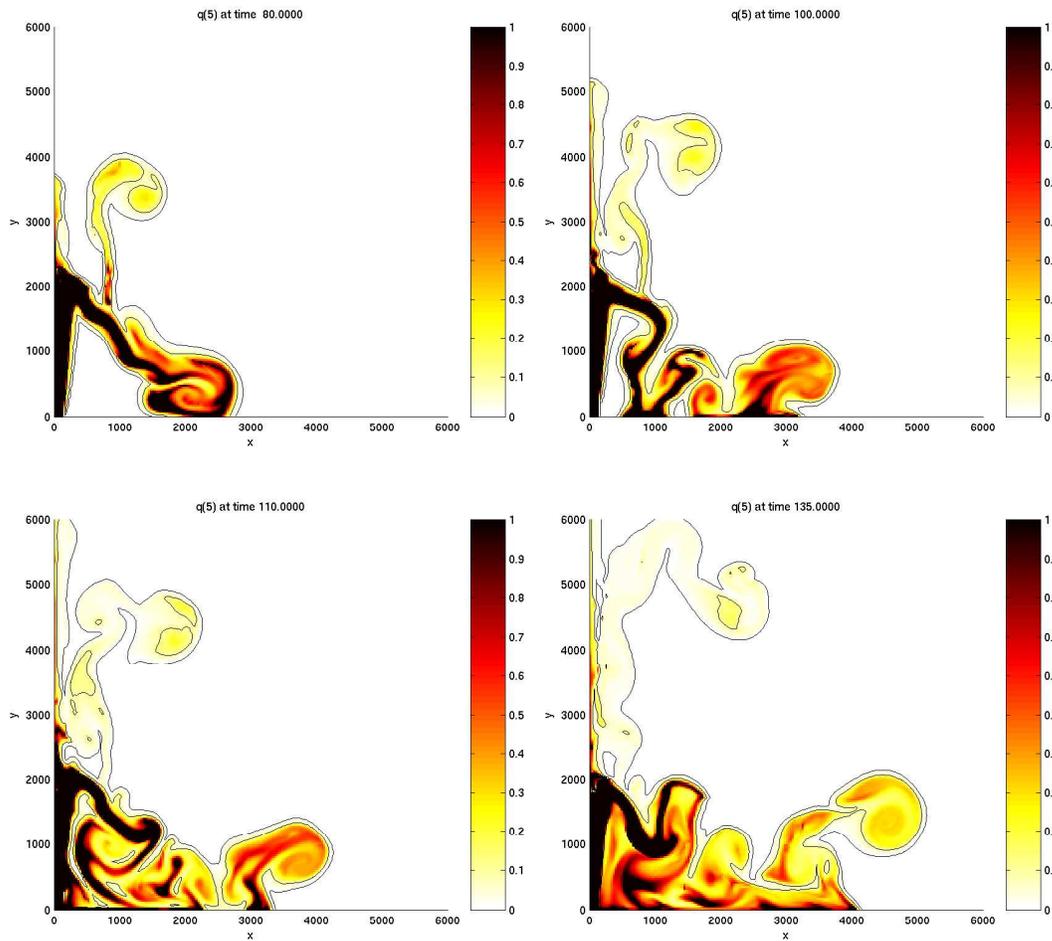


Figure 8.8: Simulation B3. Dust density at time $t = 80, 100, 110, 135$ s. Contour values $= 10^{[-5:1:0]}$ [kg/m$^3$]. Computational domain: $7800$ m $\times$ $9000$ m. Uniform grid with cell size $= 30$ m ($260 \times 300$ cells).

*Simulation B5: Transitional Column.*

Results for simulation B5 are displayed in Figure 8.9. Here the vent diameter is the same as for B3, $D_v = 300\,\mathrm{m}$, but the exit velocity is higher: $v_v = 300\,\mathrm{m}$. This eruption exhibits transitional features. After the building of the fountain, which reaches a height of about 5000 m, material is spread radially generating a suspended flow. Then, a portion of the column collapses, forming a pyroclastic flow on the ground, while some other material ascends buoyantly. Comparing our plots with those in [150], we observe qualitative agreement in the first stages of the column evolution (about the first two minutes). Specifically, analogous features are the radially suspended flow and the collapsing portion of material. However, while in our case the column mainly collapses, in [150] instead it develops into a Plinian column. Presumably, this discrepancy is related to the omission of the water vapor content in our model. Thus, referring to Figure 8.2, we can still collocate this eruption in the transitional region because of the development of the suspended flow and buoyancy of a part of the column, however our results should be considered closer to the edge with the collapsing regime. As already mentioned, the authors in [150] observe that a shift of this type of the transitional suspended flow region occurs varying the water content.

### 8.4.2  Conclusions

The computed results show that our model is able to capture the characteristic features of different styles of eruptions. In particular, we observe columns exhibiting an unsteady character and a transitional behaviour for some choices of the parameters. Moreover, the sensitiveness of our model to the eruption parameters $D_v$ and $v_v$ is consistent with the trend indicated by the results obtained by Neri and Dobran in [150], which also agree with laboratory studies, e.g. [25], and previous two-phase flow modeling approaches [207, 198].

Thus, despite the simplifications of our model with respect to the one of [150], we observe overall qualitative agreement, at least in the first few minutes of simulation. This confirms that the mechanisms that govern the column building and the dynamics in the first stages of the eruption are not significantly influenced by gas viscosity and turbulence.

Following again Neri and Dobran, we finally remark that the columns heights $Z_c$ obtained in our numerical experiments (which as already noted are about the same as in [150]) are comparable with the values that can be reasonably predicted through the simple formula [51]

$$Z_c = \frac{v_v^2}{2g}, \tag{8.1}$$

obtained by applying Bernoulli's equation along a stagnation streamline. For the simulations presented (8.1) gives $Z_c = 326, 2040, 4591$ m for $v_v = 80, 200, 300$ m/s.
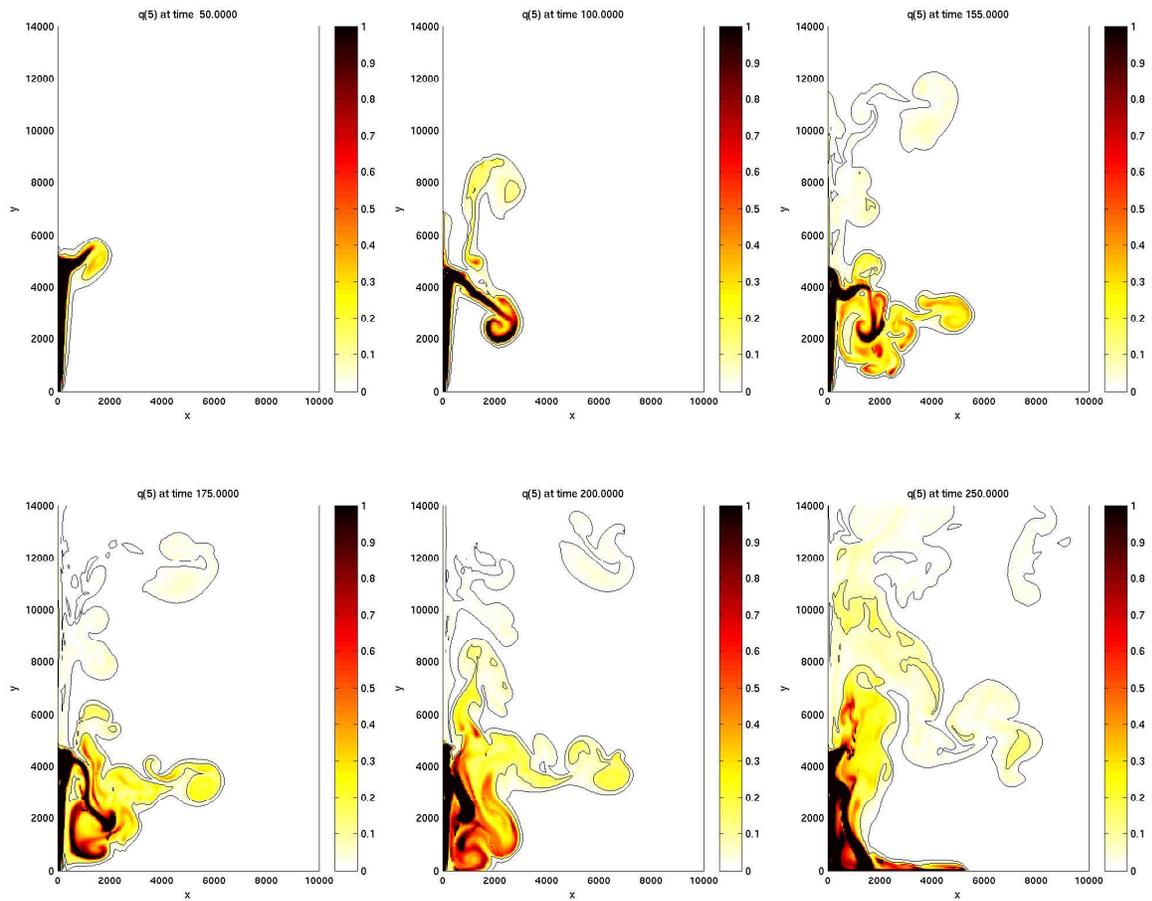
Figure 8.9: Simulation B5. Dust density at time $t = 50, 100, 155, 175, 200, 250$ s. Contour values $= 10^{[-5:1:0]}$ [kg/m$^3$]. Computational domain: 10000 m $\times$ 20000 m. Uniform grid with cell size $= 30$ m $(200 \times 400$ cells$)$.

## 8.5 Overpressured Volcanic Jets

The dynamic and thermodynamic conditions at the volcanic vent that produce explosive volcanic eruptions are determined by complex processes occurring along the conduit, which lead to the emission of a mixture of fragmented magma and exsolved volatiles at high pressure, temperature and velocity. Theoretical work [210], laboratory experiments [100] and modeling of processes along the conduit [162], give evidence that the eruptive flow at the vent exit can be largely overpressured with respect to ambient, and develop a supersonic flow in the crater and atmosphere above it. The speed of sound of gas containing particulate material can be very low [100, 136, 171] (see also Sections 3.3.3 and 7.4.1), hence particle-laden volcanic flows are often supersonic. When the overpressure of these volcanic jets is large, the flow may develop wave patterns of the type illustrated in Figure 8.10 [88].

The mechanisms of the decompression phase control the transition between the conditions of the flow in the conduit and the subsequent development of the column in the atmosphere, and this phase plays a crucial role in determining the behaviour of the eruption material in its evolution through the atmosphere [210].

The features of the expansion process are not susceptible to direct observation. In particular, as pointed out in [100], the internal shock structure of underexpanded jets is very difficult to document, because of the opacity of volcanic fluids, and because such phenomena often occur deep within the crater.

Various studies have been dedicated to the analysis of the mechanisms of the decompression process. Most experimental studies and most models assume that the multi-phase flow in the jet thrust region behaves as a single-gas or a *pseudogas*[1]. This approximation relies on the hypothesis that the momentum and energy exchange between the phases occurs rapidly enough so that they are in mechanical and thermal equilibrium. Under these conditions the mixture can be described as a perfect gas whose density is equal to that of the mixture and whose pressure is equal to that of the gaseous phase. The gas constant $R$ and the isentropic exponent $\gamma$ of the pseudogas are average values that take into account the relative mass of the solid phase (see [202]).

Kieffer and Sturtevant [100] (1984) studied volcanic overpressured jets by performing analogue laboratory experiments. Pure gases were discharged from reservoirs having pressures and geometries such that the fluid velocity in the jets was initially supersonic (and later decayed to subsonic). They used Freon 12 and Freon 22, two gases of high molecular weight and high density which are good analogs of volcanic gases carrying particulate material, and Helium, a low-molecular weight and low-density gas that was used for comparison with heavier gases. They highlighted the compressibility effects of the erupted jets, detecting atmospheric shock waves and observing, immediately after the passage of the flow head, the typical shock structures of steady underexpanded supersonic jets, such as barrel shocks and Mach disks (see again Figure 8.10). Together with the pure gas approximation, a limit of this experimental work is the lack of a scaling relation for gravity, so gravitational forces are not modeled.

Woods and Bower [210] (1995) studied the decompression process of volcanic jets by adopting a steady one-dimensional single-gas model, which also neglected gravitational forces. The one-dimensional approximation limited their analysis to very narrow craters (opening angle $< 30°$) and forced them to consider separately free decompression and decompression within a crater, while in reality there is continuous transition between these two cases.

The pseudogas approximation was adopted also by Lagmay et al. [104] (1999), who used two-dimensional computational fluid-dynamic simulations of compressible single-gas flows to investigate the role of crater asymmetry on the production of directed pyroclastic flows in small-scale (Soufrière type)

[1]Sometimes in the geophysical literature the pseudogas or homogeneous gas flow model is called dusty gas model. Here instead we intend as dusty gas model a two-phase flow model that accounts for mechanical and thermal disequilibrium between the two phases, as for instance in [176].

explosive eruptions. They showed that crater morphology affects the orientation of the volcanic jet, which can become tilted, and hence the flow path direction of pyroclastic flows produced by fountain collapse. In particular, they applied their model to the eruption of Mayon volcano in 1984.

In the framework of multiphase flows models, Neri et al. [156] (1998) performed two-dimensional axisymmetric simulations of overpressured eruptions on a fixed-geometry crater, with the objective of studying the influence of magma composition and water content in the pyroclastic dispersion dynamics. The flow conditions at the vent were computed by simulation of magma ascent in the conduit in a companion paper [162]. The work of [156] highlighted the important role played by the exit overpressure of the eruptive material, since the large expansion energy of the mixture at the conduit exit leads to high velocities in the crater region above the vent, thus affecting the column behaviour. Moreover, the authors observed that the radial component of the velocity at the crater rim due to overpressure generates a column with a diameter much greater than that of the crater (consistently with the experimental work [100]).

Numerical multiphase modeling has been extensively used in the last twenty years to study pyroclastic dispersion dynamics processes, but little work has been dedicated in this context to the details of the decompression phase and to the jet internal structure. Here our purpose is to investigate more deeply the mechanisms of the expansion of overpressured volcanic jets by applying our two-phase dusty gas flow model. In particular, we study the decompression dynamics and the wave patterns characterizing the jet structure with different exit pressures and crater geometry. This is also joint work with A. Neri and T. Esposti Ongaro at INGV (Istituto Nazionale di Geofisica e Vulcanologia, Pisa, Italy), with the aim of comparing the results of our model implemented on CLAWPACK with their Pyroclastic Dispersion Analysis Code (PDAC) [155]. Some preliminary comparative results, reported in the following, are encouraging. Let us acknowledge that the above authors already made preliminary studies on this subject [159] (1999) and suggested to us the guidelines of our work.

We focus on the very first stages of the eruptions, until the thrust region has reached its maximum height. In this phase compressibility effects are predominant, and it is reasonable to omit viscosity, turbulence and water vapor content. Also, some tests performed on the same simulations by Neri and Ongaro turning on and off these terms in their more complex model have shown their negligible influence on the small time scale.

### 8.5.1  Single-Gas Underexpanded Jets

We describe in this section some well known features of underexpanded supersonic jets on two-dimensional plane geometry, based on classical analytical studies [40, 127, 105], under the assumption of single-phase perfect gas and steady irrotational and isentropic (except across shocks) flow. First, we recall that the Mach number M of a flow is given by $M = u/c$, where $u$ is the flow velocity, and $c$ the speed of sound. Supersonic flow means $M > 1$.

Let us consider a supersonic plane jet exiting from a nozzle with a Mach number $M_e \geq 1$ and pressure $p_e \geq p_a$ , where $p_a$ is the (receiver) atmospheric pressure. At each edge of the nozzle rim a centered expansion fan develops, whose local properties are described by the *Prandtl–Meyer* function

$$\nu(M) = \sqrt{\frac{\gamma + 1}{\gamma - 1}} \arctan \sqrt{\frac{\gamma - 1}{\gamma + 1}(M^2 - 1)} - \arctan \sqrt{M^2 - 1}\,, \tag{8.2}$$

where $M$ and $\nu$ are the local Mach number and the deflection angle, respectively. In (8.2) an additive constant would in general appear, which is usually set to zero such that $\nu(1) = 0$. Denoting with $M_f$ the Mach number of the flow at the outer edge of the fan, the total deflection of the flow through the
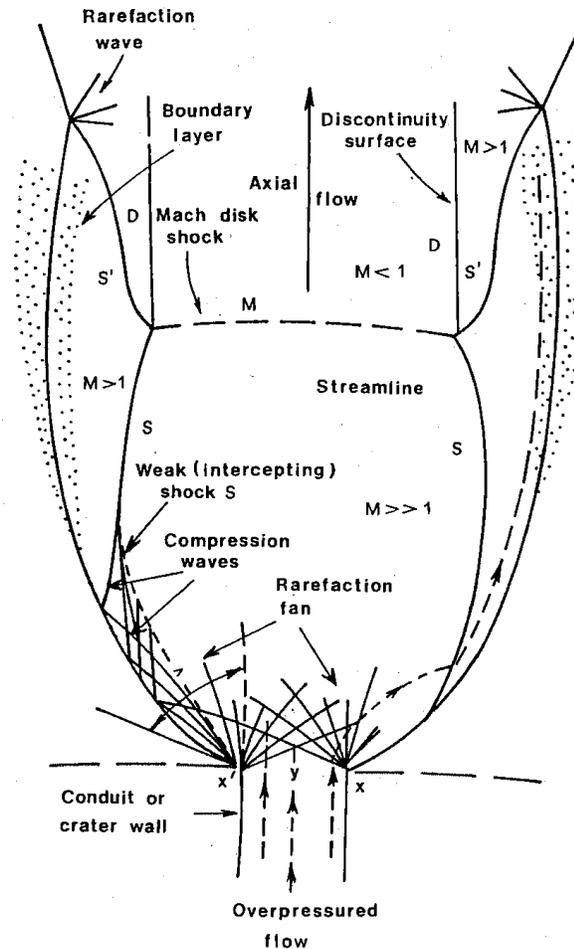
Figure 8.10: Overpressured jet (reproduced from JANNAF Publication [88] (1975), with courteous permission of CPIA).

expansion is given by $\nu(M_f) - \nu(M_e)$. Moreover, $M_f$ is related to the pressure ratio through:

$$\frac{p_e}{p_a} = \left[ \frac{1 + \dfrac{\gamma - 1}{2} M_f^2}{1 + \dfrac{\gamma - 1}{2} M_e^2} \right]^{\frac{\gamma}{\gamma - 1}} . \tag{8.3}$$

For $M \to \infty$ the Prandtl–Meyer angle tends to $\sqrt{\frac{\gamma+1}{\gamma-1}} \frac{\pi}{2} - \frac{\pi}{2}$, and, assuming initial sonic conditions, this represents the maximum angle of deflection of the flow, if vacuum does not occur before it is reached. Note that if $\gamma$ is close to 1 (nearly isothermal flow) this angle of deflection becomes very large.

The two rarefaction waves at the two edges of the nozzle reflect on the jet boundary as compression waves, and due to the inward curvature on the jet boundary (caused by the pressure gradient), each of them soon coalesces into an *intercepting shock*, as required to prevent an envelope singularity. These

two shocks then connect and reflect onto the symmetry axis of the jet. Note that the configuration is symmetric with respect to the axis. Two possible patterns of reflection can be observed, depending on $M_e$, $p_e/p_a$, and the degree of divergence of the exhaust flow. In one case, the two inward-going intercepting shocks meet each other at the symmetry axis and reflect in a configuration called *regular reflection*. This type of reflection is not possible for arbitrary values of the parameters of the incident shock, the angle of incidence $\alpha_1$ and the pressure ratio $p_2/p_1$ (pressure after the shock over pressure ahead of it). For a given shock intensity $p_2/p_1$ there is a maximum possible angle $\alpha^*$, and for $\alpha_1 > \alpha^*$ regular reflection is impossible. As $p_2/p_1 \to \infty$, the maximum angle tends to a value which depends on $\gamma$ (= 40° for air) [105]. As $p_2/p_1 \to 1$, $\alpha^*$ tends to 90°, i.e. regular reflection is possible for any angle of incidence. For $\alpha_1 > \alpha^*$ regular reflection cannot occur, and the incident shock wave must break up at a distance from the surface of reflection (here the symmetry axis), forming a pattern consisting of three shock waves and a tangential discontinuity leaving the point where the shock waves divide. This is called *Mach reflection*. The wave pattern developed in this case in the jet is the one displayed in Figure 8.10. Here a normal shock, called *Mach disk* forms in the jet, connecting the two intercepting shocks (barrel shocks). From each of the two points of intersection (Mach disk triple point) another shock forms which radiates outward, together with a surface carrying a discontinuity in the tangential velocity.

In both the case of regular and Mach reflection, the reflected outward-going shocks intersect the outer boundary of the flow, and all the pattern repeats periodically (diamond-shaped jets). However, the Mach reflection structure is subject to hydrodynamic instability of Kelvin–Helmholtz type along the slip line that destroys this sequence [140, 60].

These features of underexpanded jets that can be studied analytically on plane geometry also characterize axisymmetric jets, as it has been observed experimentally, e.g. [133, 1].

All the above information for single-gas jet flows can be useful, in combination with a pseudogas approximation, to obtain qualitative indications of the wave patterns that we can expect in the two-phase axisymmetric jets that we model, and of which parameters can affect them. First, let us remark that the isentropic exponent of the pseudogas modeling the particle-gas mixture (see [202]),

$$\gamma^{pg} = \frac{c_{pg} + m_d\, c_{vd}}{c_{vg} + m_d\, c_{vd}}, \tag{8.4}$$

where $m_d$ is the relative mass of the solid phase, has a value close to one (this also indicates a flow in nearly-isothermal conditions). Therefore, based on the Prandtl–Meyer function, we expect a very large lateral deflection of the flow at the edges of the vent, and thus a rapid growth in the jet diameter.

With regard to shock patterns, we expect that Mach reflection will be favored by larger overpressures at the vent, since this implies a greater intensity of the intercepting shocks, and by larger crater opening angles, since this increases the angle of incidence.

Although the single gas approximation could be useful to explain some effects, the particle-laden flow can be properly described only by a two-phase model, since relaxation phenomena occur during stages of rapid acceleration and heating.

### 8.5.2   Numerical Simulations

*Vent Conditions and Crater Morphology*

We consider two sets of vent conditions taken from [156] (neglecting water vapor), and, as already mentioned, obtained by numerical modeling of the magma ascent process in the conduit in [162]. We also recall that the work [156] was dedicated to the analysis of aspects of pyroclastic dispersion dynamics on a fixed topography, while here we focus on the decompression phase varying the crater morphology. Data at the vent, together with physical parameters for the particulate phase, are summarized in Table 8.3. The simulations nomenclature is the same as in [156].

Table 8.3: Vent conditions for the simulation of overpressured jets.

| Simulation | $D_v$ [m] | $v_{g,v}$ [m/s] | $v_{d,v}$ [m/s] | $p_{g,v}$ [MPa] | $T_v$ [K] | $\vartheta_{d,v}$ | $d$ [$\mu$m] | $\rho_d$ [kg/m$^3$] |
|---|---|---|---|---|---|---|---|---|
| A | 127 | 211.0 | 201.0 | 4.6 | 1100 | 0.063 | 200 | 2360 |
| E | 127 | 167.0 | 144.0 | 0.49 | 1100 | 0.018 | 200 | 2380 |

Note that here there is disequilibrium in the exit velocities of the two phases, $v_{g,v}$ and $v_{d,v}$, while thermal equilibrium is considered. Also note that the two sets of data are characterized by two very different exit pressures (but both greater than atmospheric).

Computations have been performed on two-dimensional axisymmetric configurations by using different crater geometries. The crater is simply modeled as a wedge. Here the vent diameter $D_v$, where the boundary conditions are imposed, corresponds to the inner diameter of the crater. We will denote with $R$ the crater outer radius and with $\alpha$ its opening angle relative to the vertical. The value $\alpha = 90°$ corresponds to the case of no crater (free decompression). The results that we will show pertain to simulations performed with the following configurations:

- Simulation A: $R = 254$ m, $\alpha = 90°$, $45°$, $30°$. $R = 508$ m, $\alpha = 45°$.

- Simulation E: $\alpha = 90°$.

Moreover, unless otherwise specified, computations with data A have been performed on a uniform grid of $300 \times 600$ cells and cell size $= 12.7$ m, while computations with data E have been performed on a uniform grid of $350 \times 440$ cells and cell size $= 7.9375$ m. In all cases, CFL $= 0.9$ (Courant number). In three-dimensions, results have been obtained for Simulation A for the case of free decompression only (no crater).

To highlight normal discontinuities, we will use the normal Mach number of the mixture (following [51]), defined as

$$M_{\mathrm{m}} = \frac{\mathcal{V}_{\mathrm{m}} \cdot \nabla p_g}{c_{\mathrm{m}} |\nabla p_g|}\,, \tag{8.5}$$

where the mixture sound speed is (see Section 3.3.3)

$$c_{\mathrm{m}} = \sqrt{\frac{\rho_g\, c_{g,\mathrm{isot}}^2}{\vartheta_g \rho_{\mathrm{m}}}}\,, \qquad c_{g,\mathrm{isoth}} = \sqrt{RT_g}\,, \tag{8.6}$$

and the mixture density $\rho_{\mathrm{m}}$ and mixture velocity $\mathcal{V}_{\mathrm{m}}$ are

$$\rho_{\mathrm{m}} = \rho + \beta \qquad \text{and} \qquad \mathcal{V}_{\mathrm{m}} = \frac{\rho \mathcal{V}_g + \beta \mathcal{V}_d}{\rho_{\mathrm{m}}}\,. \tag{8.7}$$

Although these formulas rely on the pseudogas approximation, which is based on the assumption of mechanical and thermal equilibrium between the two phases, and relaxation zones arise within the flow, the quantity $M_{\mathrm{m}}$ is still useful to put in evidence discontinuity patterns and give an indication of supersonic regions. However, care must be taken in interpreting the results, and plots of $M_{\mathrm{m}}$ should be evaluated together with plots of the gas pressure gradient, and plots of velocity and temperature differences between gas and dust.

*Simulation A:* $\alpha = 90°, 45°, 30°$.

Figures 8.11, 8.13, 8.15 show contour plots of the dust density at time $t = 4, 10, 20, 30$ s as computed for Simulation A with crater radius $R = 254$ m and opening angle $\alpha = 90°, 45°, 30°$, respectively. Figures 8.12, 8.14, 8.16 show the gas density, the dust density, the gas temperature, and the gas velocity at time $t = 30$ s for the same cases. Moreover, we compare the internal jet structures corresponding to the three different geometries by displaying in Figure 8.17 both the Mach number and the normal Mach number at $t = 30$ s, and in Figure 8.18 the pressure gradient at time $t = 4$ and 30 s.

A common feature to the three simulations, as expected, are the large radial velocities above the vent, and hence a jet diameter growing rapidly. For $\alpha = 45°$ and $30°$ the crater constraints the path of the lateral expansion, while in the case with no crater the jet decompresses freely in the radial direction with a strong expansion that follows the horizontal wall (see the gas velocity in Fig. 8.12), and which leads to the formation of a barrel shock starting on the ground.

Another common feature to all the simulations is the unsteady vortical structure that characterizes the jet head, and which is caused by the initial rapid acceleration of the fluid. The growth in time of this vortex can be observed in Figures 8.11, 8.13, 8.15.

As we can see from Figures 8.17 and 8.18, shock patterns develop inside the jets, and after a transition time of few seconds, they assume a steady configuration. In the case $\alpha = 30°$ regular reflection occurs, while for $\alpha = 90°$ and $\alpha = 45°$ a Mach disk is formed.

In Figure 8.19 we highlight the Mach disk shock structure, together with the gas velocity vector field, for the free decompression case. The results in the top part of the figure have been computed on a very fine uniform grid, while the results below have been obtained by employing a three-level adaptive mesh refinement, set as to have the same resolution near the shocks (to validate our AMR code, and to show how useful it is, since we typically do not use such a fine uniform grid for our computations). We can clearly recognize the type of pattern of Figure 8.10. Here the Mach disk shock assume a steady position at a height of about 870 m. The weaker shock radiating outward from the point of intersection of the Mach disk with the barrel shock is also partly visible. Preliminary results in three dimensions for the same simulation (data A with free decompression) are displayed in Figure 8.20. As already noted for the three-dimensional results of Figure 8.6, anisotropic effects can be seen caused by the discretization of the circular vent on the coarse rectangular mesh. However, there is qualitative agreement with the two-dimensional axisymmetric computation, and in particular the position of the shocks (including the atmospheric shock) is comparable during the time evolution.

The jet obtained with $\alpha = 45°$ also exhibits a Mach disk, at about $y = 960$ m, but smaller than the one that forms with no crater, and slightly less intense (the computed pressure gradient across the disk is $2.75 \times 10^3$ Pa/m for the case with no crater and $2.48 \times 10^3$ Pa/m for $\alpha = 45°$). The Mach disk branches from a barrel shock that begins at the crater rim, and which is much weaker than the barrel shock observed for $\alpha = 90°$ (about 534 Pa/m at $y = 635$ m vs. $1.18 \times 10^3$ Pa/m for the case with no crater.)

In these two cases in which Mach reflection occurs, $\alpha = 90°$ and $45°$, a shear flow develops from the Mach disk triple point, as it can be observed from the plots of the gas velocity in Figures 8.12, 8.14, and the plots of Mach number in Figure 8.17.

The regular reflection structure of the case $\alpha = 30°$ and its gradual formation in time is illustrated in Figure 8.21, where we display contour plots of the pressure. We can see that in this situation there is a repeated pattern of reflections, with discontinuities of decreasing intensity. Results have been computed with adaptive mesh refinement, so as to obtain a better resolution on shock patterns without the need of using a fine grid in the whole computational domain. In particular, in the bottom part of Figure 8.21 we put in evidence the refinement grid patches generated in the computation. Moreover, Figure 8.22 shows the type of mapped grid used for these experiments with a crater at the ground surface.

In Figures 8.23 and 8.24 we highlight relaxation regions corresponding to areas where spatial or temporal variations of the flow are too rapid for the velocity and temperature of gas and solid particles to follow. In particular, in correspondence of shocks the phenomenon of shock thickening can be observed, that is the presence of a stationary nonequilibrium region behind a frozen shock. Figure 8.23 shows the vertical velocity difference $v_g - v_d$ and the temperature difference $T_g - T_d$ along the $y$ axis at $t = 30$ s for the simulation with no crater. We can clearly notice a large disequilibrium between the two phases where the Mach disk is located, at about $y = 870$ m. Differences in velocity and temperatures characterize also the strong expansion region going from the vent exit, at $y = 0$, to the Mach disk position. Since the solid phase has much larger inertia than the gas, in this accelerating region $v_g > v_d$ (and $T_g < T_d$). Then, in correspondence of the Mach disk the gaseous phase decelerates abruptly, while the solid particles continue to move at higher velocity than the gas, hence in the relaxation region behind the shock $v_d > v_g$ (and $T_g > T_d$). The vertical velocity difference and the temperature difference along $y = 0$ and at $t = 30$ s for the case $\alpha = 30°$ are shown in Figure 8.24, together with a plot of $v_g - v_d$ in the whole domain, and a zoomed view on the region close to the crater. We can recognize several nonequilibrium zones. In particular, we notice the relaxation region with $(v_g - v_d) \leq -20$ m/s behind the first reflected shock close to the symmetry axis, which has a fairly large spatial size (note also that the presence of this nonequilibrium region affects the plot of the normal Mach number). Moreover, it is interesting to observe from the zoomed view on the top-right part of Figure 8.24 the nonequilibrium region with $v_g < v_d$ that arises at the crater rim, where the oblique shock begins to develop. As discussed in [202], p. 218, near the tip of the wedge there is no space for equilibrium to be established, and the shock angle is determined by the gas alone. Farther away the equilibrium shock angle is approached. Let us note that a part from relaxation regions behind shocks, velocity differences are are fairly small compared to the average velocity of the fluid, as it can be deduced by looking in Figure 8.16 at the large values of the gas velocity in the jet thrust region.

In Figure 8.26 we display dust density contours still obtained with $\alpha = 45°$, but with a larger crater radius: $R = 508$ m. The increase in $R$ here does not cause significant changes in the type of shock structure, which is again characterized by a Mach disk. However, differences can be seen in the distortion of the jet boundaries.

Finally, in Figure 8.27, we show preliminary results obtained by T. E. Ongaro with PDAC for this Simulation A with $\alpha = 90°$ and $30°$. Here $R = 241.3$ m. For these computations, some of the effects that can be modeled by PDAC, and specifically the gas viscous terms, turbulence, and water vapor content, have not been included in order to make a closer comparison with our results. Overall, there is qualitative agreement. There are some differences in the unstable vortical region of the columns, but this is not surprising since this zone is very sensitive to small numerical perturbations, as we also noted in the experimentation with our code.

*Simulation E: $\alpha = 90°$.*

Figure 8.28 shows contour plots of the dust density at time $t = 4, 10, 20, 30$ s as computed for Simulation E with no crater, and in Figure 8.29 the gas density, the dust density, the gas temperature, and the gas velocity at $t = 30$ s for the same simulation are displayed.

The most significant difference in the set of data E with respect to A is in the value of the pressure, much smaller for E. This lower pressure leads to a different internal structure with respect to Simulation A with no crater. In fact here regular reflection occurs, as we can see from the plot of the Mach number in Figure 8.30, and plots of the pressure gradient in Figure 8.31. The internal shock pattern is thus similar to the one of case A with $\alpha = 30°$, though here the strength of the shocks is much less intense. As for the other jets, a circulating region growing in time can be seen.

*Atmospheric Shock Waves*

As we can observe from Figures 8.18, 8.21, 8.31, atmospheric pressure waves propagate radially from the vent in every simulation. In Figure 8.25 we show plots of the so called pressure signature (pressure recorded in time) at $(x, y) = (1000, 1500)$ m for the atmospheric waves corresponding to Simulation A, $R = 254$ m, $\alpha = 90°, 45°, 30°$, and Simulation E (no crater).

The steepening clearly visible in the pressure history, which is caused by fluid-dynamic nonlinearities, indicates that the pressure perturbations at this point of recording are shocks (and not simply acoustic waves). After the wave propagates some distance, the pressure behind the front decreases below the atmospheric value, and then it increases again. This gives to the pressure trace the shape of the letter N, and these airwaves are known as *N waves*. It is well recognized that explosive volcanic eruptions may produce atmospheric shock waves characterized by these N-shaped signals. Examples include the explosion of Krakatoa back in 1883 [188] and the explosion at Mt. St. Helens, Wahington, on 1980 May 18 [166, 11, 139]. Analysis of infrasonic pressure waves generated by volcanic explosions is useful to obtain information about explosion overpressures and dust concentration, and many studies have been dedicated to this subject, e.g. [145, 94].

Shock waves caused by explosions propagate at a speed that exceeds the atmospheric sound speed as a function of shock excess pressure [94]. As the wave expands radially the excess pressure drops and the wave decays to acoustic wave. Note from Figure 8.25 that the atmospheric shock for simulations with different crater geometries but same vent conditions A passes through the point $(x, y) = (1000, 1500)$ m at the same time, $t = 4$ s, which gives an average velocity on this period of time of 450.69 m/s. The atmospheric sound speed at the same height $y = 1500$ m is 334.46 m/s. Due to the much smaller overpressure at the vent, in the case of Simulation E the pressure wave is weaker, and its propagation speed is lower. Here the shock wave passes through $(x, y) = (1000, 1500)$ m at $t = 5$ s, which gives an average speed of 360.55 m/s.

### 8.5.3   Conclusions

The proposed wave propagation numerical approach has proved to be effective in the description of wave patterns that develop in underexpanded supersonic volcanic jets. In particular, the adaptive mesh refinement technique applicable to the method is advantageous in the numerical investigation of the jet thrust region, since we are interested in resolving fluid structures in localized spatial areas, which are small compared with the computational domain needed for the simulation.

Our numerical study on overpressure jets has shown results consistent with experimental work, e.g. Kieffer and Sturtevant [100], and in particular with the computational work of Neri and Ongaro, both previous work [159] (1999), and current work pursued in the context of a joint project with us.

We summarize here the most relevant observations inferred from our numerical experiments on overpressured volcanic jets, which agree with the discussion of Neri and Ongaro in [159].

1. As expected from the considerations on the Prandtl–Meyer angle, the jets exhibit great radial velocities above the vent, and the diameter of the developing jet is much larger than the vent diameter. This is also consistent with direct observation of volcanic eruptions (e.g. Mt. St. Helens [129] and Mt. Pinatubo [191]), with experimental work [100], and numerical modeling [156].

2. We observe familiar wave patterns of steady underexpanded jets, also consistently with the experimental work [100]. In particular, as expected from considerations on features of polar shock curves of single-phase perfect gases, transition from regular to Mach reflection is induced by increasing crater opening angle and pressure at the vent. With regard to crater morphology, an important parameter that controls the decompression process and consequent jet structure is the

opening angle, according to both our results, and results of Neri and Ongaro [159]. The crater radius seems to be of minor importance.

3. Shock pressure waves with the typical N-shape signal that characterizes explosive volcanic eruptions are numerically described.

4. We highlighted nonequilibrium effects (relaxation zones), which are significant in the internal jet structure, and shock thickening phenomena.

5. Jets are characterized by unsteady phenomena that cause distortion of jet boundaries. In particular, a vortical structure growing in time is developed at the flow head.

All the observations above suggest the importance of studying the decompression process by a model that accounts for multi-dimensional topography effects, as well as nonequilibrium and unsteady phenomena.

132
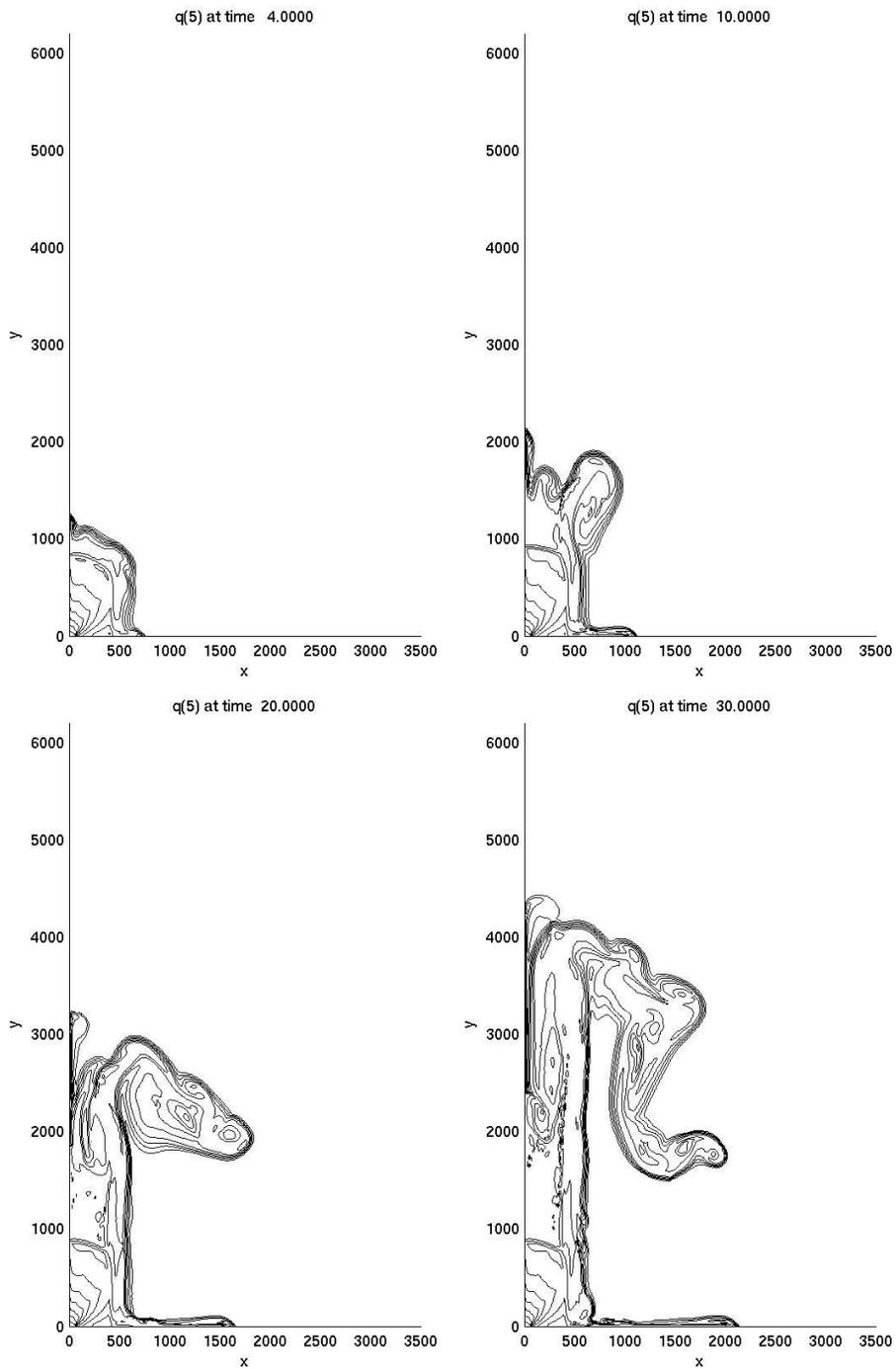


Figure 8.11: Simulation A. $\alpha = 90°$ (no crater). Dust density at $t = 4, 10, 20, 30$ s. Contour values = $10^{[-4.8:.4:2.4]}$ [kg/m$^3$].
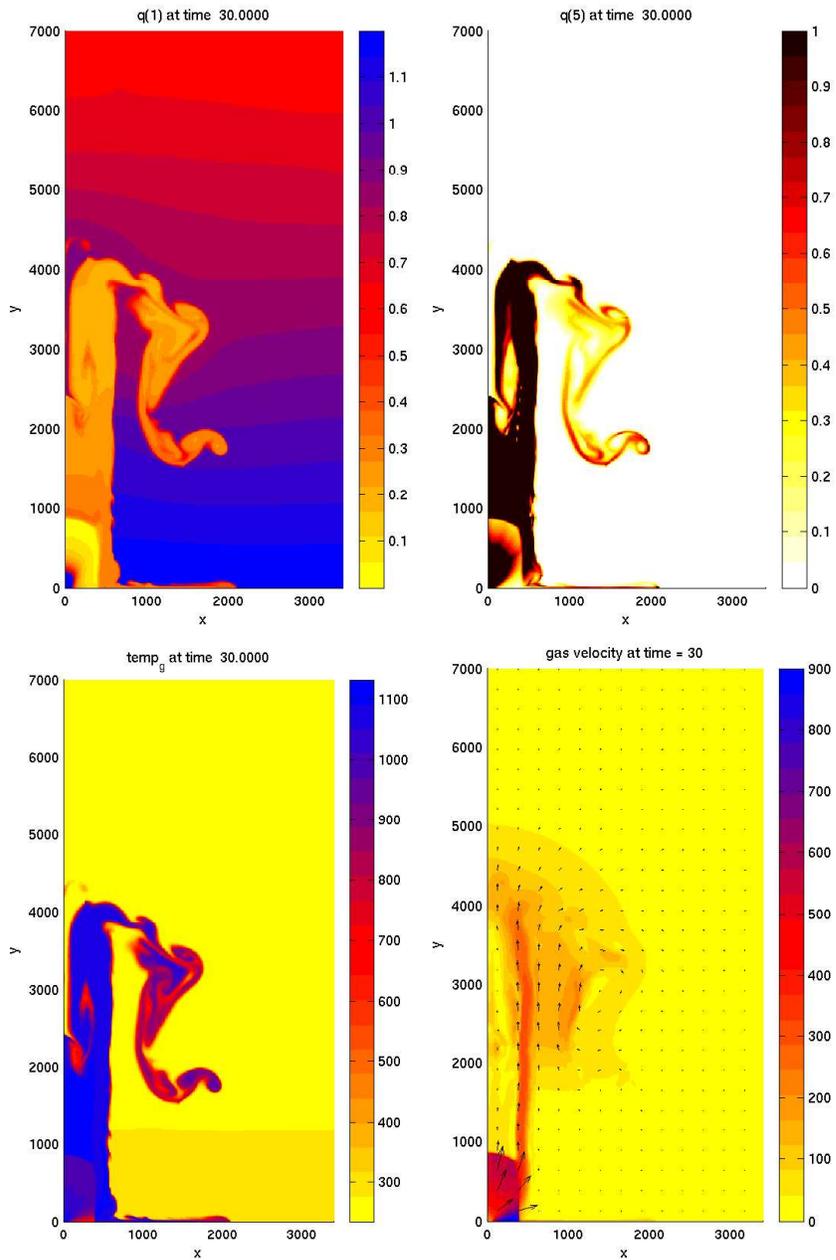
Figure 8.12: Simulation A. $\alpha = 90°$ (no crater). Gas density, dust density, gas temperature, and gas velocity at time $t = 30$ s.

q(5) at time  4.0000

q(5) at time  10.0000

q(5) at time  20.0000

q(5) at time  30.0000
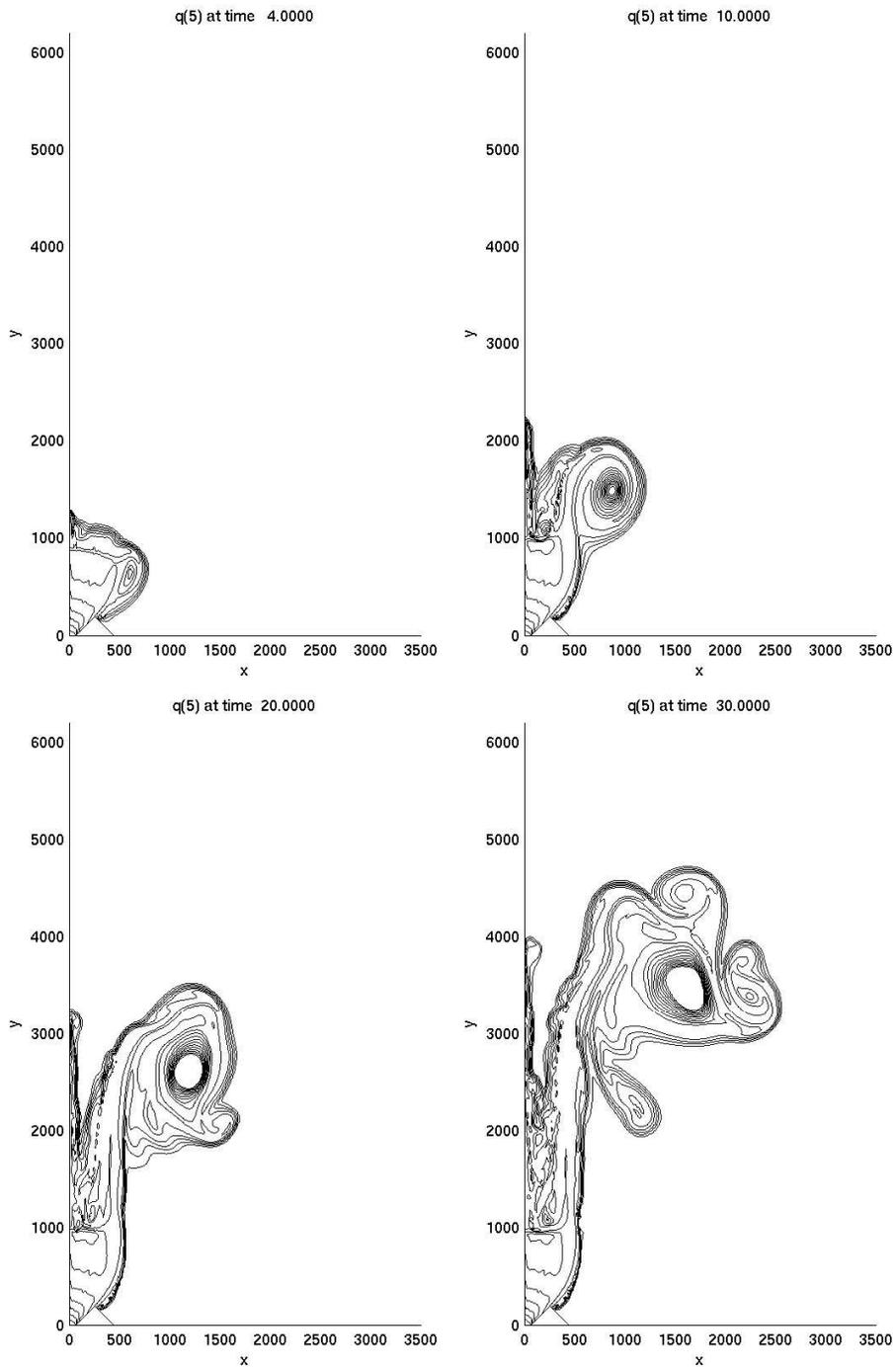
Figure 8.13: Simulation A. $R = 254$ m, $\alpha = 45°$. Dust density at $t = 4, 10, 20, 30$ s. Contour values = $10^{[-4.8:.4:2.4]}$ [kg/m$^3$].
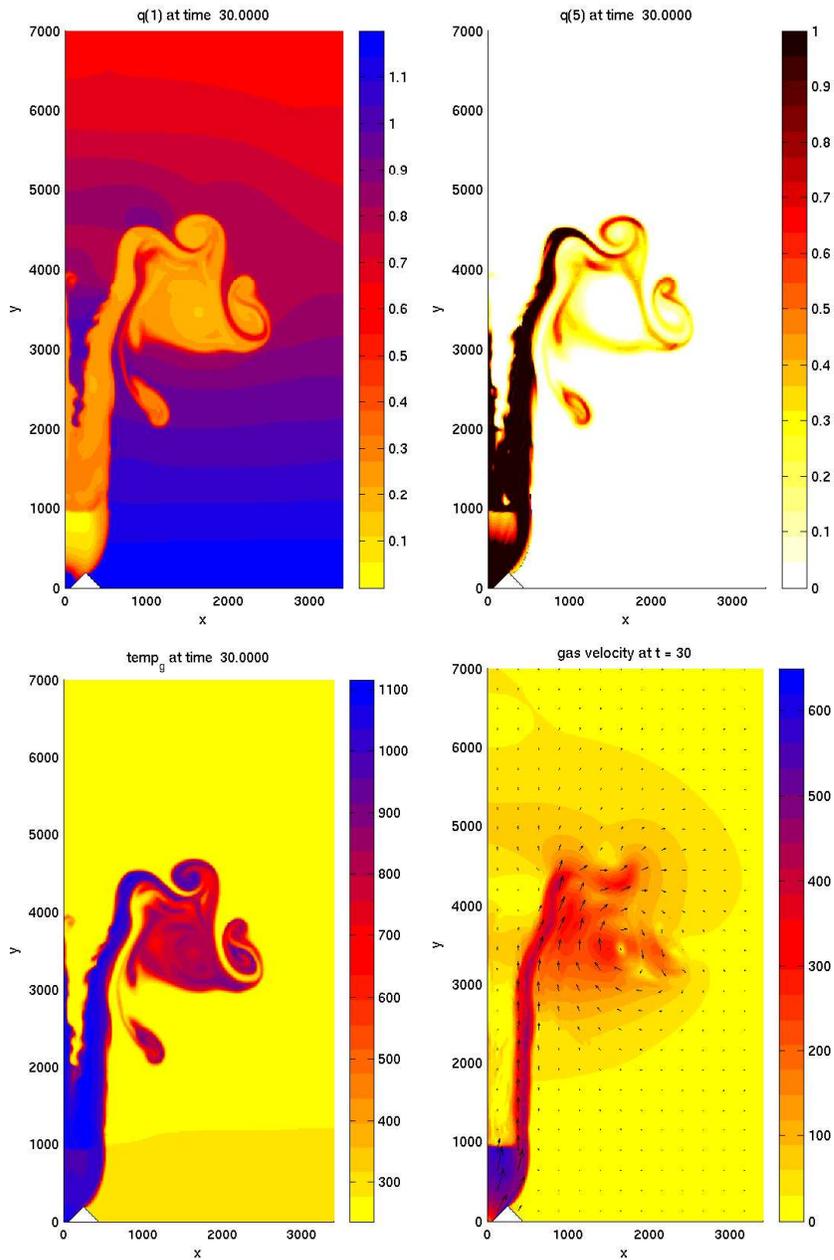
Figure 8.14: Simulation A. $R = 254$ m, $\alpha = 45°$. Gas density, dust density, gas temperature, and gas velocity at time $t = 30$.
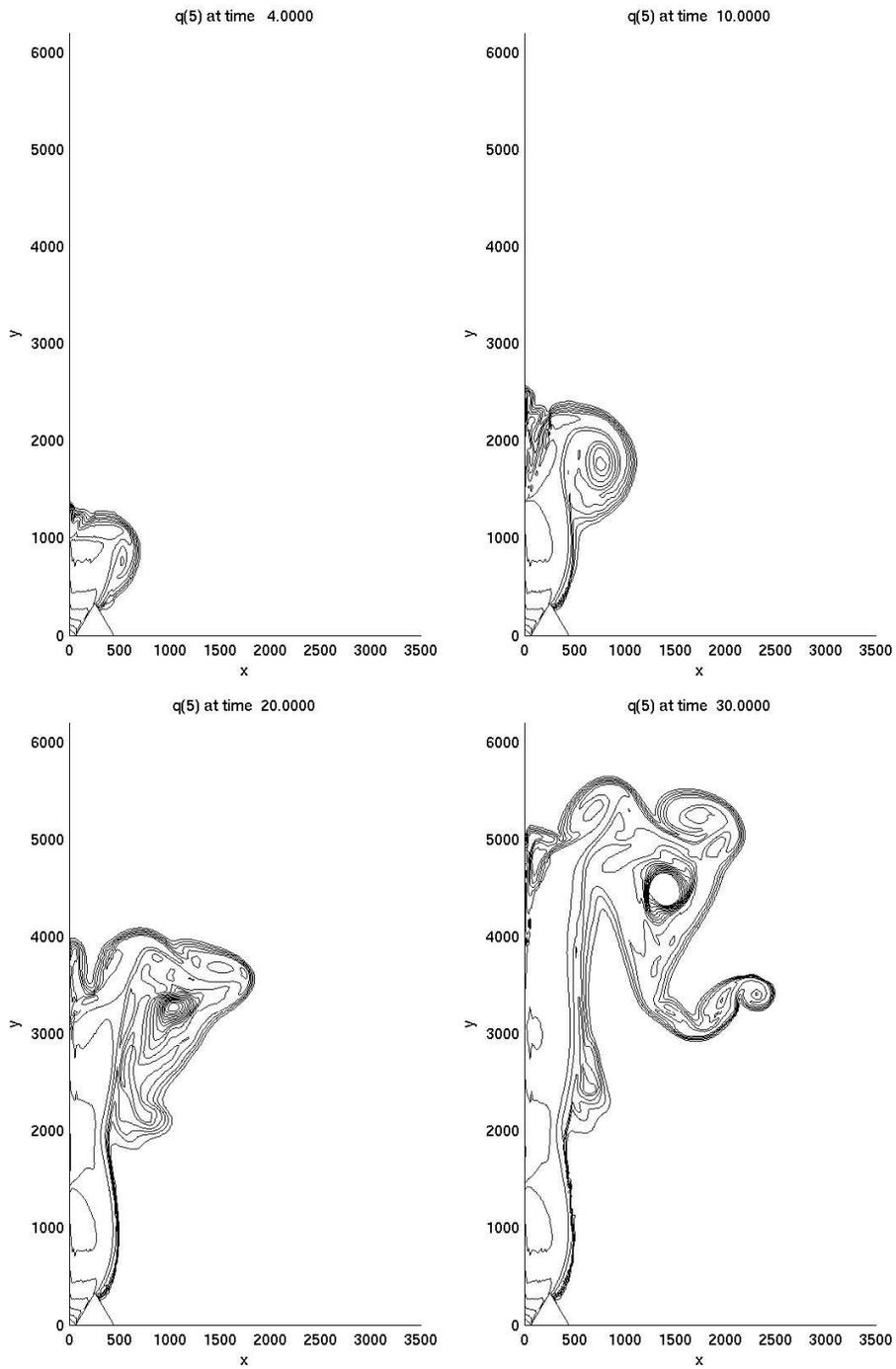
Figure 8.15: Simulation A. $R = 254$ m, $\alpha = 30°$. Dust density at $t = 4, 10, 20, 30$ s. Contour values $=$ $10^{[-4.8:.4:2.4]}$ $[\text{kg/m}^3]$.
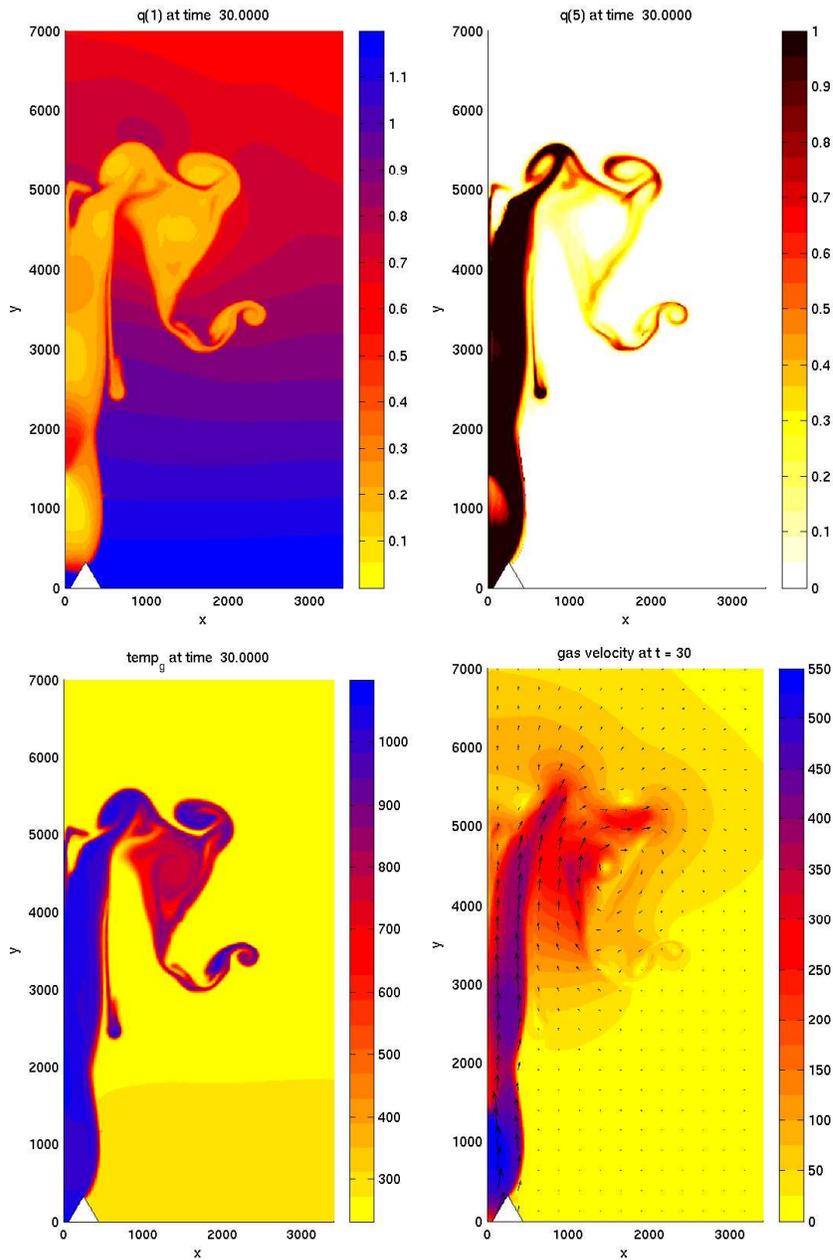
Figure 8.16: Simulation A. $R = 254$ m, $\alpha = 30°$. Gas density, dust density, gas temperature, and gas velocity at time $t = 30$.
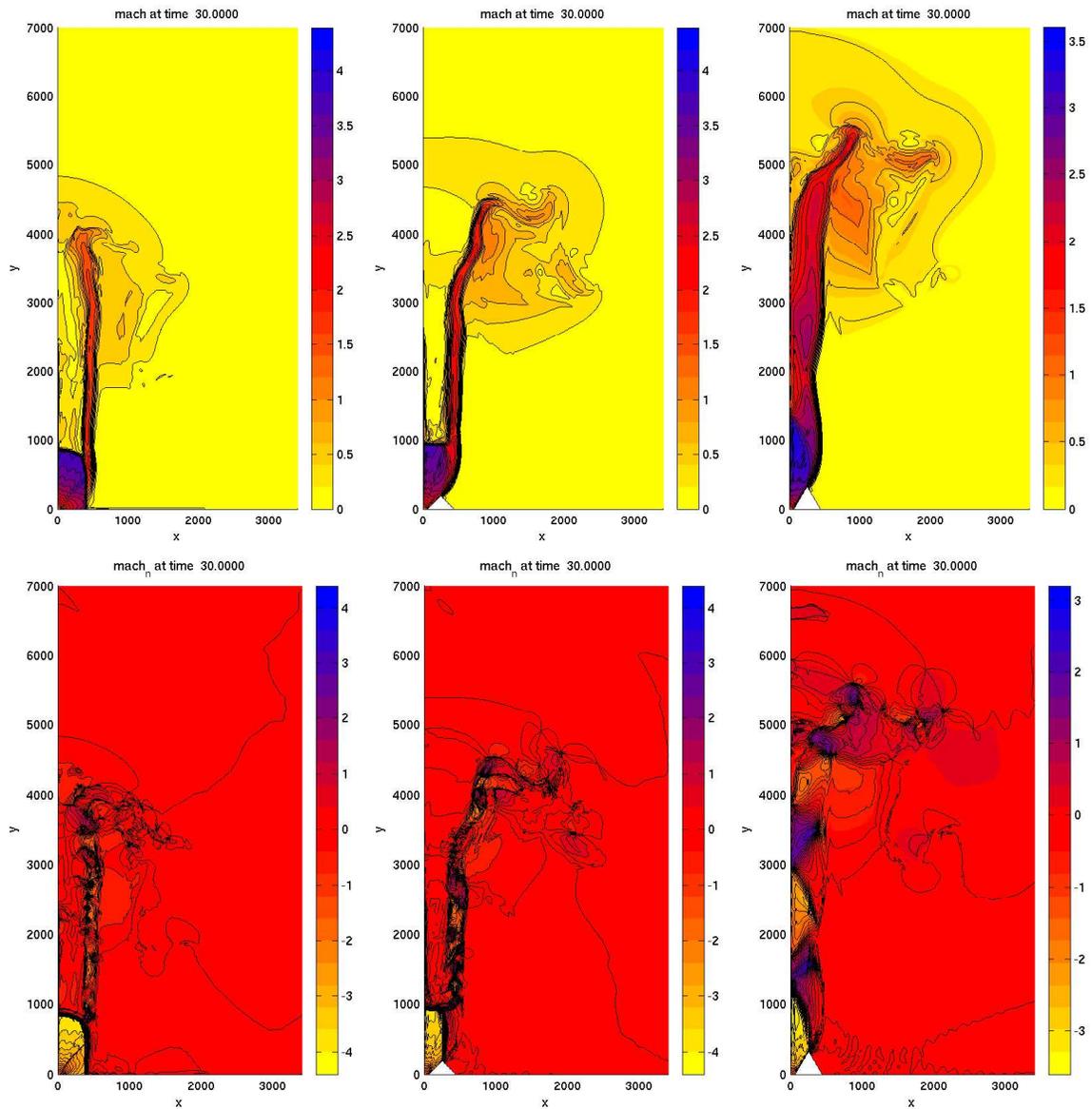
Figure 8.17: Simulation A. $R = 254$ m. Above: Mach number, contour values $= [0 : .2 : 4.4]$. Below: normal Mach number, contour values $= [-4.4 : .2 : 4.4]$. From left to right: $\alpha = 90°$, $45°$, $30°$.
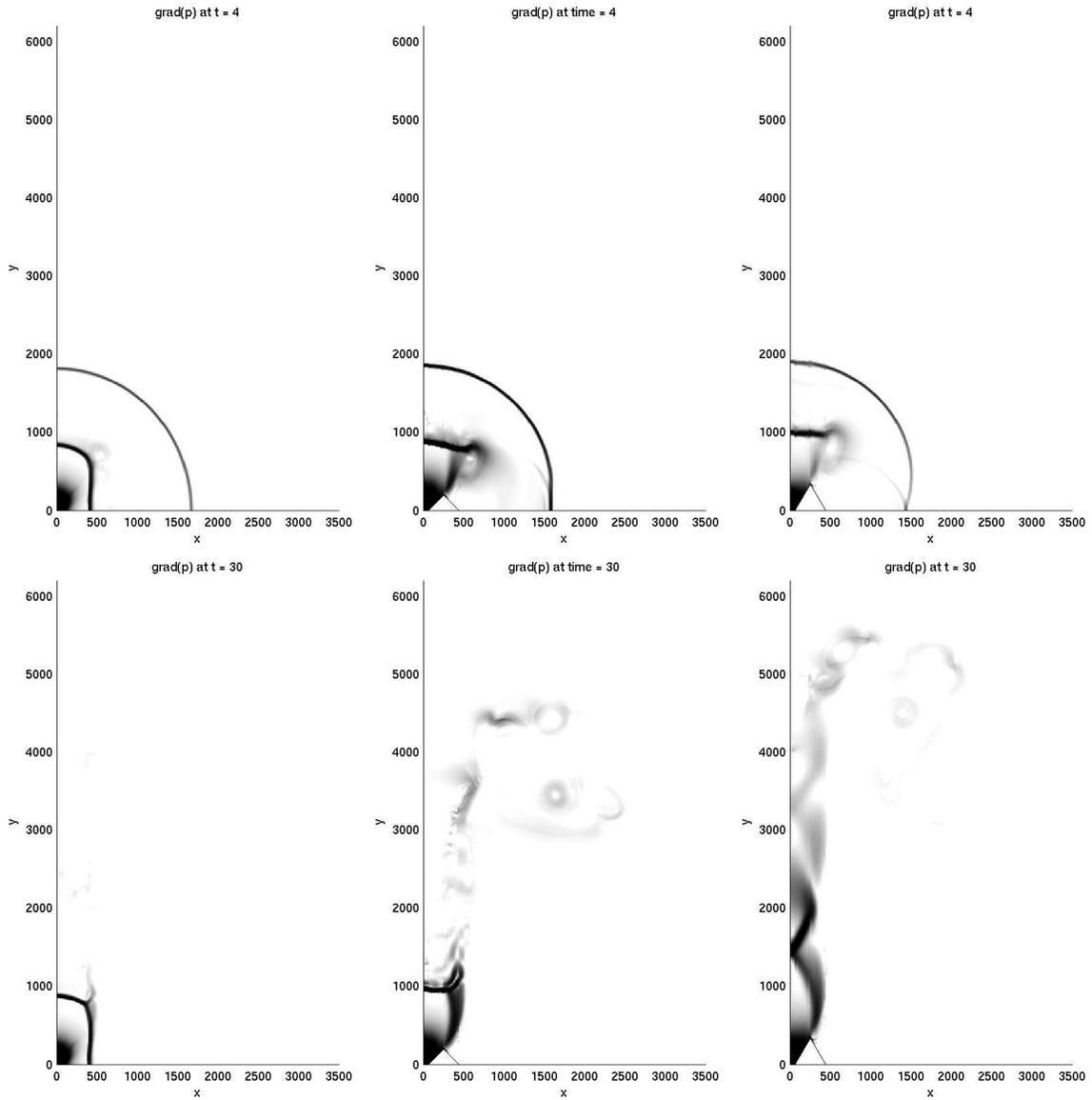
Figure 8.18: Simulation A. $R = 254$ m. Pressure gradient at $t = 4$ s (above) and $t = 30$ s (below) for $\alpha = 90°$, $45°$, $30°$, from left to right. (Black intensity scale is differently set in each plot.)
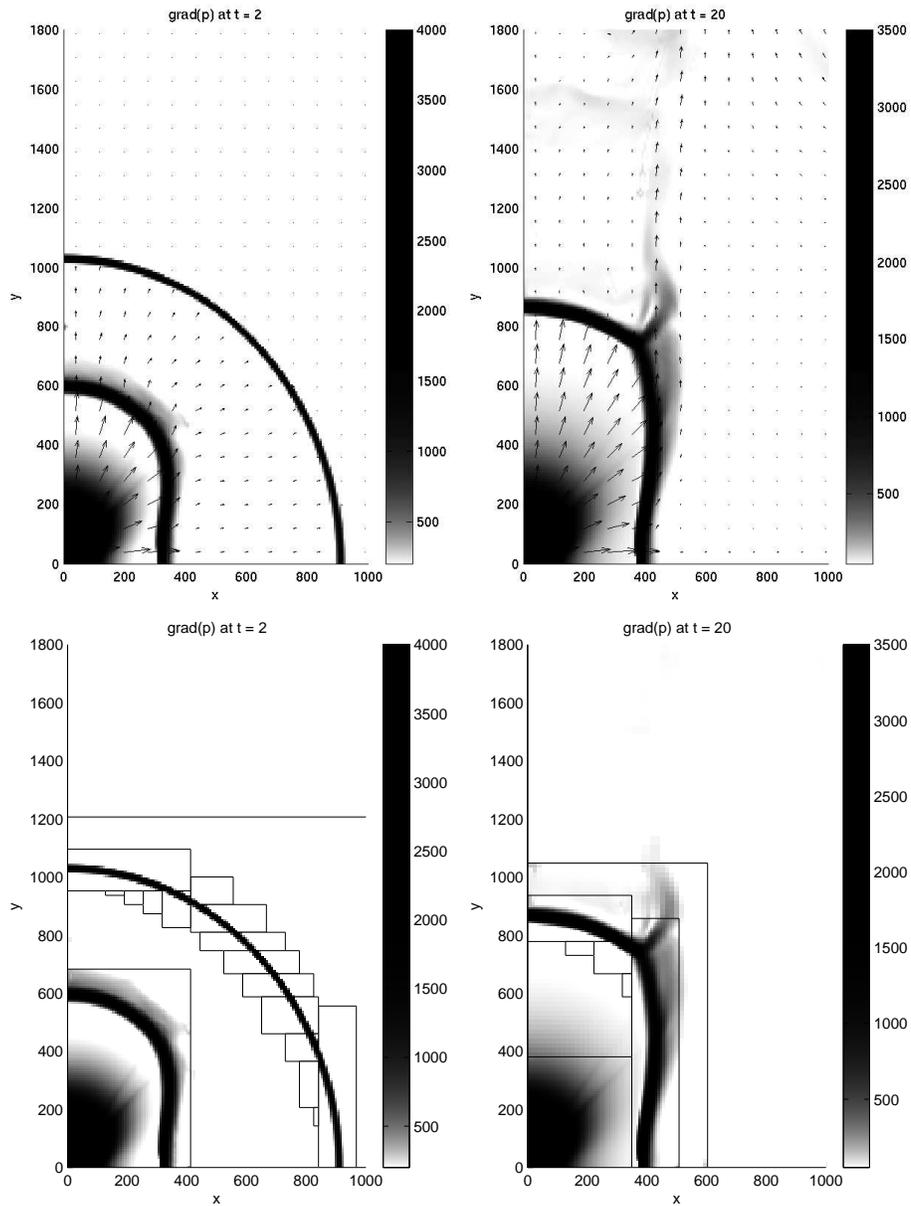
Figure 8.19: Simulation A. $\alpha = 90°$ (no crater). Pressure gradient at $t = 2$ and 20 s, highlighting the Mach disk shock structure. Above: Computation on a fine uniform grid with $368 \times 736$ cells of size = 7.9375 m. Below: Computation with adaptive mesh refinement. Coarsest grid: rectangle with $92 \times 184$ cells of size = 31.75 m. Grid levels = 3, refinement ratio = 2. CFL = 0.9.
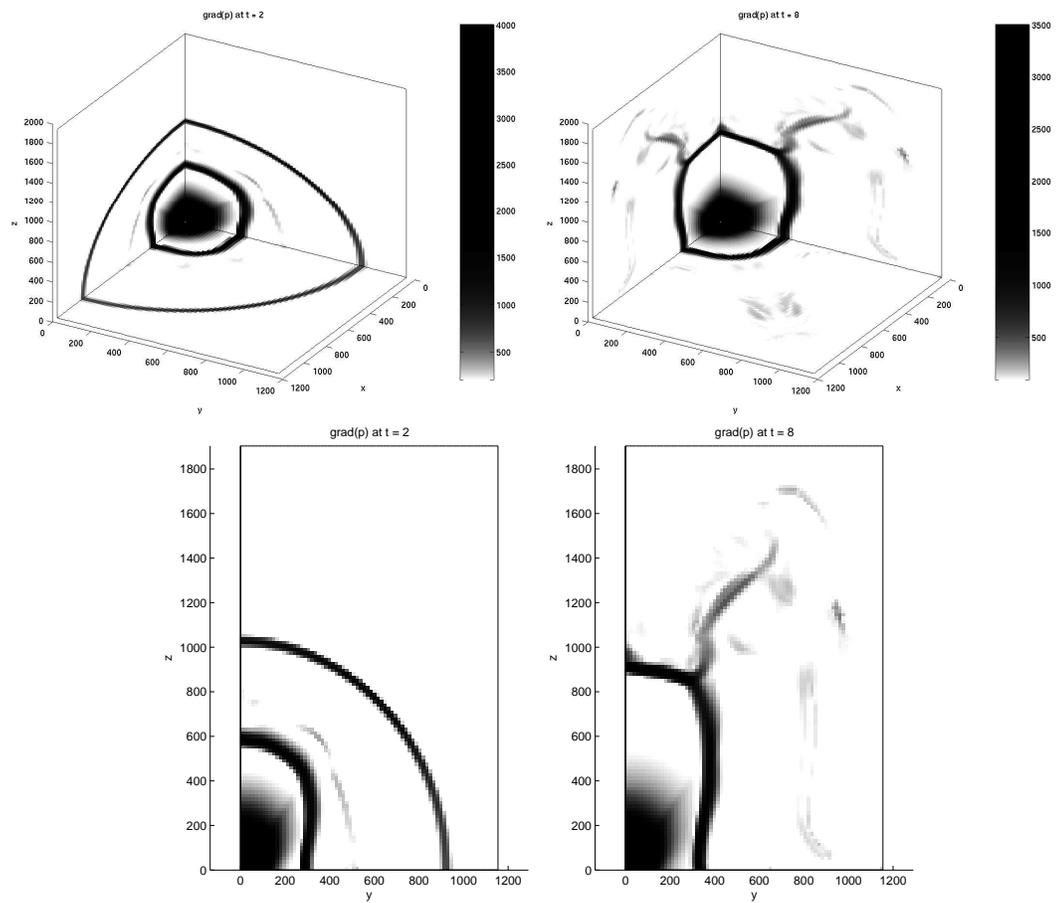
Figure 8.20: Simulation A. Three-dimensional results (no crater). Pressure gradient at $t = 2$ and $8$ s. Below: $x$-slices. Computational domain: octant with $58 \times 58 \times 95$ cells (uniform grid). Cell size = 19.9 m. CFL = 0.5.
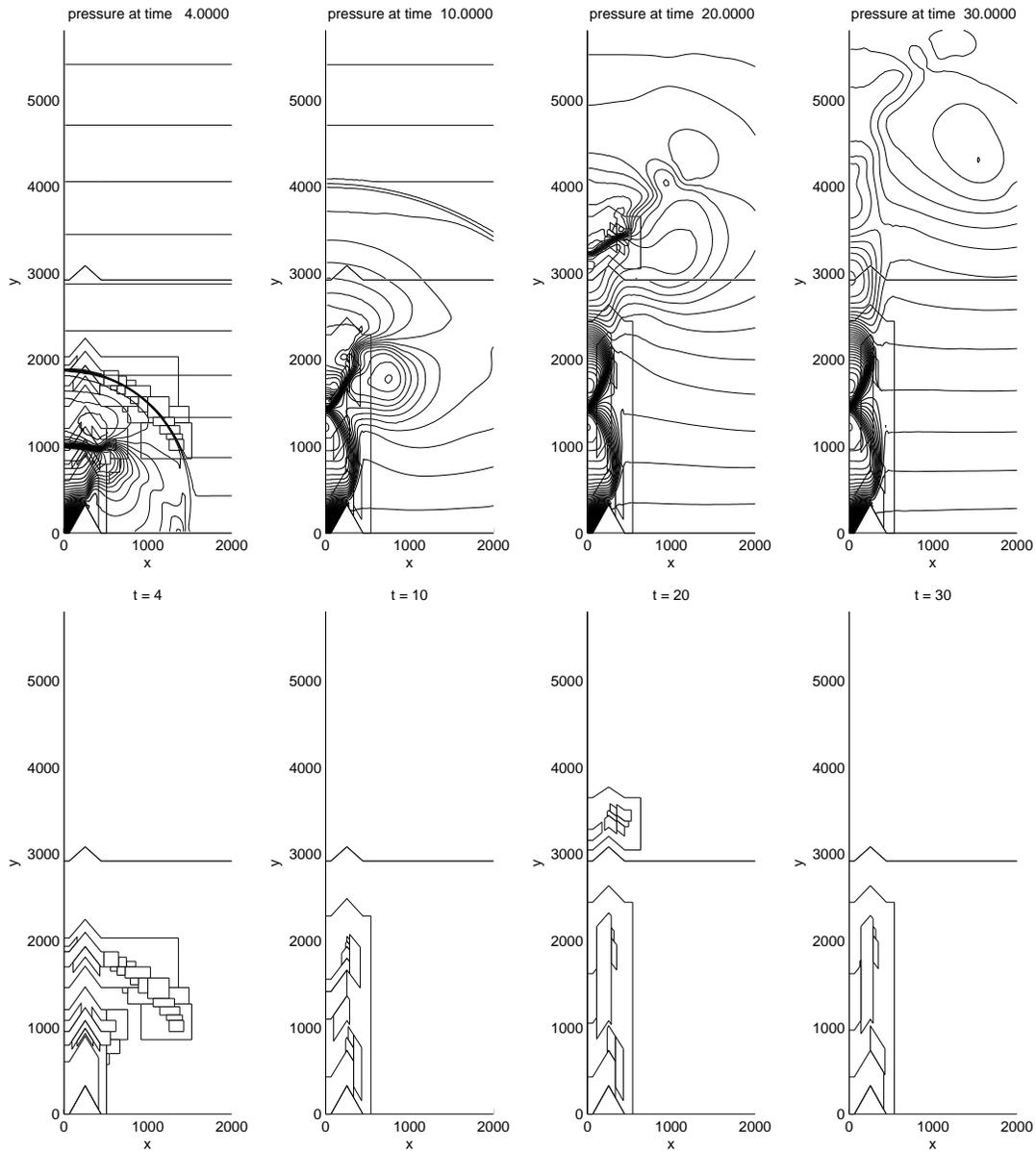
Figure 8.21: Simulation A. $R = 254$ m, $\alpha = 30°$. Above: Pressure at $t = 4, 10, 20, 30$ s. Contour values $= 10^4[1 : 0.5 : 440]$ Pa. Computation with adaptive mesh refinement. Coarsest grid: rectangle with $92 \times 184$ cells of size $= 31.75$ m. Grid levels $= 3$, refinement ratio $= 2$. CFL $= 0.9$. Cell size on the finest grid $= 7.9375$ m. Below: Refinement grid patches.
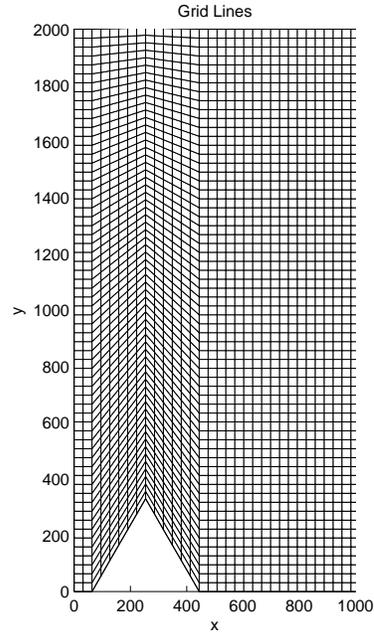
Figure 8.22: Type of mapped grid used for experiments with a crater at the ground surface. A quadrilateral logically rectangular grid is employed in which the horizontal grid lines are interpolated between the surface topography and a fixed upper elevation, while the vertical grid lines are still vertical.
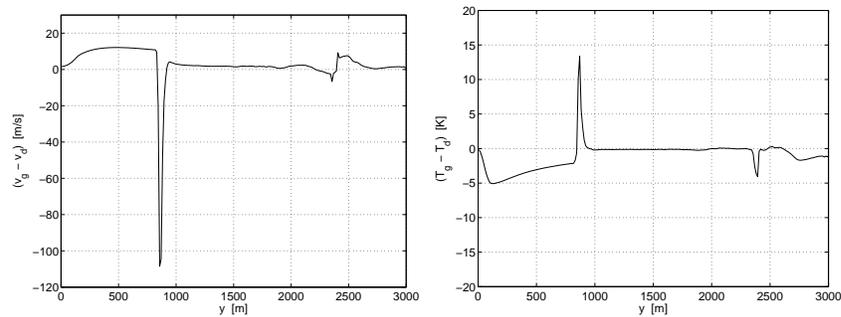


Figure 8.23: Simulation A. $\alpha = 90°$ (no crater). Vertical velocity difference (left) and temperature difference (right) between gas and solid phase along the $y$ axis at $t = 30$ s.
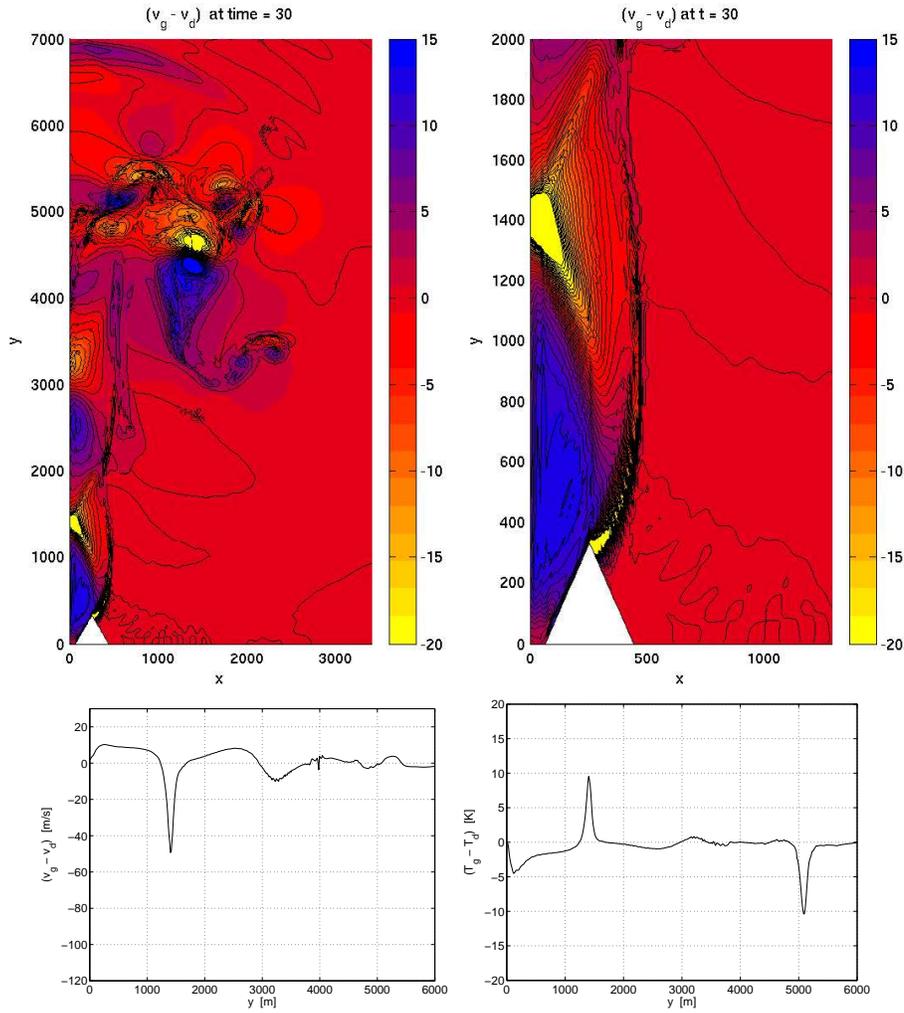
Figure 8.24: Simulation A. $R = 254$ m. $\alpha = 30°$. Above: Vertical velocity difference at $t = 30$ s between the gas and solid phase, highlighting disequilibrium zones. The figure on the right focuses on the region near the crater. Contour values $= [-22 : 2 : 22]$ m/s (left), and $= [-22 : 1 : 22]$ m/s (right). Note that the colour scale $[-20, 15]$ and the contour values have been chosen to give contast to nonequilibrium regions, but $(v_g - v_d)$ reaches about $-47$ m/s in the region behind the first reflected shock. Below: Vertical velocity difference and temperature difference between the two phases along the $y$ axis.
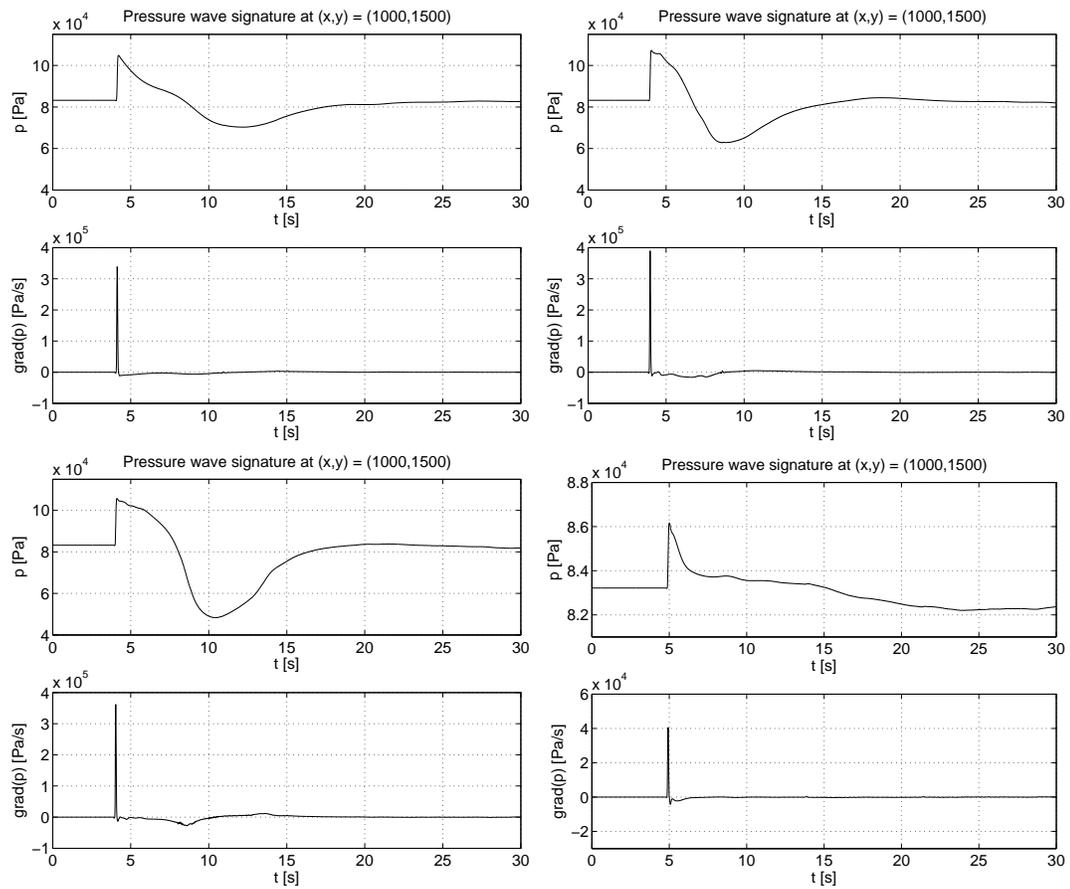
Figure 8.25: Simulation A. $R = 254$ m. Pressure wave signature at the point $(x, y) = (1000, 1500)$ m, in terms of the pressure and the time pressure gradient. Top, left: Simulation A, no crater. Top, right: Simulation A, $\alpha = 30°$. Bottom, left: Simulation A, $\alpha = 45°$. Bottom, right: Simulation E, no crater.
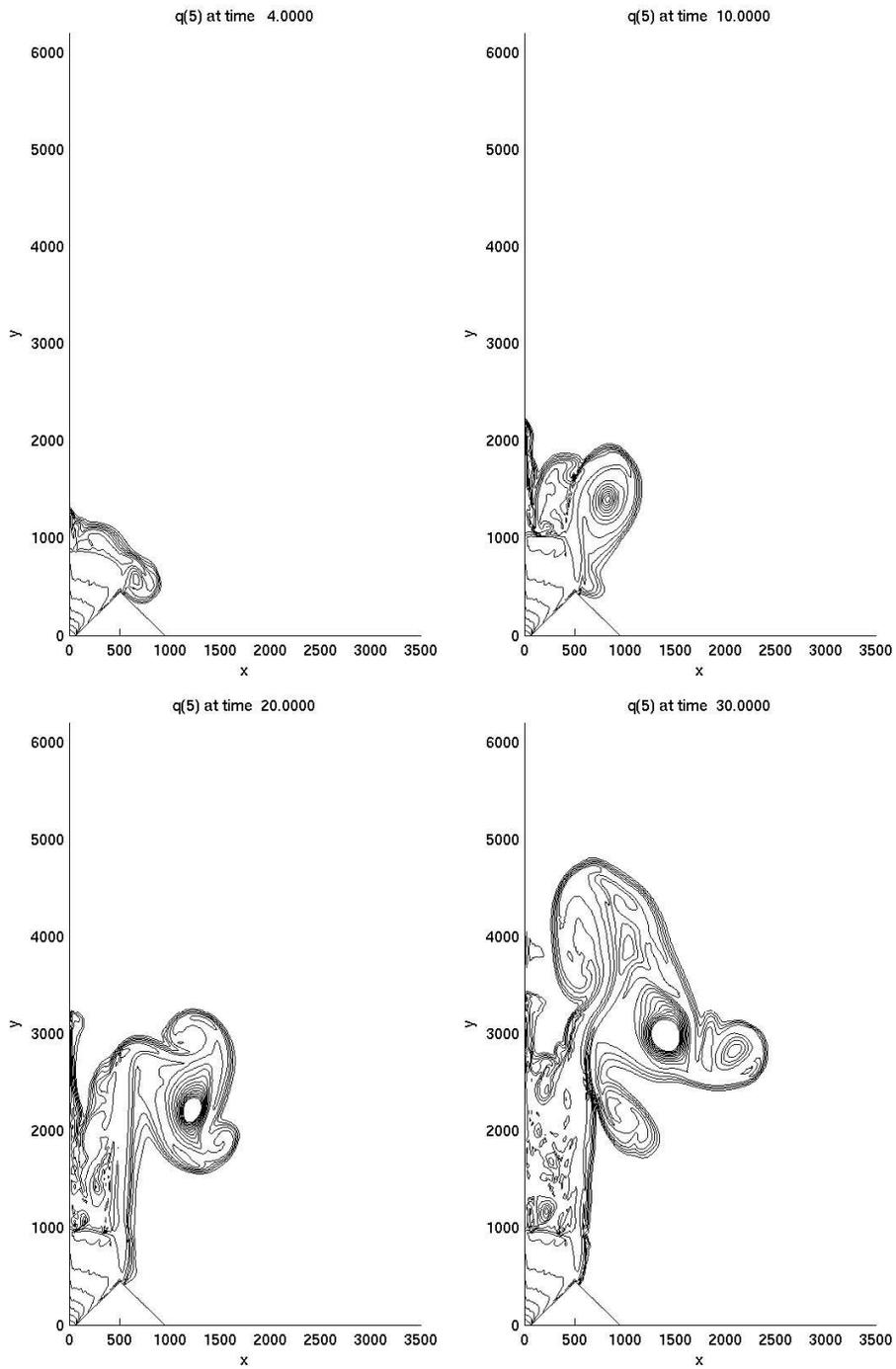
Figure 8.26: Simulation A. $R = 508$ m, $\alpha = 45°$. Dust density at $t = 4, 10, 20, 30$ s. Contour values = $10^{[-4.8:.4:2.4]}$ [kg/m$^3$].
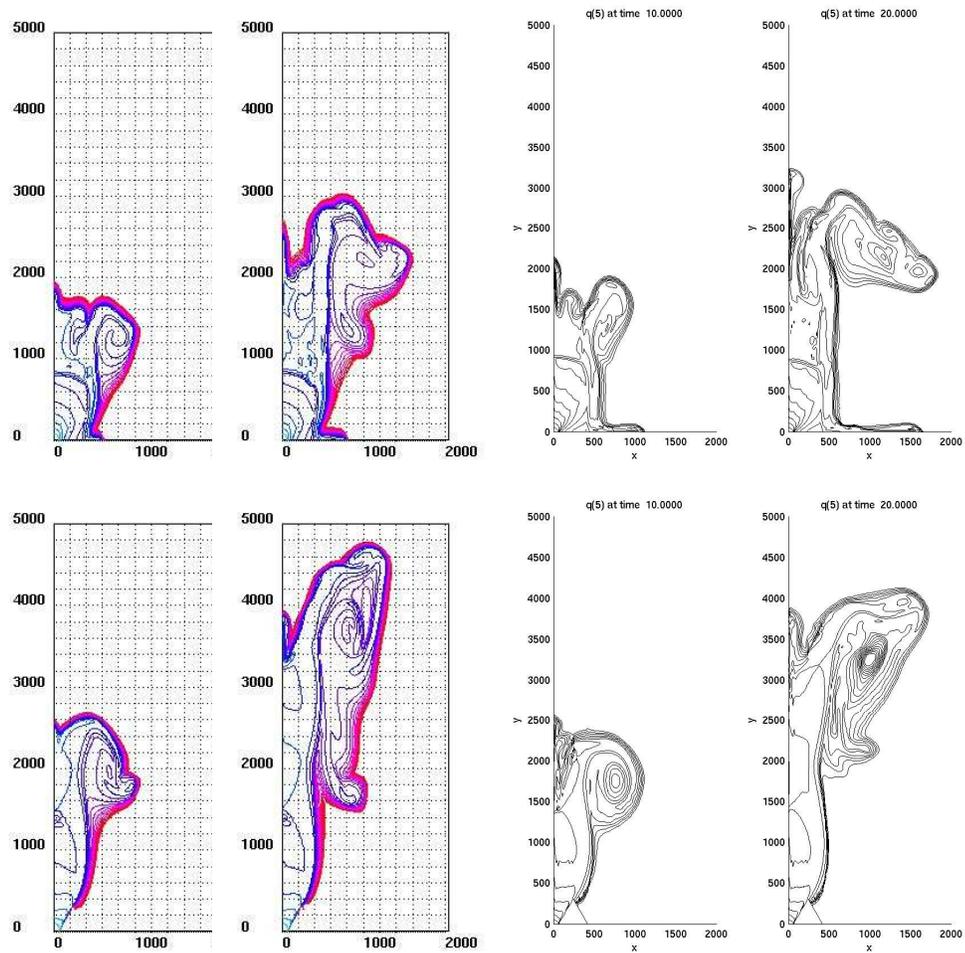
Figure 8.27: Simulation A. $R = 241.3$ m. Comparison between the results obtained with the presented model based on CLAWPACK (right) and those obtained by using PDAC by T. Esposti Ongaro at INGV (left). Above: $\alpha = 90°$ (no crater). Below: $\alpha = 30°$. Dust density contours at $t = 10$ and 20 s. (Results with PDAC reported here with courteous permission of the author.)
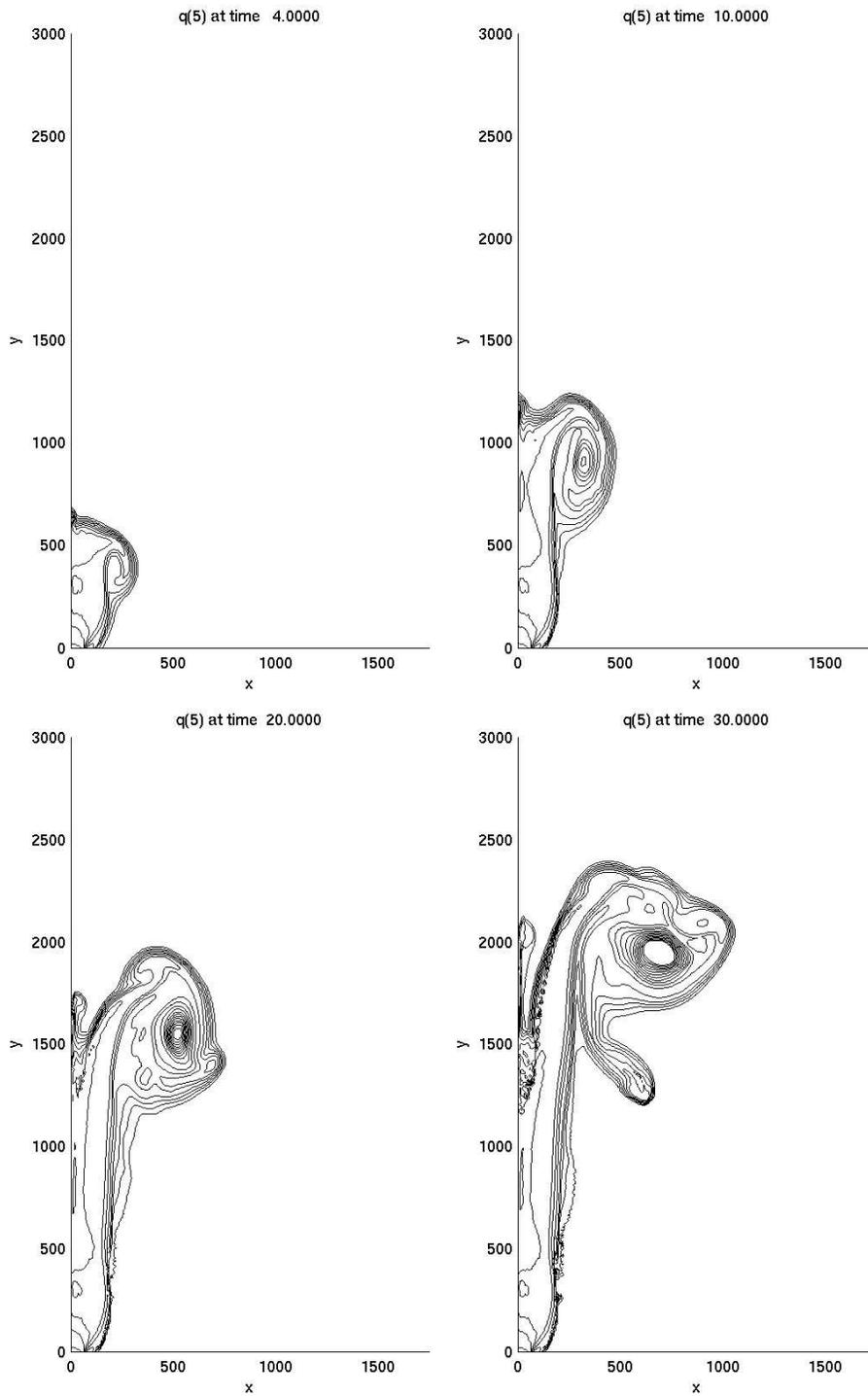
Figure 8.28: Simulation E. $\alpha = 90°$ (no crater). Dust density at $t = 4, 10, 20, 30$ s. Contours values = $10^{[-4.8:.4:2.4]}$ [kg/m$^3$].
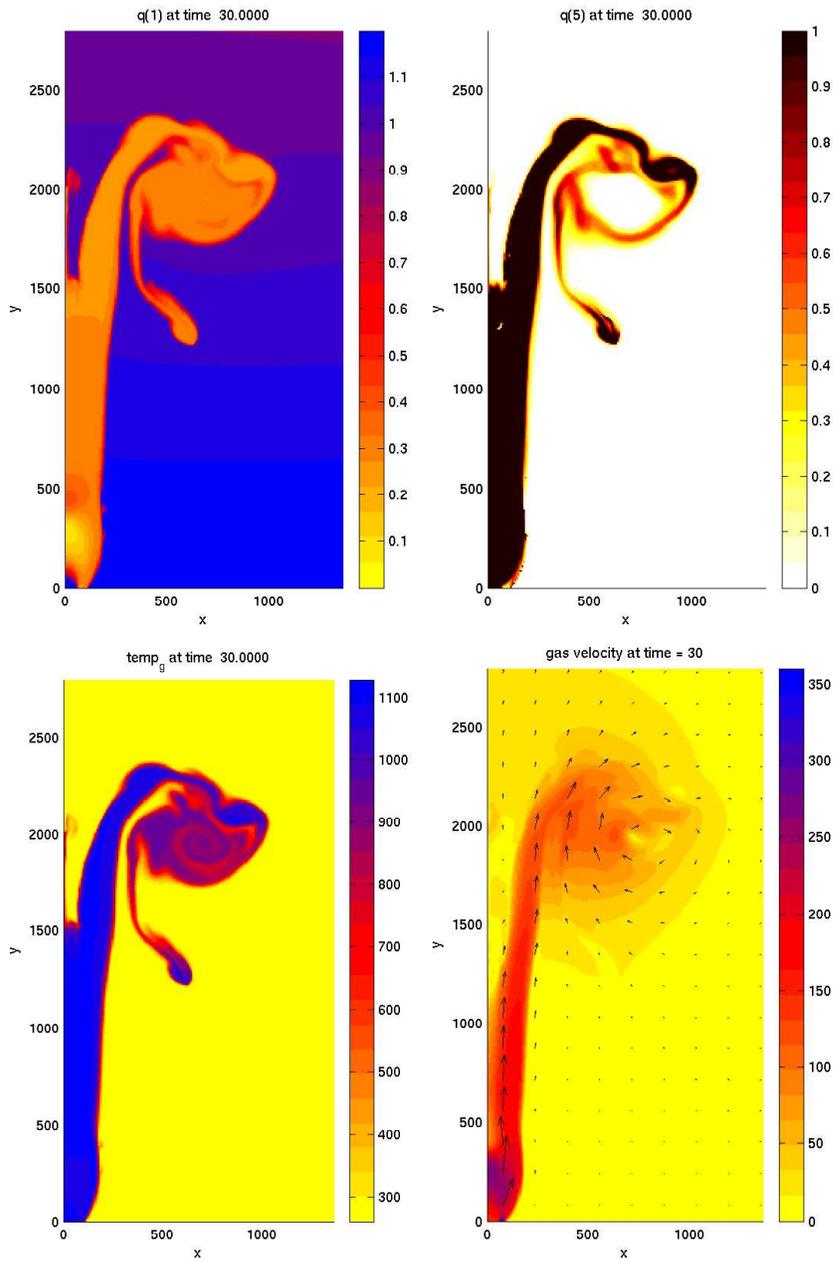
Figure 8.29: Simulation E. $\alpha = 90°$ (no crater). Gas density, dust density, gas temperature, and gas velocity at time $t = 30$ s.
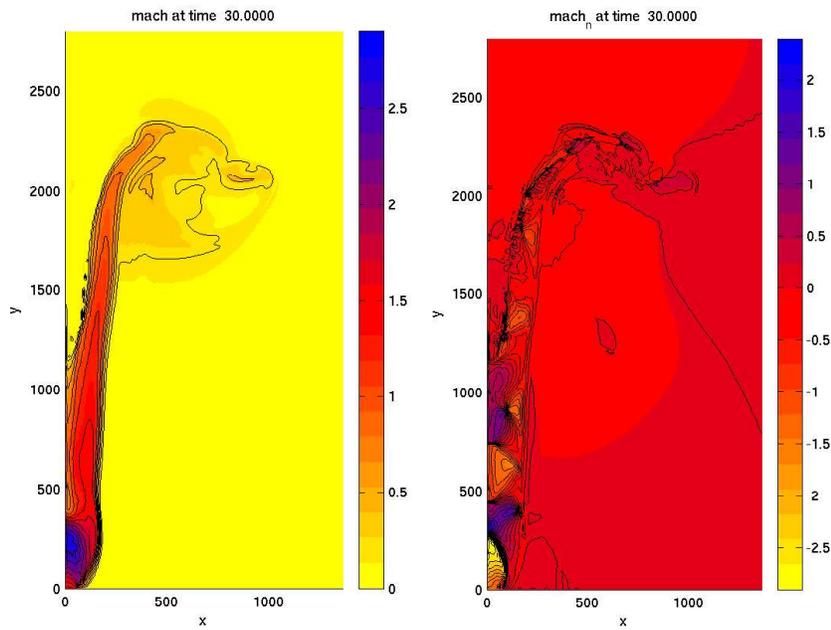
Figure 8.30: Simulation E. $\alpha = 90°$ (no crater). Left: Mach number, contour values $= [0 : .2 : 3]$. Right: normal Mach number, contour values $= [-3 : .2 : 3]$.
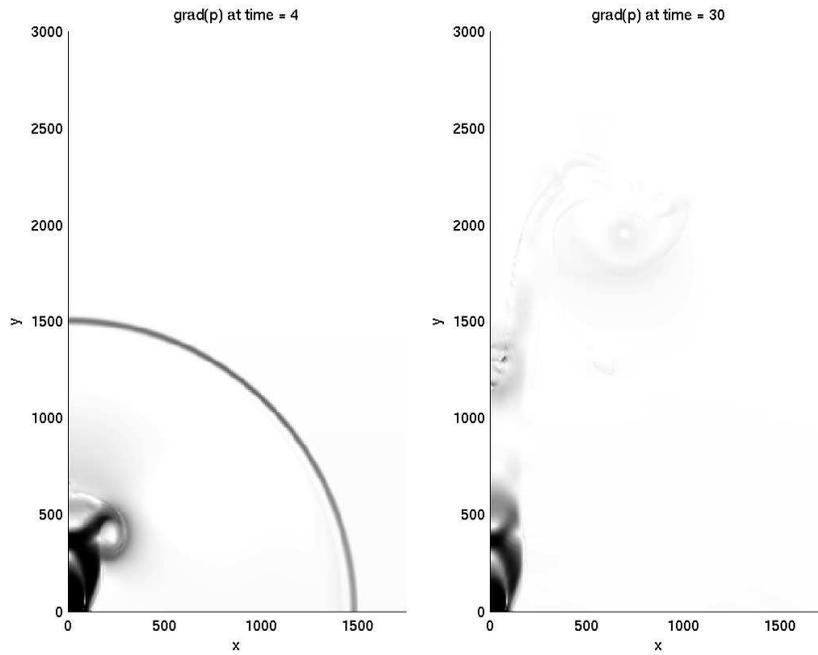


Figure 8.31: Simulation E. $\alpha = 90°$ (no crater). Pressure gradient at $t = 4$ and $30$ s.

Chapter 9

# CONCLUSIONS AND FUTURE WORK

This thesis has been devoted to the numerical modeling of compressible multicomponent flows by means of wave propagation algorithms based on approximate Riemann solvers. This work collects different but related studies, and in this chapter I summarize the results achieved and outline some future directions of research.

## 9.1  Relaxation Riemann Solvers

In an effort of contributing to the analysis and development of new and more efficient numerical schemes, I have explored the connection between a simple relaxation scheme of the kind proposed by Jin and Xin [93] and a type of approximate Riemann solvers for the original system of conservation laws. This has led to the introduction of a general class of solvers [124], called *relaxation Riemann solvers*, which for a system of $m$ conservation laws use $2m$ waves, and are based on splitting both the jump in $q$ and the jump in the flux simultaneously. Relations with classical solvers such as HLL and Roe's, as well as with standard entropy fixes of the type of Harten and Hyman [77], have been analyzed and illustrated. The added flexibility of these more general approximate Riemann solvers is advantageous in several problems, such as systems where a Roe matrix is unavailable, systems with source terms, and conservation laws with spatially varying flux functions.

In the framework of this class of solvers enters the so-called *f-wave* formulation of wave propagation algorithms. This f-wave technique has been employed in our work on particle-laden flows modeling to design a numerical algorithm that treats efficiently gravity source terms, and helps in solving the non-strictly hyperbolic equations governing the pressureless particulate phase.

## 9.2  Real Compressible Multifluid Flows

A novel Godunov-type method for compressible multifluid flows governed by a general equation of state has been proposed, based on the idea of a local linearization of the pressure law $p(\mathcal{E}, \rho)$. This method is able to prevent the appearance of spurious pressure oscillations at contact interfaces, which is a well known numerical difficulty in multifluid problems [2, 108, 96, 193]. I have analyzed the reasons of the origin of this problem, recognizing that it is related to the nonlinearity of a generic law $p(\mathcal{E}, \rho)$ through which the cell value of the pressure is computed from the conserved variables in the framework of Eulerian conservative schemes. In particular, I have remarked that this difficulty affects also single-gas flows for an arbitrary equation of state, and not only multifluid flows, an aspect that usually is not stressed adequately in the literature.

A first step in the design of the multifluid method has been the introduction of an algorithm for single-component fluids with a general equation of state. This method defines a simple and general procedure that can be applied to some classical finite volume methods designed for a restricted class of equations of state to develop a scheme for arbitrary pressure laws. In particular, I have illustrated how the idea of this approach specializes to the classical Roe's scheme. I have also shown that the presented method can be reinterpreted as a relaxation scheme for the original Euler system, thus exhibiting some similarity with the energy relaxation idea of Coquel and Perthame [39]. With respect to the latter method, the presented approach allows a local definition of propagation speeds based on satisfying

the local sub-characteristic condition for the relaxation system in the equality limit, which reduces the numerical diffusion.

A further step has been the introduction of a modified version of the single-fluid algorithm that prevents pressure oscillations at contact discontinuities. Finally this Pressure Linearization Method [163] has been extended to real multifluid flows. The resulting scheme is a flexible tool for single and multifluid flow computations with an arbitrary equation of state that guarantees pressure equilibrium at material interfaces. This is a step forward with respect to many methods proposed in the literature that are applicable only to the ideal polytropic gas law or the stiffened gas equation of state [3, 4, 178, 74, 182], or other more general laws but still with a specific form [183, 184]. With respect to the method of Allaire et al. in [5], which can also be applied to arbitrary equations of state, our algorithm avoids an iterative procedure that is needed in the general case in [5].

Further work is planned to test and possibly improve the robustness of the proposed multifluid method for problems with large density and energy ratios.

### 9.3 Dusty Gas Flows and Applications to Volcanic Jets and Plumes

An extensive part of my thesis work has been dedicated to the study of a two-phase model for gas flows carrying a particulate suspension. An f-wave propagation algorithm has been developed to solve the governing system of equations, which is able to address the numerical difficulties that arise in relation to source terms modeling, to the non-strictly hyperbolic character of the equations for the pressureless dust phase, and to the possible appearance of unphysical states with negative dust densities. Specifically, the algorithm exhibits the following features: (i) Small perturbations from gravitational steady states are modeled efficiently through a technique that incorporates the gravity source term into the Riemannn solver, as described in our work [124]. (ii) A semi-analytical solver has been designed for the treatment of inter-phase drag and heat transfer source terms that models these processes for a wide range of relaxation time scales. This allows to describe both the situation in which mechanical and thermal equilibrium is reached on a very small time scale (and the numerical problem is stiff), and, on the other hand, phenomena of formation of relaxation zones of finite width behind shock structures. (iii) The f-wave Riemann solver for the non-strictly hyperbolic equations of the pressureless particulate phase models robustly vacuum states and performs efficiently high resolution corrections.

The software used is based on the Fortran routines of CLAWPACK [115]. My contribution has been the implementation of the presented model on two-dimensional quadrilateral (curvilinear) grids with cylindrical symmetry and with adaptive mesh refinement, and on three-dimensional Cartesian grids.

I have then devoted my work to the application of the two-phase dusty flow model to the simulation of volcanic jets and plumes that characterize explosive volcanic eruptions. The employment of a wave propagation finite volume method based on Riemann solvers is a novel approach in the context of the numerical simulation of volcanic processes. In fact, many well established two-dimensional two-phase numerical methods that have been extensively used in the past twenty years to describe explosive eruption phenomena [206, 197, 51, 150, 155] are based on the Implicit MultiField finite-difference technique of Harlow and Amsden [75] (1975). The shock-capturing conservative method proposed in this thesis work has been shown particularly effective in the description of compressibility effects and shock wave patterns.

As a starting work, we have kept the model very simple, omitting some effects that are taken into account in other more complex models, such as turbulence and viscosity. These effects, however, can be reasonably neglected in eruption dynamics problems on the small time scale dominated by compressibility effects. To these I have dedicated my numerical study.

Some tests on pyroclastic dispersion dynamics and comparison with results in the literature have shown that the proposed model is able to capture the main features of various styles of eruption columns,

Plinian, collapsing, transitional, for different sets of eruption parameters.

I have then specifically focused my study on modeling the fluid dynamic structures characterizing overpressured supersonic volcanic jets. The decompression phase of these jets has been recognized [100, 210] as having a primary role in determining the subsequent development of the eruption column and its pyroclastic dispersion. The main motivation for such a study is that little work has been done in the literature by means of multiphase numerical modeling to explore in depth the mechanisms of the expansion of the eruptive gas-pyroclasts mixture, and describe the details of the structure of the jet thrust region. Experimental works such as [100] use pure gases, and cannot model gravitational effects, due to the lack of a scaling relation for gravity. Theoretical models have the drawback of the single-gas (pseudogas) approximation and the one-dimensional limit.

A relevant part of my study, which is also joint work with A. Neri and T. Esposti Ongaro of the Istituto Nazionale di Geofisica e Vulcanologia, Pisa, (Italy) (who already made preliminary work on the subject [159], 1999), is the analysis of the jet expansion process on different crater geometry. We have described shock wave patterns that may form inside volcanic jets, and we have highlighted the importance of the role played in particular by the crater opening angle in controlling the dynamics of the decompression. Effects such as transient phenomena, instabilities, and relaxation zones behind shocks, have been put into evidence. These effects can be properly modeled only by a two-phase transient model.

Regarding the numerical code, besides its applicability to mapped grids, which allows modeling crater morphology (and general topography), another advantageous feature is the adaptive mesh refinement technique. This allows a fine resolution of fluid structures in regions of strong gradients and shocks, and coarse resolution in extended parts of the domain where there are not relevant effects to capture, thus limiting the computational effort.

The modeling of a complex global phenomenon such as a volcanic event should involve the collaboration and the converging efforts of many disciplines, from Geophysics to Numerical Analysis. Experimental, theoretical and computational work should be considered as interactive areas each with a complimentary role with respect to the others. With my study I wished to give a contribution for a better understanding of some of the thermo-fluid dynamic processes that characterize explosive volcanic events.

## 9.4   Future work

My plans for future work focus mainly on further developments in the numerical modeling of volcanic processes.

Extensions of the current physical model are under study. Planned work includes the description of particles of different size and microscopic density, to be able to capture elutriation phenomena, and the modeling of the water vapor content, which might have an important role on buoyancy forces in pyroclastic dispersion problems on the long time scale. Accounting for water vapor would require considering a two-fluid gaseous phase, and in this context the algorithm developed for real compressible multifluid flows could be exploited. This method would be advantageous for example for using a gas specific heat relation dependent on the temperature, as for instance in [51, 150, 154].

An ambitious project in relation to the simulation of volcanic phenomena is the development of a fully three dimensional model with adaptive mesh refinement on hexaedral grids, which could be useful in the assessment of volcanic hazard. Such a three-dimensional model would allow to take into account real volcanic topography, anisotropic atmospheric conditions, and in particular it could simulate asymmetrical column collapse, as it has been observed in laboratory experiments, e.g. [25]. These aspects are all important for volcanic hazard analysis. Some work on this project is currently in progress in collaboration with R. J. LeVeque and D. Calhoun.

# BIBLIOGRAPHY

[1] M. Abbett. Mach disk in underexpanded exhaust plumes. *AIAA Journal*, 9(3):512–514, 1971.

[2] R. Abgrall. Generalisation of the Roe scheme for the computation of mixture of perfect gases. *Rech. Aérospat.*, 67:31–43, 1988. English edition.

[3] R. Abgrall. How to prevent pressure oscillations in multicomponent flow calculations: A quasi-conservative approach. *J. Comput. Phys.*, 125:150–160, 1996.

[4] R. Abgrall and S. Karni. Computations of compressible multifluids. *J. Comput. Phys.*, 169:594–623, 2001.

[5] G. Allaire, S. Clerc, and S. Kokh. A five-equation model for the simulation of interfaces between compressible fluids. *J. Comput. Phys.*, 181:577–616, 2002.

[6] A. A. Amsden and F. H. Harlow. KACHINA: An Eulerian computer program for multifield fluid flows. Los Alamos National Laboratory, Report LA-5680, 1974.

[7] D. Aregba-Driollet and R. Natalini. Convergence of relaxation schemes for conservation laws. *Appl. Anal.*, 61:163–193, 1996.

[8] M. Arora and P. L. Roe. On postshock oscillations due to shock capturing schemes in unsteady flow. *J. Comput. Phys.*, 130:1–24, 1997.

[9] M. R. Baer and J. W. Nunziato. A two-phase mixture theory for the deflagration-to-detonation transition (DDT) in reactive granular materials. *Intl. J. Multiphase Flows*, 12:861–889, 1986.

[10] D. Bale, R. J. LeVeque, S. Mitran, and J. A. Rossmanith. A wave-propagation method for conservation laws and balance laws with spatially varying flux functions. *SIAM J. Sci. Comput.*, 24:955–978, 2002.

[11] J. R. Banister. Pressure waves generated by the Mount St. Helens eruption. *J. Geophys. Res.*, 89(D3):4895–4904, 1984.

[12] D. J. Benson. Computational methods in Lagrangian and Eulerian hydrocodes. *Comput. Meth. Appl. Mech. Eng.*, 99:235–394, 1992.

[13] M. J. Berger and R. J. LeVeque. Adaptive mesh refinement using wave-propagation algorithms for hyperbolic systems. *SIAM J. Numer. Anal.*, 35:2298–2316, 1998.

[14] F. Bouchut. On zero pressure gas dynamics. In B. Perthame, editor, *Advances in Kinetic Theory and Computing*, volume 22 of *Ser. Adv. Math. Appl. Sci.*, pages 171–190. World Scientific, 1994.

[15] F. Bouchut. Construction of BGK models with a family of kinetic entropies for a given system of conservation laws. *J. Stat. Phys.*, 95:113–170, 1999.

[16] F. Bouchut. Entropy satisfying flux vector splittings and kinetic BGK models. *Numer. Math.*, 94:623–672, 2003.

[17] F. Bouchut and F. James. Duality solutions for pressureless gases, monotone scalar conservation laws, and uniqueness. *Commun. Math. Phys.*, 24:2173–2189, 1999.

[18] F. Bouchut, S. Jin, and X. Li. Numerical approximations of pressureless and isothermal gas dynamics. *SIAM J. Numer. Anal.*, 41:135–158, 2003.

[19] Y. Brenier. Averaged multivalued solutions for scalar conservation laws. *SIAM J. Num. Anal.*, 21:1013–1037, 1984.

[20] Y. Brenier and E. Grenier. Sticky particles and scalar conservation laws. *SIAM J. Numer. Anal.*, 35:2317–2328, 1998.

[21] T. Buffard, T. Gallouët, and J.-M. Hérard. A sequel to a rough Godunov scheme: application to real gases. *Computers and Fluids*, 29:813–847, 2000.

[22] A. Burgisser and G. W. Bergantz. Reconciling pyroclastic flow and surge: the multiphase physics of pyroclastic density currents. *Earth Planet. Sci. Lett.*, 202:405–418, 2002.

[23] M. I. Bursik and A. W. Woods. The dynamics and thermodynamics of large ash flows. *Bull. Volcanol.*, 58:175–193, 1996.

[24] H. B. Callen. *Thermodynamics and an Introduction to Thermostatistics*. John Wiley & Sons, 1985.

[25] S. N. Carey, H. Sigurdsson, and R. S. J. Sparks. Experimental studies of particle-laden plumes. *J. Geophys. Res.*, 93:15314–15328, 1988.

[26] A. Chalabi. Convergence of relaxation schemes for hyperbolic conservation laws with stiff source terms. *Math. Comput.*, 68:955–970, 1999.

[27] Y. C. Chang, T. Y. Hou, B. Merriman, and S. Osher. A level set formulation of Eulerian interface capturing methods for incompressible fluid flows. *J. Comput. Phys.*, 124:449–464, 1996.

[28] S. Chapman and T. G. Cowling. *The Mathematical Theory of Nonuniform Gases*. Cambridge University Press, 1970.

[29] G. Q. Chen, C. D. Levermore, and T. P. Liu. Hyperbolic conservation laws with stiff relaxation terms and entropy. *Comm. Pure Appl. Math.*, 47:787–830, 1994.

[30] G.-Q. Chen and H. Liu. Formation of $\delta$-shocks and vacuum states in the vanishing pressure limit of solutions to the Euler equations for isentropic fluids. *SIAM J. Math. Anal.*, 34:925–938, 2003.

[31] H.-T. Chen and R. Collins. Shock wave propagation past an ocean surface. *J. Comput. Phys.*, 7:89–101, 1971.

[32] A. B. Clarke, A. Neri, B. Voight, G. Macedonio, and T. H. Druitt. Computational modelling of the transient dynamics of the August 1997 Vulcanian explosions at Soufrière Hills Volcano, Montserrat: influence of initial conduit conditions on near-vent pyroclastic dispersion. In T. H. Druitt and B. P. Kokelaar, editors, *The Eruption of Soufrière Hills Volcano, Montserrat, from 1995 to 1999. Geological Society, London, Memoirs*, volume 21, pages 319–348. The Geological Society of London, 2002.

[33] A. B. Clarke, B. Voight, A. Neri, and G. Macedonio. Transient dynamics of vulcanian explosions and column collapse. *Nature*, 415:897–901, 2002.

[34] J.-P. Cocchi and R. Saurel. A Riemann problem based method for the resolution of compressible multimaterial flows. *J. Comput. Phys.*, 137:265–298, 1997.

[35] G. Cochran and J. Chan. Shock initiation and detonation models in one and two dimensions. Lawrence Livermore National Laboratory Report, 1979.

[36] P. Colella and H. M. Glaz. Efficient solution algorithms for the Riemann problem for real gases. *J. Comput. Phys.*, 59:264–284, 1985.

[37] P. Colella and P. Woodward. The piecewise-parabolic method (PPM) for gas-dynamical simulations. *J. Comput. Phys.*, 54:174–201, 1984.

[38] F. Coquel, K. El Amine, E. Godlewski, B. Perthame, and P. Rascle. A numerical method using upwind schemes for the resolution of two-phase flows. *J. Comput. Phys.*, 136:272–288, 1997.

[39] F. Coquel and B. Perthame. Relaxation of energy and approximate Riemann solvers for general pressure laws in fluid dynamics. *SIAM J. Numer. Anal.*, 35:2223–2249, 1998.

[40] R. Courant and K. O. Friedrichs. *Supersonic Flow and Shock Waves.* Springer, 1948.

[41] R. Courant, K. O. Friedrichs, and H. Lewy. Über die partiellen Differenzengleichungen der mathematischen Physik. *Math. Ann.*, 100:32–74, 1928.

[42] R. Courant, K. O. Friedrichs, and H. Lewy. On the partial difference equations of mathematical physics. *IBM Journal*, 11:215–234, 1967.

[43] S. Dartevelle. Numerical modeling of geophysical granular flows: 1. A comprehensive approach to granular rheologies and geophysical multiphase flows. *Geochem. Geophys. Geosyst.*, 5(8), 2004. doi:10:1029/2003GC000636.

[44] S. Dartevelle, W. I. Rose, J. Stix, K. Kelfoun, and J. W. Vallance. Numerical modeling of geophysical granular flows: 2. Computer simulations of plinian clouds and pyroclastic flows and surges. *Geochem. Geophys. Geosyst.*, 5(8), 2004. doi:10:1029/2003GC000637.

[45] S. F. Davis. An interface tracking method for hyperbolic systems of conservation laws. *Appl. Numer. Math.*, 10:447–472, 1992.

[46] R. P. Denlinger. A model for generation of ash clouds by pyroclastic flows, with application to the 1980 eruption at Mount St. Helens, Washington. *J. Geophys. Res.*, 92:10284–10298, 1987.

[47] R. L. Deschambault and I. I. Glass. An update on non-stationary oblique shock-wave reflections: actual isopycnics and numerical experiments. *J. Fluid Mech.*, 131:27–57, 1983.

[48] F. Dobran. Liquid and gas phase distributions in a jet with phase change. *Int. J. Heat Transfer*, 110:955–960, 1988.

[49] F. Dobran. *Volcanic Processes*. Kluwer Academic, 2001.

[50] F. Dobran, F. Barberi, and C. Casarosa. *Modeling of Volcanological Processes and Simulation of Volcanic Eruptions*. Gruppo Nazionale per la Vulcanologia. Giardini, Pisa, 1990.

[51] F. Dobran, A. Neri, and G. Macedonio. Numerical simulation of collapsing volcanic columns. *J. Geophys. Res.*, 98:4231–4259, 1993.

[52] R. Donat and A. Marquina. Capturing shock reflections: an improved flux formula. *J. Comput. Phys.*, 125:42–58, 1996.

[53] R. Donat, A. Marquina, and Y. Stiriba. Equilibrium real gas computations using Marquina's scheme. GrAN Report, València, 2000.

[54] D. A. Drew and S. L. Passman. *Theory of Multicomponent Fluids*. Springer, 1998.

[55] G. Dubois and G. Mehlman. A non-parameterized entropy correction for Roe's approximate Riemann solver. *Numer. Math.*, 73:169–208, 1996.

[56] J. Dufek and G. W. Bergantz. Transient two-dimensional dynamics in the upper conduit of a rhyolitic eruption: A comparison of closure models for the granular stress. Preprint, 2003.

[57] B. Einfeldt. On Godunov-type methods for gas dynamics. *SIAM J. Num. Anal.*, 25:294–318, 1988.

[58] B. Engquist and S. Osher. Stable and entropy satisfying approximations for transonic flow calculations. *Math. Comp.*, 34:45–75, 1980.

[59] R. P. Fedkiw, T. Aslam, B. Merriman, and S. Osher. A non-oscillatory Eulerian approach to interfaces in multimaterial flows (the ghost fluid method). *J. Comput. Phys.*, 152:457–492, 1999.

[60] J. A. Fejer and J. W. Miles. On the stability of a plane vortex sheet with respect to three-dimensional disturbances. *J. Fluid Mech.*, 15:335–336, 1963.

[61] T. Gallouët, J.-M Hérard, and N. Seguin. Some recent finite volume schemes to compute Euler equations using real gas EOS. *Int. J. Numer. Meth. Fluids*, 39-12:1073–1138, 2002.

[62] D. Gidaspow. *Multiphase Flow and Fluidization: Continuum and Kinetic Theory Descriptions.* Academic Press, New York, 1994.

[63] T. Gimse and N. H. Risebro. Riemann problems with a discontinuous flux function. In B. Engquist and B. Gustafsson, editors, *Proc. Third Int'l Conf. Hyperbolic Problems*, pages 488–502. Studentlitteratur, 1990.

[64] P. Glaister. An approximate linearized Riemann solver for the Euler equations for real gases. *J. Comput. Phys.*, 74:382–408, 1988.

[65] P. Glaister. An efficient numerical method for compressible flows of a real gas using arithmetic averaging. *Compututers Math. Applic.*, 28:97–113, 1994.

[66] H. M. Glaz, P. Colella, I. I. Glass, and R. L. Deschambault. A numerical study of oblique shock-wave reflections with experimental comparisons. In *Proceedings of the Royal Society of London. Series A, Mathematical and Physical Sciences*, volume 398, pages 117–140, 1985.

[67] J. Glimm, J. Grove, X. L. Li, K.-M. Shyue, Y. Zeng, and Q. Zhang. Three-dimensional front tracking. *SIAM J. Sci. Comput.*, 19:703–727, 1998.

[68] E. Godlewski and P.-A. Raviart. *Numerical Approximation of Hyperbolic Systems of Conservation Laws.* Springer-Verlag, New York, 1996.

[69] S. K. Godunov. A difference method for numerical calculation of discontinuous solutions of the equations of hydrodynamics. *Mat. Sb.*, 47:271–306, 1959.

[70] L. Gosse and A. E. Tzavaras. Convergence of relaxation schemes to the equations of elastodynamics. *Math. Comput.*, 70:555–577, 2000.

[71] B. Grossman and R. W. Walters. Analysis of flux-split algorithms for Euler's equations with real gases. *AIAA Journal*, 27:524–531, 1989.

[72] J. Grove and R. Menikoff. Anomalous reflection of a shock wave at a fluid interface. *J. Fluid. Mech.*, 219:313–336, 1990.

[73] J.-F. Haas and B. Sturtevant. Interaction of weak shock waves with cylindrical and spherical gas inhomogeneities. *J. Fluid Mech.*, 181:41–76, 1987.

[74] R. K. S. Hankin. The Euler equations for multiphase compressible flow in conservation form. *J. Comput. Phys.*, 172:808–826, 2001.

[75] F. H. Harlow and A. A. Amsden. Numerical calculation of multiphase fluid flow. *J. Comput. Phys.*, 17:19–52, 1975.

[76] A. Harten. High resolution schemes for hyperbolic conservation laws. *J. Comput. Phys.*, 49:357–393, 1983.

[77] A. Harten and J. M. Hyman. Self-adjusting grid methods for one-dimensional hyperbolic conservation laws. *J. Comput. Phys.*, 50:235–269, 1983.

[78] A. Harten, P. D. Lax, and B. van Leer. On upstream differencing and Godunov-type schemes for hyperbolic conservation laws. *SIAM Review*, 25:35–61, 1983.

[79] M. Herzog, H.F. Graf, and J. M. Oberhuber. The effect of phase changes of water in the development of volcanic plumes. *J. Volcanol. Geotherm. Res.*, 87:55–74, 1998.

[80] C. W. Hirt and B. D. Nichols. Volume of fluid (VOF) method for the dynamics of free boundaries. *J. Comput. Phys.*, 39:201–225, 1981.

[81] L. Hsiao. *Quasilinear Hyperbolic Systems and Dissipative Mechanisms*. World Scientific, Singapore, 1997.

[82] F. Huang and Z. Wang. Well posedness for pressureless flow. *Commun. Math. Phys.*, 222:117–146, 2001.

[83] H. E. Huppert, J. S. Turner, S. N. Carey, and M. A. Hallworth. A laboratory simulation of pyroclastic flows down slopes. *J. Volcanol. Geotherm. Res.*, 30:179–199, 1986.

[84] A. In. Numerical evaluation of an energy relaxation method for inviscid real fluids. *SIAM J. Sci. Comput.*, 21:340–365, 1999.

[85] M. Ishii. *Thermo-fluid Dynamic Theory of Two-phase flow*. Eyrolles, Paris, 1975.

[86] M. I. Ivings, D. M. Causon, and E. F. Toro. On Riemann solvers for compressible liquids. *Int. J. Numer. Meth. Fluids*, 28:395–418, 1998.

[87] J. W. Jacobs. Shock-induced mixing of a light-gas cylinder. *J. Fluid Mech.*, 132:91–107, 1997.

[88] JANNAF. *Handbook of rocket exhaust plume technology, Publ. 263*, chapter 2. Chemical Propulsion Information Agency, Washington, D.C., 1975.

[89] P. Jenny and B. Müller. Rankine-Hugoniot-Riemann solver considering source terms and multi-dimensional effects. *J. Comp. Phys.*, 145:575–610, 1998.

[90] P. Jenny, B. Müller, and H. Thomann. Correction of conservative Euler solvers for gas mixture. *J. Comput. Phys.*, 132:91–107, 1997.

[91] S. Jin and M. A. Katsoulakis. Relaxation approximations to front propagation. *J. Diff. Equations*, 138:380–387, 1997.

[92] S. Jin and J.-G. Liu. The effects of numerical viscosities: I. Slowly moving shocks. *J. Comput. Phys.*, 126:373–389, 1996.

[93] S. Jin and Z. P. Xin. The relaxation schemes for systems of conservation laws in arbitrary space dimensions. *Comm. Pure Appl. Math.*, 48:235–276, 1995.

[94] J. B. Johnson. Generation and propagation of infrasonic airwaves from volcanic explosions. *J. Volcanol. Geotherm. Res.*, 121:1–14, 2003.

[95] A.K. Kapila, R. Menikoff, J. B. Bdzil, S. F. Son, and D.S. Stewart. Two-phase modeling of deflagration-to-detonation transition in granular materials: Reduced equations. *Physics of Fluids*, 13:3002–3024, 2001.

[96] S. Karni. Multicomponent flow calculations by a consistent primitive algorithm. *J. Comput. Phys.*, 112:31–43, 1994.

[97] S. Karni. Hybrid multifluid algorithms. *SIAM J. Sci. Comput.*, 17:1019–1039, 1996.

[98] S. Karni and S. Canic. Computation of slowly moving shocks. *J. Comput. Phys.*, 136:132–139, 1997.

[99] M. A. Katsoulakis and A. E. Tzavaras. Contractive relaxation systems and the scalar multidimensional conservation laws. *Comm. Partial Differential Equations*, 22:195–223, 1997.

[100] S. W. Kieffer and B. Sturtevant. Laboratory studies of volcanic jets. *J. Geophys. Res.*, B10(89):8253–8268, 1984.

[101] C. Klingenberg and N. H. Risebro. Convex conservation laws with discontinuous coefficients. Existence, uniqueness and asymptotic behavior. *Comm. Partial Differential Equations*, 20:1959–1990, 1995.

[102] J. G. Knudsen and D. L. Katz. *Fluid Mechanics and Heat Transfer*. McGraw-Hill, New York, 1958.

[103] A. Kurganov and E. Tadmor. New high-resolution central schemes for nonlinear conservation laws and convection-diffusion equations. *J. Comput. Phys.*, 160:214–282, 2000.

[104] M. A. Lagmay, D. M. Pyle, B. Dade, and C. Oppenheimer. Control of crater morphology on flow path direction of Soufrière type pyroclastic flows. *J. Geophys. Res.*, B4(104):7169–7181, 1999.

[105] L. D. Landau and E. M. Lifshitz. *Fluid Mechanics*. Pergamon Press, 1959.

[106] B. Larroutourou and L. Fezoui. On the equations of multi-component perfect or real gas inviscid flow. In Carasso, Charrier, Hanouzet, and Joly, editors, *Nonlinear Hyperbolic Problems*, volume 1402 of *Lecture Notes in Mathematics*. Springer-Verlag, 1989.

[107] B. Larrouturou. How to preserve the mass fraction positive when computing compressible multicomponent flows. *J. Comput. Phys.*, 95:59–84, 1991.

[108] B. Larrouturou. How to preserve the mass fractions positivity when computing compressible multicomponent flows. *J. Comput. Phys.*, 95:59–84, 1991.

[109] C. Lattanzio and D. Serre. Convergence of a relaxation scheme for hyperbolic systems of conservation laws. *Numer. Math.*, 88:121–134, 2001.

[110] P. D. Lax. *Hyperbolic Systems of Conservation Laws and the Mathematical Theory of Shock Waves*. SIAM Regional Conference Series in Applied Mathematics, #11, 1972.

[111] P. D. Lax and X. D. Liu. Solution of two dimensional Riemann problem of gas dynamics by positive schemes. *SIAM J. Sci. Comput.*, 19:319–340, 1998.

[112] E. L. Lee, H. C. Horning, and J. W. Kury. Adiabatic expansion of high explosives detonation products. Lawrence Radiation Lab., University of California, Livermore, TID 4500-UCRL 50422, 1968.

[113] P. G. LeFloch and Nedelec. Explicit formulas for weighted scalar nonlinear hyperbolic conservation laws. *Trans. Amer. Math. Soc.*, 308:667–683, 1988.

[114] A. Letellier and A. Forestier. Le problème de Riemann en fluide quelconque. Internal Report CEA-DMT 93/451, 1993.

[115] R. J. LeVeque. CLAWPACK software. `http://www.amath.washington.edu/~claw`.

[116] R. J. LeVeque. A large time step generalization of Godunov's method for systems of conservation laws. *SIAM J. Num. Anal.*, 22:1051–1073, 1985.

[117] R. J. LeVeque. High resolution finite volume methods on arbitrary grids via wave propagation. *J. Comput. Phys.*, 78:36–63, 1988.

[118] R. J. LeVeque. *Numerical Methods for Conservation Laws*. Birkhäuser-Verlag, 1990.

[119] R. J. LeVeque. High-resolution conservative algorithms for advection in incompressible flow. *SIAM J. Numer. Anal.*, 33:627–665, 1996.

[120] R. J. LeVeque. Wave propagation algorithms for multi-dimensional hyperbolic systems. *J. Comput. Phys.*, 131:327–353, 1997.

[121] R. J. LeVeque. Balancing source terms and flux gradients in high-resolution Godunov methods: The quasi-steady wave-propagation algorithm. *J. Comput. Phys.*, 146:346–365, 1998.

[122] R. J. LeVeque. *Finite Volume Methods for Hyperbolic Problems*. Cambridge University Press, 2002.

[123] R. J. LeVeque. The dynamics of pressureless dust clouds and delta waves. *J. Hyperbolic Diff. Eq.*, 1:315–327, 2004.

[124] R. J. LeVeque and M. Pelanti. A class of approximate Riemann solvers and their relation to relaxation schemes. *J. Comput. Phys.*, 172:572–591, 2001.

[125] R. J. LeVeque and K.-M. Shyue. Two-dimensional front tracking based on high resolution wave propagation methods. *J. Comput. Phys.*, 123:354–368, 1996.

[126] J. Li and T. Zhang. On the initial-value problem for zero-pressure gas dynamics. In R. Jeltsch, editor, *Proc. 7'th Intl. Conf. on Hyperbolic Problems*, pages 629–640. Birkhäuser Verlag, 1998.

[127] H. W. Liepmann and A. Roshko. *Elements of Gas Dynamics*. Wiley, 1957.

[128] M.-S. Liou, B. van Leer, and J.-S. Shuen. Splitting of inviscid fluxes for real gases. *J. Comput. Phys.*, 87:1–24, 1990.

[129] W. Lipman and D. R. Mullineaux. The 1980 eruption at Mount St. Helens, Washington. U.S. Geol. Surv., 1981.

[130] H. L. Liu and G. Warnecke. Convergence rates for relaxation schemes approximating conservation laws. *SIAM J. Numer. Anal.*, 37:1316–1337, 2000.

[131] T. P. Liu. Hyperbolic conservation laws with relaxation. *Comm. Math. Phys.*, 108:153–175, 1987.

[132] X. D. Liu and P. D. Lax. Positive schemes for solving multi-dimensional hyperbolic systems of conservation laws. *Computational Fluid Dynamics Journal*, 5:133–156, 1996.

[133] E. S. Love, C. E. Grisby, L. P. Lee, and M. J. Woodling. Experimental and theoretical studies of axisymmetric free jets. NASA Tech. Report No. TR R-6, 1959.

[134] A. Majda and R. L. Pego. Stable viscosity matrices for systems of conservation laws. *J. Diff. Eq.*, 56:229–262, 1985.

[135] D.-K. Mao. A treatment of discontinuities for finite difference methods in the two-dimensional case. *J. Comput. Phys.*, 104:377–397, 1993.

[136] F. E. Marble. Dynamics of dusty gases. *Ann. Rev. Fluid Mech.*, 2:397–446, 1970.

[137] F. E. Marble, G. J. Hendricks, and E. E. Zukoski. Turbolent reactive flow. In R. Borghi and S. N. B. Murphy, editors, *Lectures Notes in Engineering*, volume 40, page 32. Springer-Verlag, 1989.

[138] R. Menikoff and B. J. Plohr. The Riemann problem for fluid flow of real materials. *Rev. Modern Phys.*, 61:75–130, 1989.

[139] T. Mikumo and B. A. Bolt. Excitation mechanisms of atmospheric pressure waves from the 1980 Mount St. Helens eruption. *Geophys. J. R. astr. Soc.*, 81:445–461, 1985.

[140] J. W. Miles. On the disturbed motion of a plane vortex sheet. *J. Fluid Mech.*, 4:538–552, 1958.

[141] G. H. Miller and E. G. Puckett. A high-order Godunov method for multiple condensed phases. *J. Comput. Phys.*, 128:134–164, 1996.

[142] H. Miura and I. I. Glass. On a dusty-gas shock-tube. In *Proceedings of the Royal Society of London. Series A, Mathematical and Physical Sciences*, volume 382, pages 373–388, 1982.

[143] M. Montagné, H. C. Yee, and M. Vinokur. Comparative study of high resolution shock-capturing schemes for a real gas. *AIAA Journal*, 27:1332–1346, 1988.

[144] P. Montarnal and C.-W. Shu. Real gas computation using an energy relaxation method and high-order WENO schemes. *J. Comput. Phys.*, 148:59–80, 1999.

[145] M. M. Morrissey and B. A. Chouet. Burst conditions of explosive volcanic eruptions recorded on microbarographs. *Science*, 275:1290–1293, 1997.

[146] L. Mottura, L.Vigevano, and M. Zaccanti. An evaluation of Roe's scheme generalizations for equilibrium real gas flows. *J. Comput. Phys.*, 138:354–399, 1997.

[147] W. Mulder, S. Osher, and J. A. Sethian. Computing interface motion in compressible gas dynamics. *J. Comput. Phys.*, 100:209–228, 1992.

[148] A. Murrone and H. Guillard. A five equation reduced model for compressible two phase flow problems. *J. Comput. Phys.*, 202:664–698, 2005.

[149] R. Natalini. Convergence to equilibrium for the relaxation approximations of conservation laws. *Comm. Pure Appl. Math.*, 49:795–823, 1996.

[150] A. Neri and F. Dobran. Influence of eruption parameters on the thermofluid dynamics of collapsing volcanic columns. *J. Geophys. Res.*, 99:11833–11857, 1994.

[151] A. Neri and G. Macedonio. Numerical simulation of collapsing volcanic columns with particles of two sizes. *J. Geophys. Res.*, 101:8153–8174, 1996.

[152] A. Neri and G. Macedonio. Physical modeling of collapsing volcanic columns and pyroclastic flows. In Scarpa/Tilling, editor, *Monitoring and Mitigation of Volcano Hazards*, pages 389–427. Springer-Verlag, 1996.

[153] A. Neri, G. Macedonio, D. Gidaspow, and T. Esposti Ongaro. Multiparticle simulation of collapsing volcanic columns and pyroclastic flows. VSG Report No. 2001-2, Volcano Simulation Group, Istituto Nazionale di Geofisica e Vulcanologia, 2001.

[154] A. Neri, A. Di Muro, and M. Rosi. Mass partition during collapsing and transitional columns by using numerical simulations. *J. Volcanol. Geotherm. Res.*, 115:1–18, 2002.

[155] A. Neri, T. Esposti Ongaro, G. Macedonio, and D. Gidaspow. Multiparticle simulation of collapsing volcanic columns and pyroclastic flows. *J. Geophys. Res.*, B4(108):1–22, 2003.

[156] A. Neri, P. Papale, and G. Macedonio. The role of magma composition and water content in explosive eruptions, 2. Pyroclastic dispersion dynamics. *J. Volcanol. Geotherm. Res.*, 87:95–115, 1998.

[157] H. Nessyahu and E. Tadmor. Non-oscillatory central differencing for hyperbolic conservation laws. *J. Comput. Phys.*, 87:408–463, 1990.

[158] J. M. Oberhuber, M. Herzog, H. F. Graf, and K. Schwanke. Volcanic plumes simulation on large scales. *J. Volcanol. Geotherm. Res.*, 87:29–53, 1998.

[159] T. Esposti Ongaro and A. Neri. Flow patterns of overpressured volcanic jets. European Geophysical Society, XXIV General Assembly, The Hague, 19-23 April 1999.

[160] T. Esposti Ongaro, A. Neri, M. Todesco, and G. Macedonio. Pyroclastic flow assessment at Vesuvius (Italy) by using numerical modeling. II. Analysis of flow variables. *Bull. Volcanol.*, 64:178–191, 2002.

[161] S. Osher and F. Solomon. Upwind difference schemes for hyperbolic systems of conservation laws. *Math. Comp.*, 38:339–374, 1982.

[162] P. Papale, A. Neri, and G. Macedonio. The role of magma composition and water content in explosive eruptions, 1. Conduit ascent dynamics. *J. Volcanol. Geotherm. Res.*, 87:75–93, 1998.

[163] M. Pelanti. Pressure linearization method for the computation of real fluids. In T. Hou and E. Tadmor, editors, *Hyperbolic Problems: Theory, Numerics, Applications, Proc. 9'th Intl. Conf. on Hyperbolic Problems*, pages 797–806. Springer, 2002.

[164] M. Pelanti, L. Quartapelle, and L. Vigevano. Low dissipation entropy fix for positivity preserving Roe's scheme. In E. F. Toro, editor, *Godunov Methods: Theory and Applications*. Kluwer/Plenum Academic Press, 2001.

[165] J. J. Quirk and S. Karni. On the dynamics of a shock-bubble interaction. ICASE Report No. 94-75, NASA Langley Research Center, 1994.

[166] J. W. Reed. Air pressure waves from Mount St. Helens eruptions. *J. Volcanol. Geotherm. Res.*, 92:11979–11982, 1987.

[167] T. D. Riney. Numerical evaluation of hypervelocity impact phenomena. In R. Kinslow, editor, *High-Velocity Impact Phenomena*, page p. 158. Academic Press, 1970.

[168] W. C. Rivard and M. D. Torrey. K-FIX: A computer program for transient two-dimensional, two-fluid flow. LA-NUREG-6623, Los Alamos Natl. Lab., N. M., 1977.

[169] P. L. Roe. Approximate Riemann solvers, parameter vectors, and difference schemes. *J. Comput. Phys.*, 43:357–372, 1981.

[170] P. L. Roe. A new approach to computing discontinuous flows of several ideal gases. Technical Report, Cranfield Institute of Technology, 1984. Unpublished.

[171] G. Rudinger. Some effects of finite particle volume on the dynamics of gas-particle mixtures. *AIAA J.*, 3:1217–1222, 1965.

[172] Yu. G. Rykov, Ya. G. Sinai, and E. Weinan. Generalized variational principles, global weak solutions and behavior with random initial data for systems of conservation laws arising in adhesion particle dynamics. *Commun. Math. Phys.*, 177:349–380, 1996.

[173] L. Sainsaulieu. An Euler system modeling vaporizing sprays. In A. L. Kuhl, J.-C. Leger, A. A. Borisov, and W. A. Sirignano, editors, *Dynamics of Heterogeneous Combustion and Reacting Systems (Progress Series in Aeronautics and Astronautics)*, volume 152, pages 280–305. American Institute of Aeronautics and Astronautics, Washington DC, 1993.

[174] L. Sainsaulieu. Finite volume approximation of two-phase fluid flows based on an approximate Roe-type Riemann solver. *J. Comput. Phys.*, 121:1–28, 1995.

[175] L. Sainsaulieu. Traveling waves solution of convection-diffusion systems whose convection terms are weakly nonconservative: application to the modeling of two-phase fluid flows. *SIAM J. Appl. Math.*, 55:1552–1576, 1995.

[176] T. Saito. Numerical analysis of dusty-gas flows. *J. Comput. Phys.*, 176:129–144, 2002.

[177] R. Saurel and R. Abgrall. A multiphase Godunov method for compressible multifluid and multiphase flows. *J. Comput. Phys.*, 150:425–467, 1999.

[178] R. Saurel and R. Abgrall. A simple method for compressible multifluid flow. *SIAM J. Sci. Comput.*, 71:1115–1145, 1999.

[179] R. Saurel and O. LeMetayer. A multiphase model for compressible flows with interfaces, shocks, detonation waves and cavitation. *J. Fluid Mech.*, 431:239–271, 2001.

[180] C. Searcy, K. Dean, and W. Stringer. PUFF: A high-resolution volcanic ash tracking model. *J. Volcanol. Geotherm. Res.*, 80:1–16, 1998.

[181] M. F. Sheridan. Emplacement of pyroclastic flows: a review. *Geol. Soc. Am.*, 180:125–136, 1979. Spec. Pap.

[182] K.-M. Shyue. An efficient shock-capturing algorithm for compressible multicomponent problems. *J. Comput. Phys.*, 142:208–242, 1998.

[183] K.-M. Shyue. A fluid-mixture type algorithm for compressible multicomponent flow with van der Waals equation of state. *J. Comput. Phys.*, 156:43–88, 1999.

[184] K.-M. Shyue. A fluid-mixture type algorithm for compressible multicomponent flow with Mie–Grüneisen equation of state. *J. Comput. Phys.*, 171:678–707, 2001.

[185] R. S. J. Sparks and L. Wilson. A model for the formation of ignimbrite by gravitational column collapse. *J. Geol. Soc. London*, 132:441–451, 1976.

[186] R. S. J. Sparks, L. Wilson, and G. Hulme. Theoretical modeling of the generation, movement, and emplacement of pyroclastic flows. *J. Geophys. Res.*, 83:1727–1739, 1978.

[187] H. B. Stewart and B. Wendroff. Two-phase flow: models and methods. *J. Comput. Phys.*, 56:363–409, 1984.

[188] R. Strachey. On the airwaves and sounds caused by the eruption of Krakatoa in August 1883. In G. J. Symons, editor, *The Eruption of Krakatoa and Subsequent Phenomena: Report of the Krakatoa Committee of the Royal Society*, London, 1888. Trubner.

[189] M. Syamlal. MFIX documentation: Numerical technique. DOE/MC/31346-5824, DE98002029, U.S. Department of Energy, Washington, D. C., 1998.

[190] M. Syamlal, W. Rogers, and T. J. O'Brien. MFIX documentation: Theory guide. DOE/MTEC-94/1004, DE9400,097, U.S. Department of Energy, Washington, D. C., 1993.

[191] Pinatubo Volcano Observatory Team. *EOS*, 72(49):545, 1991.

[192] M. Todesco, A. Neri, T. Esposti Ongaro, , P. Papale, G. Macedonio, R. Santacroce, and A. Longo. Pyroclastic flow assessment at Vesuvius (Italy) by using numerical modeling. I. Large scale dynamics. *Bull. Volcanol.*, 64:155–177, 2002.

[193] V. Ton. Improved shock-capturing methods for multicomponent and reacting flows. *J. Comput. Phys.*, 128:237–253, 1996.

[194] E. F. Toro. *Riemann Solvers and Numerical Methods for Fluid Dynamics*. Springer-Verlag, Berlin, Heidelberg, 1997.

[195] A. Tveito and R. Winther. The solution of nonstrictly hyperbolic conservation laws may be hard to compute. *SIAM J. Sci. Comput.*, 16:320–329, 1995.

[196] G. A. Valentine and K. H. Wohletz. Environmental hazards of pyroclastic flows determined by numerical models. *Geology*, 17:641–644, 1989.

[197] G. A. Valentine and K. H. Wohletz. Numerical models of Plinian eruption columns and pyroclastic flows. *J. Geophys. Res.*, 94:1867–1887, 1989.

[198] G. A. Valentine, K. H. Wohletz, and S. W. Kieffer. Sources of unsteady column dynamics in pyroclastic flow eruptions. *J. Geophys. Res.*, 96:21887–21892, 1991.

[199] G. A. Valentine, K. H. Wohletz, and S. W. Kieffer. Effects of topography of facies and compositional zonation in caldera-related ignimbrites. *Geol. Soc. Am. Bull.*, 104:154–165, 1992.

[200] J. D. van der Waals. *On the continuity of the gaseous and liquid states*, volume XIV. North-Holland, 1988. Reprinted.

[201] M. Vinokur and M. Montagné. Generalized flux-vector splitting and Roe average for an equilibrium real gas. *J. Comput. Phys.*, 89:276–300, 1990.

[202] G. B. Wallis. *One-Dimensional Two-Phase Flow*. McGraw-Hill, New York, 1969.

[203] C. J. N. Wilson. The role of fluidization in the emplacement of pyroclastic flows: an experimental approach. *J. Volcanol. Geother. Res.*, 8:231–249, 1980.

[204] L. Wilson. Explosive volcanic eruption, III. Plinian eruption columns. *Geophys. J. R. Astron. Soc.*, 45:543–556, 1976.

[205] L. Wilson and G. P. L. Walker. Explosive volcanic eruption, VI. Ejecta dispersal in Plinian eruptions: The control of eruption conditions and atmospheric properties. *Geophys. J. R. Astron. Soc.*, 89:657–689, 1987.

[206] K. H. Wohletz, T. R. McGetchin, M. T. Sanford II, and E. M. Jones. Hydrodynamic forming of caldera-forming eruptions: numerical models. *J. Geophys. Res.*, 89:8269–8285, 1984.

[207] K. H. Wohletz and G. A. Valentine. Computer simulations of explosive volcanic eruption. In M. P. Ryan, editor, *Magma transport and storage*, pages 113–135, New York, 1990. John Wiley.

[208] A. W. Woods. The fluid dynamics and thermodynamics of eruption columns. *Bull. Volcanol.*, 50:169–193, 1988.

[209] A. W. Woods. Observations and models of volcanic eruption columns. In J. S. Gilbert and R. S. J. Sparks, editors, *The Physics of Volcanic Explosive Eruptions*, volume 145, pages 91–114. Geological Society, London, 1998. Special Publication.

[210] A. W. Woods and S. M. Bower. The decompression of volcanic jets in a crater during explosive volcanic eruptions. *Earth Planet. Sci. Lett.*, 131:7169–7181, 1995.

[211] A. W. Woods and M. I. Bursik. A laboratory study of ash flows. *J. Geophys. Res.*, 99:4375–4394, 1994.

[212] H. C. Yee. Upwind and symmetric shock-capturing schemes. NASA Ames Technical Memorandum 89464, 1987.

# VITA

Marica Pelanti was born in Milan, Italy, on the 7th of August 1974. She earned her *Laurea* degree in Aerospace Engineering Magna cum Laude at Politecnico di Milano in 1999. She then received her Doctorate in Applied Mathematics at the University of Washington in 2005.